Regional modeling of short-lived atmospheric pollutants (aerosols, ozone) in the Arctic

Louis Marelle

UNIVERSITÉ PIERRE ET MARIE CURIE

ÉCOLE DOCTORALE
DES SCIENCES DE L'ENVIRONNEMENT D'ILE DE FRANCE

T H È S E

pour obtenir le grade de

Docteur en Sciences

de l'Université Pierre et Marie Curie

Spécialité : Physique de l'atmosphère

Présentée et soutenue par

Louis MARELLE

Modélisation régionale des polluants à courte durée de vie (aérosols, ozone) en Arctique

Thèse dirigée par Kathy S. LAW
préparée au Laboratoire ATmosphère, Milieux, Observations Spatiales
financée par TOTAL S.A. (convention CIFRE N 2012/0999)

Jury :

Président :	François RAVETTA
Rapporteurs :	Terje K. BERNTSEN
	Karine SARTELET
Examinateur :	Alfons SCHWARZENBOECK
Directrice :	Kathy S. LAW
Co-Directeur :	Jean-Christophe RAUT
Invités :	Jennie L. THOMAS
	Olivier DUCLAUX

Résumé

La région arctique s'ouvre peu à peu aux activités humaines, en raison du réchauffement climatique et de la fonte des glaces, dûs en partie à l'effet de polluants à courte durée de vie (aérosols, ozone). Dans le futur, les émissions de ces polluants liées à la navigation et à l'extraction de ressources en Arctique pourraient augmenter, et devenir prépondérantes comparées à la source historique liée au transport de pollution depuis les moyennes latitudes. Dans cette thèse, j'effectue des simulations régionales de la troposphère arctique avec le modèle WRF-Chem, combiné à de nouveaux inventaires des émissions de pollution locales en Arctique (navigation et torches pétrolières). Deux cas d'étude issus de campagnes de mesure par avion sont analysés. Premièrement, j'étudie un évènement de transport d'aérosols depuis l'Europe au printemps 2008, afin d'améliorer les connaissances sur cette source majeure de pollution Arctique. Deuxièmement, je détermine l'impact des émissions de la navigation en Norvège en été 2012, où la navigation Arctique est actuellement la plus intense. J'utilise ces cas d'étude pour valider la pollution modélisée et améliorer WRF-Chem en Arctique. J'effectue avec ce modèle amélioré des simulations des impacts actuels (2012) et futurs (2050) de la navigation et des torches pétrolières en Arctique sur la qualité de l'air et le bilan radiatif. Les résultats indiquent que les torches sont et devraient rester une source majeure d'aérosols de carbone suie réchauffants en Arctique. La navigation est une source de pollution importante en été ; et en 2050, la navigation de diversion à travers l'Arctique pourrait devenir une source majeure de pollution locale.

Abstract

The Arctic is increasingly open to human activity due to rapid warming, associated with decreased sea ice extent. This warming is due, in part, to the effect of short-lived atmospheric pollutants (aerosols, ozone). Emissions from oil and gas extraction and marine traffic should increase in the future, and their impacts might become significant compared to the now predominant source due to pollution transport from the mid-latitudes. In this thesis, regional simulations of the Arctic troposphere are performed with the WRF-Chem model, combined with new emission estimates for oil and gas extraction and shipping in the Arctic. The model is used to analyze two case studies from recent airborne measurement datasets: POLARCAT-France in 2008, ACCESS in 2012. First, I investigate an aerosol transport event from Europe to the Arctic in spring 2008, in order to improve our understanding of this major source of Arctic pollution. Second, I determine the air quality and radiative impacts of shipping emissions in Northern Norway in summer 2012, where most current Arctic shipping occurs. I use these results to validate modeled pollution, and to improve WRF-Chem for Arctic studies. The updated model is used to investigate the current (2012) and future (2050) impacts of Arctic shipping and Arctic gas flaring in terms of air quality and radiative effects. Results show that Arctic flaring emissions are and should remain a major source of local black carbon aerosols, causing warming, and that Arctic shipping is already a strong source of aerosols and ozone during summer. In 2050, diversion shipping through the Arctic Ocean could become one of the main sources of local surface aerosol and ozone pollution.

Remerciements

Je souhaiterais tout d'abord remercier Kathy Law et Jean-Christophe Raut, pour avoir accepté de diriger cette thèse. Merci de m'avoir accompagné et guidé pendant ces quatre années, du stage à la soutenance, tout en me laissant la liberté dont j'avais besoin. J'ai apprécié vos conseils toujours justes, votre disponibilité, votre soutien. Cette thèse n'aurait pas non plus été possible sans le financement de Total, et je voudrais ici remercier ceux qui se sont démenés pour la mettre en place, en particulier Philippe Ricoux et Olivier Duclaux, mais aussi tous ceux qui se sont intéressés à mon travail. Je remercie enfin mon jury de thèse, mon comité de thèse, et tous ceux qui ont contribué à améliorer ce travail.

Cette thèse n'aurait pas été ce qu'elle est sans Jennie Thomas, ma co-directrice de thèse officieuse. Jennie, you had more success in helping me write papers than in convincing me to appreciate quinoa and kale, but don't give up, maybe some day I will.

Je remrcie également le LATMOS, et l'équipe Tropo, où j'ai été chaleureusement accueilli pendant cette thèse. Je remercie tous ceux qui ont rendu ces années au LATMOS agréables, trop nombreux pour tous les nommer ici. Des remerciements particuliers à Ludivine pour sa bonne humeur, à Aurélien pour sa mauvaise humeur, et merci à tous les deux pour le café du commerce/groupe de soutien/café-philo du 3$^{\text{ème}}$ étage qui est très vite devenu une habitude et une nécessité. Merci aussi à tous les occupants du bureau 316 où je me suis tout de suite senti chez moi: Jaime, Katerina, Christophe, Thierno, Tommaso, Xiaoxa.

Après le travail, j'ai pu compter sur le soutien d'Hugues, Arnaud, Rodérick, Elsa, et de bien d'autres qui, au détour d'un verre ou d'un dîner, ont parfois dû m'écouter soliloquer au sujet des paramétrisations de cumulus ou des modules de photochimie. Je remercie aussi les musiciens avec qui j'ai produit un bruit innommable tous les dimanches matin.

Merci au delà des mots à Leïla, qui a dû me supporter plus que tous les autres, et à qui je rappelle ici pour la millième fois que je n'ai pas écrit une thèse sur «les ours polaires».

Et, ici en dernier mais avant tout, merci à Maman, Lucie, Julien et Arnaud, présents dans les bons moments comme dans les plus difficiles.

À Papa,
toujours présent,
et à qui je dois tout,
ou presque tout.

Contents

Introduction

L'Arctique est la région du monde qui se réchauffe le plus rapidement ; les températures de surface y augmented plus de deux fois plus vite que la moyenne globale (IPCC, 2013b). Ce réchauffement est dû principalement à l'effet des gaz à effet de serre « bien mélangés », comme le CO_2 et le méthane, mais aussi à l'effet d'espèces à plus courtes durées de vie : les aérosols et l'ozone (Shindell et al., 2006). Les émissions locales de pollution en Arctique sont supposées faibles. Pour cette raison, des études précédentes indiquent que la source principale de pollution à l'ozone et aux aérosols en Arctique au $20^{\text{ème}}$ siècle est le transport de polluants depuis les moyennes latitudes (Barrie, 1986), tandis que la cause principale du réchauffement Arctique est le réchauffement des moyennes latitudes suivi du transport de chaleur vers l'Arctique (Shindell, 2007).

Le réchauffement de l'Arctique et la fonte des glaces qui lui est associée (IPCC, Kirtman et al., 2013) pourraient progressivement permettre le développement industriel de cette région, en particulier des activités liées au traffic maritime et à l'extraction de ressources. Ceci pourrait entraîner une croissance importante des émissions locales de polluants à courte durée de vie et de leurs précurseurs en Arctique (IPCC, 2014), alors que dans le reste de la planète ces émissions devraient diminuer (IPCC, 2013a). Etant donné que les aérosols et l'ozone sont très sensibles aux sources d'émissions locales, l'impact des sources liées aux bateaux et à l'extraction de resources en Arctique pourrait devenir significatif comparé aux sources de pollution lointaines, et devenir une cause majeure du réchauffement futur dans cette région.

Ces questions sont particulièrement importantes pour les décideurs politiques, qui doivent savoir si la réduction des émissions de polluants à courte durée de vie et de leurs précurseurs pourrait permettre de limiter le réchauffement Arctique et le réchauffement global, et améliorer la qualité de l'air (Penner et al., 2010). La réponse à ces questions est cependant toujours incertaine, pour deux raisons principales. Premièrement, les modèles atmosphériques globaux reproduisent relativement mal les concentrations des polluants à courte durée de vie an Arctique, en particulier celles des aérosols (Koch et al., 2009). Ceci est probablement lié aux incertitudes concernant le dépôt par les précipitations et les nuages (Huang et al., 2010). Deuxièmement, des inventaires d'émissions dédiés et précis sont nécessaires pour modéliser l'impact des émissions de la navigation et de l'extraction de ressources en Arctique.

De tels inventaires ont été développés récemment par Peters et al. (2011), pour l'extraction de pétrole et de gaz en Arctique, et Corbett et al. (2010), pour la navigation en Arctique. Ces inventaires ont été combinés dans le passé avec des modèles globaux pour effectuer les premières estimations des impacts actuels et futurs des sources de locales de pollution en Arctique (e.g. Ødemark et al., 2012; Dalsøren et al., 2013; Browse et al., 2013). Cependant, de nouveaux inventaires développés plus récemment par Winther et al. (2014) et Klimont et al. (2015) indiquent que ces premières études pourraient avoir sous-estimé l'importance de la pollution due aux sources locales.

Cette thèse considère une nouvelle approche, combinant des inventaires récents des émissions de l'industrie pétrolière et de la navigation en région Arctique (Winther et al., 2014; Klimont et al., 2015) avec un modèle régional couplé de météorologie-chimie-aérosols, WRF-Chem (Weather Research and Forecasting with chemistry, Grell et al., 2005; Fast et al., 2006). Des simulations sont effectuées à l'aide de WRF-Chem de l'échelle locale (échelle des panaches de pollution) à l'échelle régionale, et les résultats de ces simulations sont comparés à de nouveaux jeux de données issus de campagnes de mesures aéroportées en Arctique : POLARCAT-France (Polar Study using Aircraft, Remote Sensing, Surface Measurements and Models, Climate, Chemistry, Aerosols and Transport, Law et al., 2014) au printemps 2008, et ACCESS (Arctic Climate Change, Economy, and Society, Roiger et al., 2015) en Juillet 2012. Les objectifs principaux de cette thèse sont les suivants :

- Quantifier les impacts actuels et futurs des émissions locales en Arctique, en termes de qualité de l'air et le bilan radiatif, relativement à la pollution issue du transport à longue distance.
- Contribuer à améliorer la connaissance du transport de pollution depuis les moyennes latitudes vers l'Arctique, et les estimations des impacts actuels de la pollution locale en Arctique.
- Évaluer la performance du modèle et améliorer la représentation des aérosols et de l'ozone zn Actique par WRF-Chem

La thèse est organisée selon le plan suivant. Le Chapitre 1 présente le contexte scientifique de cette thèse, et décrit le réchauffement climatique et la pollution de l'air en Arctique, ainsi que l'importance des sources locales de pollution. Le Chapitre 2 est consacré aux aérosols et à l'ozone troposphériques, et présente leurs sources et puits principaux, leurs principaux processus physiques et chimiques, et leur influence sur le bilan radiatif. Le Chapitre 3 décrit les modèles numériques utilisés dans cette thèse, WRF-Chem et FLEXPART-WRF (FLEXible PARTicle model coupled with WRF), les inventaires d'émission (en particulier, Winther et al., 2014, ECLIPSEv5, Evaluating the Climate and Air Quality Impacts of Short-Lived Pollutants version 5 Klimont et al., 2015) et les campagnes de mesures (POLARCAT-France, ACCESS) utilisées. Les résultats principaux de la thèse sont ensuite divisés en trois études.

Premièrement, plusieurs études précédentes indiquent que les aérosols présents en Arctique ne sont pas bien représentés dans les modèles (e.g. Koch et al., 2009; Lee et al., 2013), et que la source principale d'aérosols arctiques est le transport à longue distance depuis l'Europe en hiver et au printemps (Rahn, 1981). Afin de valider le comportement du modèle WRF-Chem en Arctique et afin d'améliorer notre compréhension de cette source lointaine de pollution, le Chapitre 4 présente l'analyse d'un cas d'étude de transport de pollution à longue distance de l'Europe vers l'Arctique au printemps 2008, issu du jeu de données de la campagne aéroportée POLARCAT-France (Marelle et al., 2015).

Deuxièmement, une des principales sources actuelles de polluants à courte durée de vie en Arctique est la navigation le long de la côte Norvégienne. Dans le Chapitre 5, des simulations WRF-Chem sont combinées avec les mesures aéroportées de la pollution liée au traffic maritime au nord de la Norvège en juillet 2012, afin de quantifier les impacts actuels de cette source en termes de qualité de l'air et d'effets radiatifs, et d'évaluer de nouveaux inventaires des émissions de cette source (Marelle et al., 2016).

Troisièmement, les résultats des deux cas d'étude précédents sont utilisés pour identifier les processus principaux responsables de la pollution liée à l'ozone et aux aérosols en région Arctique, et pour améliorer le modèle pour les simulations en Arctique. Cette version améliorée de WRF-Chem est utilisée dans le Chapitre 5 pour effectuer des simulations quasi-hémisphériques centrées sur l'Arctique, afin de quantifier l'impact des émissions locales liées aux bateaux et à l'extraction de gaz et de pétrole, relativement aux impacts des émissions antrhopiques transportées depuis les moyennes latitudes et aux émissions des feux de biomasse (Marelle et al., in preparation).

Introduction

The Arctic is the fastest warming region in the world, with surface temperatures rising more than twice as fast as the global average (IPCC, 2013b). Arctic warming is mostly due to the effect of well-mixed greenhouse-gases, such as CO_2 and methane, combined with the effect of shorter lived species: aerosols and ozone (Shindell et al., 2006). Studies indicate that, during the 20^{th} century, aerosol and ozone pollution in the Arctic was mostly due to transport from the mid-latitudes (Barrie, 1986), while Arctic climate change was mostly due to warming in the mid-latitudes followed by heat transport to the Arctic (Shindell, 2007).

Future Arctic warming and the associated decline in sea ice (IPCC, Kirtman et al., 2013) will increasingly open the region to human activity, especially shipping and resource extraction. Local Arctic emissions of air pollutants could rise dramatically as a result (IPCC, 2014), whereas global emissions of several short-lived pollutants and their precursors are expected to decrease (IPCC, 2013a). Since aerosols and ozone are very sensitive to local emissions, the impacts of local Arctic emissions could become significant compared to remote sources, and these rising local emissions could become a major driver of Arctic climate change.

These questions are especially important for policymakers, who need to know if reducing emissions of short-lived pollutants and their precursors is the right course of action to curb Arctic and global warming, and improve local air quality (Penner et al., 2010). Unfortunately, the answer to these questions is currently unclear, for two main reasons. First, global models struggle to represent short-lived pollutants, especially aerosols, in the Arctic (Koch et al., 2009). This is likely due to uncertainties in the treatment of aerosol removal by precipitation and clouds (Huang et al., 2010). Second, assessing the impact of Arctic shipping and Arctic resource extraction requires accurate emission inventories, which were not available until recently. Such inventories were developed by Peters et al. (2011) for Arctic oil and gas extraction and Corbett et al. (2010) for Arctic shipping. These emission inventories were combined with global models to perform the first assessments of the current and future impacts of local emissions in the Arctic (e.g. Ødemark et al., 2012; Dalsøren et al., 2013; Browse et al., 2013). However, new inventories developed recently by Winther et al. (2014) and Klimont et al. (2015) suggest that earlier studies could have been underestimating the magnitude of Arctic pollution from local sources.

In this thesis, a new approach is taken, combining the recent Arctic emission inventories for shipping and oil and gas extraction by Winther et al. (2014) and Klimont et al. (2015) with a regional meteorology-chemistry-aerosol-transport model, WRF-Chem (Weather Research and Forecasting with chemistry, Grell et al., 2005; Fast et al., 2006). In this thesis, WRF-Chem is run from the plume scale to the regional scale, and simulation results are compared to new measurement datasets from airborne campaigns in the European Arctic: POLARCAT-France (Polar Study using Aircraft, Remote Sensing, Surface Measurements and Models, Climate, Chemistry, Aerosols and Transport, Law et al., 2014) in spring 2008, and ACCESS (Arctic Climate Change, Economy, and Society, Roiger et al., 2015) in July 2012,. The main objectives of this thesis are the following:

- Quantify the current and future air quality and radiative impacts of local Arctic emissions, relative to the source from long-range pollution transport.
- Gain new insights on pollution transport from the mid-latitudes to the Arctic, and on the current impacts of local Arctic emissions.
- Assess model performance and improve model representations of Arctic aerosols and ozone.

The thesis is organized as follows. Chapter 1 introduces the scientific context of this work, describing Arctic warming, Arctic air pollution and the importance of local Arctic emission sources. Chapter 2 is focused on aerosols and ozone, presenting the main sources and sinks; the physical and chemical processes; and the impacts on the radiative budget. Chapter 3 describes the modeling tools, WRF-Chem and FLEXPART-WRF (FLEXible PARTicle model coupled with WRF), emission inventories (with a special focus on inventories by Winther et al., 2014 and ECLIPSEv5, Evaluating the Climate and Air Quality Impacts of Short-Lived Pollutants version 5 Klimont et al., 2015) and measurement campaigns (POLARCAT-France, ACCESS) used in this thesis. The main results from this thesis are divided into three studies.

First, it is known from previous studies that Arctic aerosols are not well represented in models (e.g. Koch et al., 2009; Lee et al., 2013), and that one of the main sources of Arctic aerosols is long-range transport from Europe in late winter and early spring (Rahn, 1981). In order to assess the performance of WRF-Chem in the Arctic and improve our understanding of this remote source of Arctic pollution, Chapter 4 presents the analysis of a case of long-range transport of aerosols from Europe to the Arctic in spring 2008 from the POLARCAT-France airborne measurement dataset (Marelle et al., 2015).

Second, shipping along the Norwegian coast is thought to be one of the main current local sources of short-lived pollution in the Arctic. In Chapter 5, WRF-Chem simulations are combined with airborne measurements of shipping pollution in Northern Norway in July

2012, in order to assess the current impacts of Arctic shipping in terms of air quality and radiative effects, and to evaluate new Arctic shipping emission inventories (Marelle et al., 2016).

Third, insights gained from these case studies are used to identify the important processes controlling short-lived pollution in the Arctic, and to improve the model for Arctic studies. The updated version of WRF-Chem is used in Chapter 5 to perform quasi-hemispheric simulations to assess the current (2012) and future (2050) impacts of local emissions from shipping and oil- and gas-related flaring in the Arctic, relative to the impacts of anthropogenic emissions transported from the mid-latitudes and emissions from biomass burning (Marelle et al., in preparation).

Chapter 1

Climate change and air pollution in the Arctic

1.1 Global air pollution and climate change

Human activities have an increasing impact on the global environment. Specifically, the combustion of fossil fuels and biomass associated with industrialization significantly alters atmospheric composition, with two main consequences: air pollution and climate change.

1.1.1 Air pollution

Air pollution is defined as the introduction in the atmosphere of a compound with harmful effects on human health or on the environment. Air quality has long been a problem in populated cities. The deleterious effects of air pollution in Rome were already mentioned by Seneca in 61 AD (Moral Letters to Lucilius, Letter CIV):

> "As soon as I escaped from the oppressive atmosphere of the city, and from that awful odour of reeking kitchens which, when in use, pour forth a ruinous mess of steam and soot, I perceived at once that my health was mending."

Air pollution became a larger concern with the industrial revolution and the development of coal burning for industries, domestic heat, and later combustion engines and power generation. As the prejudicial effect of air pollution became obvious, countries implemented regulations, such as the 1875 Public Health Act in the UK. Other countries implemented similar rules and stricter controls in the 20^{th} century. In spite of these regulations, outdoor air pollution still leads to 3.3 million premature deaths per year worldwide (Lelieveld et al., 2015), by contributing to the development of respiratory diseases, cardiovascular diseases and cancer (WHO, 2014).

The health impacts of air pollution are mostly due to aerosols and ozone (e.g. Lelieveld et al., 2015). Aerosols, also called particulate matter, are defined as all airborne solid or liquid

matter, excluding cloud droplets, ice crystals, and other hydrometeors. Aerosols can be emitted directly in the atmosphere (primary aerosols, such as ash, soot and desert dust), or can be formed in the atmosphere from precursor gases (secondary aerosols, such as sulfate). Ozone (O_3) is a trace gas that is naturally abundant in the stratosphere (altitudes 10 to 100 km), but it is also present in the troposphere (altitudes 0 to 10 km). Tropospheric ozone, which is consideed a pollutant, can be chemically produced from precursor gases such as nitrogen oxides (NO_x) and volatile organic compounds (VOC) in the presence of solar radiation. O_3 and aerosols are presented in more detail in Chapter 2.

Aside from its impacts on human health, ozone pollution can harm vegetation (Reich, 1983), and reduce crop production and yields (Dingenen et al., 2009). Aerosol pollution contributes to acid rain (Cowling, 1982), damaging soils, terrestrial ecosystems (Johnson et al., 1990) and aquatic ecosystems (Muniz, 1990). In addition, acid rain contributes to the weathering of stone buildings and corrosion of metal structures (Likens et al., 1972).

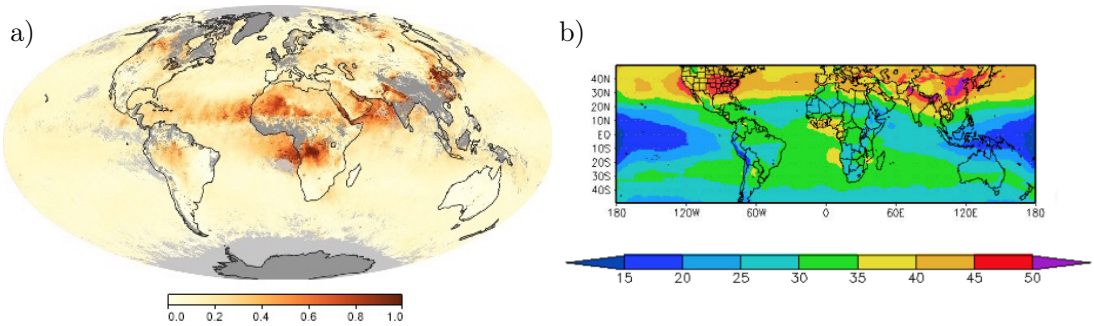

Figure 1-1 – Satellite measurements of (a) MODIS-Terra aerosol optical depth measured at 550 nm (dimensionless), showing global aerosol distributions in August 2014 (NASA Earth observatory) (b) TOMS tropospheric ozone during summer (Dobson units), 1979-2000 average (adapted from Fishman et al. (2003)).

Aerosols and ozone can be produced by human activity, but also by natural sources, e.g. forest fires, desert dust storms, volcanic eruptions, lightning, or biogenic activity. Figure 1-1a shows the global distribution of aerosol optical depth in August 2014, which can be used as a proxy for aerosol burdens; Figure 1-1b shows the global distribution of total tropospheric ozone during summer, averaged over the period 1979–2000. These maps illustrate that the main regions of high aerosol and ozone pollution are urbanized areas such as Eastern Asia, as well as boreal and tropical forests (where large forest fires occur). Aerosol optical depths are also enhanced above deserts (where dust storms occur). Figure 1-1 also illustrates the inhomogeneous distribution of aerosols and ozone. Their amounts are stronger close to emission regions, because of their relatively short lifetime in the troposphere (1 to 10 days for aerosols, Textor et al., 2006; 22 days for O_3, Stevenson et al., 2006). Since intercontinental transport times are about 5 to 10 days (Wild and Akimoto, 2001), aerosols and ozone can

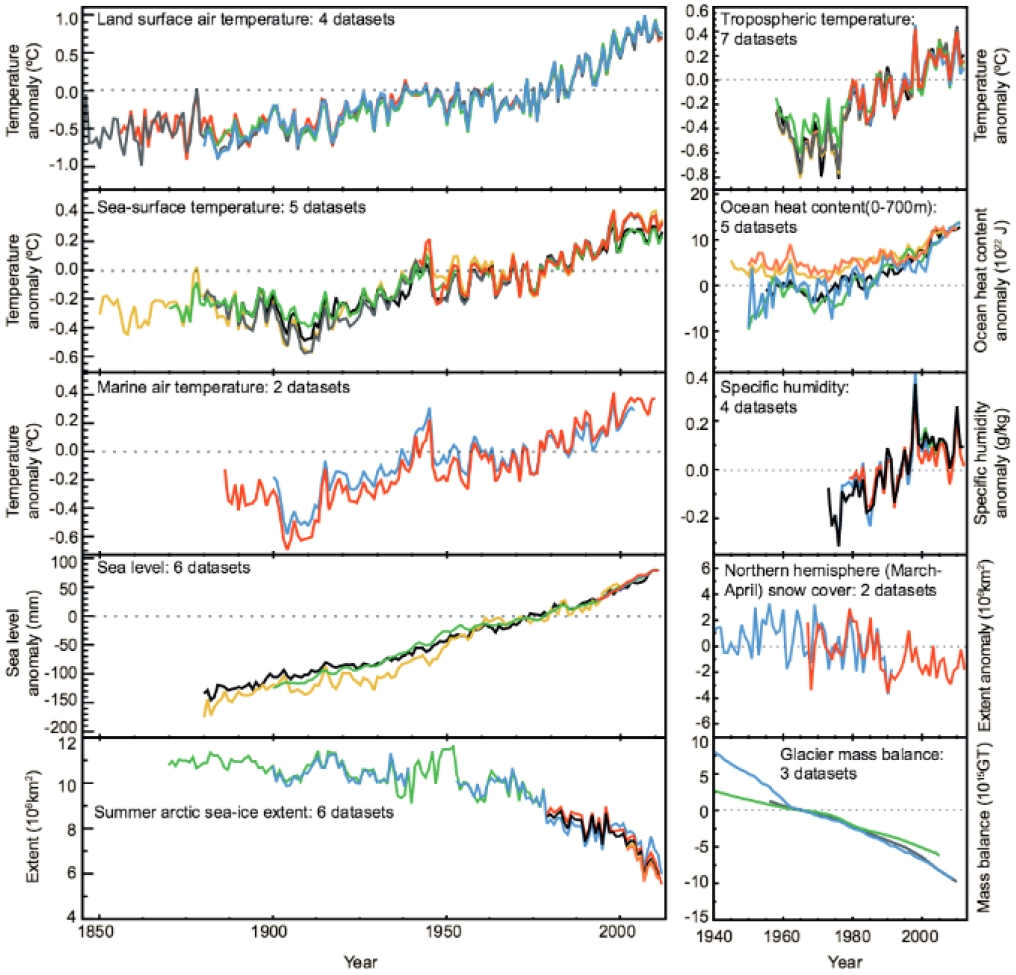

Figure 1-2 – Multiple independent indicators of a changing global climate, from IPCC (Hartmann et al., 2013)

.

still be transported over relatively long distances. Mitigating aerosol and ozone pollution therefore demands both local and international action.

1.1.2 Global climate change

Global mean surface temperatures have increased by 0.85 C since the beginning of the industrial era (IPCC, Hartmann et al., 2013). This global warming is also associated with increasing ocean heat content, increasing atmospheric water vapor concentrations, rising sea levels, decreasing snow and sea ice cover, and decreasing glacier and polar ice sheet mass (Figure 1-2; IPCC, Hartmann et al., 2013).

It is now widely known that this global warming is mainly caused by human activity. It is primarily due to the enhanced greenhouse effect due to rising greenhouse gas (GHG)

concentrations in the atmosphere, combined with the climate effect of increased aerosols (IPCC, Bindoff et al., 2013).

1.1.2.1 The effect of greenhouse gases on climate

The mean temperature of the Earth is primarily determined by the balance between incoming shortwave (SW) solar radiation and outgoing longwave (LW) terrestrial radiation (Figure 1-3).

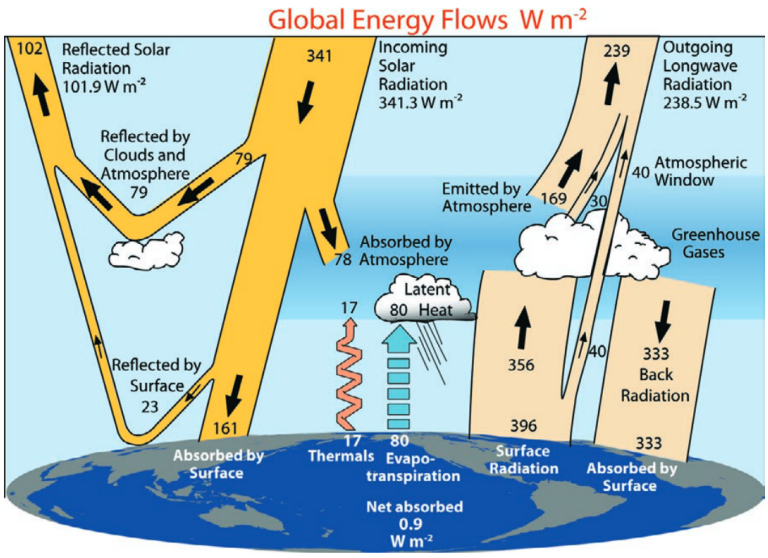

Figure 1-3 – Global annual mean energy budget of the Earth for the period from March 2000 to May 2004 ($\mathrm{W\,m^{-2}}$); Trenberth et al. (2009)

.

Schematically, solar radiation warms the Earth when it is absorbed by the Earth's surface, and the surface cools down by reemitting heat to the atmosphere and to space as infrared radiation, approximately following Stefan-Boltzmann's law for blackbody radiation,

$$E_s = \quad T_s^{\,4} \tag{1.1}$$

where T_s (K) is the temperature of the Earth's surface, E_s ($\mathrm{W\,m^{-2}}$) the energy radiated in the infrared by the Earth per unit surface and unit time, and the Stefan-Boltzmann constant. This terrestrial infrared radiation is absorbed in the atmosphere by certain gases, called GHG, which reemit infrared radiation downward to the surface and upward into space. The solar radiation is often called shortwave radiation (wavelengths 0.1 to 4.0 µm), while the terrestrial and atmospheric infrared radiation is called longwave radiation (wavelengths 4.0 to 50 µm). In the lower atmosphere (the troposphere), temperature decreases with altitude, which means that greenhouse gases reemit longwave radiation to space at an atmo-

spheric temperature $T_a < T_s$. Because of this, and following the Stefan-Boltzmann law, the amount of longwave radiation E_a lost to space by the atmosphere is lower than E_s. Thus, in the presence of greenhouse gases, less energy is lost to space and more is trapped in the surface-troposphere system. This warming effect is called the greenhouse effect.

The main greenhouse gases in the atmosphere by abundance are water vapor, carbon dioxide (CO_2), methane (CH_4), nitrous oxide (N_2O) and ozone (O_3). Since the beginning of the industrial era, the global average tropospheric concentrations of CO_2, CH_4, N_2O and O_3 have risen from 280 ppm, 722 ppb, 270 ppb and 237 ppb, to, respectively, 395 ppm, 1800 ppb, 325 ppb and 337 ppb, due primarily to human activity (Blasing, 2014; IPCC, Hartmann et al., 2013). These enhanced greenhouse gas concentrations cause an enhanced greenhouse effect, warming the planet.

This warming influence can be quantified in terms of radiative forcing (RF, in $W\,m^{-2}$), defined as the change in net (down minus up) total (SW + LW) irradiance at the tropopause due to a change in the climate system (IPCC, 2013b). For example, the RF due to CO_2 is calculated as

$$RF_{CO_2} = F_{CO_2} - F_{noCO_2} \tag{1.2}$$

$$= (F_{CO_2} - F_{CO_2}) - (F_{noCO_2} - F_{noCO_2}) \tag{1.3}$$

where F is the total (SW + LW) radiative flux. Based on this definition, $RF > 0$ means that the substance has a warming effect. In the framework of the IPCC, the radiative forcing of a GHG usually has a more restrictive meaning, and represents the change in irradiance due to changes in GHG concentrations from the preindustrial to the present-day period, once the stratospheric temperatures have adjusted to the change in irradiance.

$$RF_{CO_2} = F_{presentCO_2} - F_{preindustrialCO_2}$$

Figure 1-4 shows the radiative forcing of the main anthropogenic GHGs, as estimated by the IPCC (Myhre et al., 2013).

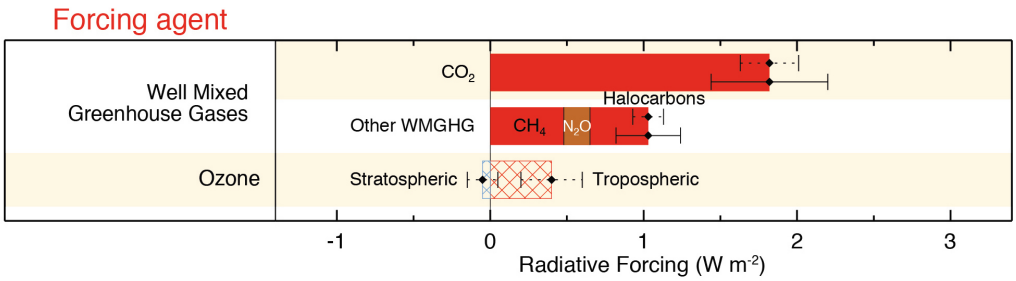

Figure 1-4 – Radiative forcing of climate by well-mixed greenhouse gases and ozone between 1750 and 2011, adapted from IPCC (Myhre et al., 2013). For ozone, the figure shows the effective radiative forcing.

This figure shows that, in terms of radiative forcing, CO_2 is the main anthropogenic greenhouse gas affecting the troposphere, followed by CH_4 and tropospheric O_3. For ozone, the effective RF is showed, which is the RF corrected by the efficacy of the O_3 forcing. This efficacy is defined as the ratio of the rapid temperature response to the RF of O_3 divided by the rapid temperature response to the RF of CO_2 ($_{O_3}$/ $_{CO_2}$, where is the climate sensitivity defined in Section 1.1.2.3). CO_2 and CH_4 are often called well-mixed greenhouse gases, because their lifetimes are long compared to the global atmospheric mixing time (1 to 3 yr, IPCC, 2013b), while tropospheric O_3 is considered a short-lived (22 days) climate forcer. In addition to its greenhouse effect (LW effect, Section 2.1.7), O_3 can directly absorb solar radiation (SW effect, Section 2.1.7). Both effects are included in Figure 1-4, but the global effect of tropospheric ozone is estimated to be 80 % due to its LW effect (Stevenson et al., 2013). CO_2 increasing in the stratosphere also results in stratospheric cooling, while decreasing stratospheric ozone cause stratospheric cooling and weak tropospheric cooling, however, these stratospheric processes are out of the scope of this thesis.

1.1.2.2 Aerosol effects on climate

Human activities also change the Earth's climate by increasing the global burden of aerosols. Once in the atmosphere, aerosols can influence climate in several ways, presented on Figure 1-5.

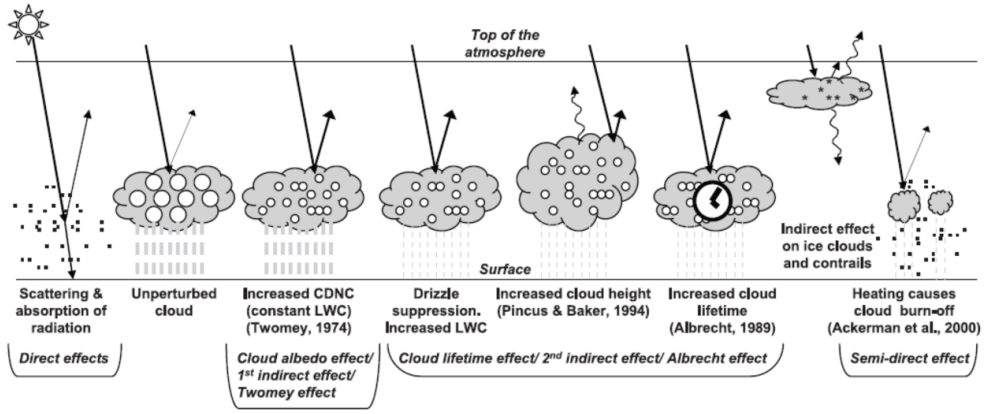

Figure 1-5 – Main radiative effects of atmospheric aerosols, based on Haywood and Boucher (2000).

First, aerosols can directly absorb solar radiation (warming effect), or scatter it back into space (cooling effect) (Ångström, 1929; Haywood and Shine, 1995). Large aerosol particles can also directly absorb terrestrial infrared radiation (greenhouse warming effect) (Haywood and Shine, 1997). These effects are called the *direct aerosol radiative effects*. Second, these direct effects modify the atmospheric profiles of temperature and relative humidity, which

can inhibit or enhance cloud formation (Hansen et al., 1997). These effects are called the *semi-direct aerosol radiative effects*. Third, aerosols, when co-located with clouds, have an impact on cloud formation, cloud optical properties, cloud height and cloud lifetime (Twomey, 1977; Albrecht, 1989). These effects are called the *indirect aerosol radiative effects*, or are referred to as the radiative effects of *cloud-aerosol interactions*. Absorbing aerosols, such as black carbon (BC), also contribute to warming when deposited on snow and ice, by darkening the snow or ice surface and increasing snow-grain size, which increases absorption of solar radiation (*snow-albedo effect*) (Warren and Wiscombe, 1980). More details on these effects are given in Section 2.2.5. The climate effect of all of these aerosol processes can also be quantified in terms of radiative forcing. This is shown on Figure 1-6.

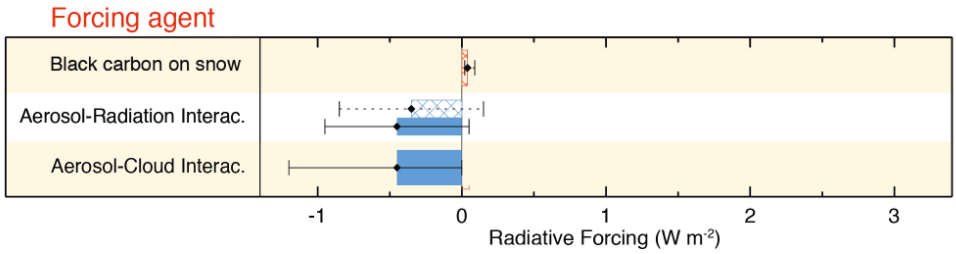

Figure 1-6 – Radiative forcing of climate by aerosols between 1750 and 2011, adapted from IPCC (Myhre et al., 2013).

Figure 1-6 shows that the total radiative forcing of aerosols since 1750 is negative. This is mostly due to sulfate aerosols. Globally, aerosols thus have a cooling effect which counteracts part of the warming effect of greenhouse gases. The radiative effect of aerosols is also more uncertain than the radiative effect of greenhouse gases, due to uncertainties in aerosol sources, aging processes, sinks and forcing mechanisms..

1.1.2.3 Climate sensitivity and feedbacks

RF values presented in Figure 1-4 and Figure 1-6 represent the radiative imbalance of the troposphere due to anthropogenic influences in the climate system. This imbalance causes a change in global temperature T_s, which is often assumed to depend linearly on RF,

$$T_s = \cdot RF$$

where is the climate sensitivity. If everything else than temperature remained equal in the climate system, would be approximately equal to $_0 = 0.3\,\mathrm{K\,W^{-1}\,m^2}$ (Forster et al., 1997). However, any rise in temperature leads to further changes, which can amplify or dampen this initial response. For example, rising temperatures lead to declining sea ice and snow cover. This melt uncovers the underlying surface, which has a lower albedo than snow or ice and absorbs more solar radiation. This process, called the surface albedo feedback, amplifies the response to RF. There are other climate feedbacks, such as the water vapor

feedback, cloud feedbacks... A feedback that amplifies an initial warming perturbation is called a positive feedback, while a feedback that reduces this initial warming is called a negative feedback. The current understanding of the climate system indicates that the sum of feedbacks is positive and that the actual climate sensitivity is larger than $_0$ (best estimate, $= 1.0 \pm 0.5\,\mathrm{K\,W^{-1}\,m^2}$, IPCC, Flato et al., 2013).

1.2 Arctic climate change: causes and future projections

1.2.1 What is the Arctic?

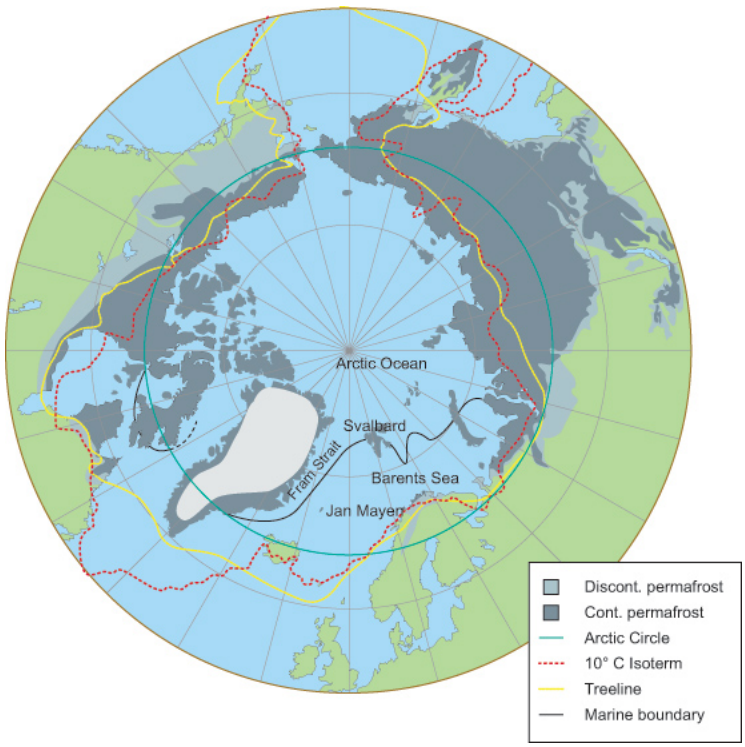

Figure 1-7 – Several definitions of the Arctic boundary: the Arctic Circle (green), the 10 C summer isotherm (red), the tree line (yellow), the marine salinity boundary (black) and the location of permafrost (gray). Source: The Arctic System project, `http://www.arcticsystem.no/en/arctic-inc/headquarters.html`.

The Arctic region is traditionally defined as the region of the Northern Hemisphere where the 24-hour long polar day and polar night occur. This corresponds to the area north of the Arctic Circle, located at a latitude of 66°33 N. The Arctic can also be defined as the area north of the tree line (the northern limit of tree growth), the area north of the 10 C summer surface isotherm, or other definitions based on the location of permafrost or on reduced ocean salinity. The Arctic boundaries corresponding to these definitions are shown

in Figure 1-7. In atmospheric studies, the Arctic is often more broadly defined as the area from 60 N to 90 N. This last definition is used in this thesis.

The Arctic is different from other regions because of several characteristics such as a high surface albedo due to sea ice, land ice and snow; long periods of darkness (polar night during winter) and sunlight (polar day during summer); high solar zenith angles; low temperatures; low relative humidities and strong atmospheric stability. The Arctic region is also especially sensitive to climate change (IPCC, 2013b).

1.2.2 Current Arctic warming

The Arctic surface is warming faster than the rest of the Earth (Figure 1-8(a)), a situation known as *Arctic amplification*. Arctic amplification was predicted using early climate model simulations (Kellogg, 1975; Manabe et al., 1990), and is mainly due to the positive surface-albedo climate feedback, combined with changes in heat transport to the Arctic, in Arctic clouds and in Arctic water vapor caused by climate change (Serreze and Barry, 2011). The enhanced radiative effects of black carbon aerosols in the Arctic are also thought to contribute to Arctic amplification (Serreze and Barry, 2011). This warming has important

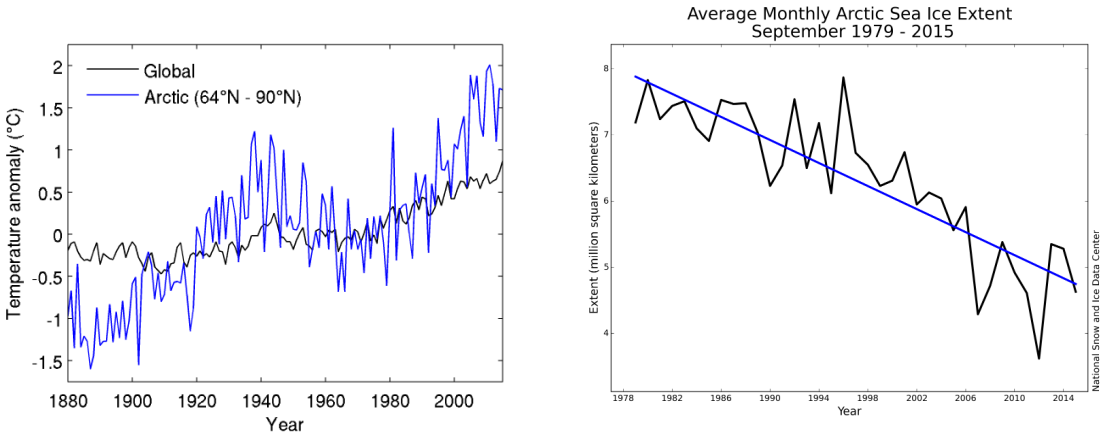

(a) (b)

Figure 1-8 – (a) Annual mean Arctic surface temperature anomalies from 1880 to 2015 (blue), compared to the global average (black). Temperature anomalies are from the GISS surface temperature analysis (GISTEMP), and are relative to the 1951-1980 base period. (b) September Arctic sea ice cover, 1979-2015, with trend line (Figure from the National Snow and Ice Data Center, NSIDC).

consequences for the Arctic cryosphere. Figure 1-8(b) shows the evolution of September sea ice extent in the Arctic (when the yearly minimum cover is reached) between 1979 and 2015. Since satellite measurements began, September Arctic sea ice cover has declined at a rate of $-13.4\,\%$ per decade (details in Stroeve et al., 2007). Arctic warming is also causing

the melt of the Greenland ice cap ($-215 \pm 59\,\mathrm{Gt\,yr^{-1}}$; IPCC, Vaughan et al., 2013), and of Arctic glaciers ($-138 \pm 33\,\mathrm{Gt\,yr^{-1}}$, excluding Greenland; IPCC, Vaughan et al., 2013), contributing to sea level rise. Snow cover is also declining in the Northern Hemisphere, by 1 % to 2 % per year (IPCC, Vaughan et al., 2013).

1.2.3 Causes of Arctic warming

The Arctic is warming due to anthropogenic influences. Shindell et al. (2006) estimated that, during the 20$^{\mathrm{th}}$ century, surface temperatures in the Arctic increased mostly because of well-mixed greenhouse gases such as CO_2 and CH_4 (+1.65 C). However, short-lived climate forcers also appear to have played an important role (O_3, +0.30 C; aerosols, including sulfate, black carbon, organic carbon, and nitrate in air, BC on snow, and indirect effects, −0.76 C). Shindell (2007) also found that aerosols and O_3 have a stronger Arctic warming effect per unit forcing than well-mixed GHGs (see also Sections 2.1.7 and 2.2.5).

The literature review of Quinn et al. (2008) indicates that the direct effect of aerosols on Arctic surface temperatures is −0.98 C, the indirect effect −0.70 C and the snow albedo effect (BC on snow) +0.043 C. However, based on a multi-model analysis, AMAP (2015) estimate that the direct effect of aerosols on Arctic surface temperatures is positive, +0.35 C (+0.40 C from BC in air, +0.22 C from BC in snow, and −0.27 C from OC and SO4). Results from AMAP (2015) also indicate a weaker effect of O_3 than previous studies, +0.12 C.

Arctic warming is due to both local and remote forcings. Local forcings are due to the radiative effect of rising concentrations of greenhouse gases and aerosols within the Arctic, but Arctic warming can also be caused by remote forcings (located outside of the Arctic), which indirectly warm the Arctic through heat transport. Shindell (2007) estimated that most of the Arctic warming from 1880 to 2003 was caused by remote forcings, except during summer when local forcings made at least a similar contribution. However, Shindell and Faluvegi (2009) also showed that Arctic surface temperature was especially sensitive to local forcings.

1.2.4 Future projections

Future Arctic warming will depend on current and future action to limit climate change. Multi-model CMIP5 (Coupled Model Intercomparison Project Phase 5) future projections as part of the IPCC's 5th assessment report (IPCC, 2013b) indicate that the Arctic will continue to warm the most, but that the magnitude of this warming will depend strongly on future emission pathways. For the lowest emission scenario used in the framework of CMIP5 (RCP2.6 scenario, Representative Concentration Pathway $2.6\,\mathrm{W\,m^{-2}}$), Arctic temperatures are expected to rise by 2.2 ± 1.7 C in 2100 compared to 1986-2005. In the highest emission scenario (RCP8.5, Representative Concentration Pathway $8.5\,\mathrm{W\,m^{-2}}$), Arctic temperatures could rise by 8.3 ± 1.9 C (IPCC, Collins et al., 2013).

As a result, in the RCP8.5 scenario most CMIP5 models predict an ice-free Arctic Ocean during summer (less than $1 \times 10^6\,km^2$ sea ice cover) by 2100. However, most models underestimate recent sea ice loss (Stroeve et al., 2007), and models which reproduce past changes the most indicate that the Arctic could be seasonaly ice-free in summer months before mid-century (Wang and Overland, 2012). Future Arctic warming is also expected to accelerate the loss of ice from ice sheets and glaciers, and contribute to sea-level rise. Under a medium-range warming scenario, Nick et al. (2013) predict that sea level will rise by 19 to 30 mm by 2200 due to the Greenland ice sheet alone.

1.3 Arctic air pollution

1.3.1 Arctic Haze

The Arctic troposphere was long thought to be extremely clean, until the 1950s, when pilots observed a reduction of visibility in the springtime North American Arctic (Greenaway, 1950; Mitchell, 1956). Further analysis showed that this Arctic Haze, which builds up every winter and spring, was of anthropogenic origin (Rahn et al., 1977). It contains enhanced levels of aerosols, mostly composed of sulphate and sea salt, as well as organic matter, nitrate and black carbon (Quinn et al., 2002). Arctic haze also contains elevated levels of several trace gases, such as carbon monoxide (CO), (NO_x) and VOC (Solberg et al., 1996).

This peak in aerosol concentrations in late winter and early spring can be clearly seen in time series of aerosol measurements at Arctic surface stations. Figure 1-9, shows 1997-2004 and 1981–2003 sulfate and nitrate aerosol observations at Barrow (Alaska, USA) and Alert (Canada) (Quinn et al., 2007).

This Figure illustrates the strong seasonal variation of surface aerosol concentrations in the Arctic, reaching a maximum every year between January and April. These enhanced background levels at the surface (peaking below 2 km, Quinn et al., 2007) are called “Arctic Haze”. In addition to this background haze, the Arctic troposphere can be polluted by episodic transport events, which bring dense localized pollution plumes in the Arctic. These plumes should not strictly be called “Arctic Haze” but contribute to Arctic pollution (Brock et al., 2011).

1.3.2 Arctic air pollution transported from the mid-latitudes

In late winter and early spring, Eurasian pollution can be efficiently transported to the Arctic at low altitudes (Rahn, 1981), causing Arctic Haze. This strong influence of Eurasian emissions is due, in part, to the position of the Arctic front. Air masses traveling from the mid-latitudes to the Arctic usually rise along surfaces of constant potential temperature (isentropic transport). These surfaces form a fictional "dome" called the Arctic front, which

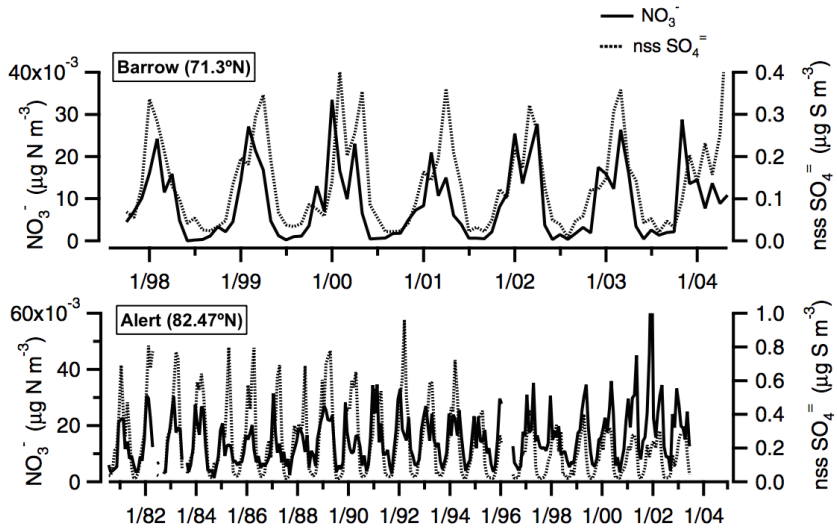

Figure 1-9 – Time-series of monthly averaged particulate sulfate and nitrate concentrations (in µgS m^{-3} and µgN m^{-3} respectively), at (a) Barrow, Alaska and (b) Alert, Canada. Figure from Quinn et al. (2007).

isolates the lower Arctic troposphere from the mid-latitudes (Klonecki et al., 2003; Stohl, 2006). In addition, these rising air masses are usually associated with precipitation, which remove pollutants from the atmosphere ("wet removal") during transport. On the contrary, pollutants emitted North of the Arctic front can be easily transported to the Arctic surface. Figure 1-10 shows the position of the Arctic front during winter and during summer, as well as the main atmospheric pathways from the mid-latitudes to the Arctic.

During winter and spring, the Arctic front can extend south down to 40 N over Europe and Russia due to the extensive snow cover and low temperatures there. Eurasian emissions within the Arctic front can then be transported into the lower Arctic troposphere. In winter and spring, pollution removal processes are also lower in Eurasia and in the Arctic due to strong atmospheric stability and reduced precipitation (Shaw, 1995; Garrett et al., 2011), causing the buildup of Arctic Haze. During summer, the Arctic front is located further north, and removal processes are higher, isolating the Arctic atmosphere from pollution in the mid-latitudes.

The main source regions of Arctic pollution are presented on Figure 1-11. This Figure shows the result of an earlier multi-model analysis (Shindell et al., 2008), estimating the relative contributions of Europe, South Asia, East Asia, and North America to Arctic pollution at the surface and in the upper troposphere (250 hPa). These contributions were estimated for two aerosol components (BC and sulfate) and two trace gases (CO and ozone), by performing simulations with 20 % reduction in anthropogenic emissions of pollution precursors from each source region.

Figure 1-11 illustrates that, on average over the year, modeled surface aerosol and CO

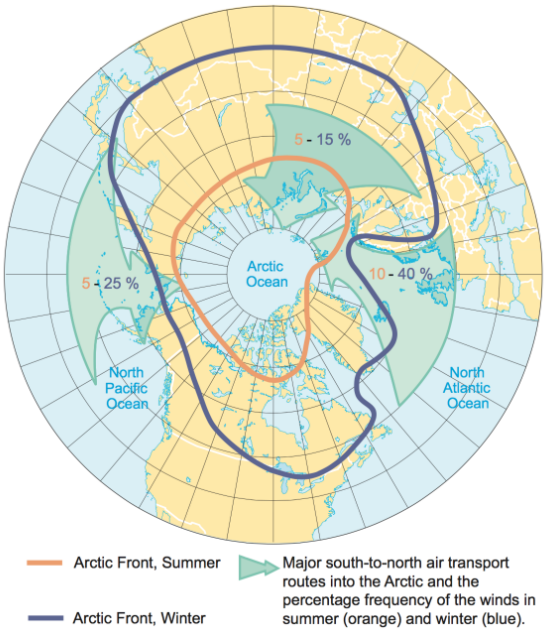

Figure 1-10 – Position of the Arctic front in winter (blue) and summer (yellow), and main pathways of atmospheric transport to the Arctic. From AMAP (2006).

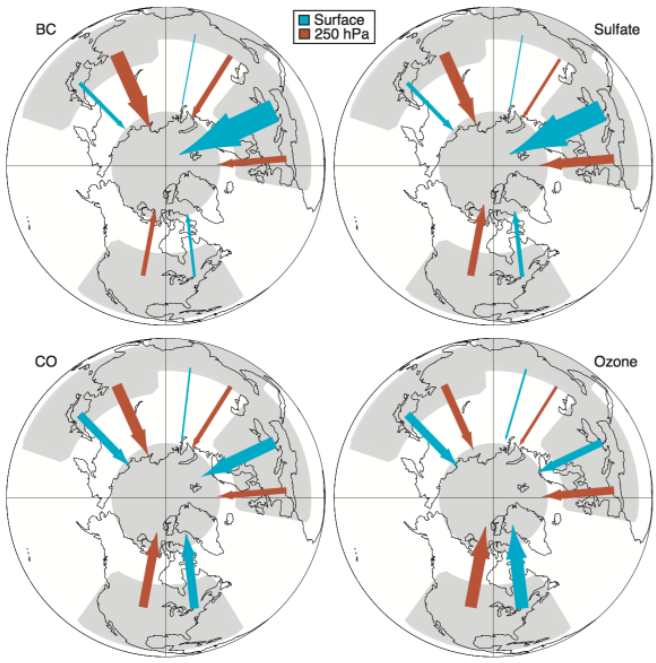

Figure 1-11 – Relative importance of different source regions to annual mean Arctic concentration at the surface and in the upper troposphere (250 hPa) for the indicated species. Arrow width is proportional to the multi-model mean percentage contribution from each region to the total from these four source regions. From Shindell et al. (2008).

pollution in the Arctic (blue arrows) are mostly influenced by European emissions. However, Asian emissions play a more important role at higher altitudes (see also Fisher et al., 2011; Wang et al., 2014a). Figure 1-11 also indicates that, in these simulations, Arctic ozone is mostly sensitive to North American emissions, but Wespes et al. (2012) estimated that European anthropogenic emissions could have a similar or larger importance. Other modeling studies have shown that, aside from anthropogenic emissions, Eurasian biomass burning could be a major source of Arctic pollution (Stohl, 2006; Warneke et al., 2010), but the scale of this contribution remains uncertain.

1.3.3 Developing local sources of Arctic pollution

Aerosols and ozone can be chemically destroyed or deposited during transport. These removal processes (described in Chapter 2) limit the efficiency of long-range transport of pollution from the mid-latitudes. Furthermore, pollution transport from the mid-latitudes occurs along rising isentrops, which tend to bring remote pollution at high altitudes in the Arctic (Stohl, 2006). Local Arctic emissions are, by definition, directly emitted in the Arctic boundary layer and do not experience aging during transport. For this reason, local sources can influence Arctic surface pollution (Sand et al., 2013) and Arctic pollution burdens (Wang et al., 2014a) with much higher per-emission efficiency than remote sources.

However, anthropogenic emissions in the Arctic are thought to be small compared to other regions. There are very few large cities north of the Arctic circle, the most populated being Murmansk in Russia (300,000 inhabitants); other large cities include Norilsk in Russia (175,000 inhabitants), Tromsø and Bodø in Norway (70,000 and 50,000 inhabitants). There are some industrial sources of pollution north of the Arctic circle, such as mines and metal smelters in Norilsk, Russia (AMAP, 2006), and metal smelters in the Kola Peninsula, Russia (Prank et al., 2010). Oil and gas related activities in northern Russia and Norway (AMAP, 2006; Peters et al., 2011) are thought to be an important local source of Arctic pollution (especially for BC), and recent studies (Stohl et al., 2013; Huang et al., 2015) indicate that these emissions might be higher than previously thought.

Arctic shipping emissions are another noteworthy local source of pollution, emitting NO_x, SO_2 (forming sulfate) and BC along with other pollutants. The Arctic council's AMSA report (Arctic Marine Shipping Assessment, Arctic Council, 2009) found that, in 2004, about 6000 ships operated within the Arctic (latitude $>$ 60 N). This traffic mostly takes place along the Norwegian Coast, in northwestern Russia, around Iceland, in southwestern Greenland and in the Bering Sea. Arctic shipping is made up of a combination of supply ships for Arctic communities, bulk transport of resources extracted within the Arctic region, fishing ships, passenger ships and cruise ships (Arctic Council, 2009).

In addition to this local Arctic shipping, it has long been known that the routes through the Arctic Ocean are the shortest way from northern Europe and northwestern America

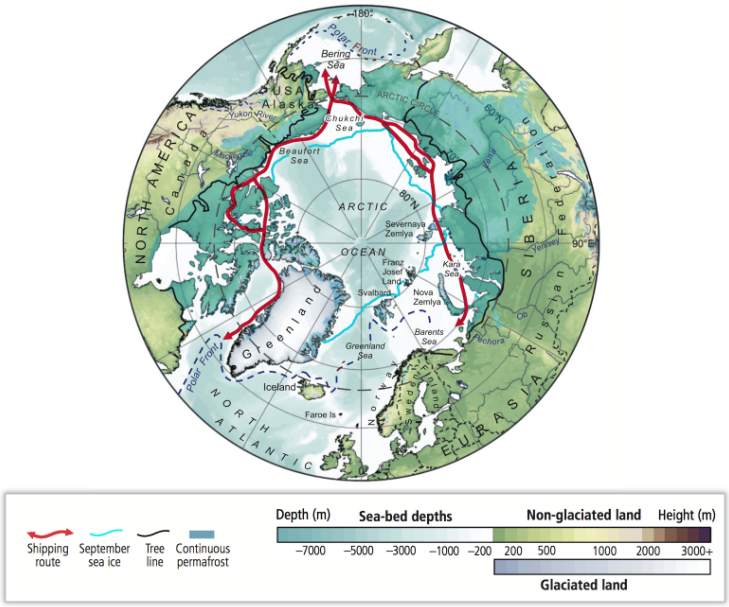

Figure 1-12 – Location of transit shipping routes through the Arctic (in red): Northern Sea Route (NSR, along the Russian coast) and Northwest Passage (NWP, along the Canadian coast). Adapted from IPCC (2014).

to Asia. For example, the Arctic route between the Netherlands and Eastern Asia (called the Northern Sea Route, NSR, or Northeast passage, NEP) is 40 % shorter than the corresponding route through the Suez Canal (Liu and Kronbak, 2010). The Arctic route from Northeastern America to Eastern Asia (the northwest passage, NWP) is 15 to 30 % shorter than the corresponding route through the Panama canal (Somanathan et al., 2009). These routes (shown in Figure 1-12) could be used to save trip distance and costs and might already be profitable, but they are not widely used yet due to the presence of sea ice, leading to additional costs, additional risks due to potential ice damage, and reduced vessel speeds (Liu and Kronbak, 2010; Somanathan et al., 2009).

The NSR and NWP could become more economically competitive along with Arctic sea ice decline. Models and observations indicate that the number of ice-free days per year along the NSR and NWP increased by 22 and 19 days between 1979–1988 and 1998–2007 (Mokhov and Khon, 2008). As a result, transit along these routes is increasing: a record number of 71 ships transited through the NSR in 2013 (Northern Sea Route information office, 2013). At the same time, decreasing sea ice extent also contributed to a rise in Arctic cruise tourism (Stewart et al., 2009). The ice-free shipping season is expected to continue to lengthen due to climate change (Prowse et al., 2009; Khon et al., 2009). This will allow increased traffic along the NSR and NWP, by opening these routes to ships with no hull ice strengthening (Smith and Stephenson, 2013). As a result, Corbett et al. (2010) estimate that Arctic shipping emissions of NO_x and BC could increase by a factor of 10 between 2004

and 2050 (high-growth scenario).

Increased shipping access in the Arctic is also expected to facilitate resource extraction in this region (Prowse et al., 2009). The Arctic contains vast resources of minerals (Lindholt, 2006), oil, and gas (Gautier et al., 2009). Arctic oil and gas resources are already being exploited, and the Arctic is expected to remain an important producer of oil by 2050, while its relative importance in gas production could decrease due to its high extraction prices (Lindholt and Glomsrød, 2012; Peters et al., 2011, projections shown in Figure 1-13). The oil and gas sector is expected to keep contributing to future local pollutant emissions in the Arctic (Peters et al., 2011), although current and future emission inventories from this source remain very uncertain.

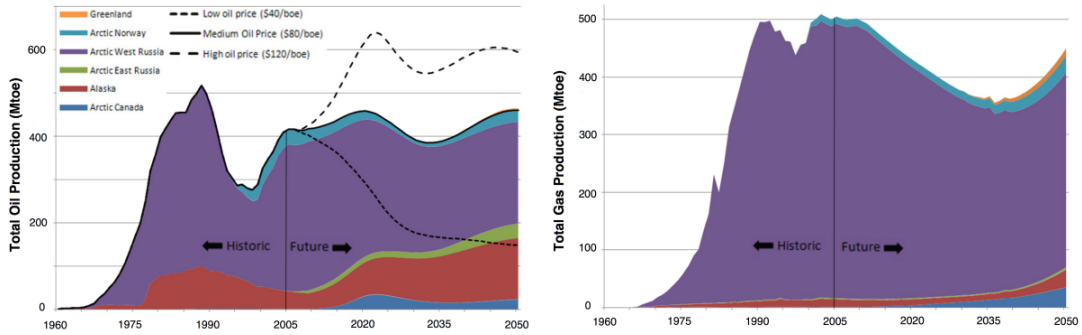

Figure 1-13 – Historic and estimated oil (left) and gas (right) production in the Arctic, from 1960 to 2050. From Peters et al. (2011).

Local natural sources of aerosols, ozone and of their precursors in the Arctic are not well-known. They include boreal wildfires; sea salt, dimethylsulfide (DMS, forming sulfate) and organic matter from oceans; mineral dust; ozone transported from the stratosphere; NO_x from soils and snow. Vegetation is sparse in the Arctic, which limits the formation of biogenic VOCs from plants; and the lack of local thunderstorms (e.g., Cecil et al., 2014) prevents NO_x formation from lightning. These natural sources are not the focus of this thesis, but are included in the simulations presented in Chapter 4, 5 and 6 when estimates or emission models are available.

1.4 Scientific challenges in modeling Arctic aerosols and ozone and their impacts

In this thesis, aerosol and ozone pollution in the Arctic is studied using regional simulations of the Arctic troposphere, and new global and local emission inventories of Arctic pollution. Model results are used to analyze recent aircraft measurements in the Arctic. This approach (details in Chapter 3) was motivated by results from previous studies, which showed that

modeling aerosol and ozone pollution in the Arctic was especially challenging.

1.4.1 Modeling aerosol and ozone pollution from long-range transport

Models do not represent aerosols well in the Arctic. Shindell et al. (2008) showed that models often underpredicted sulfate at Arctic surface stations, and greatly underpredicted BC, while several models struggled to reproduce the seasonal cycle of surface aerosol concentrations. Shindell et al. (2008) attributed this poor agreement to the treatment of aerosol aging and removal within models. Koch et al. (2009) and Schwarz et al. (2010) compared global models to different sets of aircraft observations of BC in the Arctic, and found that models underestimated BC at the surface but overestimated it aloft. A more recent intercomparison by Lee et al. (2013) also indicates that most models strongly underestimate surface BC observations in the Arctic, especially during winter and spring. Several studies (Huang et al., 2010; Liu et al., 2012; Browse et al., 2012; Wang et al., 2013) showed that Arctic BC could be improved by the use of more complex wet removal schemes within models. However, implementing these schemes does not fully resolve model disagreement with measurements (Browse et al., 2012; Wang et al., 2013, 2014b; Eckhardt et al., 2015).

Additionally, most models included in the recent intercomparison in the Arctic of Emmons et al. (2015) underestimate ozone in the middle and high Arctic troposphere by 10 to 30 %, and exhibit stronger biases for ozone precursors such as NO_x, carbon monoxide (CO), peroxyacetyl nitrate (PAN) and several VOCs. Results from another recent model intercomparison in the Arctic performed by AMAP (Arctic Monitoring and Assessment Programme, AMAP, 2015) indicates that models are strongly biased for both O_3 and its precursors. These biases are attributed to uncertainties in emissions, errors in stratosphere-troposphere exchange and uncertainties related to the hydroxyl radical OH (these processes are described in Section 2.1).

1.4.2 Modeling aerosol and ozone pollution from local Arctic sources

Emissions from local Arctic sources are not well quantified, which makes investigating their impacts difficult. There are very few specific emission inventories focused on local Arctic sources, and existing inventories are known to be incomplete. The current and future Arctic shipping inventories of Corbett et al. (2010) do not include fishing ships, which constitute a significant proportion of Arctic shipping (McKuin and Campbell, 2016). In addition, these inventories are based on the AMSA shipping dataset, which might underestimate Arctic marine traffic (Arctic Council, 2009). Other shipping inventories (Dalsøren et al., 2007, 2009; Peters et al., 2011) are also known to be biased towards specific ship types (i.e. container ships and large ships). Furthermore, Arctic shipping inventories can quickly become out of date as the local traffic increases and new emission control regulations are implemented (e.g., (Jonson et al., 2015)). A new Arctic shipping inventory based on ship

positioning by satellite was developed recently by Winther et al. (2014), but it has not yet been validated against measurements.

Emissions from the oil and gas sector are also very uncertain, as most oil and gas activity in the Arctic is located in northern Russia, where very few observations are available to validate inventories. Peters et al. (2011) estimated current and future emissions from Arctic oil and gas activities, but recent inventories (Huang et al., 2015; Klimont et al., 2015) indicate that this earlier estimate might be too low, especially in terms of BC emissions (Stohl et al., 2013).

For these reasons, earlier studies based on the inventories of Corbett et al. (2010), Dalsøren et al. (2007) and Peters et al. (2011), could be underestimating the impacts of Arctic shipping emissions. Furthermore, models do not represent well aerosol pollution in the Arctic. This could have a strong impact on results when studies report relative impacts of local emissions over this uncertain background.

Until recently, there was also no specific field measurements focused on Arctic shipping or Arctic resource extraction that could be used to study the impacts of local Arctic emissions, to assess model performance, and to validate inventories. Such a dataset is now available from the ACCESS aircraft campaign (Roiger et al., 2015), which took place in northern Norway in summer 2012 and specifically targeted ships and oil and gas platforms in the Norwegian and Barents seas.

Chapter 2

Tropospheric ozone and tropospheric aerosols in the Arctic

Aerosols and ozone are responsible for most of the health impacts of air pollution. They are also short-lived climate forcers. The processes governing aerosol and ozone pollution in the Arctic are complex, but underestanding these processes is critical in order to understand the impacts of Arctic aerosols and ozone on air quality and climate. This section presents the main chemical and physical processes governing ozone (Section 2.1) and aerosols (Section 2.2) in the troposphere, as well as their radiative impacts.

2.1 Tropospheric ozone

In this section, we only focus on the mechanisms which are the most important to understand ozone pollution in the Arctic (Jacob, 1999).

2.1.1 Introduction: stratospheric and tropospheric ozone

Ozone is a trace gas in the atmosphere, with mixing ratios ranging from 1 ppbv to 10 ppmv. The highest ozone concentrationss are found in the stratosphere between 20 to 30 km altitudes, a region known as the ozone layer (Figure 2-1) .

In the stratosphere, UV radiation ($< 240\,\text{nm}$) can dissociate O_2 and form O_3:

$$O_2 + h \xrightarrow{< 240\,\text{nm}} O(^3P) + O(^3P) \tag{2.1}$$

$$O(^3P) + O_2 + M \text{ —} \quad O_3 + M \tag{2.2}$$

Where $O(^3P)$ is the oxygen atom in its triplet state and M is a third body, usually O_2 or N_2. Reactions 2.1 and 2.2 produce O_3, but O_3 can also dissociate in the presence of UV

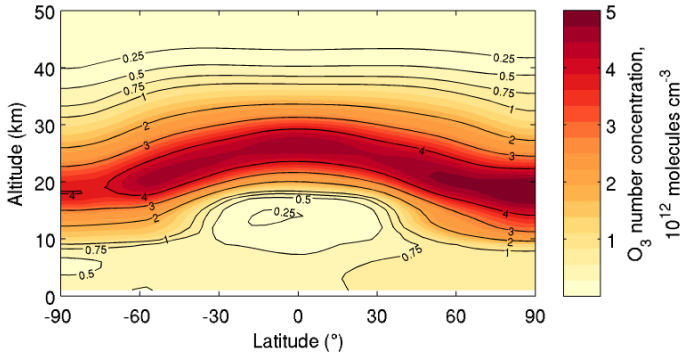

Figure 2-1 – Zonal mean ozone number concentrations (1979-2008 average), showing the location of the ozone layer around 25 km altitudes. Data from NOAA CDR (Bodeker et al., 2013).

radiation to make atomic oxygen, which can react with O_3 to reform O_2:

$$O_3 + h \xrightarrow{< 320\,nm} O_2 + O(^1D) \tag{2.3}$$

$$O(^1D) + M \text{ —} \quad O(^3P) + M \tag{2.4}$$

$$O_3 + O(^3P) \text{ —} \quad 2\,O_2 \tag{2.5}$$

Where $O(^1D)$ is the oxygen atom in its singlet state. This cycle (2.1–2.5) is called the Chapman cycle (Chapman, 1930). A steady-state analysis of this system reveals that it explains the location of the ozone layer, which is due to the simultaneous abundance of O_2 and UV radiation (reaction 2.1) at altitudes 20 to 30 km (Chapman, 1930). At lower altitudes, UV radiation at < 240 nm is filtered by the overhead O_2 and O_3, and reaction 2.1 cannot produce much O_3.

However, O_3 is also found at lower altitudes, in the troposphere (Figure 2-1). Since high-energy UV radiation does not penetrate into the troposphere, it was once thought that tropospheric O_3 was transported from the stratosphere. However, this theory could not explain the observations of enhanced O_3 at low altitudes and in polluted regions. Ripperton et al. (1971); Chameides and Walker (1973); Crutzen (1974) later proved that O_3 could also be produced locally in the troposphere from natural and anthropogenic compounds.

2.1.2 Chemical O_3 production in the troposphere from NO_x and VOC

2.1.2.1 Ozone production from NO_2

The main chemical reaction producing O_3 in the troposphere is the photolysis of NO_2:

$$NO_2 + h \xrightarrow{< 424\,nm} NO + O(^3P) \tag{2.6}$$

$$O_2 + O(^3P) + M \text{ —} \quad O_3 + M \tag{2.7}$$

However, ozone can also react with NO to reform NO_2:

$$NO + O_3 \text{ —} \quad NO_2 \tag{2.8}$$

Reactions 2.6–2.7 and 2.8 are fast, and correspond to a quick interconversion between NO and NO_2. For this reason, we can define the NO_x chemical family as the sum $NO + NO_2$. This interconversion also means that ozone can only be produced in the troposphere from NO_2 if there is another source of NO_2 than reaction 2.8.

2.1.2.2 Oxidation of CO, CH_4 and other hydrocarbons as ozone sources

Earlier studies identified that NO_2 could be produced in the troposphere during the oxidation of CO (Levy, 1972):

$$CO + OH \text{ —} \quad CO_2 + H \tag{2.9}$$

$$H + O_2 + M \text{ —} \quad HO_2 + M \tag{2.10}$$

$$HO_2 + NO \text{ —} \quad NO_2 + OH \tag{2.11}$$

Where OH is the hydroxyl radical and HO_2 the hydroperoxyl radical. Similarly to NO_x, a HO_x family can be defined as $OH + HO_2$. OH can be produced in the troposphere by several photochemical reactions, notably:

$$O_3 + h \xrightarrow{< 320\,\text{nm}} O_2 + O(^1D) \tag{2.12}$$

$$O(^1D) + H_2O \text{ —} \quad 2\,OH \tag{2.13}$$

Reaction 2.12 can occur from photons at wavelengths $300\,\text{nm} < \quad < 320\,\text{nm}$, which are found in the troposphere (photons at $\quad < 300\,\text{nm}$ are filtered by overhead stratospheric O_3 and O_2). From reactions 2.12–2.13, one O_3 molecule can produce 2 OH molecules, and each OH molecule can form one NO_2 molecule by oxidizing CO (2.9). This can result in net O_3 production if other reactions do not consume HO_x or NO_2. OH is an especially critical compound in the troposphere, since it controls the lifetime of a large number of tropospheric trace gases such as CO. For example, OH can also oxidize hydrocarbons such as CH_4:

$$CH_4 + OH \text{ —} \quad CH_3 + H_2O \tag{2.14}$$

$$CH_3 + O_2 + M \text{ —} \quad CH_3O_2 + M \tag{2.15}$$

$$CH_3O_2 + NO \text{ —} \quad CH_3O + NO_2 \tag{2.16}$$

Reactions 2.14–2.16 provide another source of NO_2 which can potentially produce O_3. Furthermore, the methyl peroxy radical, CH_3O_2, can be oxidized to form methoxy radicals, CH_3O, and formaldehyde, CH_2O (details in Jacob, 2000). Under high NO_x, these pathways lead to the formation of additional HO_2 and CO, and one molecule of CH_4 can produce an average of 3.7 molecules of O_3 (Crutzen and Zimmerman, 1991). Under low NO_x however,

these additional reactions are a net sink of HO_x and can decrease O_3. Longer hydrocarbon chains R−H can also be oxidized by a mechanism similar to 2.14–2.16 to form RO_2 and NO_2. Organic compounds present in the gas phase in the atmosphere are called Volatile Organic Compounds (VOC).

2.1.2.3 Global emissions of NO_x, CO, CH_4 and non-methane VOC (NMVOC)

Tropospheric O_3 is produced from NO_x, CO, CH_4, and other (non-methane) VOC. At the global scale, the main source of NOx and CO is human activity (Table 2.1). Natural emissions of NO_x are due to soils, lightning and wildfires. VOC emissions are mostly natural, due to methane sources from wetlands, and emissions of isoprene and terpenes by vegetation. Human VOC emissions include methane, several alkanes and alkenes, and aromatic compounds such as benzene and toluene. The non-methane VOC category represents a large variety of compounds with different reactivities and different impacts on ozone production.

Table 2.1 – Global NO_x, CH_4 and NMVOC emissions by source, from IPCC (Ciais et al., 2013; IPCC, 2013a), Wiedinmyer et al. (2011) and Sindelarova et al. (2014)

Source	NO_x ($TgN\,yr^{-1}$)	CH_4 ($Tg\,yr^{-1}$)	CO ($Tg\,yr^{-1}$)	NMVOC ($Tg\,yr^{-1}$)
Anthropogenic, excluding agriculture	28.3	96	1071	213
Agriculture	3.7	204.5	-	-
Biomass burning	5.5	32.5	372.5	81.3
Soils	7.3	-	-	-
Lightning	4	-	-	-
Vegetation	-	-	-	950
Oceans and geological sources	-	54	49	4.9
Wetlands, other natural sources	-	228.5	-	-

2.1.3 Photochemical sinks of ozone, HO_x and NO_x in the troposphere

The main chemical sinks of ozone in the troposphere are the following reactions:

$$O_3 + h \quad — \quad O_2 + O(^1D) \tag{2.12}$$

$$O(^1D) + H_2O \ — \quad 2\,OH \tag{2.13}$$

$$O_3 + OH \ — \quad O_2 + HO_2 \tag{2.17}$$

$$O_3 + HO_2 \ — \quad OH + 2\,O_2 \tag{2.18}$$

In addition, since there is an interconversion between O_3, NO_2 and HO_x, loss of HO_x and NO_2 results in a net destruction of ozone. HO_x are very reactive and several reactions can

compete with ozone formation. The reaction of HO_2 with itself is an important sink of HO_x:

$$HO_2 + HO_2 \text{ —} \quad H_2O_2 \tag{2.19}$$

Hydrogen peroxide, H_2O_2, is soluble in water and can be removed by precipitation (wet deposition). Likewise, NO_2 can react to form nitric acid, HNO_3, which can be efficiently removed by rain. During the day, when OH is available,

$$NO_2 + OH + M \text{ —} \quad HNO_3 + M \tag{2.20}$$

At night, there is less OH and NO_x is mostly found as NO_2 because NO_2 cannot be photolyzed. NO_2 can then react with O_3:

$$NO_2 + O_3 \text{ —} \quad NO_3 + O_2 \tag{2.21}$$

$$NO_3 + NO_2 + M \text{ —} \quad N_2O_5 + M \tag{2.22}$$

$$N_2O_5 + H_2O \xrightarrow{aerosol} 2\,HNO_3 \tag{2.23}$$

Wet removal of HNO_3 formed by reactions 2.20–2.23 is the main sink of NO_x.

2.1.4 Dry deposition of NO_x and O_3

NO_x and O_3 can also be removed by dry deposition, which constitutes an important sink for O_3. Dry deposition is the process by which a molecule or a particle is transferred to the surface where it is removed. Dry deposition is especially fast over vegetation, due to uptake in plants during respiration and transpiration (Erisman et al., 1994). Dry deposition depends mostly on the strength of the exchanges between the surface and the rest of the atmosphere: to reach the surface, a compound has to be transported by turbulence within a few centimeters of the surface, and then by molecular diffusion through the laminar boundary layer near the surface (Wesely, 1989). The speed of these processes depends on the properties of the surface and on the state of the atmosphere.

2.1.5 Peroxyacetyl nitrate (PAN) as a NO_x reservoir in the troposphere

NO_x have a relatively short lifetime of 0.5–2 days in the troposphere and therefore cannot be transported over long distances. However, research has shown that NO_x could be transported at the hemispheric scale through the formation of a reservoir species, peroxyacetyl nitrate (PAN, $CH_3C(O)OONO_2$) (e.g. Singh et al., 1986). PAN is formed by the oxidation of carbonyl compounds (e.g. acetaldehyde, CH_3CHO) by NO_2, and its main sink is thermal decomposition:

$$PAN \text{ —} \quad CH_3C(O)OO + NO_2 \tag{2.24}$$

The lifetime of PAN against thermolysis is 1 h at 295 K, and several months at 240 K (Jacob, 2000). As a result, PAN can be formed during high-altitude pollution transport, and can be decomposed to release NO_2 in remote regions when reaching lower altitudes. PAN is thought to be an important source of surface and lower tropospheric ozone in the Arctic during summer (e.g. Mauzerall et al., 1996).

2.1.6 The global budget of tropospheric ozone

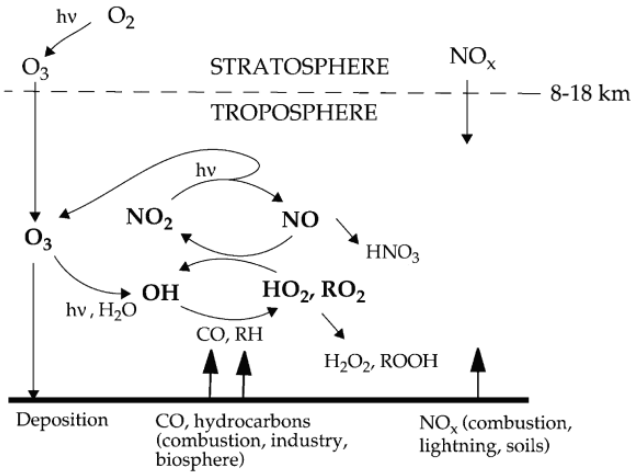

Figure 2-2 – Ozone chemistry and processes in the troposphere, adapted from Jacob (2000).

The main processes controlling ozone concentrations in the troposphere are shown in Figure 2-2. The sources of tropospheric ozone are both transport from the stratosphere and in situ production from NO_x and VOC, as presented in Section 2.1.2. The main sinks of ozone are chemical loss, dry deposition, and, indirectly, the loss of HO_x and NO_x from dry deposition, as well as wet deposition of H_2O_2 and HNO_3.

Table 2.2 – Global tropospheric ozone budget from 17 model studies, from Wild (2007)

Chem. prod. ($Tg\,yr^{-1}$)	Chem. loss ($Tg\,yr^{-1}$)	Prod - Loss ($Tg\,yr^{-1}$)	Stratosphere ($Tg\,yr^{-1}$)	Deposition ($Tg\,yr^{-1}$)
4465 ± 514	4114 ± 409	396 ± 247	529 ± 105	949 ± 222

Table 2.2 shows an estimate of the global budget of tropospheric ozone, based on 17 model studies published between 2000 and 2007 (Wild, 2007). Chemical production is the largest source of tropospheric ozone, and chemical destruction its largest sink. The net effect of tropospheric chemistry is to produce ozone, but this production and the stratospheric source are balanced by dry deposition (note that the budget is not perfectly balanced because not

all studies or models reported every statistic). Models can also be used to estimate the lifetime of ozone in the troposphere. Based on results from 26 models, Stevenson et al. (2006) report a mean lifetime of 22 days, but this average hides strong variations from a few days to a few months, depending on location, altitude and season.

2.1.7 Radiative effects of tropospheric ozone

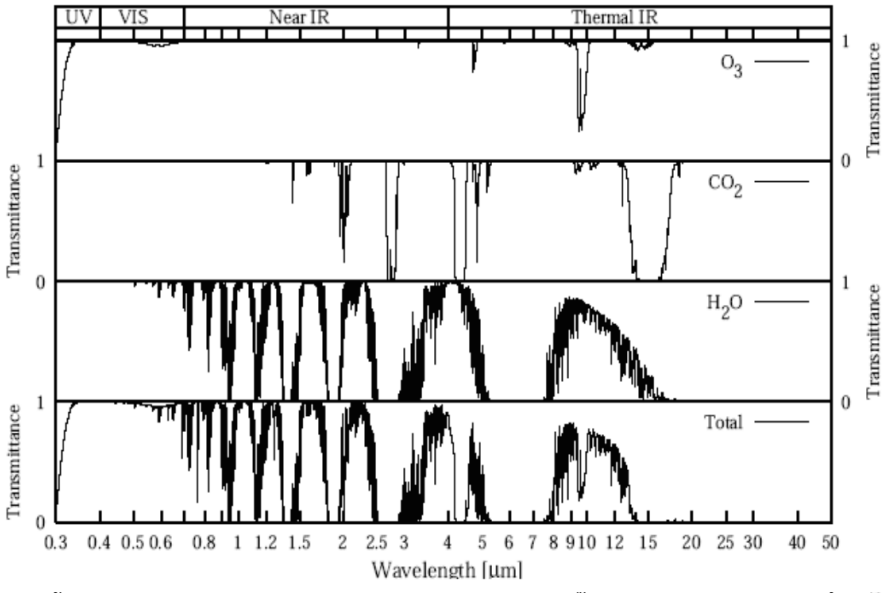

Figure 2-3 – Zenith atmospheric transmission spectrum, (0.3 to 50 µm), and the contributions from the 3 strongest greenhouse gases H_2O, CO_2 and O_3. Figure from Petty (2006).

O_3 is the third most important gas causing global and Arctic warming, in terms of radiative forcing and impacts on surface temperature (Section 1.1.2.1). Ozone has a LW (greenhouse) radiative effect and a SW (solar absorption) radiative effect. Figure 2-3 shows the spectrum of atmospheric transmittance between 300 nm and 50 µm wavelengths (near UV, visible and infrared). The contributions of H_2O, CO_2 and O_3 to this spectrum are also shown in Figure 2-3. O_3 absorbs strongly at < 300 nm, in the near-UV, and can thus absorb near-UV radiation from the sun (warming SW effect). O_3 has another strong absorption band in the infrared, near 9.6 µm. This wavelength overlaps with the spectrum of Earth's thermal radiation, and is located in a spectral region where other atmospheric gases do not absorb much (the 8 to 12 µm atmospheric window). This absorption band is responsible for most of the greenhouse effect due to ozone. The greenhouse (LW) effect of a greenhouse gas is stronger when there is a large temperature contrast between the surface and the altitude where the gas absorbs. As a result, the radiative effect of ozone is stronger near the tropopause (Lacis et al., 1990). Ozone also has an indirect radiative effect

by increasing OH, decreasing the methane lifetime. Furthermore, dry deposition of ozone via plant stomatal uptake also damages plants, reducing primary productivity, reducing the land carbon sink and indirectly increasing CO_2 forcing (Sitch et al., 2007).

2.1.8 Tropospheric ozone in the Arctic

This section presents Arctic O_3 pollution, its origins, as well as Arctic-specific processes influencing O_3 pollution and O_3 radiative impacts.

2.1.8.1 Arctic ozone pollution

O_3 concentrations measured at Arctic surface sites are usually between 10 and 50 ppbv (AMAP, 2015). Arctic surface O_3 is often higher during winter and spring, due to stronger pollution transport from the mid-latitudes and weaker removal processes, but several sites exhibit a winter/spring minimum due to ozone depletion events caused by catalytic cycles over snow and ice involving halogens (Bottenheim et al., 1990). Previous studies do not agree on the exact relative contributions of different remote emission regions, but indicate that European anthropogenic emissions are an important source of ozone pollution year-round in the lower Arctic troposphere. At higher altitudes, emissions from North America and Asia are also thought to make important contributions (Shindell et al., 2008; Wespes et al., 2012), as well as boreal and agricultural fires. Ozone formed in polluted regions can be directly transported to the Arctic. During summer, Arctic ozone can also be produced locally from NO_x transported PAN (Jacob et al., 1992). Stratosphere-troposphere transport is the main source of O_3 in the upper troposphere, and is highest during spring.

Several specific factors influence ozone pollution in the Arctic. The Arctic experiences polar night during winter, and low solar zenith angles year-round, which reduce the amount of UV radiation available for photochemistry. However, the sun does not set during polar day in summer, and snow and ice have a very high UV-albedo (0.96 for pure snow, Grenfell et al., 1994) which nearly doubles the available UV flux. Local emissions of NO_x are thought to be low in the Arctic, due to the relative lack of industrial emissions, the lack of lightning activity, and the low soil NO_x emissions. Nitrate photochemistry in snow is thought to be an important source of NO_x at the Arctic surface (Grannas et al., 2007), but this source is still relatively poorly known and is not included in most atmospheric models. Sources of VOC are also rare in the Arctic, but NO_x/VOC ratios are thought to be low (Jacob et al., 1992), and local O_3 production is thus more sensitive to perturbations in NO_x than to perturbations in VOC (e.g. Sillman, 1999 for a presentation of the NO_x and VOC sensitivity regimes).

O_3 and NO_x have a relatively long lifetime in the Arctic, due, in part, to lower dry deposition caused by the strong atmospheric stability over snow and ice (causing reduced atmosphere-surface exchanges) and the relative lack of vegetation (causing reduced uptake

by plants). There are also less liquid clouds and liquid precipitation in the Arctic during winter and spring, which decreases the efficiency of HNO_3 and H_2O_2 wet removal.

2.1.8.2 Radiative impacts from Arctic ozone pollution

In the Arctic, the temperature contrast between the surface and the atmosphere is lower than in other regions, and the greenhouse effect of ozone is reduced. However, the SW radiative effect of ozone is higher in the Arctic due to the the high UV albedo of snow and ice, and the longer path lengths for solar radiation. At the global scale, the radiative effect of troposperic ozone is mostly due to its LW effect, but in the Arctic both effects might be approximately equal (Berntsen et al., 1997).

2.2 Tropospheric aerosols

Aerosols are defined as all liquid or solid particles suspended in the atmosphere, excluding cloud droplets, ice crystals, and other hydrometeors. Atmospheric aerosols vary strongly in chemical composition, size, and spatial distribution.

2.2.1 Global aerosol sources

The main sources and types of aerosols at the global scale are presented in Table 2.3. Aerosol emissions are mostly natural, due to sea salts emitted from oceans and mineral dust emitted from deserts. Less than 10 % of total aerosol emissions and production is of anthropogenic origin, but anthropogenic sources contribute significantly to the global budget of sulfate, nitrate, black carbon and organic aerosols. In Table 2.3, biomass burning is presented separately because it can be due to both human and natural causes. Aerosols emitted directly as particles (e.g. dust, sea salt, ashes) are called primary aerosols, and aerosols formed from gas to particle conversion (involving complex microphysical and chemical processes) are called secondary aerosols (e.g. sulfate, nitrate, ammonium, secondary organic aerosols).

2.2.2 Aerosol properties: chemical composition, mixing state, size

2.2.2.1 Composition

Table 2.3 illustrates the chemical variety of aerosols, which can be separated into 5 main categories: black carbon, organic aerosols, inorganic soluble aerosols, sea salt, and other inorganics.

- Black carbon is mostly made of elemental carbon atoms in graphite aggregates, but what constitutes BC is not well defined and can include other light-absorbing compounds (Petzold et al., 2013). In the present work, black carbon (BC) designates pure elemental carbon (EC), unless indicated otherwise.
- Organic aerosols are carbon-containing particles of organic origin (other than BC), which can come from anthropogenic or biogenic activity. Primary organic aerosols (POA) are directly emitted (e.g. non-volatile organic compounds, organic debris), while secondary organic aerosols (SOA) are formed from gas-phase reactions involving VOCs. The volatility of organic gases is a continuum (volatile OC, semi-volatile OC, non-volatile OC), and some compounds can either be in the gas phase or the condensed phase, depending on environmental conditions.
- Inorganic soluble aerosols in the atmosphere are secondary aerosols such as sulfate SO_4^{2-}, nitrate NO_3^- or ammonium NH_4^+, which are very hygrophilic.

Table 2.3 – Global sources of aerosols by composition, from (1) IPCC (Boucher et al., 2013) (2) Delmas et al. (2005), (3) Spracklen et al. (2011), (4) Seinfeld and Pandis (2006), (5) Adams et al. (1999). POA are Primary Organic Aerosols, SOA Secondary Organic Aerosols

Source	Emissions & Secondary production ($Tg\,yr^{-1}$)
Natural	
Primary aerosols	
Sea spray	1400-1800[(1)]
including marine POA	2–20[(1)]
Mineral dust	1000 – 4000[(1)]
Volcanic ash	33[(2)]
Biogenic POA	56[(2)]
Secondary aerosols	
Sulfate from oceanic DMS	90[(2)]
Sulfate from volcanic SO_2	21[(2)]
SOA from biogenic VOC	20–380[(1)]
Nitrate from NO_x	4[(2)]
Ammonium from NH_3	13.4[(5)*]
Anthropogenic	
Primary aerosols	
BC	3.6–6.0[(1)]
POA	6.3–15.3[(1)]
Secondary aerosols	
Sulfate from SO_2	120[(2)]
SOA from VOC	100[(3)]
Nitrate from NO_x	21.3[(4)]
Ammonium from NH_3	20.2[(5)*]
Biomass burning	
Primary aerosols	
BC	5.7[(2)]
POA	54[(2)]
Secondary aerosols	
SOA from VOC	3[(3)]
Sulfate and nitrate	90[(4)]

* Assuming 60 % of atmospheric ammonium is of anthropogenic origin (Asman et al., 1998).

- Sea salt aerosols are mostly composed of NaCl, uplifted by winds from the ocean surface.
- Other inorganic aerosols are relatively non-reactive and insoluble particles, such as mineral dust, ashes, industrial dust, metals...

Aerosol composition in the Arctic is variable (Schmale et al., 2011; Frossard et al., 2011; Brock et al., 2011), but measurements (e.g. Figure 2-4) usually indicate that fine aerosols in the Arctic contain mostly sulfate and organic matter, while coarse aerosols can also contain mineral dust and sea salt.

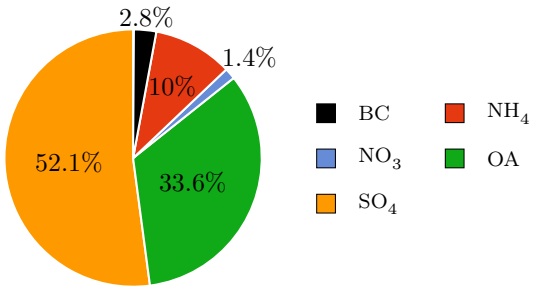

Figure 2-4 – Average composition (mass proportion) of submicron aerosols measured in the free troposphere in the Alaskan Arctic in spring 2008 (Brock et al., 2011). Measurements are for background (haze) conditions. The chart does not include dust or sea salts, which represent respectively 6 % and 4 % of fine particles, and 49 % and 23 % of coarse particles (number proportions).

2.2.2.2 Mixing state

Aerosols are rarely made of a single pure compound, and are often mixed. Figure 2-5 represents several possible mixing states of an aerosol population.

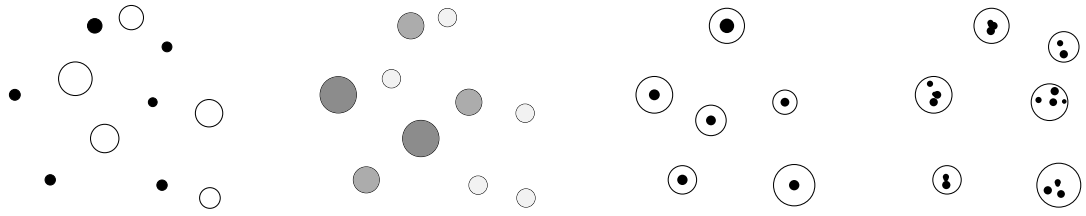

Figure 2-5 – Aerosol mixing states: (a) External mixing, (b) Internal mixing, well-mixed (c) Core-shell mixing, (d) Random spherical inclusions

External mixing occurs when each particle size is associated to a single composition. Another common model of aerosol mixing is internal mixing, which assumes that aerosols

of a given size have the same (mixed) composition. Components of an aerosol can be well-mixed, or can be separated within the particle: core-shell mixing represents aerosols as separated between an internal refractory "core" (often made of BC) and a coating "shell" (secondary components often composed of sulfate, nitrate, ammonium, organic matter and water). This refractory part can also be represented as scattered in the volatile phase, in the form of randomly-distributed spherical inclusions. These different mixing states or a combination of them can be found in the atmosphere, but numerical models often make the assumption of a single mixing state. This assumption can have a strong influence on the calculated optical, microphysical and chemical properties of the aerosols (Chýlek et al., 1988; Wang et al., 2010).

2.2.2.3 Size distributions

Aerosol diameters range from 2 nm to 100 µm. Although aerosols are often non-spherical, their size can be characterized by an equivalent diameter D (e.g. the aerodynamic diameter, or the Stokes diameter). Aerosol optical, chemical and microphysical properties are very sensitive to particle size (Bohren and Huffman, 1983; Dusek et al., 2006). Dust, ashes and sea salt are usually large particles ($D > 1\,\mu m$), while black carbon, organic aerosols and soluble inorganic aerosols are often fine ($D < 1\,\mu m$).

An aerosol population in a given volume of air contains particles of different diameters; this population can be described by a function $n(D) = dN/dlogD$ (cm^{-3}) called a number size distribution. Figure 2-6 shows (thin line and circles) the size distribution of aerosols from anthropogenic pollution measured in the Scandinavian Arctic in spring 2008 (Quennehen et al., 2012). The aerosol distribution presents two main modes, with modal diameters of 35 nm and 100 nm. Each of these modes can be approximated by a lognormal size distribution (2 modes, shown in Figure 2-6).

$$n_i(D) = \frac{dN_i(D)}{dD} = N_i \frac{1}{\ln(\ _i) D \ \overline{2}} exp \quad - \frac{\ln^2 \ \frac{D}{D_i}}{2 \ln^2(\ _i)} \tag{2.25}$$

Where dN_i is the number of particles in mode i with a diameter between D and $D + dD$, N_i the total number of particles in mode i, D_i the modal diameter, and $_i$ its geometric standard deviation. Other approaches can be used to approximate a size distribution, such as the use of discrete size bins (sectional approach, also shown in Figure 2-6).

Aerosol size distributions in the atmosphere are usually distributed in a limited number of modes (typically, 1 to 4). A mode centered between 0 to 10 nm is called a nucleation mode, 10 to 100 nm is the Aitken mode, 0.1 to 1 µm is the accumulation mode. Larger modes ($D > 1\,\mu m$) are called coarse modes. These names, and the existence of these modes, are due to the processes governing aerosol formation, growth and removal. In general, the

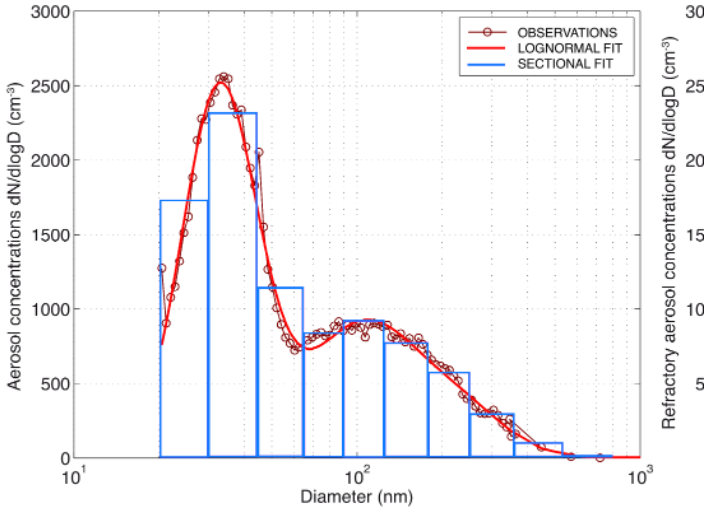

Figure 2-6 – Aerosol number size distribution in a pollution plume sampled in the Scandinavian Arctic in spring 2008, showing measurements (thin line and circles), a statistical fit with two lognormal modes (thick red line) and an approximate fit by 10 discrete size bins (blue). Adapted from Quennehen et al. (2012).

fine and coarse particle modes have different origins, are transformed separately, are removed from the atmosphere by different mechanisms, and have different compositions and optical properties.

For air quality applications, aerosol amounts are often given as Particulate Matter (PM) mass, for example PM_{10}, representing the total mass of aerosols with aerodynamic diameters smaller than 10 µm. $PM_{2.5}$ ($D < 2.5$ µm) are also often used.

2.2.3 Aerosol processes: from nucleation to removal

The main aerosol processes, including primary emissions, nucleation, coagulation, condensation, activation in clouds, dry deposition and wet removal, are schematically represented in Figure 2-7.

2.2.3.1 Aerosol formation: primary emissions and nucleation

Aerosols can be formed by two processes: primary emission or nucleation. Fine primary aerosols are usually combustion residues from fossil fuel or biomass burning. Coarse primary aerosols are formed by mechanical processes, e.g. uplift by winds of mineral dust from an erodible surface, or uplift of ocean water containing sea salt.

Nucleation is the formation of aerosols from precursor gases (e.g. sulfuric acid, H_2SO_4, ammonia, NH_3, nitric acid, HNO_3). NH_3 is directly emitted by human activity, especially agriculture; HNO_3 is formed from NO_x (Sect. 2.1.3); H_2SO_4 can be formed from dimethyl-

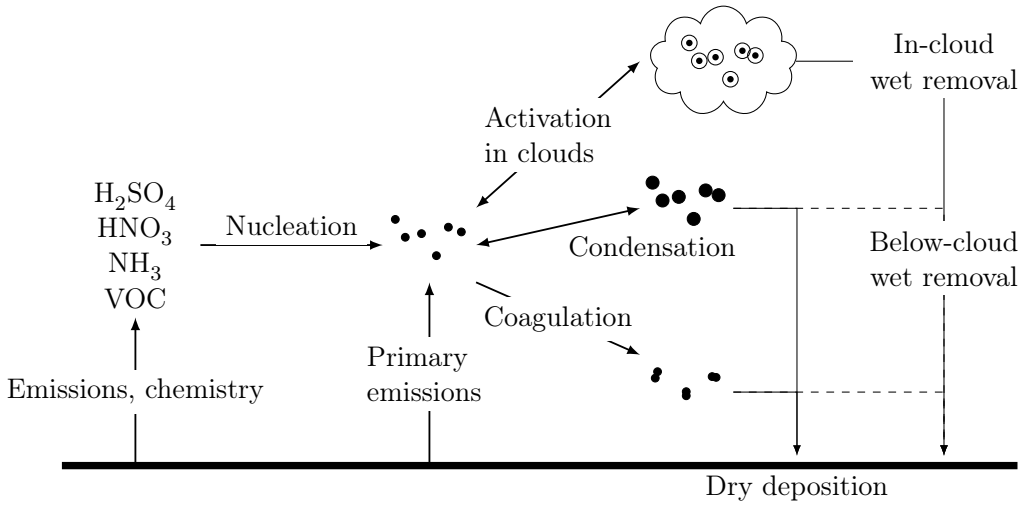

Figure 2-7 – Aerosol physical processes. The coagulation, condensation and activation processes are represented separately for clarity, but all of these processes can occur in the same aerosol population.

sulfide (DMS, emitted by biogenic activity in oceans) or by the oxidation of SO_2:

$$SO_2 + OH + M \text{ —} \quad HSO_3 + M \tag{2.26}$$

$$HSO_3 + O_2 + M \text{ —} \quad SO_3 + HO_2 \tag{2.27}$$

$$SO_3 + H_2O + M \text{ —} \quad H_2SO_4 + M \tag{2.28}$$

Homomolecular nucleation (nucleation of a single pure compound) is very inefficient in the atmosphere, and new particle formation usually involves binary nucleation by H_2SO_4-H_2O, or ternary nucleation by H_2SO_4-NH_3-H_2O. These mechanisms form very small clusters (1 to 2 nm, nucleation mode particles).

2.2.3.2 Aerosol growth by coagulation, condensation, and aqueous chemistry

Once formed, small aerosol clusters can grow by coagulation or condensation. Coagulation is caused by particle collisions and coalescence (Fuchs, 1964). For small particles, these collisions are mostly caused by Brownian motion. For larger particles, coagulation can be caused by differences in fall speed during sedimentation or by turbulent motion. Coagulation decreases aerosol number concentrations but conserves aerosol mass and volume.

Gaseous NH_3, HNO_3, H_2SO_4 and organic gases can condensate on preexisting particles. H_2SO_4 is non-volatile in the atmosphere and its condensation on particles is irreversible, but other gases (HNO_3, HCl, organic gases) are semi-volatile and can evaporate depending on physical conditions (e.g. Zaveri et al., 2008).

Aerosols can also grow by water uptake if they are sufficiently hygrophilic (e.g. sulfate, sea salt, see also Section 2.2.3.3). A number of particle-gas reactions forming aerosols can

occur in the aqueous phase, forming e.g. NH_4^+:

$$NH_3(g) \quad NH_3(aq) \tag{2.29}$$

$$H_2O(aq) + NH_3(aq) \quad OH^-(aq) + NH_4^+(aq) \tag{2.30}$$

and NO_3^-:

$$HNO_3(g) \text{ —} \quad H^+(aq) + NO_3^-(aq) \tag{2.31}$$

Aqueous oxidation in clouds is a major pathway for SO_4^{2-} formation from SO_2:

$$SO_2(g) \quad SO_2 \cdot H_2O \tag{2.32}$$

$$SO_2 \cdot H_2O \text{ —} \quad HSO_3^- + H^+ \tag{2.33}$$

$$HSO_3^- + H_2O_2(aq) + H^+ \text{ —} \quad SO_4^{2-} + 2\,H^+ + H_2O \tag{2.34}$$

Condensation and aqueous chemistry conserves aerosol number but increases aerosol mass. Coagulation and condensation are more efficient for small particles ($D < 100\,\text{nm}$), and explain the growth of aerosols up to the accumulation mode, hence the name of this mode.

2.2.3.3 Aerosol activation in clouds

Cloud droplets cannot form on their own from pure water in the atmosphere. This is because the equilibrium water vapor pressure over the curved surface of a small droplet is much greater than over a flat surface (Kelvin effect). For this reason, very small pure water droplets are unstable even when relative humidity (RH) is much greater than 100 %. In the atmosphere, cloud droplet formation always involves consensation of water over a preexisting aerosol for two reasons (Andreae and Rosenfeld, 2008). First, the surface of a preexisting aerosol is less curved than the surface of a freshly formed pure-water cluster. Second, if the aerosol is hygroscopic, the equilibrium water vapor pressure over its surface is lowered even more (Raoult effect).

Ice clouds can form by homogeneous nucleation when temperatures are −38 C or lower, but the presence of aerosols can facilitate ice cloud formation at higher temperatures. Aerosols facilitating cloud ice formation are called ice nuclei (IN), and aerosols activated as liquid cloud droplets are called cloud condensation nuclei (CCN). At the global scale, CCN are mostly composed of sea salt or sulfate, and IN are often mineral dust, or primary organic particles (e.g. pollen, spores) (Andreae and Rosenfeld, 2008).

2.2.3.4 Aerosol dry and wet removal

Aerosols activated in clouds can be removed by rainout when cloud and ice droplets grow and precipitate. Precipitation can also remove aerosols below clouds by impaction. Aerosols

can also be removed by dry deposition (Section 2.1.4), which is especially efficient for coarse particles due to gravitational settling. Wet removal is the main pathway for aerosol removal for BC (79 % of total removal, standard deviation = 17 %), POA (80 %, = 16 %), and SO_4^{2-} (89 %, = 8 %) (Textor et al., 2006). In the Arctic during spring, Wang et al. (2011) estimate that 85 to 91 % of BC deposition is due to wet removal.

2.2.4 Aerosol optical properties

Aerosols can interact with solar and terrestrial radiation by absorbing and scattering light. This interaction is responsible for the direct radiative effect of aerosols, which contributes to their impact on climate. These aerosol/radiation interactions can be quantified by calculating the optical properties of the aerosols.

2.2.4.1 Scattering and absorption by a single particle

The interaction of an aerosol with solar and terrestrial radiation can be described as the sum of a scattering term (describing the change in direction of light due to the presence of the aerosol) and an absorption term (describing the transfer of energy from photons to the particle). This is illustrated in Figure 2-8.

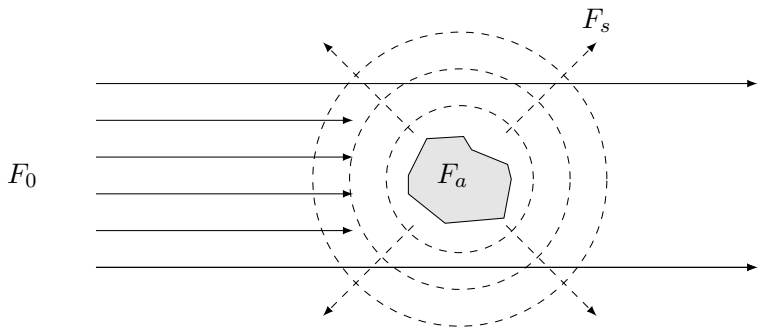

Figure 2-8 – Direct aerosol-radiation interactions: incident flux, absorbed flux and scattered flux.

If the radiative flux per unit surface reaching a particle is F_0 ($\mathrm{W\,m^{-2}}$), the flux F_a (W) being absorbed by this particle is

$$F_a = \ _a F_0, \tag{2.35}$$

while the scattered flux is

$$F_s = \ _s F_0, \tag{2.36}$$

where $\ _a$ and $\ _s$ ($\mathrm{m^2}$) are the single-particle absorption cross-section and scattering cross-section, and the sum $\ _{ext} = \ _a + \ _s$ is called the extinction cross-section. These cross-sections

can be calculated using Mie theory (Mie, 1908), knowing the wavelength of the incident radiation, the complex refractive index of the aerosol $m = n - ik$ and the size of the aerosol, given as an adimensional size parameter $x = \frac{D}{}$ (aerosol diameter D).

2.2.4.2 Scattering phase function

Mie calculations show, in agreement with observations, that scattering by an aerosol is not isotropic. The angular distribution of light scattered by an aerosol can be described by the phase function $p(\ )$ of the particle, representing the intensity $F(\ )$ scattered in direction (relative to the incident beam), normalized by the total scattered intensity:

$$p(\ ) = \frac{F(\ )}{F(\ )\frac{d}{4}} \tag{2.37}$$

Where is the solid angle. Figure 2-9 shows the typical shape of the phase function for small aerosols ($x << 1$, Rayleigh regime) and for typical aerosols (x 1, Mie regime). It illustrates that typical aerosols scatter mostly in the forward direction, but that a portion of the radiation is backscattered.

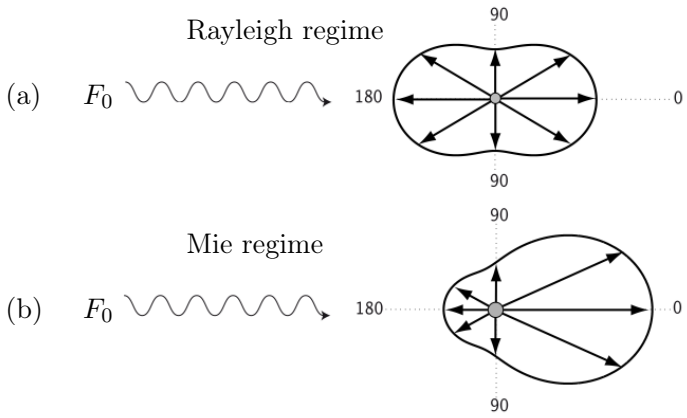

Figure 2-9 – Scattering by a spherical aerosol: shape of the phase function in the (a) Rayleigh regime (b) Mie regime. From Quennehen (2011)

2.2.4.3 Absorption by a single particle, relation to the refractive index and mixing state

Optical absorption is mostly due to the imaginary part of the refractive index m of a particle ($m = n - ik$). The refractive indices (visible wavelengths) of several pure aerosol components are given in Table 2.4. Most components are non-absorbing at these wavelengths, except BC, dust, and (not shown here) other compounds such as brown carbon and metal oxides.

An atmospheric aerosol often contains a mixture of absorbing and non-absorbing compounds (Section 2.2.2.2). The effective refractive index of this mixed aerosol depends on the

Table 2.4 – Real and imaginary parts of the refractive indices of aerosol components at 589 nm (unless otherwise indicated). Values are from Kanakidou et al. (2005); Seinfeld and Pandis (2006); Bond et al. (2006).

Species	Refractive index, real	Refractive index, imaginary
Liquid water	1.333	0
NaCl	1.544	0
H_2SO_4	1.426	0
NH_4HSO_4	1.473	0
$(NH_4)_2H_2SO_4$	1.521	0
OA (= 300 nm to 800 nm)	1.45	0
BC (= 550 nm)	1.85	-0.71
Mineral dust (= 550 nm)	1.56	-0.006

mixing state of the particle. For a well-mixed aerosol, we can assume that the refractive index, m_{mix}, of the mixture is the volume average of the indices of the individual components i (volume V_i) of refractive index m_i,

$$m_{mix} = \frac{V_i m_i}{V_i} \tag{2.38}$$

If the aerosol is not well-mixed (core-shell, random spherical inclusions), calculations of the effective refractive index are more complex (Heller, 1965) and result in a lower imaginary part (−15 to 30 % for core-shell mixing, Schuster et al., 2005). Scattering also depends on the refractive index of the particle and on mixing state assumptions.

2.2.4.4 Optical properties of an aerosol population

The absorption and scattering cross sections calculated by Mie theory for individual particles can be integrated to define the bulk scattering, absorption and extinction coefficients ($_s$, $_a$ and $_{ext}$, in m^{-1}) of an aerosol population of number size distribution dN/dD.

$$_s( ) = \int_0^{D_{max}} {}_s(, D)\frac{dN}{dD}dD \tag{2.39}$$

$$_a( ) = \int_0^{D_{max}} {}_a(, D)\frac{dN}{dD}dD \tag{2.40}$$

$$_{ext}( ) = \int_0^{D_{max}} {}_{ext}(, D)\frac{dN}{dD}dD \tag{2.41}$$

The backscattered fraction of $_s$ is noted . The optical depth of an aerosol layer (altitudes z_1 to z_2, often from the surface to the top of the atmosphere, also noted AOD) is defined as

$$( ) = \int_{z_1}^{z_2} {}_{ext}(z ,)dz \tag{2.42}$$

The single-scattering albedo of the aerosol population is

$$(\ ) = \frac{_s(\ )}{_{ext}(\ )} \tag{2.43}$$

The bulk coefficients $_s$, $_a$ and $_{ext}$ describe the interaction of an aerosol population with radiation, and can be used to calculate the radiative impacts of atmospheric aerosols.

2.2.5 Aerosol radiative effects

The radiative effects of aerosols are due to their direct interaction with radiation (direct radiative effects, due to scattering and absorption); to their impacts on cloud formation, properties and lifetime (indirect and semi-direct radiative effects); and to their effect on the albedo of snow.

2.2.5.1 Direct aerosol-radiation interactions: absorption and scattering by an aerosol layer

The interaction between an optically thin aerosol layer (optical depth , single scattering albedo , backscatter fraction , here equal to the upscatter fraction because the solar zenith angle is 0°) and solar radiation (radiative flux F_0) can be modeled as in Figure 2-10.

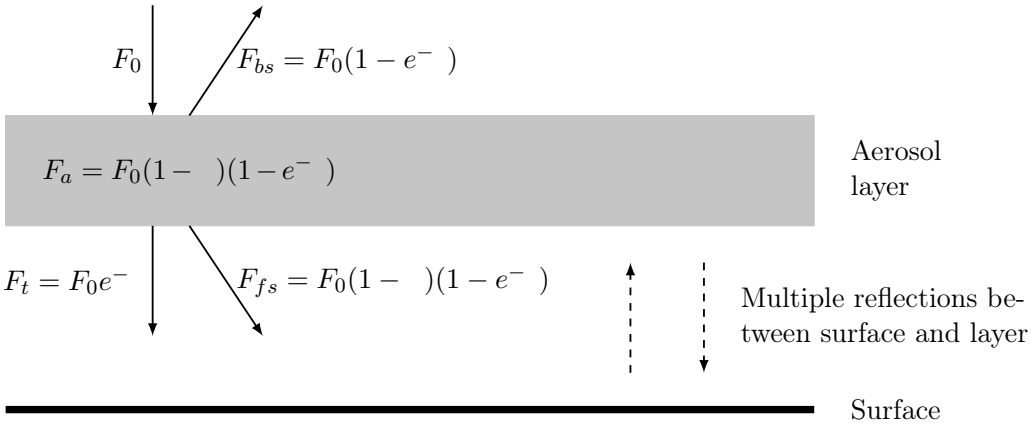

Figure 2-10 – Interactions between solar radiation and an aerosol layer, in clear sky conditions.

Where $F_a = aF_0$ is the absorbed flux, $F_{bs} = rF_0$ is the backscattered flux, F_{fs} is the forward-scattered flux, and F_t the transmitted flux, and

$$a = (1 - \ )(1 - e^{-\ }) \tag{2.44}$$

$$r = (1 - e^{-\ }) \tag{2.45}$$

The total transmitted flux ($F_t + F_{fs} = tF_0$, and $t = e^{-}$ $+ (1 -$ $)(1 - e^{-}$ $)$) can be reflected multiple times between the surface (surface albedo R_s) and the aerosol layer, and the resulting total upward flux leaving the system at TOA is

$$F_{aer} = F_0 \quad r + \frac{R_s t^2}{1 - rR_s} \tag{2.46}$$

Without the aerosol layer, the upward flux at TOA would be $F_{noaer} = F_0 R_s$, which means that the radiative effect of the aerosol layer at TOA is

$$F = F_{aer} - F_{noaer} = F_0 \quad r + \frac{R_s t^2}{1 - rR_s} - R_s \tag{2.47}$$

The resulting radiative effects are the following:

- Within the aerosol layer, aerosols cause warming ($F_a > 0$).
- At the surface, any aerosol layer aloft reduces downward radiation and causes cooling ($tF_0 < F_0$), but aerosols at the surface can cause warming ($F_a > 0$).
- At TOA (radiative effect F on the whole surface-atmosphere system) : aerosols can cause cooling or warming depending on , and R_s.

This "direct radiative effect" of aerosols is negative at the global scale, but it depends strongly on the surface albedo R_s (Haywood and Shine, 1995). Over high-albedo surfaces in the Arctic, aerosol layers have a stronger warming effect and weaker cooling effect, and even particles with weak absorbing properties cause a net warming at TOA (Pueschel and Kinne, 1995). For the same reason, weakly absorbing aerosol layers located above high-albedo clouds can also cause warming at TOA. The Arctic is very often covered by thick, low clouds (Cesana et al., 2012). For this reason, the direct effect of aerosols can either be increased due to the high cloud albedo if the aerosol layer is located above clouds, or decreased due to the reduced downwelling solar radiation (reduced F_0) if the aerosol layer is located below clouds.

Absorbing aerosols such as BC, when present aloft, will reduce the amount of SW radiation reaching the surface while having a warming effect within the layer. Since the Arctic troposphere is generally stably stratified, BC present in the planetary boundary layer can heat the surface, but BC aloft will usually cool the surface (Flanner, 2013).

Figure 2-10 only shows the interaction between aerosols and shortwave radiation. Aerosols can also interact with longwave radiation, but this direct LW effect is only significant for large particles (e.g. mineral dusts) transported at high altitudes (Tegen 1996). Most pollution aerosols are located in the accumulation mode, and the global direct LW effect of pollution aerosols is much lower than their SW effect (Myhre et al., 2013). For this reason, the direct radiative effect of aerosols in the Arctic during winter is weak.

2.2.5.2 Aerosol effects on Arctic clouds and resulting radiative effects

In addition to their direct effects, aerosols have an effect on the radiative budget through their impacts on cloud properties (semi-direct and indirect aerosol radiative effects). These cloud/aerosol radiative effects are different in the Arctic than elsewhere in the globe, due to the particularities of Arctic meteorology and Arctic clouds.

2.2.5.2.1 Arctic clouds

The Arctic is often covered with low-altitude stratus clouds. At the global scale, stratus clouds usually have a cooling effect due to their high albedo (increasing the loss of solar radiation to space and reducing solar radiation at the surface) and their weak greenhouse effect (due to the weak temperature contrast between surface and cloud tops). In the Arctic, the SW cooling effect of clouds is reduced, due to the lack of SW radiation during winter and spring, and due to the low contrast in albedo between clouds and snow- or ice-covered surfaces. As a result, the LW (greenhouse) effect of clouds dominates in the Arctic, and clouds have a net warming effect at the surface (Shupe and Intrieri, 2004). During the Arctic summer, snow and ice cover decreases and solar radiation increases, and Arctic clouds mostly cause surface cooling due to their high albedo.

2.2.5.2.2 Semi-direct aerosol radiative effects in the Arctic

An aerosol layer located in altitude cools the surface and warms aloft; this results in increased atmospheric stability. The cloud response to this increased stability is relatively complex, with several competing processes. First, this increased stability can reduce the cloud-top entrainment rate, increasing stratus cloud cover. Second, increased stability can also inhibit convection, reducing the amount of cumulus clouds, even if cumuli are relatively rare in the Arctic. Third, absorbing aerosol layers located at low altitudes can increase temperatures and lower relative humidities enough to evaporate low-level clouds (cloud burn-off, Hansen et al., 1997; Koch and Del Genio, 2010).

In the Arctic, the direct aerosol radiative effects are very low during winter and spring, due to lack of SW radiation during polar night. As a result, semi-direct effects (which are consequences of the direct effects) are also low during winter and spring. During the Arctic summer, direct and semi-direct effects are higher, but the sign of the semi-direct effect depends on the aerosol vertical distribution. Aerosol enhancements at low altitudes have a warming (positive) semi-direct effect (cloud burn-off, decreased SW cloud cooling), and aerosols enhancements at higher altitudes have a cooling (negative) semi-direct effect (reduced cloud-top entrainment rates, increased cloud-cover, increased SW cloud cooling). Because of this, semi-direct effects of aerosols from local Arctic emission sources (stronger at the surface) are more likely to cause warming than aerosols from remote sources (often

transported at higher altitudes). This sensitivity of Arctic semi-direct effects to vertical aerosol distributions is discussed in detail in Flanner (2013).

2.2.5.2.3 Radiative effects of cloud-aerosol interactions in the Arctic

Increased aerosol concentrations usually lead to increased CCN concentrations, increasing cloud droplet number and decreasing droplet sizes. These changes in cloud microphysical properties increase the cloud albedo (SW cooling effect, Twomey, 1977) but also increase the LW emissivity of clouds (LW warming effect, Garrett and Zhao, 2006), and increase the cloud lifetime by reducing precipitation (Albrecht, 1989). These cloud-aerosol effects are called the indirect effects of aerosols. At the global scale, the indirect SW cooling effect outweighs the indirect LW warming effect and cloud aerosol interactions cause a net cooling (Myhre et al., 2013).

Arctic clouds are especially sensitive to aerosol-cloud interactions due to the relative lack of CCN in the Arctic (Mauritsen et al., 2011). In addition, as discussed in Section 2.2.5.2.2, the warming LW effect of Arctic clouds is stronger than their SW cooling effect, except during summer. As a result, cloud-aerosol interactions also cause warming in the Arctic during all seasons except summer, by increasing cloud optical depth, cloud emissivity, cloud cover and cloud lifetime. At Barrow (Alaska), Zhao and Garrett (2015) found that cloud-aerosol interactions had a warming effect in October–May and a cooling effect during June–September. The yearly-averaged effect of cloud-aerosol interactions at Barrow was found by Zhao and Garrett (2015) to be a weak warming.

2.2.5.3 Radiative effects of absorbing aerosols deposited on snow

In the Arctic, absorbing aerosols (e.g. BC, dust) can significantly contribute to local warming by being deposited on snow and ice (Warren and Wiscombe, 1980). Aerosol deposition on snow lowers the surface albedo, and leads to earlier snow melt, revealing the darker underlying surface. BC can also indirectly increase snow absorption by increasing the average snow grain size (Flanner et al., 2007). These snow-albedo effects are also more sensitive to local sources emitted at the Arctic surface (Shindell, 2007; Flanner, 2013).

Chapter 3

Methods: modeling tools, emission inventories and Arctic measurements

One of the objectives of this thesis is to quantify the impacts of remote and local sources of pollution on Arctic aerosols and ozone. These impacts can be estimated using 3D atmospheric models predicting the state and composition of the atmosphere. In these models, estimated emissions of aerosols and trace gases are transported based on results from a meteorological model (e.g. wind, temperature), and are transformed based on physical (e.g. advection, diffusion, interaction with clouds) and chemical (e.g. gas-phase chemistry, dry deposition, aerosol aging) processes.

Such atmospheric models can be used to calculate the effect of a source of pollutant emissions on the state and composition of the atmosphere. The impacts of a specific pollution source (or region) can be determined by performing simulations with and without pollutant emissions from this source, since this perturbation in emissions leads to a change in 3D modeled pollutant concentrations, meteorological properties and radiative budgets. This perturbation approach is used in Chapters 4, 5 and 6.

This Chapter presents the main atmospheric modeling tools used in this thesis, the air pollutant emission inventories used as input for model simulations; and the Arctic measurements of atmospheric constituents and meteorological properties used to validate model results and used as a basis for case studies analyzing Arctic pollution.

3.1 Modeling the air quality and radiative impacts of short-lived pollutants in the Arctic.

To date, studies investigating aerosols and ozone pollution in the Arctic have mostly relied on global chemical-transport models (CTM) and global climate models (GCM). However, as mentioned in Section 1.4.1, intercomparisons have shown that most global models struggle

to represent aerosols in the Arctic, due to uncertainties in the treatment of precipitation and clouds. This could be due to limited grid resolution, incomplete representations of aerosol and clouds processes, or other approximations in models. For this reason, simulations are performed in this thesis using a regional meteorology-chemistry-aerosol model, WRF-Chem (Grell et al., 2005; Fast et al., 2006). Compared to global models, using a regional model has two main advantages. First, using smaller, regional domains is less computationally costly, allowing the use of higher grid resolutions or more detailed chemistry, aerosol and physics schemes. Second, regional models such as WRF-Chem can use *ad hoc* grids centered on the Arctic (i.e., polar stereographic grids), while global model simulations are typically run on latitude-longitude grids, where the North Pole is a singularity and the grid is strongly anisotropic near the poles. In order to preserve numerical stability, models run on latitude/longitude grids require special filtering at the pole (Takacs et al., 1999), which do not scale well on parallel computers (Skamarock et al., 2012).

WRF-Chem is called "online" (as opposed to "offline") because it performs simultaneously meteorological and chemical calculations. Online models such as WRF-Chem can take into account the aerosol/meteorology and trace gas/meteorology interactions, since calculated chemical and aerosol compositions can influence the meteorological fields (e.g. through changes in the radiation budget or clouds). Unless otherwise specified, these interactions are always included in the simulations presented in this thesis.

3.1.1 Regional meteorology-chemistry-aerosol modeling with WRF-Chem

In this thesis, regional chemical-transport simulations are performed with the fully coupled, online WRF-Chem model (Weather Research and Forecasting model, including chemistry, Grell et al., 2005; Fast et al., 2006) version 3.5.1. WRF-Chem is a regional atmospheric model based on the mesoscale meteorological model WRF-ARW (Advanced Research WRF, Skamarock et al., 2008). WRF-Chem is fully integrated within WRF, and uses the same grid, time step, advection scheme and physics schemes as WRF. WRF-Chem is a community model and is highly modular: meteorological, aerosol and gas-phase processes can be represented by different schemes of different complexities. WRF-Chem has been widely used to study air quality over emission regions, and has been extensively validated over Europe (e.g. Tuccella et al., 2012; Zhang et al., 2013a,b), Asia (e.g. Kumar et al., 2012; Quennehen et al., 2015) and North America (e.g. Fast et al., 2006; Tessum et al., 2015). In relation to this thesis, WRF-Chem has also been used in the past to study e.g. the impacts of shipping at high latitudes (Mölders et al., 2010), to analyze aircraft observations of CO and aerosols (Fast et al., 2012), and to investigate pollution transport to the Arctic (Sessions et al., 2011).

Since WRF-Chem is a coupled meteorological-chemistry-aerosol model, it can be setup in a way that allows predicted aerosol and trace gas concentrations to influence modeled meteorology. In all of the simulations presented in this thesis, aerosols influence meteorological

properties by their direct effect on radiation, and their indirect effect on cloud properties, precipitation and cloud lifetime.

The base model setup is presented in Table 3.1. This setup is mostly based on recommendations found in Peckham et al. (2015); it is used in the study presented in Chapter 4. Later studies (Chapters 5 and 6) use different options, presented in Table 5.2 (Chapter 5) and Table 6.1 (Chapter 6); these changes were motivated by earlier results, and the reasons for these modifications are presented in each chapter.

Table 3.1 – WRF-Chem base setup in this thesis (as used in Chapter 4).

Option name	Selected option
Chemistry & aerosol options	
Gas-phase chemistry	CBM-Z (Zaveri and Peters, 1999)
Aerosols	MOSAIC 8-bins (Zaveri et al., 2008)
Photolysis	Fast-J (Wild et al., 2000)
Metrorological options	
Planetary boundary layer	MYJ (Janji , 1994)
Surface layer	Monin-Obukhov Janjic Eta scheme (Janji , 1994)
Land surface	Unified Noah land-surface model (Chen and Dudhia, 2001)
Microphysics	Morrison (Morrison et al., 2009)
SW radiation	Goddard (Chou and Suarez, 1999)
LW radiation	RRTM (Mlawer et al., 1997)
Cumulus parameterization	Grell-3 (Grell and Dévényi, 2002)

3.1.1.1 WRF-Chem gas-phase chemistry and aerosol schemes

WRF-Chem aerosols are represented by the MOSAIC (Model for Simulating Aerosol Interactions and Chemistry, Zaveri et al., 2008) model. MOSAIC represents aerosol size distributions by eight discrete size bins between 39 nm and 10 µm. Within each size bin and each grid cell, MOSAIC calculates aerosol number concentrations, as well as the mass concentrations of SO_4^{2-}, NO_3^-, NH_4^+, BC (EC), OA, Na^+, Cl^-, and "other inorganics" (OIN, including mineral dusts). Aerosols are assumed to be internally mixed within each bin; because of this, EC can become instantaneously hygrophilic when emitted in grid cells already containing small water-soluble aerosols. Nucleation is based on the H_2SO_4–H_2O scheme of Wexler et al. (1994), and new particles are grown (as SO_4^{2-} and NH_4^+) to the lower-bound of the MOSAIC 8-bin scheme (39 nm). Coagulation is calculated following the approach of Jacobson et al. (1994). MOSAIC includes aerosol/cloud interactions, and predicts aerosol activation in clouds, aqueous chemistry in clouds, and within- and below-cloud wet scaveng-

ing. Interstitial and cloud-borne aerosol particles are treated explicitly, and modeled aerosols can be activated or re-suspended depending on saturation, particle size, and aerosol composition, based on the parameterizations of Abdul-Razzak and Ghan (2000, 2002). Aqueous chemistry in clouds is based on Fahey and Pandis (2001), and includes oxidation of S(IV) by H_2O_2, O_3 and other radicals, as well as non-reactive uptake of NH_3, HNO_3, HCl, and other trace gases. In-cloud wet removal occurs when cloud droplets containing activated aerosols are converted to precipitation, and model-predicted precipitation can also remove a fraction of below-cloud aerosols by impaction. Dry deposition velocities are calculated using the resistance scheme of Wesely (1989).

In the version presented here, MOSAIC includes 176 advected aerosol species: 8 bins $\times$ 11 species (mass concentrations for 8 chemical species + 2 species for aerosol water+ 1 bulk number concentration) $\times$ 2 (activated or interstitial aerosol). As a result, it is one of the most computationally costly mechanisms available in WRF-Chem, and cannot currently be used to perform high resolution simulations over long periods and large domains.

In WRF-Chem, MOSAIC is coupled to 3 different gas-phase chemistry schemes of similar complexities: CBM-Z (Carbon Bond Mechanism, version Z; 73 species, 237 reactions ; Zaveri and Peters, 1999), SAPRC-99 (Statewide Air Pollution Research Center, 1999 version; 79 species, 235 reactions; Carter, 2000) and MOZART (Model for Ozone and Related chemical Tracers; 85 species and 196 reactions; Emmons et al., 2010). The base configuration uses CBM-Z, chemistry, which is the gas-phase chemistry scheme recommended by the MOSAIC development team (Peckham et al., 2015). CBM-Z/MOSAIC does not include both cloud-aerosol interactions and SOA formation. These processes were added to the SAPRC-99/MOSAIC WRF-Chem setup by Shrivastava et al. (2011), and for this reason SAPRC-99/MOSAIC is used in Chapter 6.

Aerosol optical properties are calculated by a Mie code (Mie, 1908; Barnard et al., 2010). Mie calculations are performed assuming spherical aerosols and an average refractive index within each bin. This refractive index is calculated in this thesis as the volume average of the indices of the chemical components within each bin. Photolysis rates used in the gas-phase chemistry calculations are determined by the Fast-J scheme (Wild et al., 2000), and take into account the influence of hydrometeors and aerosols on actinic fluxes.

Initial and boundary conditions for trace gases and aerosols are taken from the global chemical-transport model MOZART-4 (Emmons et al., 2010); boundary conditions are updated every 6 h. WRF-Chem does not include stratospheric chemistry. In order to include realistic concentrations of chemical species in the stratosphere and upper troposphere, stratospheric mixing ratios of CO, O_3, NO, NO_2, HNO_3, N_2O_5 and N_2O are constrained by a zonal-mean climatology, following the approach used in MOZART-4 (Emmons et al., 2010). The species are fixed to climatological values at the model top (50 hPa), and relaxed to model values down to the tropopause. WRF-Chem does not include detailed chemistry,

sources and sinks of CH_4 and CO_2; these species are set to a single global value based on measurements.

3.1.1.2 Meteorological (WRF) setup

Table 3.1 also presents the options selected for the meteorological (WRF) part of the model. The choice of several options is constrained by the use of MOSAIC. The recommended microphysical scheme to use with MOSAIC is the Morrison 2-moment scheme (Morrison et al., 2009). The Morrison 2-moment scheme calculates cloud formation, cloud properties, and precipitation at the grid scale, but for simulations at horizontal resolutions coarser than 10 km, it is recommended to use an additional parameterization for sub-grid cumulus clouds. The Grell-3D cumulus scheme (Grell and Dévényi, 2002) was chosen because it was until recently the only scheme in WRF-Chem representing sub-grid cloud interactions with radiation and tracer convection. There are several possible options for planetary boundary layer schemes (PBL), which compute turbulent vertical mixing and fluxes, and for surface layer schemes, which compute friction velocities and surface exchange coefficients. The Mellor-Yamada-Janjic (MYJ) scheme (Janji , 1994) was chosen to represent the PBL as well as the associated Janjic Eta surface layer scheme (Janji , 1994). These schemes are among the most commonly used within WRF-Chem. The land surface is represented by the unified Noah Land-Surface Model (Noah-LSM, Chen and Dudhia, 2001). Radiative transfer calculations in the atmosphere are performed by the Rapid Radiative Transfer Model (RRTM) in the longwave (terrestrial radiation, Mlawer et al., 1997), and the Goddard scheme in the shortwave (solar radiation, Chou and Suarez, 1999). Both radiation schemes are coupled with the aerosol optical properties calculated by the Mie code. Iacono and Nehrkorn (2010) compared different WRF radiation schemes, including RRTM and Goddard, to surface measurements of SW and LW radiative fluxes in the USA. This comparison showed a good agreement for both schemes chosen here, although discrepancies (up to $50\,\mathrm{W\,m^{-2}}$) were possible due to errors in modeled cloud fractions.

Initial and boundary conditions for meteorology are specified using the NCEP GFS (National Center for Environmental Prediction, Global Forecast System) FNL (final) analysis; boundary conditions are updated every 6 h. In addition, WRF-Chem winds, temperature and humidity are nudged to FNL every 6 h in the free troposphere.

3.1.1.3 WRF dynamical setup, discretization and numerical integration

WRF-ARW integrates the fully compressible and non hydrostatic Euler equations in flux form (Ooyama, 1990). Details on the numerical schemes used in WRF-ARW are given in the technical description of the model by Skamarock et al. (2008). Briefly, the equations are formulated in Cartesian horizontal coordinates, and in a pressure-based terrain-following "eta" vertical coordinate (Laprise, 1992). The spatial discretization uses an Arakawa C-

grid staggering (Skamarock et al., 2008). Time discretization is based on a Runge-Kutta 3rd-order time-split integration (Skamarock and Klemp, 1992), with a smaller time step for acoustic and gravity-wave modes. A 5th-order scheme is used for horizontal scalar and momentum advection, and a 3rd-order scheme for vertical advection. Advection schemes conserve mass, and use a monotonic flux limiter, following the recommendations of Wang et al. (2009). Sub-grid-scale horizontal turbulent mixing is performed by a 2nd-order scheme, and vertical mixing is performed by the chosen PBL scheme.

Gas-phase chemistry equations in the SAPRC-99 and CBM-Z schemes are solved by a RODAS3 Rosenbrock-type solver (Sandu et al., 1997). The integration of gas-particle partitioning in MOSAIC is done by a dedicated scheme called ASTEM (Adaptive Step Time-Split Euler Method), described in detail in (Zaveri et al., 2008).

3.1.1.4 Aerosol and ozone radiative effects in WRF-Chem

Aerosols predicted by WRF-Chem/MOSAIC influence the modeled radiation budget in two ways. First, predicted aerosols are used to compute aerosol optical properties. These optical properties are passed to the RRTM and Goddard radiation modules (aerosol direct effect), where they are used in radiative transfer calculations (direct radiative effect). As a result, this interaction also modifies the modeled meteorology and can affect cloud formation (semi-direct effect). Second, aerosol activation changes the cloud droplet number concentrations and cloud droplet radii in the Morrison microphysics scheme, and these properties are used in the radiation schemes to calculate cloud optical properties (first indirect aerosol effect). Aerosol activation in MOSAIC can also influence cloud lifetime by changing cloud properties and precipitation rates (second indirect aerosol effect).

Radiation modules (e.g., Goddard and RRTM) do not use the WRF-Chem predicted atmospheric profiles of O_3 to perform calculations, and use climatological profiles instead. As part of this thesis, predicted O_3 was coupled to SW and LW radiation in Chapter 6 to quantify its direct radiative effect (See Section 6.8).

3.1.2 Lagrangian modeling with FLEXPART-WRF

The Lagrangian particle dispersion model FLEXPART-WRF (Fast and Easter, 2006; Brioude et al., 2013) is used in this thesis to calculate pollution transport and dispersion from an individual source, and to identify the origin of measured pollution. FLEXPART-WRF, is a version of the dispersion model FLEXPART (Stohl et al., 2005), modified to be driven by meteorological fields from WRF.

In its "forward mode", FLEXPART-WRF uses meteorological fields from a WRF or WRF-Chem simulation to compute the transport and dispersion of a large number of particles released along time from a box source. Each particle is associated with a given mass of tracer, and after a given time the particles can be counted on a grid to estimate the tracer

concentration from this source.

FLEXPART-WRF can also be used in "backward mode" to estimate source-receptor relationships. In this case, particles released at a receptor point are transported backward in time using the meteorological fields from the WRF simulation. This calculation can be performed because equations included in FLEXPART-WRF are symmetric in time. The model can then compute "potential emission sensitivities" (PES) on a grid, which represent the amount of time (in seconds) spent by backward-moving particles in each of the cells of an output grid. Footprint PES (FPES) are often defined as the PES integrated over the lowest atmospheric layers, typically 0–250 m. FPES can be applied to surface emissions fluxes in kg/m3/s to estimate concentrations (kg/m3) at the receptor (origin) point due to this specific emission source.

FLEXPART-WRF does not include gas-phase and aerosol chemistry, but can represent the exponential decay of a tracer based on its lifetime. Dry and wet removal can also be calculated based on WRF precipitation and given dry and wet deposition velocities.

In this thesis, FLEXPART-WRF is used to identify the origins and transport pathways of pollution plumes measured in the Arctic (Chapter 4) and to compute plume dispersion and transport from shipping point sources in order to derive emissions from measurements (Chapter 5).

3.2 Air pollutant emissions from global and local Arctic pollution sources

In order to represent atmospheric composition, WRF-Chem simulations need air pollutant emissions as input. Anthropogenic and biomass burning emissions are usually taken from emission inventories, containing geographically distributed and time-resolved emissions of relevant pollutants. Natural emissions can often be calculated directly within the model during simulations, since they are usually tied to specific physical phenomenons (e.g. NO_x emissions from lightning). This section presents how anthropogenic, biomass burning and natural emissions are implemented in the WRF-Chem simulations performed in this thesis.

3.2.1 Global anthropogenic emissions from ECLIPSEv5 and HTAPv2

WRF-Chem simulations presented in this thesis use global anthopogenic emissions of NO_x, NMVOC, CO, BC, POA, SO_2 and NH_3 from the HTAPv2 (Hemispheric transport of air pollution, version 2, Janssens-Maenhout et al., 2015) or ECLIPSEv5 (Evaluating the Climate and Air Quality Impacts of Short-Lived Pollutants, version 5, Klimont et al., 2015) inventories. HTAPv2 and ECLIPSEv5 emissions are presented in Figures 3-1 and 3-2 respectively.

Figure 3-1 represents HTAPv2 emissions from the energy, industrial, residential, trans-

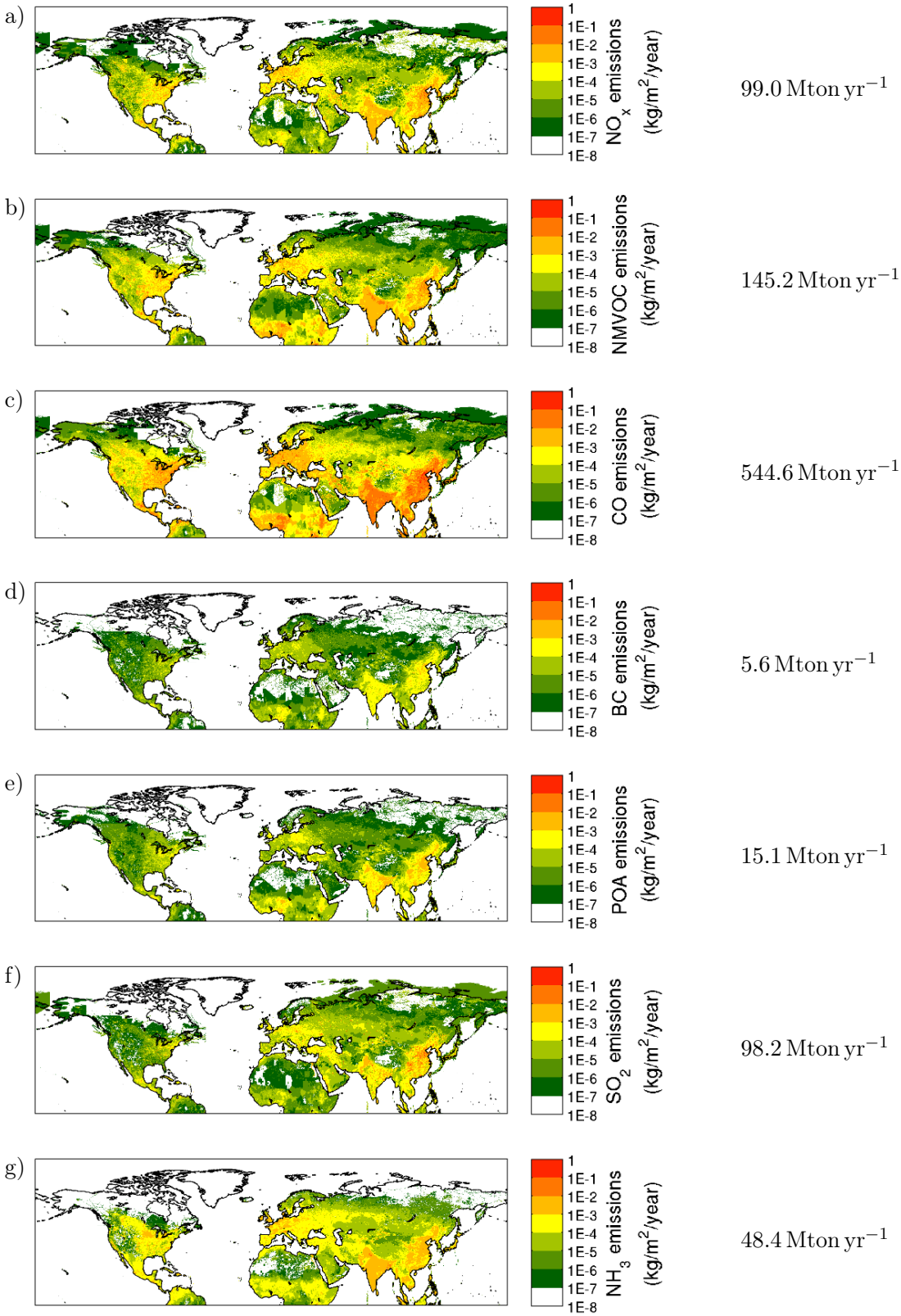

Figure 3-1 – 2010 yearly averaged HTAPv2 anthropogenic emissions in the northern hemisphere (excluding shipping and aviation emissions) for (a) NO_x (as NO_2) (b) NMVOC (as carbon) (c) CO (d) BC (e) POA (1.4×OC) (f) SO_2 (g) NH_3. Global yearly emission totals are indicated on the right of each panel.

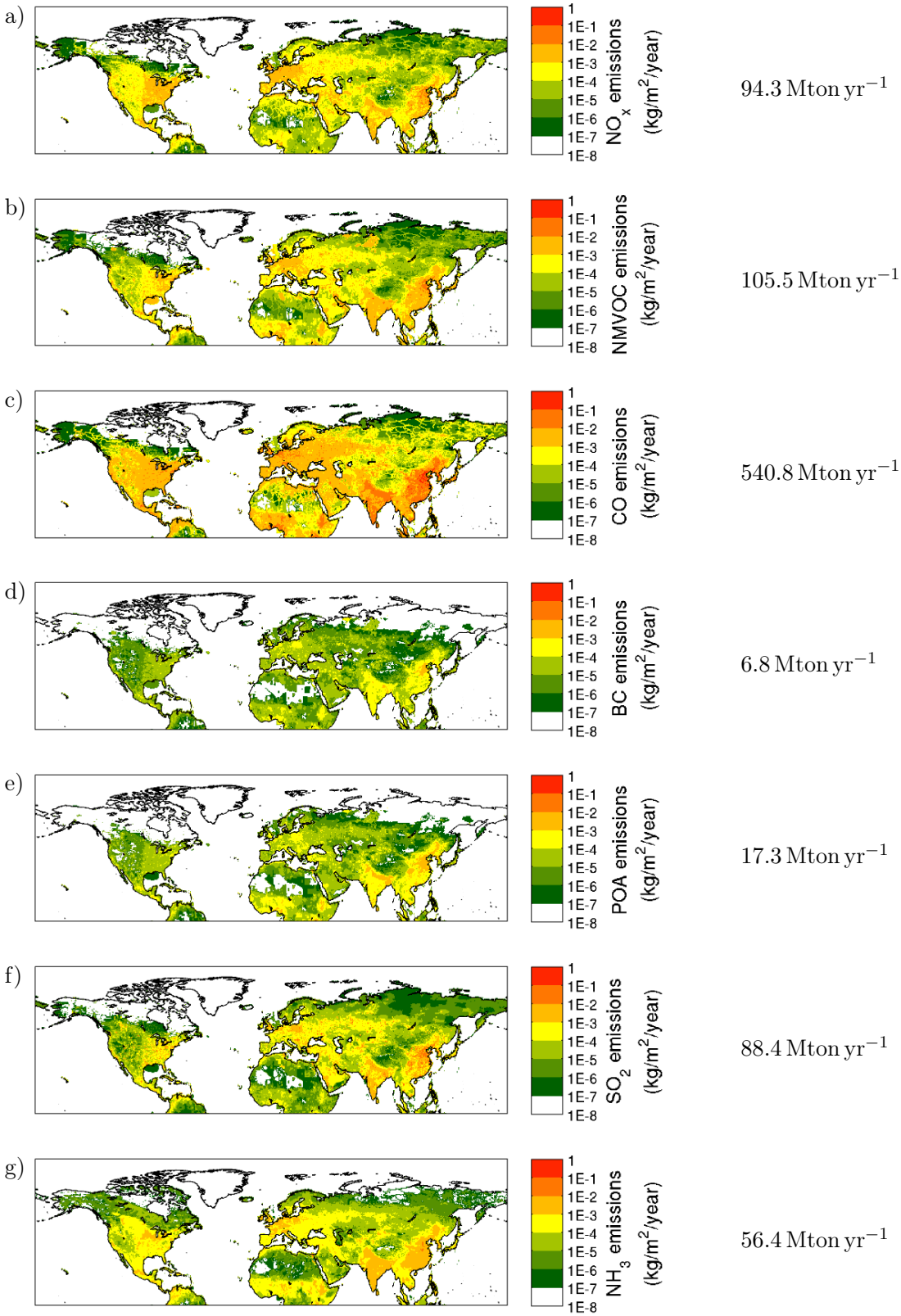

Figure 3-2 – 2010 yearly averaged ECLIPSEv5 anthropogenic emissions in the northern hemisphere (excluding agricultural waste burning) for (a) NO_x (as NO_2) (b) NMVOC (as NMVOC) (c) CO (d) BC (e) POA (f) SO_2 (g) NH_3. Global yearly emission totals are indicated on the right of each panel.

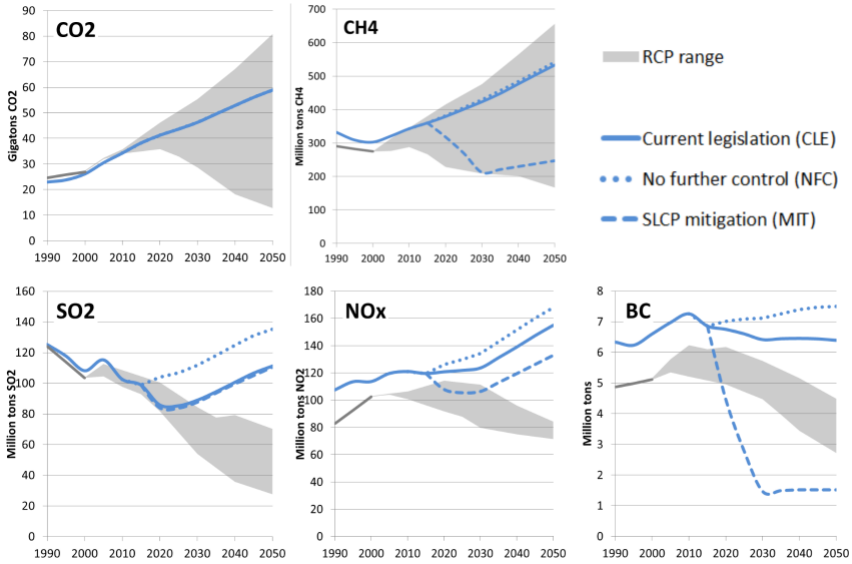

Figure 3-3 – Global ECLIPSEv5 emissions of CO_2, CH_4, SO_2, NO_x and BC between 1990 and 2050 (Figure from Stohl et al., 2015). NFC, CLE and MIT scenarios are represented in blue, along with the IPCC RCP scenario range in gray (Lamarque et al., 2010).

port and agriculture sectors. ECLIPSEv5 emissions in Figure 3-2 include emissions from the same sectors, and additional emissions from the "waste processing" and "solvent" sectors (included as part of the residential and industrial sectors in HTAPv2). Ship emissions are not included in Figures 3-1 and 3-2, but are discussed in detail in Section 3.2.5. "Agricultural waste burning" emissions from ECLIPSEv5 are excluded from all simulations (and from Figure 3-2), to avoid double counting with biomass burning emissions discussed in Section 3.2.2.

Figures 3-1 and 3-2 illustrate that global yearly emission totals are very similar between the two inventories despite the different methodologies. However, the distribution of the emissions can be quite different, especialy in remote regions (Northern Russia, deserts, oceans). Another difference between the 2 inventories is that HTAPv2 is available at a higher resolution (0.1 $\times$ 0.1) than ECLIPSEv5 (0.5 $\times$ 0.5). For this reason, HTAPv2 is used in Chapters 4 and 5, where WRF-Chem simulations are performed with a horizontal grid-spacing less than 0.5 $\times$0.5 (50 km $\times$ 50 km). ECLIPSEv5 emissions include a recent estimate of Arctic oil and gas flaring emissions (Stohl et al., 2013, oil and gas emissions discussed in Section 3.2.4). For this reason ECLIPSEv5 emissions are used in Chapter 6 in simulations assessing the present and future impact of emissions from Arctic oil and gas extraction.

ECLIPSEv5 future projections are based on results from the GAINS (Greenhouse gas-Air pollution Interactions and Synergies) model (Amann et al., 2011), and include several possible scenarios. NFC (No Further Control) is a high-emission, business-as-usual scenario

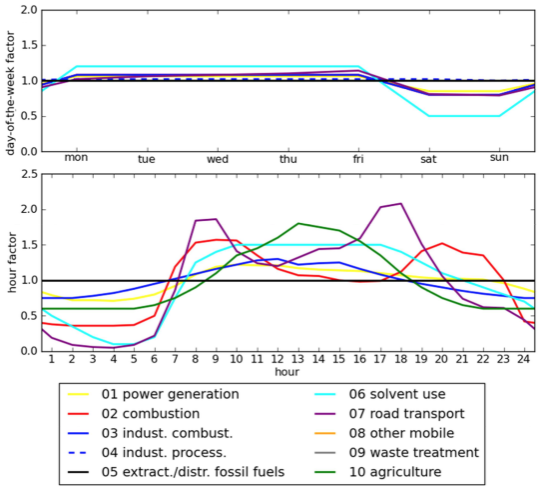

Figure 3-4 – Day-of-week and hour-of-day profiles applied to anthropogenic emissions. Figure from Denier van der Gon et al. (2011).

assuming that no new emission controls are implemented after 2005. CLE (Current Legislation) includes lower emissions, assuming that already committed future emission reductions will be implemented. MIT (MITigation) is a low-emission mitigation scenario including further additional mitigation of short-lived climate forcers (Stohl et al., 2015). The CLE scenario is used in the present work, because it represents mid-range, more probable future emissions. Figure 3-3 shows the evolution of global emissions of CO_2, CH_4, SO_2, NO_x and BC in the ECLIPSEv5 inventories between 1990 and 2050. 2050 CO_2 and NOx emissions are larger than today in the CLE scenario, but, due to regulations, BC emissions decrease globally and SO_2 emissions remain approximately the same.

ECLIPSEv5 and HTAPv2 give NMVOC emissions as a bulk total mass by emission sector, but gas-phase chemistry mechanisms within WRF-Chem include several individual NMVOC species. As a result, NMVOC emissions from inventories need to be speciated to mechanism species during emission preprocessing. This speciation is done in two steps. First, bulk anthropogenic VOCs from a given emission sector are disaggregated into individual VOC chemical species based on a detailed anthropogenic VOC inventory for the UK (Table 2.13 in Murrells et al., 2010). These individual VOC species are then assigned to individual WRF-Chem VOC species, using a database compiled for this purpose by Carter (2014). NO_x emissions are given as a NO_2 total in ECLIPSEv5 and HTAPv2 inventories. For all anthropogenic emission sectors except shipping, NO_x emissions are assigned as 90 % NO and 10 % NO_2 (Finlayson-Pitts and Pitts, 1999). Shipping NO_x are assigned as 94 % NO and 6 % NO_2 (EPA, 2000). In Chapters 4 and 5, Organic Carbon (OC) emissions from HTAPv2, are converted to WRF-Chem (MOSAIC) POA using a factor of 1.4 (Turpin et al., 2000).

HTAPv2 and ECLIPSEv5 emissions are given as monthly files. Finer daily and hourly temporal variations are implemented for each anthropogenic emission sector in WRF-Chem

(Figure 3-4), using factors from Denier van der Gon et al. (2011), shown in Figure 3-4.

3.2.2 Biomass burning emissions

Emissions from boreal biomass burning are an important source of Arctic pollution during summer (Stohl, 2006). Warneke et al. (2010) also showed that agricultural fires located at lower latitudes could be transported in the Arctic in spring. In order to represent this contribution, biomass burning emissions from the FINNv1 (Fire inventory from NCAR version 1; Wiedinmyer et al., 2011; Chapters 4 and 5) and FINNv1.5 (Wiedinmyer et al., 2014; Chapter 6) inventories are included in WRF-Chem simulations. FINN emissions are based on fire detections by the space-borne MODIS instrument, and combine MODIS-derived area-burned and land cover type with emission factors to estimate daily resolved global fire emissions. FINN documentation does not include estimates of year to year variations of biomass burning emissions in the Arctic, but this information is available from another biomass burning inventory, GFED (Global Fire Emissions Database, Figure 3-5). Studies presented in Chapters 4, 5 and 6 use fire emissions for 2008 and 2012, which were rather strong fire years in the Arctic.

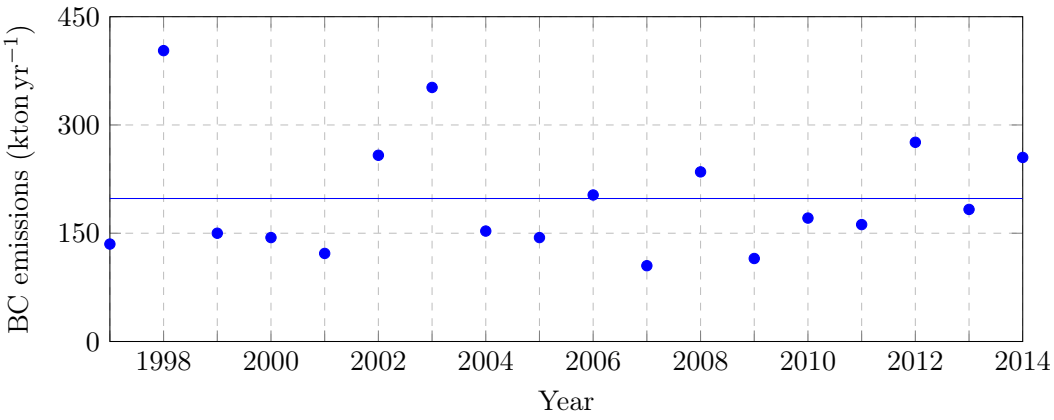

Figure 3-5 – Total boreal (boreal Asia + boreal North America) biomass burning BC emissions (kton yr^{-1}) in the GFED4.1 inventory between 1997 and 2014, individual years (blue markers) and average (blue line).

Daily FINN emissions implemented in WRF-Chem are transformed into hourly emissions by applying a daily emission cycle, peaking at local (solar) 1 pm. WRF-Chem simulations also includes a fire plume rise model (Freitas et al., 2007; Sessions et al., 2011), which takes into account the transport in altitude of fire emissions due to pyroconvection based on fire size, land use and WRF-Chem meteorology.

3.2.3 Natural emisssions calculated online within WRF-Chem

Dust and sea salt aerosol emissions are calculated online within WRF-Chem. Dust emissions are based on the GOCART emission scheme (Chin et al., 2002), combining model-predicted 10 m wind speed, model-predicted soil water content and input maps of soil erodability from GOCART. Sea salt emissions from oceans are based on Gong et al. (1997), and also use 10 m wind speeds as the main input parameter.

Biogenic emissions from vegetation are from an online version of MEGAN (Model of Emissions of Gases and Aerosols from Nature, Guenther et al., 2006) within WRF-Chem. MEGAN estimates biogenic emissions from solar radiation, WRF-Chem predicted temperature, and climatological input maps of leaf area index and vegetation types. In addition, soil NO_x emissions developped for the POLMIP (POLARCAT model intercomparison) project (Emmons et al., 2015) are used in the simulations presented in Chapters 4 and 6.

DMS emissions by oceans are an important source of SO_2 and SO_4 in the Arctic during summer months over the open ocean. DMS emissions and chemistry were included in the studies presented in Chapters 5 and 6. Lighting NO_x emissions were included in the simulation presented in Chapter 6. Additional details on model setup and emissions are given at the beginning of each chapter.

Snow NO_x emissions are still poorly understood. For this reason, they are not included in the simulations presented in this thesis. Volcanic emissions are difficult to quantify, episodic, and are not thought to be a major source of high-latitude SO_2 except during strong events, and were not included in this work either.

3.2.4 Local Arctic pollutant emissions from oil and gas extraction

Emissions from the petroleum extraction sector are included in global emission inventories (e.g. HTAPv2), but they are usually lumped with other emissions from the whole energy sector. Furthermore, global inventories might not be suited for regional applications in the Arctic if the location and magnitude of Arctic oil and gas emissions are not precisely implemented in inventories. For these reasons, it is preferable to use an inventory with a specific focus on the Arctic, such as the inventory of Peters et al. (2011), or the ECLIPSEv5 gas flaring emissions (Klimont et al., 2015), both shown in Figure 3-6.

ECLIPSEv5 oil and gas emissions emissions shown here only represent emissions associated with gas flaring, which is the process of burning excess gas for disposal in petroleum production and processing facilities. Emissions from Peters et al. (2011) are not directly comparable, since they also include other emissions associated with the petroleum sector, such as emissions from diesel engines, leaks, and venting. In spite of this, oil and gas related emission totals are 10–50 times higher in ECLIPSEv5 than in Peters et al. (2011) for all species except NO_x. Specifically, gas flaring is the most important source of Arctic anthro-

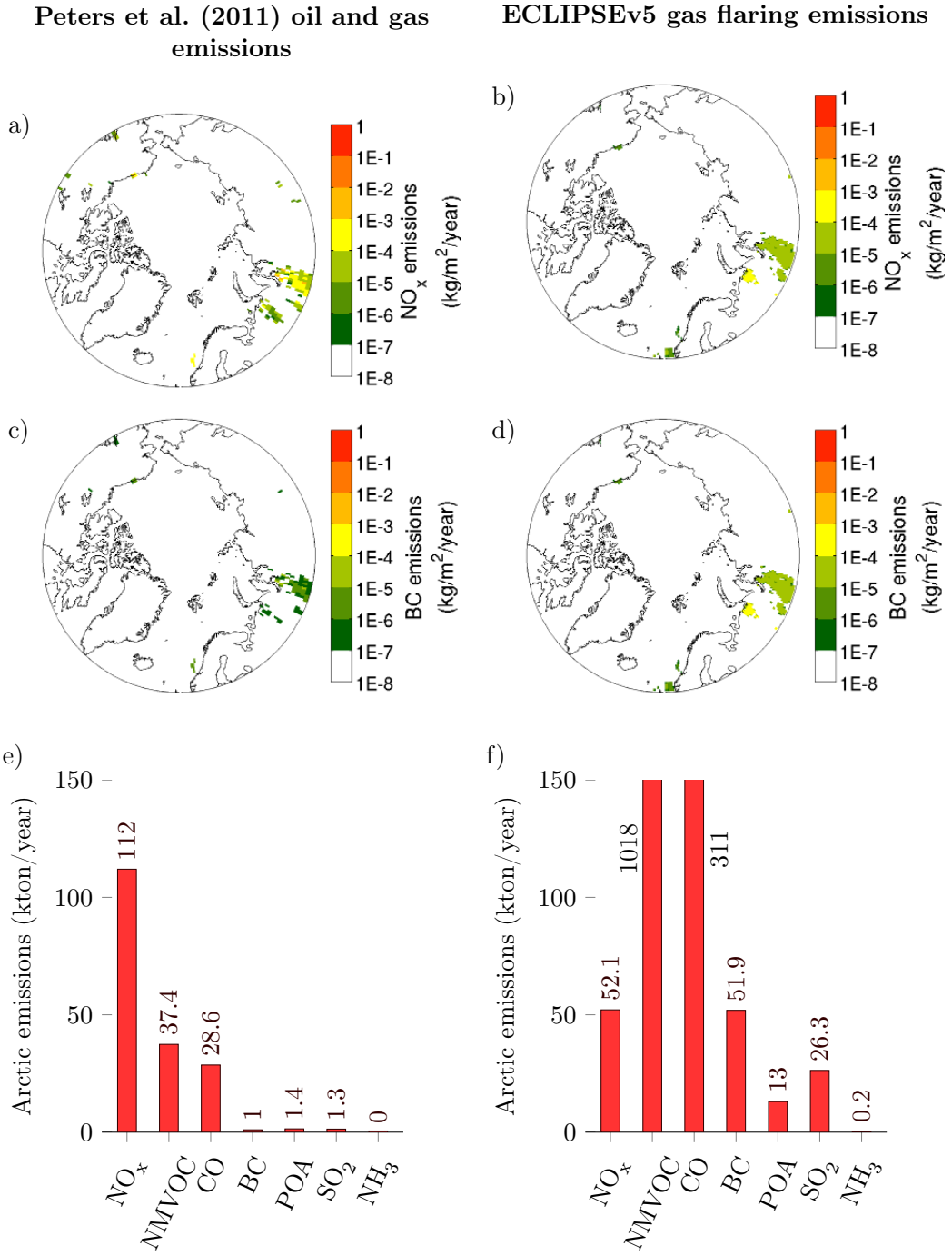

Figure 3-6 – Yearly averaged oil and gas emissions in the Arctic (latitude > 60 N) in the inventories of Peters et al. (2011) (year 2004, left), and ECLIPSEv5 (flaring layer, year 2010, right). (a-b) NO_x emissions, (c-d) BC emissions, (e-f) yearly emission totals in the Arctic.

pogenic BC in the ECLIPSEv5 dataset (Stohl et al., 2013). This is mostly due to the high recent estimates of flared gas volumes in this region by Elvidge et al. (2007, 2009). Flared volumes were estimated using "night light" satellite measurements from DMSP-OLS (U.S. Air Force Defense Meteorological Satellite Program - Operational Linescan System). Flares were identified based on their emission spectrum, and locations were later confirmed flare-by-flare from satellite pictures. In addition, the BC emission factor for flares in ECLIPSEv5 ($1.6\,\mathrm{g\,Nm^{-3}}$ gas flared) is higher than previous values from laboratory studies ($0.51\,\mathrm{g\,Nm^{-3}}$ McEwen and Johnson, 2012). Emissions from flares are very uncertain due to the lack of dedicated field campaigns to measure emission factors *in situ*. However, another recent approach by Huang et al. (2015) estimates an even higher BC emission factor, $2.27\,\mathrm{g\,Nm^{-3}}$. ECLIPSEv5 emissions indicate that previous studies based on Peters et al. (2011) emissions (e.g., Ødemark et al., 2012) could have been underestimating the atmospheric impacts of oil and gas activity in the Arctic.

ECLIPSEv5 also contains estimates of future flaring emissions in the Arctic, based on projections from the GAINS model (Table 3.2). Using CO emissions as a proxy for flared volumes indicates that ECLIPSEv5 flaring increases slightly between 2010 and 2050 (+4.7 %). This is coherent with projections from Peters et al. (2011) shown in Section 1.3.3 (Figure 1-13). For SO_2 and NMVOC, this increase is compensated by a decrease in emission factors. ECLIPSEv5 gas flaring emissions are used in Chapter 6 to estimate the current and future air quality and radiative impacts of the petroleum extraction sector in the Arctic.

Table 3.2 – Evolution of total Arctic gas flaring emissions ($\mathrm{kton\,yr^{-1}}$) between 2010 and 2050 in ECLIPSEv5 (CLE scenario).

Year	NO_x	NMVOC	CO	BC	POA	SO_2	NH_3
2010	52.1	1018	311	51.9	13.0	26.3	0.156
2050	54.3	937	325	54.3	13.6	26.5	0.163
	(+4.3 %)	(−7.9 %)	(+4.7 %)	(+4.7 %)	(+4.7 %)	(+0.78 %)	(+4.23 %)

3.2.5 Local Arctic emissions from shipping

Air pollutant emissions from marine traffic can be estimated using top-down or bottom-up approaches. In top-down approaches, ship fuel consumption is estimated based on fuel sales or on characteristics of the total fleet. Emission factors are applied to the fuel consumption (total or by ship type) to estimate emissions, which can be allocated geographically based on known ship routes. In bottom-up approaches, emissions are modeled for a single ship, based on this ship's speed and location, and on a technical description of the ship (e.g. engine type, size, fuel type). Emissions from single ships are aggregated to produce emissions for the total fleet. The principle of this approach is presented in Figure 3-7.

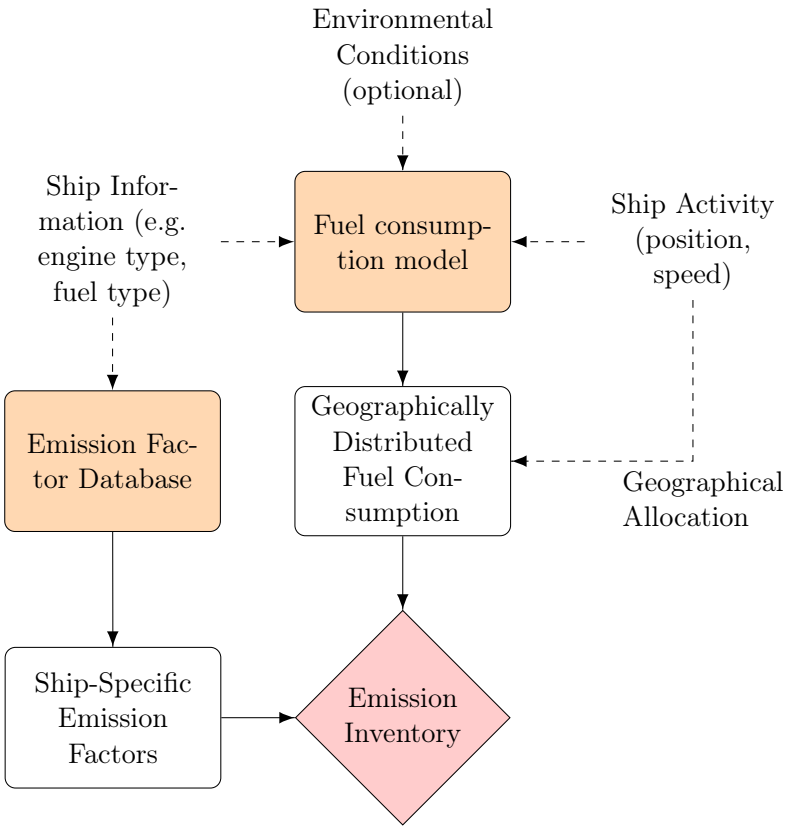

Figure 3-7 – Description of a bottom-up ship emission model (for a single ship).

Top-down approaches were used to produce early inventories (e.g. Corbett and Koehler, 2003), but these inventories were uncertain due to simplifying assumptions when applying average emission factors for a large part of the fleet (Eyring et al., 2010). Most recent inventories are based on bottom-up approaches, which were made possible by the availability of detailed databases of ship activity, AMVER (Automated Mutual-assistance Vessel Rescue) and COADS (Comprehensive Ocean-Atmosphere Data Set, now ICOADS). AMVER is a tracking system used by merchant ships for search and rescue, and COADS/ICOADS is based on self-reporting of ship journeys by ship crews. Although using either COADS or AMVER datasets was an improvement compared to earlier approaches, Endresen et al. (2003) showed that the use of these 2 datasets produced very different regional shipping emissions. In addition, both datasets are known to be biased towards specific ship types, ship sizes and locations (Endresen et al., 2003; Eyring et al., 2010). Corbett et al. (2010) used an Arctic specific ship activity dataset, AMSA, based on self-reporting (Arctic Council, 2009) to produce emissions for 2004. However, the AMSA dataset is also thought to under-report Arctic shipping (Arctic Council, 2009), and fishing ship emissions were not included by Corbett et al. (2010), since fishing ships do not usually follow straight routes.

Several recent emission inventories (Jalkanen et al., 2009; Winther et al., 2014) used AIS

(Automatic Identification System) ship activity data. AIS is a real-time ship positioning on board ships, which is mandatory for large ships (gross tonnage> 300 ton) and voluntary for smaller ships. In order to be included in databases, AIS signals have to be received either by terrestrial stations, with a limited range from shore (50 km) but high temporal resolutions (6 min); or by polar orbital satellites, with higher coverage but limited time resolutions (20 min–2 h). AIS is known to be very representative in the Baltic Sea, where 90 % of ships are equipped (Miola and Ciuffo, 2011).

Figure 3-8 shows the geographical distribution of 3 recent bottom-up shipping emission inventories, based on activity data from AMVER/ICOADS (RCP8.5, (Riahi et al., 2011)), AMSA (Corbett et al., 2010) and AIS (Winther et al., 2014). The repartition of Arctic shipping emissions is very different between these inventories, but all datasets indicate that the highest shipping activity occurs along the Norwegian Coast and around Iceland.

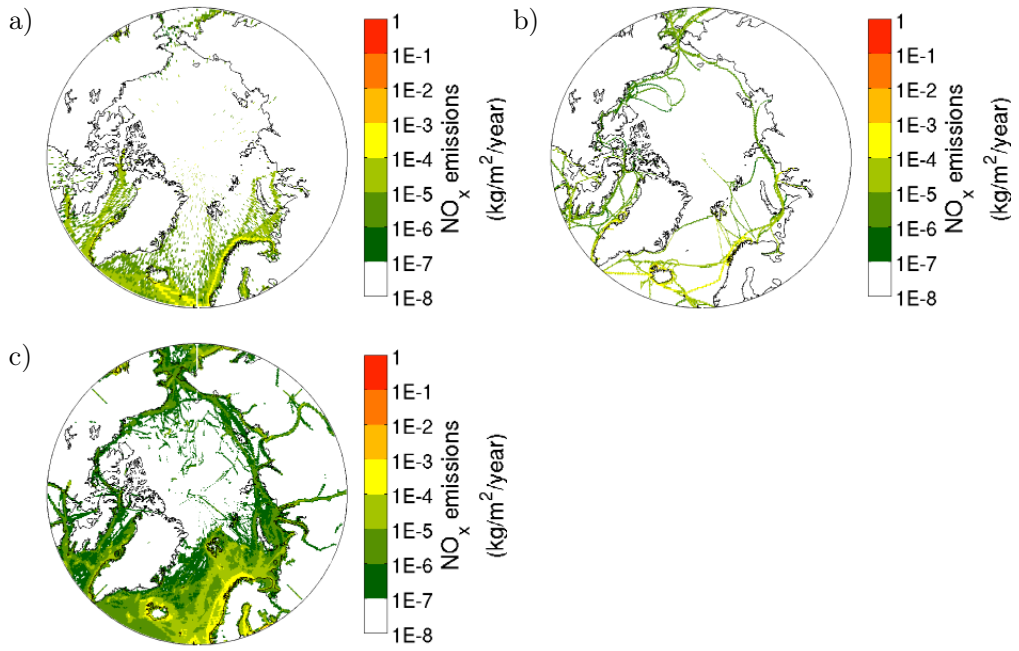

Figure 3-8 – Yearly averaged shipping NO_x emissions (as NO_2) in the Arctic (latitude > 60 N), (a) RCP8.5 (Riahi et al., 2011) in 2010, (b) Corbett et al. (2010) in 2004 and (c) Winther et al. (2014) in 2012.

Emission totals for several recent shipping emission inventories are presented in Table 3.3. Inventories representing recent years contain higher emissions, due either to growing Arctic traffic or, in the case of the Winther et al. (2014) inventory, due to a better representativity from using the AIS dataset. Recent inventories also tend to contain lower NO_x and SO_2 emissions relative to CO. This is because earlier inventories do not include the effect of recent regulations for NO_x and SO_2 emissions from ships, as implemented by the EU and

the IMO (IMO MARPOL Annex VI, IMO, 2008). Briefly, the North Sea and Baltic Sea, part of which are located north of 60 N, were designated as Sulfur Emission Control Areas (SECAs) in 2007 and 2006. In SECAs, the sulfur content of ship fuel was limited to 1.5 % for all ships, and reduced further to 1.0 % in 2010. The global average fuel sulfur content is about 2.4 % (IMO, 2010). Sulfur contents were also limited to 0.1 % in European harbors in 2010 by the EU sulfur directive. Ships manufactured or heavily modified recently must also comply to lower NO_x emissions factors limits, reducing emission factors (in $g\,kW^{-1}\,h$) by approximately −10 % for ships produced after 2000, and another −15 % for ships produced after 2011 (compared to ships built before year 2000, IMO, 2010).

Table 3.3 – Total local Arctic (latitude > 60 N) shipping emissions ($kton\,yr^{-1}$) in several recent shipping emission inventories.

Inventory	Year	NO_x (as NO_2)	NMVOC	CO	BC	POA	SO_2
RCP8.5	2000	185.5	29.5	12.3	1.36	2.03	115
Corbett et al. (2010)	2004	95.7	N/A	9.1	0.431	1.84	66.5
HTAPv2	2010	146	7.61	14.2	0.346	6.46	88.6
RCP8.5	2010	206	33.8	14.1	1.56	2.33	130
Winther et al. (2014)	2012	225	8.57	27.4	1.18	2.49	66.4

Because of recent emission regulations and because of the better representativity of new AIS-based inventories, earlier shipping inventories cannot be expected to represent accurately current Arctic shipping. For this reason, the recent Winther et al. (2014) inventory is used in Chapter 6 to assess the impacts of Arctic-wide shipping emissions. Another AIS-based inventory, generated by the STEAM2 emission model (Jalkanen et al., 2012), is used in Chapter 5. STEAM2 emissions are based on high-resolution terrestrial AIS data, which are better suited than Winther et al. (2014) emissions for high-resolution WRF-Chem simulations and direct comparisons of WRF-Chem simulations with airborne measurements behind individual ships (as performed in Chapter 5).

For each ship in the Winther et al. (2014) inventory, ship engine work (in kW h) is calculated based on vessel speed, ship length and engine and fuel characteristics. Fishing ships (accounting for 25 % of sailed distance in 2012) are assumed to function at engine loads of 60 %, as engine work is not directly related to vessel speed for fishing ships. Emission factors (in $g\,kW^{-1}\,h$) depend on fuel type, engine type and engine production year, and take into account IMO MARPOL Annex VI requirements. The emission factor for BC does not depend on engine load or fuel sulfur content.

The Winther et al. (2014) inventory also includes future projections in 2012, 2020 and 2050. These projections represent the growth in local traffic and do not include the effect of the diversion of international shipping through the Arctic through the NSR and NWP

due to summer sea ice melt. Winther et al. (2014) estimate the growth in local traffic from 2012 by scaling 2012 traffic with ship type-specific growth factors based on Corbett et al. (2010) and IMO (Buhaug et al., 2009). Future projections also take into account changes in emission factors due to new regulations and improved engine efficiencies. The resulting changes in emissions between 2012 and 2050 are presented in Table 3.4.

Table 3.4 – Evolution of total local Arctic (latitude > 60 N) shipping emissions between 2010 and 2050 (kton yr^{-1}), as estimated by Winther et al. (2014), Business As Usual (BAU) and High-Growth (HiG) scenarios.

Year	NO_x (as NO_2)	NMVOC	CO	BC	POA	SO_2
2012	225	8.57	27.4	1.18	2.49	66.4
2050 BAU	179	10.6	17.0	1.31	2.04	29.1
	(−20 %)	(+24 %)	(−28 %)	(+11 %)	(−18 %)	(−56 %)
2050 HiG	215	12.7	20.4	1.56	2.44	33.9
	(−4.4 %)	(+49 %)	(−26 %)	(+32 %)	(−2.2 %)	(−49 %)

Resulting future emissions shown in Table 3.4 are due to a combination of new regulations and increased traffic. SO_2 emissions decrease strongly due to further reductions of sulfur contents to 0.1 % in SECAs in 2015, and less strict worldwide sulfur content controls (0.5 %), expected at the latest for 2025 (Jonson et al., 2015). NO_x emissions also decrease in 2050 in all scenarios, as older ships are replaced with new ships complying with IMO regulations. In this thesis, "high-growth" scenarios are used for future shipping emissions in Chapter 6, in order to estimate the upper-bound of future shipping impacts in the absence of regulations, and because some earlier estimates (e.g. Browse et al., 2013) indicate that these future impacts could be limited.

Future emissions presented in Table 3.4 do not include the effect of future diversion of international shipping through the Arctic (the reasons for this possible future large scale diversion of shipping through the Arctic are presented in Section 1.3.3). The emissions from future diversion shipping have been estimated by Peters et al. (2011) and Corbett et al. (2010). The Arctic-wide future simulations presented in Chapter 6) use high-growth 2050 diversion shipping emissions from Corbett et al. (2010), who assumed that 5 % of global shipping traffic would be diverted through the Arctic during summer and fall, when sea ice cover is low (July–November in 2050). The total yearly emissions associated with this future scenario are presented in Table 3.5, illustrating that, in 2050, emissions from Arctic diversion shipping could be much higher than emissions from local Arctic shipping (Table 3.4).

Corbett et al. (2010) also determine several possible future diversion routes through the Arctic Ocean, presented in Figure 3-9, including trans-polar routes. In this thesis (Chapter 6), diversion shipping emissions are assumed to be distributed equally between

Table 3.5 – Total Arctic (latitude > 60 N) diversion shipping emissions in 2050 (kton yr^{-1}), estimated by Corbett et al. (2010) (High-Growth, scenario). NMVOC emissions are calculated by assuming a VOC/CO ratio of 53.15 % (Corbett and Koehler, 2003), and POA are calculated by assuming a POA/OC ratio of 1.25 (Shrivastava et al., 2011).

Year	NO_x (as NO_2)	NMVOC	CO	BC	POA	SO_2
2050 HiG	1476	110.0	206.9	9.61	13.8	308

the Northern Sea Route along the Russian Coast, and the Northwest Passage through the Canadian archipelago. It is important to note that estimates of future Arctic diversion shipping emissions and their onset are very uncertain, and that emission totals and geographical locations of diversion routes are still poorly constrained.

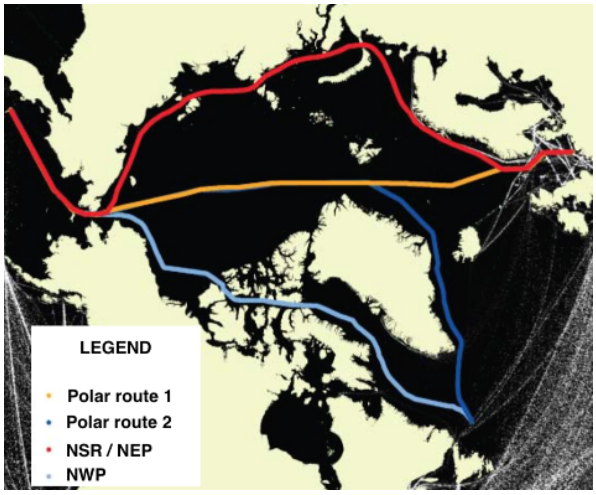

Figure 3-9 – Potential global shipping diversion routes through the Arctic Ocean in 2030/2050, adapted from Corbett et al. (2010).

3.3 Aerosol and ozone measurements in the Arctic

Surface and aircraft measurements of aerosols, ozone, and their precursors are used throughout this thesis to validate model results. WRF-Chem and FLEXPART-WRF simulations are also used to analyze airborne measurements of aerosols and ozone (model case studies), in order to learn about the origins and impacts of short-lived pollution observed in the Arctic. The main Arctic measurement datasets used in this thesis are presented in the following sections.

3.3.1 Surface measurements

There are several groundbased stations measuring ozone and aerosols in the Arctic, as part of the European Monitoring and Evaluation Programme (EMEP), the US Clean Air Status and Trends Network (CASTNET), and the World Meteorological Organization's Global Atmosphere Watch (WMO-GAW). Aerosol stations can measure the total $PM_{2.5}$ or PM_{10}, or can include speciated measurements of e.g. NO_3^-, SO_4^{2-}, NH_4^+, OA and BC. Long-term measurements of BC in the Arctic are derived from light absorption. BC concentrations derived from light absorption measurements, also called equivalent black carbon (EBC), are calculated using the relation $EBC = {}_{abs} \times MAC^{-1}$, where ${}_{abs}$ is the measured light-absorption coefficient in m^{-1}, and MAC is the mass-specific absorption coefficient at the same wavelength, in $m^2\,kg^{-1}$. Both ${}_{abs}$ measurements and assumptions about MAC introduce significant uncertainties in EBC calculations (Petzold et al., 2013).

Figure 3-10 shows the location of surface stations measuring ozone and aerosols *in situ* in the Arctic. These measurements are used in Chapter 6 to validate large scale WRF-Chem simulations. European EMEP measurements of aerosols in the Arctic and at lower latitudes are also used in Chapter 4 to characterize pollution in source regions during a transport event from Europe to the Arctic.

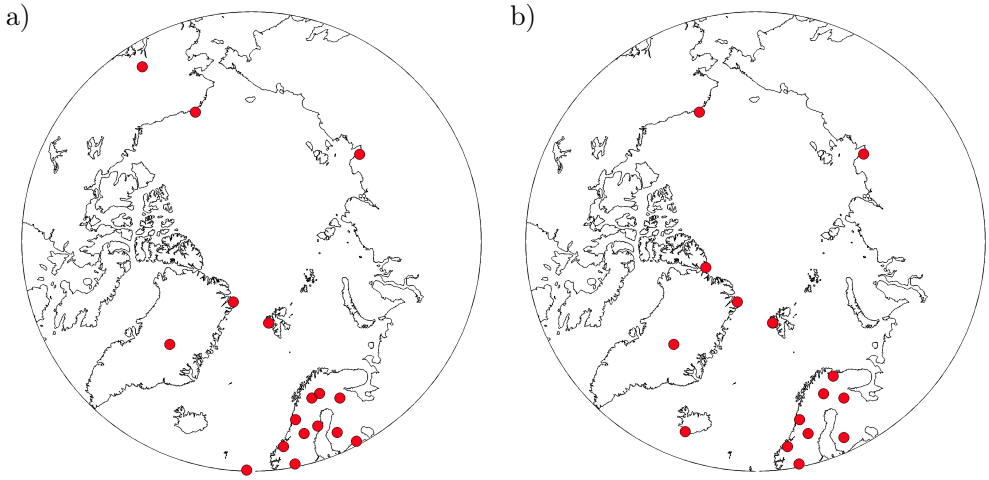

Figure 3-10 – Surface stations measuring (a) ozone and (b) aerosols *in situ* in the Arctic in 2012 (Red dots).

3.3.2 POLARCAT-France and ACCESS aircraft measurement campaigns in the Arctic

In this thesis, WRF-Chem simulations are used to analyze airborne measurement datasets from the POLARCAT-France (Polar Study using Aircraft, Remote Sensing, Surface Mea-

surements and Models, Climate, Chemistry, Aerosols and Transport, Law et al., 2014) and ACCESS (Arctic Climate Change, Economy, and Society, Roiger et al., 2015) airborne campaigns. These datasets are also used to validate simulation results. Flight tracks for all of the POLARCAT-France and ACCESS flights are presented in Figure 3-11.

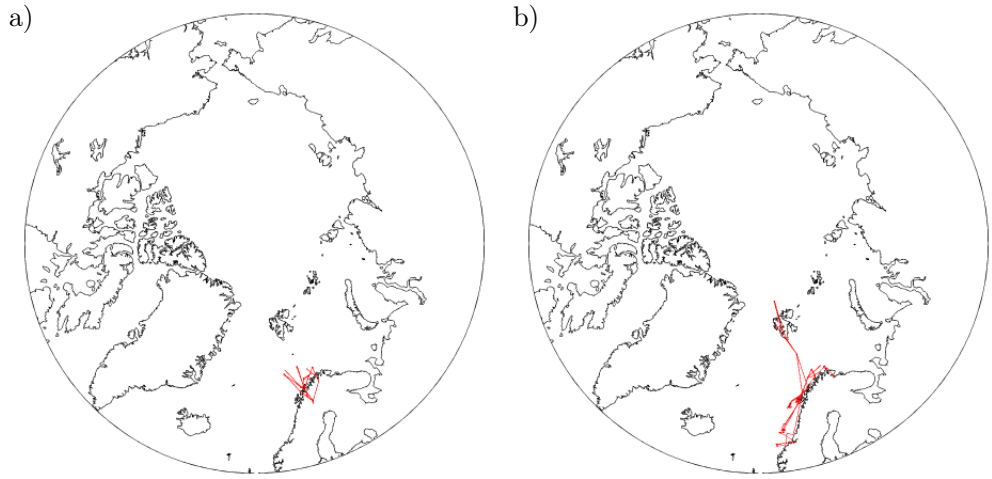

Figure 3-11 – Flight tracks (red) from the (a) POLARCAT-France spring campaign in March–April 2008, (b) ACCESS aircraft campaign in July 2012.

The POLARCAT-France airborne campaign took place from Kiruna, Sweden (67.8 N, 20.2 E) from 30 March to 11 April 2008. 10 flights were dedicated to validating satellite measurements (Pommier et al., 2010), and studying cloud-aerosol interactions in the Arctic and pollution transport from the mid-latitudes to the Arctic (Adam de Villiers et al., 2010; Quennehen et al., 2012; Ancellet et al., 2014). POLARCAT-France spring measurements include meteorological properties, cloud properties, trace gases (CO, O_3) aerosol size distributions, and aerosol optical properties (backscatter coeffcient measured by an airborne LIDAR, LIght Detection and Ranging). Additional details and an overview of results from the other measurement campaigns of the POLARCAT project are given in Law et al. (2014).

The 9 flights of the ACCESS aircraft campaign took place from Andenes, Norway (69.29 N, 16.14 E), from 9 to 27 July 2012. The main objectives of the campaign were to study local sources of Arctic pollution from shipping and oil and gas extraction along the Norwegian Coast (6 flights), to investigate the impact of Russian industrial emissions from the Kola Peninsula (1 flight) and to study the transport of Siberian biomass burning emissions to the Arctic (2 flights). ACCESS measurements include meteorological properties, cloud properties, aerosol number concentrations, aerosol size distributions, refractive BC (rBC) concentrations measured by SP2, as well mixing ratios of CO, NO, NO_2, and O_3. Additional details on the ACCESS campaign are given in Roiger et al. (2015).

Chapter 4

Transport of pollution from the mid-latitudes to the Arctic during POLARCAT-France

4.1 Motivation

The lower Arctic troposphere (altitudes $<$ 3 km) is polluted each year in winter/spring, a phenomenon known as Arctic Haze (Quinn et al., 2002). This Arctic Haze contains enhanced aerosol, NO_x and VOC concentrations, and was shown to be mostly due to long-range transport of anthropogenic pollution from Europe and Western Asia (Rahn, 1981). Although the phenomenon is relatively well-known, it is not well represented in models, which often underestimate aerosol concentrations at the surface (Lee et al., 2013) and overestimate concentrations aloft (Schwarz et al., 2010). These biases were found to be due to uncertainties in the treatment of aerosol wet removal (Browse et al., 2012), and although many models have updated their representation of these processes recently, significant difficulties remain (Eckhardt et al., 2015).

In order to improve our understanding of Arctic pollution, several airborne measurement campaigns were organized in 2008 as part of the POLARCAT project. The POLARCAT-France spring campaign took place from Kiruna, Sweden in April 2008. Studies by Quennehen et al. (2012) and Adam de Villiers et al. (2010) showed that, during several campaign flights, aerosol pollution plumes transported from Europe were sampled in the European Arctic. These studies also showed that aerosols contained in those plumes aged significantly by coagulation, condensation and wet removal proceses during transport. However, these observation-based studies were unable to precisely quantify the the magnitude of these aging processes, the contributions from different sources (anthropogenic, biomass burning), or the large scale air quality and radiative impacts of these pollution aerosols in the Arctic.

In this chapter, WRF-Chem is combined with HTAPv2 anthropogenic emissions, FINNv1 biomass burning emissions and POLARCAT-France airborne measurements for a case study investigating long-range transport of pollution from Europe to the Arctic during the campaign. In the context of this thesis, an important objective of this study is to validate the representation of aerosol transport events from Europe to the Arctic in spring in WRF-Chem. These types of transport events are known to be an important source of Arctic aerosols in winter/spring, and need to be well-reproduced by the model in order to perform other large-scale studies of Arctic aerosol pollution (see Chaper 6). This study also aims to improve our knowledge of these transport events, specifically:

- Identify pollution transport pathways and European sources of Arctic pollution in April 2008., and quantify aerosol wet removal during transport.
- Determine if WRF-Chem simulations can reproduce the complex vertical layering of pollution observed in the Arctic troposphere, *in situ* and by airborne LIDAR (LIght Detection and Ranging), during POLARCAT-France, and if these layers correspond to different sources, transport pathways and aging processes.
- Determine the regional impacts of the observed transport events in terms of aerosol concentrations and radiative effects in the European Arctic.

This study was published as

Marelle, L., Raut, J.-C., Thomas, J. L., Law, K. S., Quennehen, B., Ancellet, G., Pelon, J., Schwarzenboeck, A., and Fast, J. D., Transport of anthropogenic and biomass burning aerosols from Europe to the Arctic during spring 2008, *Atmospheric Chemistry and Physics*, 15(7), 3831–3850, doi: 10.5194/acp-15-3831-2015, URL `http://www.atmos-chem-phys.net/15/3831/2015/`, 2015.

This article is reproduced in the following sections.

4.2 Transport of anthropogenic and biomass burning aerosols from Europe to the Arctic during spring 2008 (Marelle et al., 2015).

4.2.1 Abstract

During the POLARCAT-France airborne campaign in April 2008, pollution originating from anthropogenic and biomass burning emissions was measured in the European Arctic. We compare these aircraft measurements with simulations using the WRF-Chem model to investigate model representation of aerosols transported from Europe to the Arctic. Modeled $PM_{2.5}$ is evaluated using European Monitoring and Evaluation Programme (EMEP) measurements in source regions and POLARCAT aircraft measurements in the Scandinavian Arctic. Total $PM_{2.5}$ agrees well with the measurements, although the model overestimates nitrate and underestimates organic carbon in source regions. Using WRF-Chem in combination with the Lagrangian model FLEXPART-WRF, we find that during the campaign the research aircraft sampled two different types of European plumes: mixed anthropogenic and fire plumes from eastern Europe and Russia transported below 2 km, and anthropogenic plumes from central Europe uplifted by warm conveyor belt circulations to 5–6 km. Both modeled plume types had undergone significant wet scavenging ($>50\,\%$ PM_{10}) during transport. Modeled aerosol vertical distributions and optical properties below the aircraft are evaluated in the Arctic using airborne lidar measurements. Model results show that the pollution event transported aerosols into the Arctic (>66.6 N) for a 4-day period. During this 4-day period, biomass burning emissions have the strongest influence on concentrations between 2.5 and 3 km altitudes, while European anthropogenic emissions influence aerosols at both lower (1.5 km) and higher altitudes (4.5 km). As a proportion of $PM_{2.5}$, modeled black carbon and $SO_4^=$ concentrations are more enhanced near the surface in anthropogenic plumes. The European plumes sampled during the POLARCAT-France campaign were transported over the region of springtime snow cover in northern Scandinavia, where they had a significant local atmospheric warming effect. We find that, during this transport event, the average modeled top-of-atmosphere (TOA) shortwave direct and semi-direct radiative effect (DSRE) north of 60 N over snow and ice-covered surfaces reaches $+0.58\ \mathrm{W\,m^{-2}}$, peaking at $+3.3\ \mathrm{W\,m^{-2}}$ at noon over Scandinavia and Finland.

4.2.2 Introduction

Arctic haze, which is present during winter and spring, is a well-known phenomenon that includes elevated concentrations of anthropogenic aerosols transported to the Arctic region (e.g., Rahn et al., 1977; Quinn et al., 2007). It was identified for the first time in the 1950s, when pilots experienced reduced visibility in the springtime North American Arctic (Greenaway, 1950; Mitchell, 1956). Further analysis showed that Arctic haze aerosols are mostly composed of sulfate, as well as organic matter, nitrate, sea salt, and black carbon (e.g., Quinn et al., 2002). Since local Arctic emissions are rather low, most air pollutants in the Arctic originate from transport from the mid-latitudes (Barrie, 1986). In late winter and early spring, Eurasian emissions can be efficiently transported at a low level in the Arctic (Rahn, 1981), when removal processes are particularly slow (Shaw, 1995; Garrett et al., 2011), causing elevated pollution concentrations in the lower troposphere. Surface aerosol concen-

trations in the Arctic are mostly influenced by European and west Asian emissions, while east Asian emissions have a larger influence in the upper troposphere (Fisher et al., 2011). Eurasian biomass burning emissions are thought to be major sources of Arctic pollution (Stohl, 2006; Warneke et al., 2010), but the magnitude of this contribution is still uncertain.

Aerosols play a key role in the climate system, through their absorption and scattering of solar radiation (direct effect, e.g., Haywood and Shine, 1995; Charlson et al., 1992), and through their impacts on cloud formation by modifying relative humidity and atmospheric stability (semi-direct effect, Ackerman et al., 2000) and by changing cloud properties, lifetime, and precipitation (indirect effects, Twomey, 1977; Albrecht, 1989). In the Arctic, several processes enhance the radiative impact of aerosols, including soot deposition on snow (Flanner et al., 2007), increased longwave emissivity in clouds in polluted conditions (Garrett and Zhao, 2006), and the increased atmospheric heating effect of aerosols with weak absorbing properties over snow- or ice-covered surfaces (Pueschel and Kinne, 1995; Haywood and Shine, 1995). Modeling studies by Shindell and Faluvegi (2009) and Jacobson (2010) suggest that a good representation of aerosol composition and optical properties is critical to understand the Arctic energy budget. However, it is well known that aerosols amounts and properties in the Arctic are not well represented in global chemical transport models (Shindell et al., 2008). For example, Schwarz et al. (2010) showed that black carbon in global simulations does not agree well with observations in the Arctic and varies greatly between models. This discrepancy, especially at high altitudes, may be caused, in part, by insufficient rainout (e.g., Wang et al., 2013).

To improve our understanding about air pollution in the Arctic, several airborne campaigns were conducted in the Arctic region during the International Polar Year in 2008 in the framework of POLARCAT (POLar study using Aircraft, Remote sensing, surface measurements and models, of Climate, chemistry, Aerosols, and Transport; see Law et al., 2014). As part of the international project POLARCAT, the POLARCAT-France spring campaign took place from 30 March to 14 April 2008, based in Kiruna, Sweden (67.8 N, 20.2 E. This campaign focused on Arctic cloud–aerosol interactions, satellite measurement validation, and transport of pollution plumes from mid-latitudes to the Arctic. During the campaign, several anthropogenic and biomass burning plumes originating in Europe and Asia were transported to the flight area and sampled during flights in April 2008 (Adam de Villiers et al., 2010; Quennehen et al., 2012). Adam de Villiers et al. (2010) analyzed the optical properties of aerosol plumes measured by airborne and spaceborne lidar, and Quennehen et al. (2012) studied aerosol ageing from size distributions measured in situ during the POLARCAT-France spring campaign. These studies pointed out the need for modeling to quantify the influence of different processes and sources on aerosols observed during the campaign.

The present study aims to improve our understanding about Arctic aerosol originating from Europe. In particular, we investigate the role of anthropogenic and biomass burning sources, transport pathways, aerosol ageing, and processes controlling the vertical distribution of aerosol plumes transported to the European Arctic in spring, and how they impact the aerosol burden and the aerosol radiative effect in this region. To achieve this objective, measurements from the POLARCAT-France airborne campaign in the Scandinavian Arctic in April 2008 are analyzed in combination with simulations using the regional WRF-Chem model to investigate cases of aerosol transport from Europe to the Arctic. In Sect. 4.2.3, we describe the methods used in our study,

including a description of the POLARCAT-France spring airborne aerosols measurements, and the European Monitoring and Evaluation Programme (EMEP) ground-based aerosol measurements used to validate the model over European source regions. Section 4.2.3 also includes an overview of the modeling tools employed, WRF-Chem and FLEXPART-WRF, and describes the simulations performed in this study. In Sect. 4.2.4, we present the synoptic-scale meteorological conditions over Europe during the campaign, and how these conditions impacted long-range aerosol transport from Europe to the Arctic. In Sect. 4.2.5, the performance of the WRF-Chem simulation is evaluated using POLARCAT-France spring meteorological measurements and ground-based aerosol measurements in source regions. In Sect. 4.2.6, modeled aerosol physical and optical properties are compared to POLARCAT-France spring airborne in situ and lidar measurements. We also investigate in Sect. 4.2.6 the sources of aerosols observed during the campaign. The results are used in Sect. 4.2.7 to evaluate the regional impact of this transport event in terms of aerosols burden and direct radiative effects.

4.2.3 Methods

4.2.3.1 POLARCAT-France spring campaign airborne measurements

During the POLARCAT-France campaign, the French ATR-42 research aircraft payload included two instruments to measure the particle size distribution: a scanning mobility particle sizer (SMPS, size range of 20 to 467 nm, 88 channels, 140 s resolution) and a GRIMM optical particle counter (OPC, size range of 0.1 to 2 µm, eight channels, 1 s resolution). For the full-size distributions (20 nm to 2 µm), data from the two instruments are combined as described in Quennehen et al. (2012). The ATR-42 was equipped with a counterflow virtual impactor (CVI) inlet (Schwarzenboeck et al., 2000) to sample aerosol particles and cloud droplets. In clouds, the CVI inlet was activated to remove interstitial aerosols and study cloud droplets only. Therefore, aerosol size distributions are only available out of clouds. However, clouds mostly impacted in situ measurements at lower altitudes (< 2 km) and data are available for most periods of interest for modeling long-range transport of aerosols to the region (SMPS: 158 data points, 98 % coverage above 1.5 km; GRIMM: 22 013 data points, 88 % coverage above 1.5 km). $PM_{2.5}$ concentrations along the flight track are estimated by integrating the size distributions (20 nm to 2 µm), assuming that all particles are spherical and have a density of 1700 $kg\,m^{-3}$ (Quennehen et al., 2011). The contribution of particles in the 2–2.5 µm diameter range to $PM_{2.5}$ is missing from this estimation. However, we determine that it is negligible because 94 % of the measured 20 nm to 2 µm mass distribution in the POLARCAT-France data set is located in the lower size range of 20 nm to 1.6 µm, and because large particles are unlikely to be transported over long distances.

During the campaign, airborne aerosol lidar profiles were measured below or above the aircraft by the LNG instrument (lidar LEANDRE Nouvelle Génération) (Flamant and Pelon, 1996; Adam de Villiers et al., 2010; Ancellet et al., 2014). Specifically, the LNG instrument measured aerosol optical properties at two wavelengths (532 and 1064 nm) providing information about the location of aerosol layers vertically (in our case below the aircraft). The vertical resolution of the data presented is 30 m (four-point average) and the horizontal resolution is 450 m (average of 100 lidar profiles). In this work, we use the LNG measurements to study the spatial structure of aerosol layers below the aircraft and to analyze the representation of these aerosol layers in regional chemical transport modeling. For this purpose, we use the LNG measurements

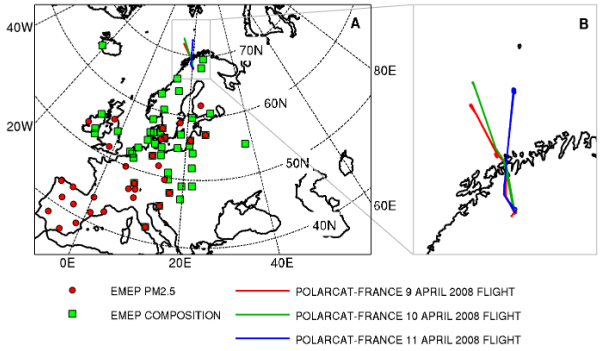

Figure 4-1 – **(a)** WRF-Chem domain including the location of ground-based EMEP measurement stations used for this study. Stations measuring $PM_{2.5}$ are marked by red circles, and stations measuring aerosol composition are marked by green squares. Stations with both measurements are indicated with both symbols. The POLARCAT-France spring flight tracks are shown in red, green, and blue, with a close up over the flight region shown in **(b)**.

to calculate the pseudo-backscatter ratio (PBR), defined as the ratio of the measured lidar total attenuated backscatter (including Rayleigh and aerosol contributions) to simulated molecular backscatter at a certain wavelength. The uncertainty for this ratio is estimated to be 10 % for the 532 nm channel and 20 % for the 1064 nm channel by Adam de Villiers et al. (2010). For this reason, we only use the 532 nm PBR in this study. In moderately polluted conditions (as observed during the POLARCAT-France spring campaign), the PBR is close to the true backscatter ratio, defined as $R_T = \frac{(\beta_A + \beta_M)}{\beta_M}$, where β_A is the aerosol backscatter coefficient and β_M is the molecular backscatter coefficient, noting that the true backscatter ratio is equal to 1 in clear sky conditions, and is greater than 1 in aerosol layers. Several aerosol plumes were sampled in situ and measured by lidar during three flights on 9, 10, and 11 April 2008. The associated flight tracks, over northern Norway and the Norwegian Sea/Barents Sea region, are represented in Fig. 4-1.

4.2.3.2 EMEP ground-based measurements

The EMEP network of ground-based measurements includes both aerosol $PM_{2.5}$ mass and aerosol chemical composition (available online from the EMEP database – `http://www.nilu.no/projects/ccc/`). Stations from the EMEP network are typically outside of urban centers and are intended to represent air free of recent pollution sources. We use the EMEP measurements of $PM_{2.5}$, as well as chemical composition in $SO_4^=$, organic carbon (OC), black carbon (BC), NH_4^+, and NO_3^- to evaluate model aerosols from 1 April to 11 April 2008, using data from stations with either daily or hourly data. Stations are excluded if they have less than 75 % data coverage during this period, and OC and BC measurements are excluded because of the lack of spatial coverage of measurements (four stations for BC, five for OC). The locations of stations used for model comparison are shown in Fig. 4-1, including stations that measure $PM_{2.5}$ (33 stations) and stations that measure aerosol mass of $SO_4^=$, NH_4^+, and NO_3^- (34, 31, and 28 stations, respectively). The average data coverage for selected stations is 98 %.

Table 4.1 – Parameterizations and options used for the WRF-Chem simulations.

Atmospheric process	WRF-Chem option
Planetary boundary layer	MYJ (Janji , 1994)
Surface layer	Monin–Obukhov Janjic Eta scheme (Janji , 1994)
Land surface	Unified Noah land-surface model (Chen and Dudhia, 2001)
Microphysics	Morrison (Morrison et al., 2009)
SW radiation	Goddard (Chou and Suarez, 1999)
LW radiation	RRTM (Mlawer et al., 1997)
Photolysis	Fast-J (Wild et al., 2000)
Cumulus parameterization	Grell-3 (Grell and Dévényi, 2002)
Gas-phase chemistry	CBM-Z (Zaveri and Peters, 1999)
Aerosol model	MOSAIC eight bins (Zaveri et al., 2008)

4.2.3.3 Model calculations: WRF-Chem and FLEXPART-WRF

4.2.3.3.1 WRF-Chem

Regional chemical transport model simulations are performed with the version 3.5.1 of the WRF-Chem (Weather Research and Forecasting, including Chemistry) model to provide further insight into the POLARCAT-France spring aerosol measurements. WRF-Chem is a fully coupled, online meteorological and chemical transport mesoscale model (Grell et al., 2005; Fast et al., 2006). It has been successfully used in previous studies focused on the Arctic region (Sessions et al., 2011; Thomas et al., 2013) and to analyze airborne aerosols measurements (e.g., Fast et al., 2012). The model setup, including the representation of the planetary boundary layer (PBL), surface, radiative properties, convection, microphysics, gas-phase chemistry, and aerosols, is shown in Table 4.1. Specifically, gas-phase reactions were simulated with the CBM-Z mechanism (Carbon Bond Mechanism, version Z, Zaveri and Peters, 1999) and aerosols are represented using the eight-bin sectional aerosol model MOSAIC (Model for Simulating Aerosol Interactions and Chemistry, Zaveri et al., 2008). MOSAIC aerosol processes include nucleation, evaporation, coagulation, condensation, dry deposition, and aerosol/cloud interactions, including aerosol activation as cloud condensation nuclei, cloud chemistry, and within- and below-cloud wet scavenging. Eight bins represent the size distribution of each aerosol species between 39 nm and 10 µm. Interstitial and cloud-borne aerosol particles are treated explicitly, and modeled aerosols can be activated or re-suspended depending on saturation, particle size, and aerosol composition. Aerosol activation changes cloud droplet number concentrations in the Morrison microphysics scheme, which is linked with the Goddard shortwave radiative scheme. Aerosol activation also affects cloud lifetime by influencing precipitation. Aqueous chemistry in clouds is based on Fahey and Pandis (2001), and includes oxidation of S(IV) by H_2O_2, O_3, and other radicals, as well as non-reactive uptake of NH_3, HNO_3, HCl, and other trace gases. Nucleation is based on Wexler et al. (1994). The CBM-Z-MOSAIC eight-bin scheme is not coupled to a secondary organic aerosol (SOA) scheme in our version of WRF-Chem (3.5.1). According to Bessagnet et al. (2009), 75–95 % of annually averaged SOA in Europe is associated with biogenic sources. However, biogenic VOC (volatile organic compounds) emissions are relatively low in Europe during the months of March and April (Karl et al., 2009). In addition, Bessagnet et al. (2009) point out that

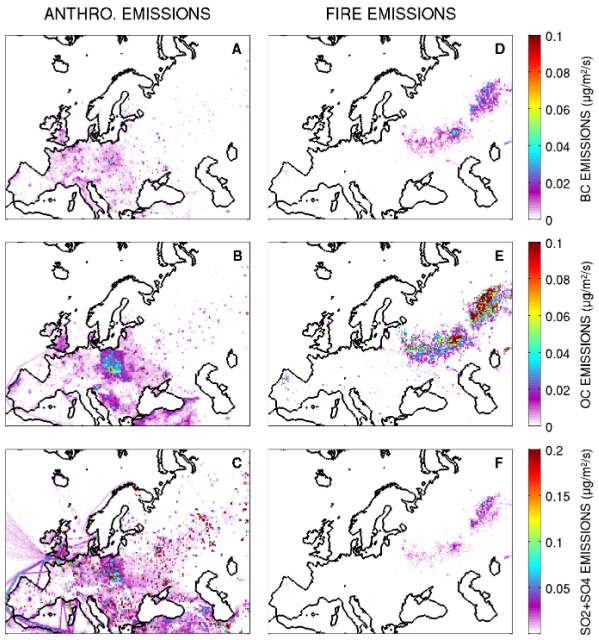

Figure 4-2 – Averaged emissions within the model domain during the simulation period (1 April 2008–12 April 2008) due to anthropogenic activities (HTAP v2) and biomass burning (FINN v1). Anthropogenic BC, OC, and $SO_2^+SO_4$ emissions are shown in **(a–c)** and biomass burning BC, OC, and $SO_2^+SO_4$ emissions are shown in **(d–f)**.

SOA concentrations are much lower in northern Europe than in other European regions. For all of these reasons, and since current SOA mechanisms are highly uncertain (e.g., Hodzic et al., 2010; Gustafson et al., 2011), the present simulations do not include SOA formation. However, we note that Frossard et al. (2011) determined that SOA formation contributed in part to the organic aerosol fraction in the Scandinavian marine boundary layer during the period of the POLARCAT-France flights (April 2008), and that our simulations cannot reproduce this contribution. MOSAIC considers aerosols as internally mixed in each bin, and in our simulations optical properties are calculated using volume averaging.

The simulation domain, focused on the POLARCAT-France spring flights, is shown in Fig. 4-1 and covers Europe north of 40 N and west of 70 E. The spatial resolution is 30 km × 30 km horizontally, with 50 vertical levels up to 50 hPa. Anthropogenic emissions were taken from the Hemispheric Transport of Air Pollution version 2 (HTAPv2) 0.1 × 0.1 inventory (`http://edgar.jrc.ec.europa.eu/htap_v2/index.php?SECURE=123`). HTAP VOCs are given as a bulk VOC mass, and are distributed into CBM-Z emission categories assuming the speciation of UK VOCs determined by Murrells et al. (2010). Time profiles are applied to anthropogenic emissions to account for the daily and weekly cycle of each emission sector Denier van der Gon et al. (2011). Fire emissions are from the FINN v1 inventory (Wiedinmyer et al., 2006, 2011), and are injected at altitude by an online plume rise model described in Freitas et al. (2007). Figure 4-2 shows black carbon (BC), organic carbon (OC), and sulfur oxides (SO_x) emissions during our simulation, from both anthropogenic sources (panels a, b, and c) and biomass burning sources (panels d, e, and f). In-domain biomass burning emission totals are 13 kton for

SO_x, 12 kton for BC, and 75 kton for OC. For anthropogenic emissions, in-domain emission totals from HTAPv2 are 575 kton for SO_x, 21 kton for BC, and 46 kton for OC. Anthropogenic emissions are stronger in western and central Europe, especially in Poland and Slovakia. Biomass burning emissions are located in the eastern part of the domain because of intense agricultural fires in Ukraine, Russia and Kazakhstan during early April 2008 (Warneke et al., 2009). Biogenic emissions are calculated online in WRF-Chem by the model MEGAN (Guenther et al., 2006). Finally, sea salt aerosol emissions are calculated online, while mineral dust emissions are not included.

Boundary and initial meteorological conditions in the simulation are given by the global NCEP Final Analysis (FNL), and WRF-Chem temperature, humidity, and winds are nudged every 6 h to the reanalysis above the atmospheric boundary layer. Trace gases and aerosol initial and boundary conditions (updated every 6 h) are taken from the global chemical transport model MOZART-4 (Emmons et al., 2010).

WRF-Chem simulations include a control run (CTL) from 00:00 UTC 1 April to 00:00 UTC 12 April using the model and emissions as described above. We also perform four sensitivity simulations for the same period to investigate the sources, processes along transport, and regional impacts of aerosols sampled during POLARCAT: (1) removing the HTAPv2 emissions (NOANTHRO), (2) without biomass burning emissions (NOFIRES), (3) a simulation with wet scavenging turned off (NOWETSCAV), and (4) a simulation with the aerosol direct interaction with shortwave radiation disabled, thus switching off the direct and semi-direct aerosol effects (NODIRECT). The NOANTHRO and NOFIRES simulations are used in Sect. 4.2.6.1 to estimate the contribution of European anthropogenic and biomass burning emissions to Arctic aerosols measured during POLARCAT. The NOWETSCAV simulation allows us to quantify in Sect. 4.2.6.2 the magnitude of the wet scavenging of aerosols during their transport from Europe to the Arctic. The NODIRECT simulation is used in Sect. 4.2.7 to estimate the direct and semi-direct shortwave radiative effect (DSRE) of aerosols associated with this transport event.

To compare simulations with airborne lidar measurements, modeled backscatter ratio profiles at the plane position are calculated by using the aerosol backscattering coefficient at 400 nm simulated by WRF-Chem. This coefficient is computed within WRF-Chem from the method of Toon and Ackerman (1981), using a bulk, volume-averaged, refractive index derived from the modeled size distribution (Bond et al., 2006). The backscattering coefficient is then estimated at 532 nm by using the simulated Angström exponent, and the effect of aerosol transmission is ignored because aerosol optical depths (AODs) of observed layers were low ($< 4\,\%$) during POLARCAT-France (Adam de Villiers et al., 2010). The backscatter ratio is calculated following the definition in Sect. 4.2.3.1, where the molecular backscattering is estimated by an empirical formulation of the Rayleigh scattering (Nicolet, 1984) using meteorological profiles from the CTL simulation.

4.2.3.3.2 FLEXPART-WRF

We also use FLEXPART-WRF, a Lagrangian particle dispersion model (Brioude et al., 2013) adapted from the model FLEXPART (Stohl et al., 2005), to study air mass origins and transport processes using WRF meteorological forecasts. In this study, we use FLEXPART-WRF in backward mode to study the origin and transport pathways of plumes measured during the POLARCAT-France spring campaign, and to provide insight into the WRF-Chem representation of aerosols. The meteorological fields from the WRF-Chem simulation CTL described in 3.1 are used as input. Every minute, 10 000 particles are released along the aircraft flight tracks

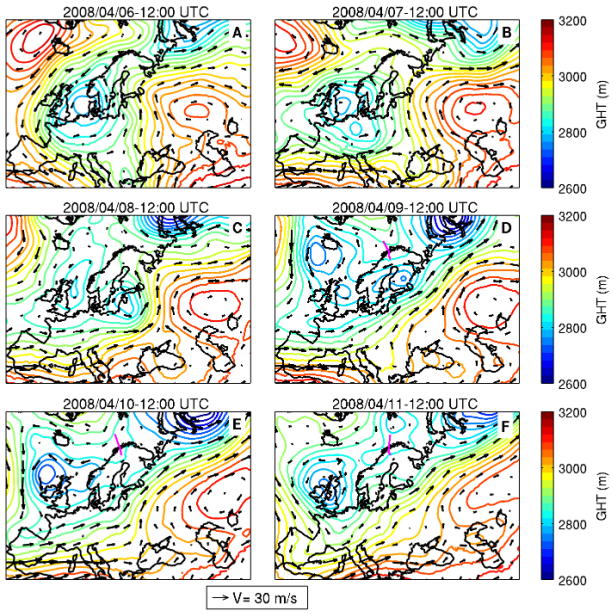

Figure 4-3 – Meteorological conditions simulated by WRF-Chem during the POLARCAT-France spring campaign period, represented by the 700 hPa geopotential height (contour lines) and 700 hPa wind vectors (30 $\mathrm{m\,s^{-1}}$ vector given for scale) on 6–11 April 2008 (12:00 UTC). The POLARCAT-France flight tracks on 9, 10, and 11 April 2008 are indicated in magenta.

in a volume 10 km × 10 km (horizontally) and 400 m (vertically). Each of the simulations is run backwards for 7 days to track the air mass origin over the source regions of interest (transport times are typically less than 7 days). Specifically, we use FLEXPART-WRF potential emission sensitivity (PES) to study source–receptor relationships for air measured by the ATR-42 as part of the POLARCAT-France spring flights.

4.2.4 Meteorological context during the spring POLARCAT-France campaign

Long-range transport of aerosol from Europe to the Arctic is usually associated with specific synoptic meteorological conditions over Europe, causing large-scale meridional transport (e.g., Iversen and Joranger, 1985). In order to investigate the origin and transport of aerosols measured during the POLARCAT-France spring campaign, the synoptic meteorological conditions during the campaign as represented by WRF-Chem are shown in Fig. 4-3. Specifically, WRF-Chem simulated geopotential height contours and wind arrows (700 hPa) are shown from 6 to 11 April 2008. A similar figure showing wind speed at 700 hPa instead of geopotential height is shown in Fig. S1 in the Supplement[1]. Low pressure over the North Sea and high pressure over southwestern Russia and Kazakhstan caused southerly winds over central and eastern Europe from 6 to 8 April. On 8 April, the low pressure in North Sea moved over the Baltic Sea, pushing those southerly winds deeper into the Scandinavian Arctic. On 9 April, the low pressure weakened and moved over Finland, while a deep trough formed over the Kara Sea, stopping north-

[1] http://www.atmos-chem-phys.net/15/3831/2015/acp-15-3831-2015-supplement.pdf

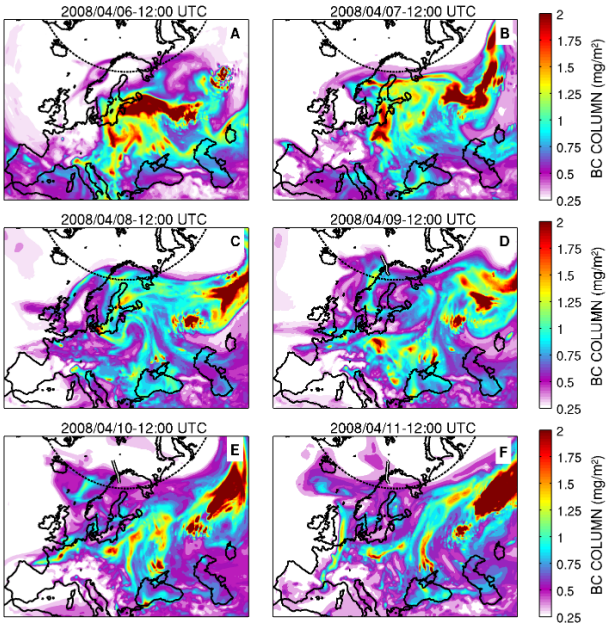

Figure 4-4 – Simulated BC column on 6–11 April 2008 (12:00 UTC). POLARCAT-France flight tracks are indicated in white, with a black border.

ward transport and producing strong westerly winds over Europe and western Russia through the end of the aircraft campaign on 11 April.

Aerosols and other pollution are transported from lower latitudes in Europe in these synoptic meteorological systems, which determine the main pollution transport pathways. We show vertically integrated black carbon as a proxy for pollution transported during this time period in Fig. 4-4 (CTL simulation). The intersection of the low over the North Sea and the high located over Russia lead to the northward transport of a large polluted air mass from central and eastern Europe. A portion of this air mass was carried eastward at mid-latitudes, while another portion reached Arctic Scandinavia on 8 to 9 April. This polluted air mass was sampled by POLARCAT-France flights on 9, 10, and 11 April 2008, the flights that are the main focus of this study. However, this air mass did not penetrate deep into the Arctic and mix significantly with Arctic air due to the position of the polar front (Ancellet et al., 2014). On 10–11 April, the Arctic outflow intensified in the Barents and Norwegian seas, slowly transporting the polluted European air back to lower latitudes. On 10–11 April, pollution (represented as elevated BC) can be seen entering the simulation domain from the northern boundary over Svalbard (in our simulations via the MOZART-4 boundary conditions), and crossing the POLARCAT flight track on 11 April. This last polluted air mass is not the focus of the present study and has been identified as a mixed anthropogenic and biomass burning plume originating from northeast Asia. It has already been studied in detail by Adam de Villiers et al. (2010) and Quennehen et al. (2012).

4.2.5 Model validation

Results from WRF-Chem are compared to POLARCAT-France 1 s resolution measurements of temperature, relative humidity, wind speed, and wind direction (CTL simulation) for the POLARCAT-France flights included in our study. This comparison is presented in Fig. 4-5. Modeled and measured quantities are in good

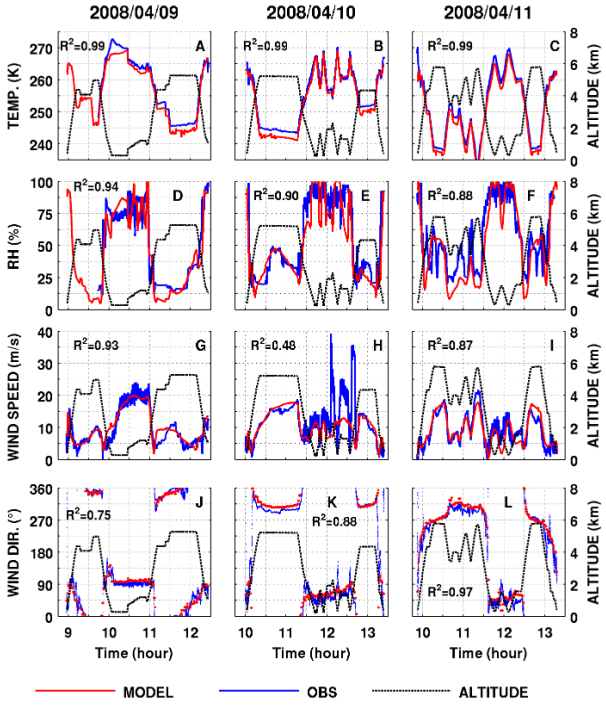

Figure 4-5 – Time series of modeled (red) and measured (blue) **(a–c)** temperature, **(d–f)** relative humidity, **(g–i)** wind speed, and **(j–l)** wind direction extracted along the POLARCAT-France flight tracks. The corresponding aircraft altitude is shown in black.

agreement with the exception of fine-scale features that are not reproduced by the model due to the horizontal grid spacing (30 km). In particular, we note that relative humidity (RH) is well reproduced by the model ($R^2 > 0.88$). Pilinis et al. (1995) showed that RH, through aerosol water uptake, is a key parameter for modeling aerosol optical properties. The main discrepancies are between the measured and modeled wind speeds on 10 April 2008, when high winds were observed below 1 km (middle portion of the flight) over the Norwegian Sea. However, discrepancies between modeled and measured wind speeds in the marine boundary layer over the Norwegian Sea during this portion of the flight do not impact the results for the pollution events we focus on, which were encountered higher up in the Scandinavian free troposphere and were emitted over continental Europe. The model performance in the Arctic troposphere indicates that the model captures the changing meteorological conditions in the European Arctic at the end of the POLARCAT-France spring campaign (discussed earlier in Sect. 4.2.4). This provides confidence that plume transport and dispersion are adequately represented to study aerosol transport and processing.

We evaluate model performance over the European source regions by comparing background aerosol levels from the EMEP network with model results (CTL simulation) extracted at the station locations. Figure 4-6 shows the comparison for $PM_{2.5}$, $SO_4^=$, NO_3^-, and NH_4^+, daily averaged for all stations. Error bars show the standard deviation between stations for both measured and modeled aerosols. Overprediction of aerosols on 1 April for $PM_{2.5}$, NO_3^-, and NH_4^+ correspond to positive biases for these species in the initial conditions (MOZART-4), but WRF-Chem results are in better agreement

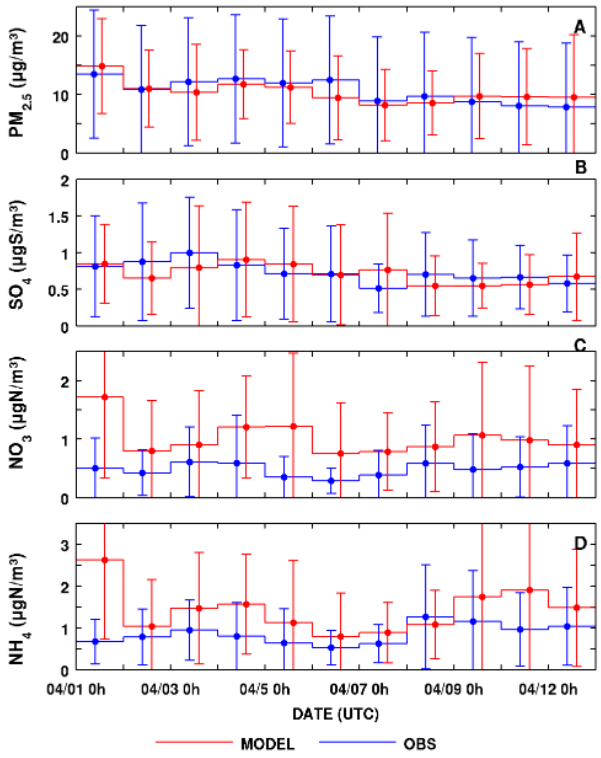

Figure 4-6 – Daily mean aerosol mass measured at EMEP stations within the domain (in blue) and WRF-Chem aerosol mass extracted at the position of the stations (in red) for **(a)** $PM_{2.5}$, **(b)** sulfate aerosol, **(c)** nitrate aerosol, and **(d)** ammonium aerosol. The standard deviation between stations is indicated by the error bars.

with measurements after 1 day of simulation. This first day is considered as model spin-up, and is excluded from further analysis. We evaluate the model performance in reproducing European background aerosol levels in terms of normalized mean bias (NMB). It is defined as $\mathrm{NMB} = 100\,\% \times 1/N \times \sum_{i=1}^{N} (M_i - O_i)/O_i$, where M_i and O_i are modeled and observed daily values, averaged over all sites, and the summation is over the $N = 10$ days between 2 and 11 April. $PM_{2.5}$ levels are well reproduced by the model ($\mathrm{NMB} = -0.9\,\%$). There are more significant differences in measured and modeled aerosol composition: while $SO_4^=$ agrees well with measurements ($\mathrm{NMB} = -0.6\,\%$), NO_3^- ($\mathrm{NMB} = +107\,\%$) and NH_4^+ ($\mathrm{NMB} = +53\,\%$) are overestimated. This suggests that the overestimation of NO_3^- and NH_4^+ might be compensated in terms of overall mass by an underestimation of organic carbon (OC) aerosols, resulting in relatively good $PM_{2.5}$ agreement. Due to a lack of available OC measurement from EMEP stations for this period, this hypothesis cannot be verified. If we use the very limited EMEP OC data (5 stations, 67 % coverage), we find that OC is indeed underestimated for those stations ($\mathrm{NMB} = -38\,\%$). This underestimation could be caused, in part, by the fact that SOA is not included in our model run. Since SOAs can be formed by the oxidation of VOCs by gas-phase NO_3, it is also possible that the lack of SOA is related to the overestimation of nitrate aerosols in our simulations. However, we also note that previous studies including SOA can report errors on OC of the same magnitude or larger (e.g., $-74\,\%$ in Tuccella et al., 2012,

who attribute this deficiency in modeling OC to an incomplete description of SOA formation in their mechanism).

The overestimation of NO_3^- and NH_4^+ and underestimation of OC by WRF-Chem in Europe were also seen in the simulations of Tuccella et al. (2012), using different emissions as well as gas and aerosol schemes. That study suggested the discrepancy was due to missing aqueous reactions causing an underestimation of sulfate formation, leading to less neutralization of ammonium by sulfate and favoring the formation of ammonium nitrate (see Meng et al., 1997). The possible role of uncertainties in the simplified wet scavenging scheme used for that study is also highlighted. Our study includes a more complete wet scavenging scheme and the full range of aqueous reactions included in MOSAIC, keeping in mind that cloud–aerosol interaction processes in MOSAIC are only accounted for in dynamically resolved clouds, which should be underestimated in our simulation (30 km horizontal resolution). The inclusion of these processes, and the use of different anthropogenic emissions (EMEP in Tuccella et al., 2012, vs. HTAPv2 in the present study), can explain the better agreement on sulfate compared to Tuccella et al. (2012). However, this better agreement also means that, in our case, sulfate concentrations do not drive the overestimation of modeled ammonium and nitrate. Using EMEP measurements of ammonia (19 stations) and NO_x (10 stations), we found that NH_3 is overestimated by a factor of 2 in our simulation (NMB $= +108\,\%$), while NO_x is slightly underestimated (NMB $= -23\,\%$). This overestimation of NH_3 could cause an enhanced formation of ammonium nitrate, which would explain the model overestimation of ammonium and nitrate.

While the CTL simulation is able to reproduce $PM_{2.5}$ levels observed in source regions, this good performance is due in part to compensating effects between different chemical components of the aerosols. The bulk hygroscopicity of OC ($=0.14$) is lower than the one for NO_3^- and NH_4^+ ($=0.5$) in MOSAIC. This means that the underestimation of OC in our simulation might lead to overestimated aerosol activation in clouds and wet scavenging. However, refractive indices for OC, NH_4NO_3, and $(NH_4)_2SO_4$ are close (1.45, 1.50, and 1.47 in MOSAIC), meaning that compensation between these different components should not have a strong impact on modeled aerosol optical properties, and that our model represents European aerosols sufficiently well to investigate the direct and semi-direct aerosol radiative effects in the Arctic.

4.2.6 The origin and properties of springtime aerosols during POLARCAT-France

In this section, modeled aerosols in the Arctic are compared with POLARCAT-France spring measurements, to investigate in detail the aerosol transport event from Europe to the Arctic. We combine WRF-Chem simulations with FLEXPART-WRF to identify the source regions and transport pathways of plumes sampled during the campaign, and show how they impact processes along transport and the vertical structure of Arctic pollution. First, aerosol particles detected in plumes in April 2008 are described in terms of mass concentrations, chemical composition, and number size distributions. The role of transport pathways and wet scavenging along transport on those properties is also investigated. Aerosol optical properties are then used to quantify the vertical distribution of aerosols as a function of their emission sources.

4.2.6.1 Modeling aerosols measured in situ on 9, 10, and 11 April 2008

POLARCAT-France measured (in situ) $PM_{2.5}$ is compared with modeled $PM_{2.5}$ interpolated in

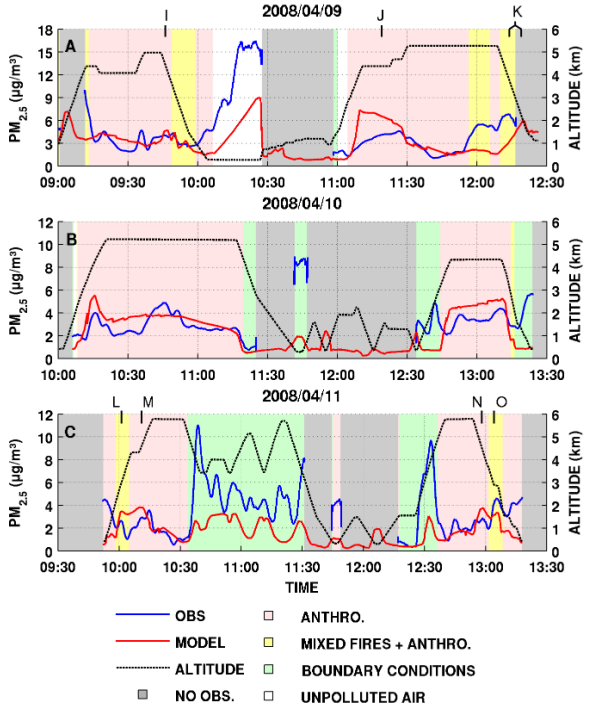

Figure 4-7 – Time series of $PM_{2.5}$ measured during POLARCAT-France (blue) and modeled (red) with the aircraft altitude indicated in black for the three POLARCAT-France flights on **(a)** 9 April 2008, **(b)** 10 April 2008, and **(c)** 11 April 2008. Grey shading indicates times when no measurements are available. Colors indicate when $PM_{2.5}$ was significantly influenced (> 20 % of $PM_{2.5}$) by source: green shows air entering the domain from the northern boundary conditions, pink shows anthropogenic emissions within the domain, yellow shows fire emissions within the domain, and white shows unpolluted air (free of recent pollution sources). Letter labels indicate anthropogenic (I, J, M, N) and mixed anthropogenic/fire (K, L, O) plumes investigated further.

space (model results using hourly output) along the flight tracks on 9, 10, and 11 April 2008 (Fig. 4-7). The time series of measured $PM_{2.5}$ shows plumes containing enhanced aerosols were encountered during the flights. Aerosol mass in plumes ranged from 3 to 16 $\mu g\,m^{-3}$, while baseline levels were 1 $\mu g\,m^{-3}$. It should be noted that unpolluted air and marine boundary layer air were less frequently sampled due to the planned flight patterns, which targeted anthropogenic and biomass burning influenced plumes. Gray shading denotes periods when in situ measurements are not available, usually due to the presence of clouds.

Air mass origins indicated on Fig. 4-7 are determined using a combination of WRF-Chem and FLEXPART-WRF (simulations described below). The influence of anthropogenic and biomass burning emissions on the flight track is estimated using the NOANTHRO and NOFIRES sensitivity runs. Specifically, this influence is deemed significant if aerosol mass increased by more than 20 % upon including either anthropogenic or biomass burning emissions, according to the ratios [CTL $PM_{2.5}$] / [NOANTHRO $PM_{2.5}$] and [CTL $PM_{2.5}$] / [NOFIRES $PM_{2.5}$]. The val-

[2] http://www.atmos-chem-phys.net/15/3831/2015/acp-15-3831-2015-supplement.pdf

Table 4.2 – Modeled $PM_{2.5}$ aerosol composition by source type along POLARCAT-France spring flights. BC, OC, and SS are black carbon, organic carbon, and sea salt, respectively.

Flight	Source type	BC (%)	OC (%)	$SO_4^=$ (%)	NH_4^+ (%)	NO_3^- (%)	SS (%)
9 Apr 2008	Anthro.	2.5	7.0	24.1	20.6	40.2	5.6
	Mixed fires + anthro.	3.2	12.6	35.0	20.1	26.0	3.2
10 Apr 2008	Anthro.	2.3	5.5	21.7	20.9	42.4	7.3
11 Apr 2008	Anthro.	2.7	8.7	34.4	19.5	27.3	7.4
	Mixed fires + anthro.	2.8	11.9	33.9	19.4	28.5	3.4

ues of these ratios along the three flight tracks are presented in the Supplement, Fig. S2[2]. We used a threshold of 20 % to highlight the difference between air masses significantly influenced by biomass burning (BB) and air masses mostly influenced by anthropogenic emissions. This threshold excludes air masses weakly influenced (5 to 15 %) by BB on 10 and 11 April (as seen on Fig. S2[3]) and identifies air masses significant influenced by BB, up to 30–40 %. We used the same threshold of 20 % for anthropogenic plumes for consistency. On Fig. 4-7, pink shading indicates that the modeled $PM_{2.5}$ are influenced by European anthropogenic emissions. Yellow shading indicates portions of the flight influenced by both biomass burning and anthropogenic emissions (mixed plumes). It should be noted that portions of the flight track that are influenced by biomass burning emissions are also influenced by anthropogenic emissions. Green shading indicates that the modeled air mass is significantly influenced by the domain's northern boundary conditions (i.e., air transported from Asia). This influence is identified using FLEXPART-WRF, run in backwards mode with particles released every minute along the flight tracks (10 km × 10 km horizontally by 400 m vertically). When the FLEXPART-WRF retroplume mean trajectory passes closer than five grid cells (150 km) from the northern end of the domain, the air mass is considered as influenced by the northern boundary conditions. The typical transport pathway of such a plume is shown in the Supplement, Fig. S3[4]. Finally, white shading indicates air masses that are not attributed to a specific source using the methods described above and are referred to as unpolluted air.

In the free troposphere, the model is able to reproduce the baseline $PM_{2.5}$ levels and the main peaks observed in European air masses for all three flights. The NMB for $PM_{2.5}$ for all three flights, excluding unpolluted air and boundary condition air, is +8.8 %. Peaks attributed to European anthropogenic emissions are reproduced, although the model cannot capture some small-scale features due to its resolution. At the end of the 9 April flight, two concentrated plumes were sampled in situ around 12:00 and 12:15 UTC. The model identifies these plumes as mixed (anthropogenic/biomass burning), meaning that significant (> 40 %) enhancements in modeled $PM_{2.5}$ at these times are due to biomass burning or anthropogenic European emissions. The first $PM_{2.5}$ peak is underestimated by the model (around 12:00 UTC), and the second plume (around 12:15 UTC) is located 1.5 km too low in altitude. This may be due to uncertainties in the injection height for fires or in the intensity and timing of the emissions. However, the issue does not appear to be system-

[3] http://www.atmos-chem-phys.net/15/3831/2015/acp-15-3831-2015-supplement.pdf
[4] http://www.atmos-chem-phys.net/15/3831/2015/acp-15-3831-2015-supplement.pdf

atic in our simulation because mixed plume peaks and enhancements are correctly represented during the 11 April flight. Modeled anthropogenic $PM_{2.5}$ are underestimated below 1 km at the beginning and end of the 11 April flight above Sweden (discussed in detail in Sect. 4.2.6.3). Plumes coming from the northern domain boundary, which are not studied in detail here, reflect a general underestimation of aerosols in the MOZART-4 simulation used as the boundary conditions. On 9 April, WRF-Chem also reproduces a large $PM_{2.5}$ peak located in the marine boundary layer. This peak is composed of more than 95 % sea salt in the model, and corresponds to sea spray uplifted by the strong 20 $m\,s^{-1}$ winds present in the marine boundary layer in the region of the flight.

The modeled composition of $PM_{2.5}$ aerosols in anthropogenic and mixed polluted air masses is presented in Table 4.2. On 9 and 10 April, anthropogenic plumes are mostly composed of nitrate, sulfate, and ammonium aerosol. Mixed plumes contain relatively less nitrate, but more sulfate, organic carbon, and black carbon. The proportion of sulfate is higher in mixed plumes than in anthropogenic plumes, despite the fact that sulfate and SO_2 emissions from biomass burning emissions are low. We show in the next section focused on plume origins that the proportion of sulfate is high for mixed plumes because they originate in a region of high anthropogenic SO_2 emissions. On 11 April, the composition of anthropogenic plumes and mixed plumes are similar, except for organic carbon, which is still lower in anthropogenic plumes. In Sect. 4.2.5, we showed that the model was overestimating nitrate and ammonium at the surface, while probably underestimating organic matter in the European source regions. Measurements of aerosol chemical composition are not available along the POLARCAT-France flights, but were determined during other POLARCAT campaigns in other parts of the Arctic. In situ measurements during other campaigns generally indicate less nitrate and more organic matter (OM) in Arctic aerosols. For example, Brock et al. (2011) found 78 % OM and 20 % NO_3^- in biomass burning aerosols in the Alaskan Arctic during ARCPAC (32 and 1 % for anthropogenic plumes). Airborne aerosol mass spectrometer measurements in the summer in Greenland during POLARCAT-France (Schmale et al., 2011) also indicate very low NO_3^- concentrations (below the detection limit) and high proportions of OM (50 to 90 %) in polluted plumes. During the International Chemistry Experiment in the Arctic Lower Troposphere (ICEALOT) campaign, at the same time and location as the POLARCAT-France measurements, Frossard et al. (2011) found (excluding sea salt and black carbon) 30 % OM, 60 % $SO_4^=$ and 1 % NO_3^- in aerosols found in the Scandinavian marine boundary layer. This comparison with other POLARCAT data also indicates that in our simulations, nitrate aerosols might have been formed at the expense of organic matter, probably due to the lack of a SOA mechanism. The proportion of black carbon modeled in the present study is 2.5 % in anthropogenic air masses (2.6 % for submicron particles), and 3 % in mixed plumes (3.1 % for submicron particles). These values are comparable with results from the study of Brock et al. (2011), which found on average 2.4 % submicron mass of BC in anthropogenic plumes and 3.5 % in fire plumes in the Alaskan Arctic during spring 2008.

We evaluate model predictions of aerosol size distributions, which are known to be important for the optical properties (Boucher, 1998) presented in Sects. 4.2.6.3 and 4.2.7. It is also important to note that activation in clouds, which is outside the scope of the present study, is also sensitive to aerosol size distributions (Dusek et al., 2006). Plumes for which we compare modeled and measured size distributions are indicated by ticks in Fig. 4-7 (referring to the modeled aerosol peak). Four anthropogenic plumes (I, J, M,

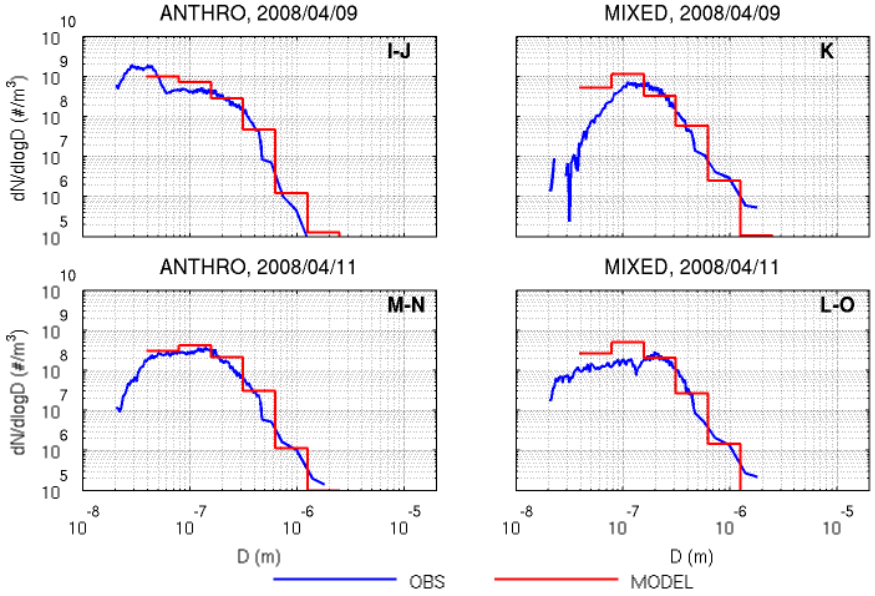

Figure 4-8 – Modeled (red) and measured (blue) number size distributions of plumes labeled (I–O) in Fig. 4-7, influenced by (I, J, M, N) European anthropogenic and (K, L, O) mixed European anthropogenic and fire emissions. Modeled and observed size distributions corresponding to two consecutive samplings of the same plume during the same flight (I–J, M–N, L–O) were averaged together.

N) and three mixed plumes (K, L, O) are investigated. In the case of plume K, the modeled plume peak is located 1 km lower in the model than in observations, which results in it being displaced later in time along the flight track. For this plume, we compare the modeled and measured plumes using the peak aerosol mass encountered in the model (12:19 UTC) and measurements (12:14 UTC), respectively. This comparison is shown in Fig. 4-8. It indicates that the model adequately represents the aerosol size distributions with three exceptions. First, the model overestimates the number of particles larger than 300 nm in the 9 April anthropogenic plumes (I, J). Second, the model cannot be compared to measurements in the smallest MOSAIC bin (aerosols 39 to 78 nm), due to the fact that the model does not explicitly resolve nucleation, but relies on a parameterization for nucleation and growth of particles with diameters less than 39 nm. Third, number concentrations are overestimated in the second smallest MOSAIC bin (aerosols 78 to 156 nm) for mixed plumes (K and L–O) but not for anthropogenic plumes. We show in Sect. 4.2.6.2 that mixed plumes are 2 days older than anthropogenic plumes. This means that this overestimation is probably caused by underestimated growth processes, which have the largest impact on older plumes. However, aerosol optical properties are mostly sensitive to particles in the accumulation mode, which is correctly reproduced for all plumes (Stokes diameter ranges for these modes are 90–500 nm for the anthropogenic plumes, and 110–700 nm for the fire plumes; Quennehen et al., 2012).

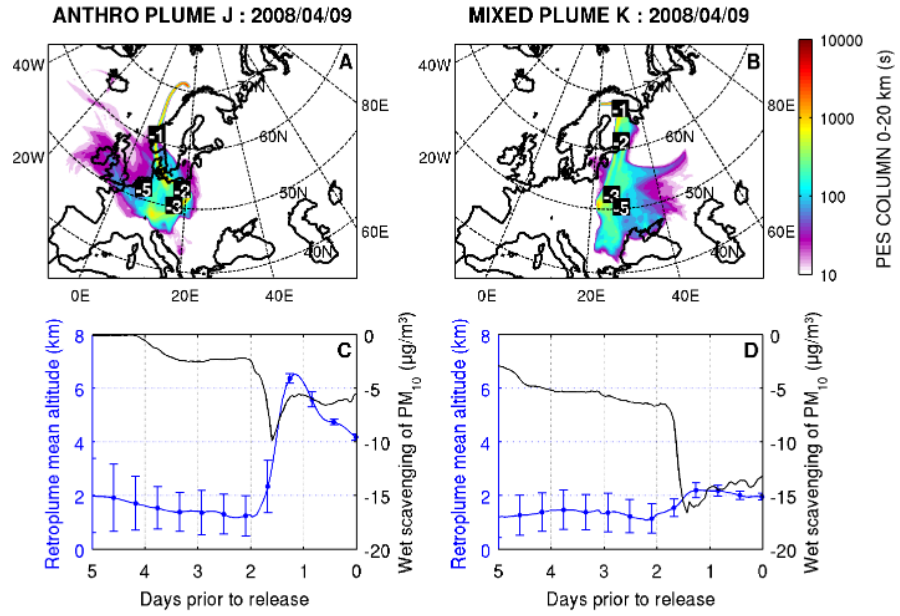

Figure 4-9 – Backward mode FLEXPART-WRF column-integrated PES **(a** and **b)**, showing typical transport pathways for an anthropogenic plume (left, plume J, originating on 9 April 2008 at 11:19 UTC on the POLARCAT flight track) and a mixed anthropogenic/biomass burning plume (right, plume K, originating on 9 April 2008 at 12:19 UTC on the flight track). Numbers in white indicate the plume age, in days. Panels **(c)** and **(d)** show each plume's mean altitude with rms error bars showing vertical dispersion (blue) and the difference between the CTL PM_{10} and the NOWETSCAV PM_{10} along transport, indicating wet scavenging events (black).

4.2.6.2 Origins and transport pathways of anthropogenic and biomass burning plumes sampled during POLARCAT-France

Different types of aerosols transported to the Arctic during POLARCAT-France display different physical properties and vertical distributions. We investigate how different plume origins and transport pathways result in different aerosol properties in the Arctic. We focus on the role of wet scavenging during transport, which is the largest source of uncertainty in the representation of Arctic aerosols (Schwarz et al., 2010; Browse et al., 2012). Figure 4-9 shows typical plume transport pathways of an anthropogenic plume (plume J, Fig. 4-9a and c) and a mixed plume (plume K, Fig. 4-9b and d) measured during the campaign. Figure 4-9a and b shows the 0–20 km column of FLEXPART-WRF PES integrated for 7 days for both plumes. It indicates that anthropogenic plumes were mostly influenced by sources in central Europe 2–3 days prior to the measurements, while the mixed plume is 3 to 5 days old and under the influence of emissions in a large region over eastern Europe and western Russia. This region corresponds to the location of agricultural fires in early April 2008, as well as significant anthropogenic emissions, especially of SO_2, as seen in Fig. 4-2. The larger age of mixed plumes explain why their size distribution is shifted toward larger sizes than younger anthropogenic plumes, as discussed in Quennehen et al. (2012).

Figure 4-9c and d show the mean altitude

for each plume as a function of age. The anthropogenic plume experienced a rapid uplift from 1.5 to 6.5 km over Poland and the North Sea on 7 or 8 April, associated with the surface low over this region, while the mixed plume was transported to the Arctic below 2 km and slowly uplifted. Between 9 April and 11 April, FLEXPART-WRF trajectories (not shown here) inform us that mixed plume K mixed with air from fresher anthropogenic plumes I and J. This mixing explains why the chemical composition of the 11 April mixed plumes, shown in Table 4.2 and discussed above, is intermediate between 9 April mixed plume K and the 9 April anthropogenic plumes I and J.

The magnitude of wet scavenging along transport, also represented in Fig. 4-9c and d, is estimated using the difference between CTL PM_{10} and NOWETSCAV PM_{10} along the retroplumes positions. As expected, strong PM_{10} depletions, reaching $-10\ \mu g\,m^{-3}$ ($-74\,\%$) are associated with precipitation during uplift of the anthropogenic plume in the frontal system over Poland, between 37 and 46 h before it was measured. Although the mixed plume does not experience such a rapid uplift, aerosols are also scavenged by rainout over Finland, between 35 and 45 h before sampling, decreasing PM_{10} levels by $17\ \mu g\,m^{-3}$ ($-55\,\%$). The accumulated precipitation in the simulation compared to the E-OBS European daily gridded precipitation data set (Haylock et al., 2008), shows that while WRF-Chem correctly reproduces the precipitation patterns observed during this period, it generally underestimates their intensity (see Supplement, Fig. S4[5]). However, we have shown that average $PM_{2.5}$ levels are well reproduced in the source regions and in the Arctic, indicating that losses along transport are relatively well reproduced. This could be explained by compensations between underestimated precipitations and an overestimated wet scavenging rate in our simulation. An overestimation of the wet scavenging rate could be caused by the overestimated hygroscopy of the modeled aerosol, which contains too much ammonium and nitrate, and not enough organic matter.

4.2.6.3 Vertical aerosol distributions: 9 April 2008

The vertical structure of aerosol layers transported to the Arctic is often complex (Brock et al., 2011), and the vertical distribution of absorbing aerosol layers can have a large influence on their radiative effects (e.g., Meloni et al., 2005; Raut and Chazette, 2008). Here, the modeled vertical structure of aerosol layers in the Arctic troposphere is evaluated using the pseudo-backscatter ratio at 532 nm (PBR) measured by the airborne lidar shooting at nadir. The measured PBR is represented in Fig. 4-10b for the 9 April flight, clouds and data below clouds are masked in white. The altitude of the aircraft, which flew north to south and returned to Kiruna, is shown as a black line on panels b to e. We choose to show the 9 April flight because modeled low-level pollution is not influenced by the model northern boundary conditions on this day. The model-to-observation comparison is therefore not affected by the performance of the global model MOZART-4. Figure 4-10a shows the $PM_{2.5}$ measured in situ by the aircraft during the same period. The $PM_{2.5}$ and lidar-derived PBR just below the aircraft present a very similar evolution: the $PM_{2.5}$ and PBR signals are enhanced during the whole leg between 4 and 5 km, at the aircraft altitude, and just below. This good correlation ($r^2 = 0.86$, see Fig. S5[6]) between aerosol mass and optical properties allows us to validate aerosol concentrations' vertical distributions through their optical properties.

The PBR at 532 nm is compared to cross sec-

[5] http://www.atmos-chem-phys.net/15/3831/2015/acp-15-3831-2015-supplement.pdf
[6] http://www.atmos-chem-phys.net/15/3831/2015/acp-15-3831-2015-supplement.pdf

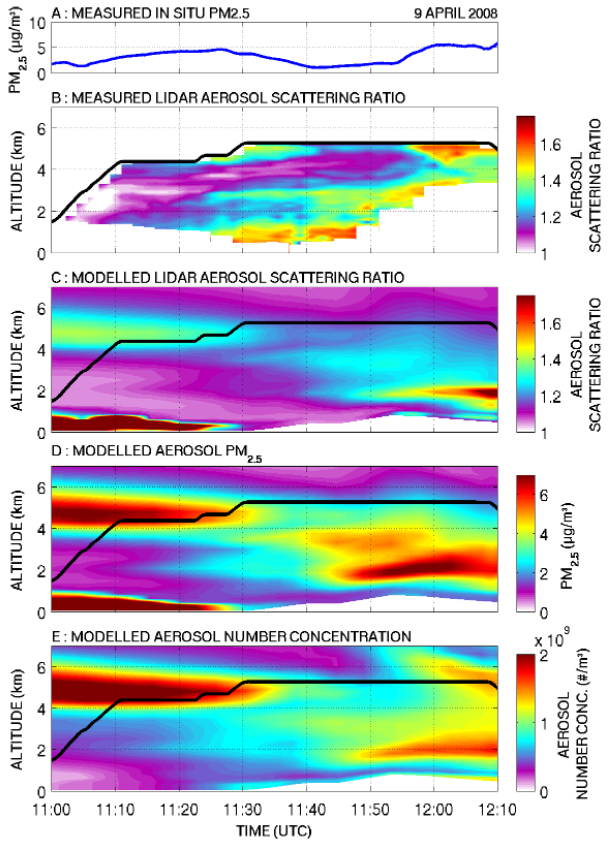

Figure 4-10 – **(a)** $PM_{2.5}$ measured in situ during the last part of the 9 April 2008 flight, **(b)** lidar 532 nm pseudo-backscatter ratio measured at nadir during the same portion of the flight (altitude in black, white areas represent topography or cloudy areas where no aerosol data is available), **(c)** simulated WRF-Chem lidar 532 nm pseudo-backscatter ratio, **(d)** modeled $PM_{2.5}$ cross section at the same position, and **(e)** modeled aerosol number concentration cross section at the same position.

tions of the simulated backscatter ratio (Fig. 4-10c), simulated $PM_{2.5}$ (Fig. 4-10d) and simulated aerosol number concentration (Fig. 4-10e) extracted along flight tracks from the WRF-Chem simulation. The magnitude of the PBR is correctly reproduced, with background regions between 1 and 1.1, and visible aerosol layers reaching values of 1.3 to 1.5. Peak intensities in plumes transported to the Arctic region tend to be underestimated by the model, as the modeled plumes are too diluted vertically. Plume locations are reasonably well reproduced with an enhanced layer at 5 km during the whole flight leg, and two main layers at lower latitudes and altitudes, between 1.5–2 and 3–4 km. One enhanced layer measured between 11:30 and 11:50 UTC at 1 km is missing from the modeled PBR cross section because it is displaced 50 km to the southwest in the simulation (see Supplement, Fig. S6[7]). This displacement is probably due to the cumulative effect of small errors on wind speed and wind direction over the 3 to 5 days of long-range transport. The model underestimates the PBR in the intense layer measured in situ

[7] http://www.atmos-chem-phys.net/15/3831/2015/acp-15-3831-2015-supplement.pdf

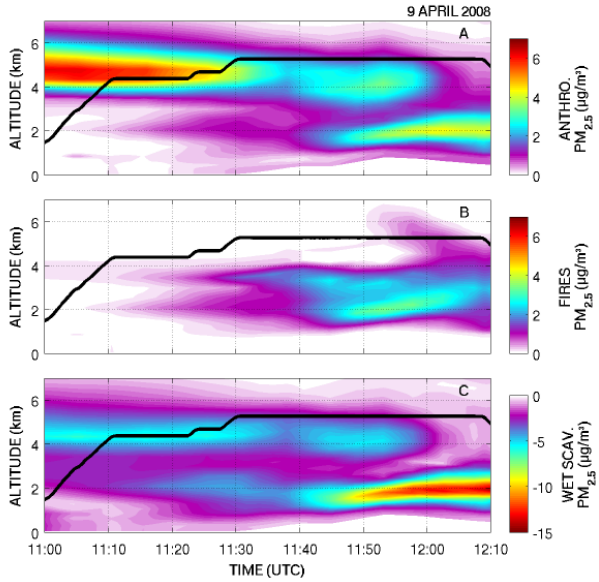

Figure 4-11 – Modeled aerosol cross sections along the flight track (plane altitude in black), showing the sensitivity of the modeled $PM_{2.5}$ to **(a)** anthropogenic emissions, **(b)** fire emissions, and **(c)** wet scavenging.

and by the lidar at 5 km at 12:00 UTC, which is in agreement with the underestimation observed on $PM_{2.5}$ levels previously described in Fig. 4-7. This layer, identified as a 5-day old mixed plume in the model, features low $PM_{2.5}$ but high aerosol number concentrations (Fig. 4-10e), suggesting it is mostly composed of small particles. This means that the discrepancy in this layer probably corresponds to underestimated growth by condensation, which could be associated with underestimated precursor emissions including a lack of SOA. This is in agreement with the comparison of the modeled and observed size distributions of aerosols in mixed plumes, discussed in Sect. 4.2.6.1, which indicated underestimated particle growth in the older mixed plumes.

We investigate the vertical distribution of modeled anthropogenic and biomass burning aerosols during this profile, and the impact of wet scavenging on the vertical distribution. Figure 4-11 shows the sensitivity of the $PM_{2.5}$ vertical cross section to anthropogenic emissions (Fig. 4-11a), biomass burning emissions (Fig. 4-11b), and wet scavenging (Fig. 4-11c). During the 9 April flight, anthropogenic emissions have the largest influence in the mid- to upper troposphere, above 4 km and in the PBL and lower troposphere, below 2 km, while the impacts of biomass burning emissions are more pronounced between 2 and 4 km. Figure 4-11b confirms that the plume missing at 5 km in Fig. 4-10c is indeed due to biomass burning emissions, but the associated enhancement above background is very low, around 1 $\mu g\,m^{-3}$. According to Fig. 4-11c, this low enhancement is not due to high wet scavenging in this layer. As discussed before, this confirms that the underestimation of $PM_{2.5}$ in this layer may be due to insufficient growth by condensation in this plume. The impact of wet scavenging is the strongest for the lower-level mixed pollution, as discussed in the case of plume K in Fig. 4-9d. It is negligible in biomass burning layers located between 2 and 4 km, and strong relatively to total $PM_{2.5}$ in the southernmost and low-altitude anthropogenic layer.

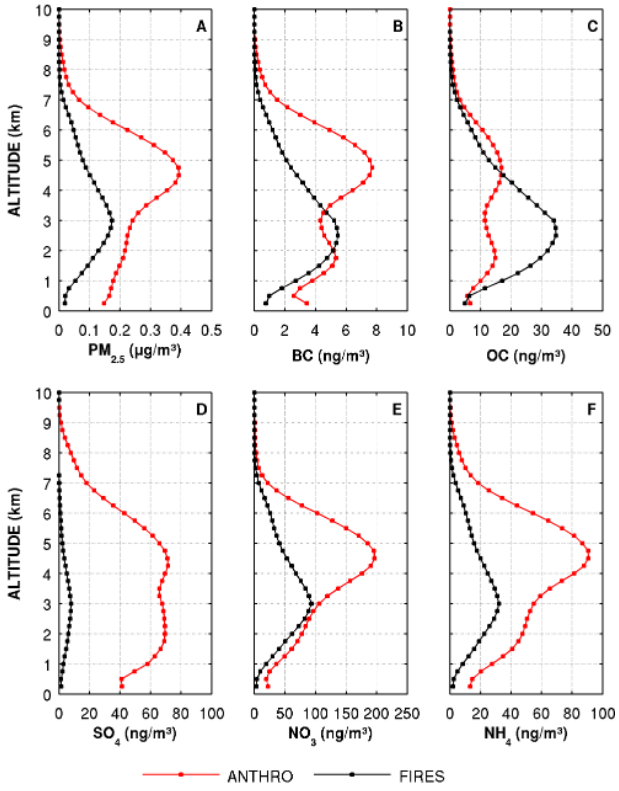

Figure 4-12 – Modeled vertical profiles of enhancements in **(a)** $PM_{2.5}$, **(b)** BC, **(c)** OC, **(d)** $SO_4^=$, **(e)** NO_3^-, and **(f)** NH_4^+ $PM_{2.5}$, due to anthropogenic (red) and fire (black) emissions within the WRF-Chem model domain, averaged in the Arctic (latitude $>$ 66.6 N) and over the period from 00:00 UTC 8 April 2008 to 00:00 UTC 12 April 2008.

4.2.7 Impacts of European aerosol transport on the Arctic

Results presented so far give us confidence in the way this transport event is represented in our simulation in terms of meteorology, $PM_{2.5}$ levels, size distributions, spatial extent, and vertical structure of the plumes. We now investigate the regional impacts of this transport event in the European Arctic region. Figure 4-12 shows the average vertical profiles of the modeled anthropogenic and biomass burning contributions to $PM_{2.5}$ (total and chemically speciated) north of the Arctic Circle (within the model domain) during the period from 00:00 UTC 8 April to 00:00 UTC 12 April. The very low aerosol concentrations are due to area-weighted averaging of European enhancements confined in the lower Scandinavian Arctic with the rest of the clean Arctic region contained in the domain. Because of this, we will not discuss the absolute enhancements and instead focus on relative values. This average profile shows the same general features as were observed in situ and by lidar during POLARCAT-France, with anthropogenic emissions separated between a low-altitude (1.5 km) and a high-altitude (4.5 km) contribution, and biomass burning emissions impacting intermediate altitudes (2.5–3 km). Different species display different vertical structures: for the anthropogenic contribution, BC, OC, and $SO_4^=$ are enhanced at low altitudes. This corresponds to the mixed layers from eastern Europe and Russia. High-altitude anthropogenic plumes from

central Europe contain enhanced NH_4^+, NO_3^-, and BC. Biomass burning plumes contain larger mass fractions of BC and OC than anthropogenic plumes, and BC and OC influence lower altitudes than other $PM_{2.5}$ species from biomass burning. These results are in agreement with earlier studies by Stohl et al. (2007) and Lund Myhre et al. (2007), who analyzed cases of transport of biomass burning plumes from eastern Europe to the Arctic in spring 2006. Using FLEXPART simulations and lidar measurements, they showed that biomass burning aerosols were mostly confined below 3 km altitudes in the Arctic. Fisher et al. (2011) investigated aerosol transport from the mid-latitudes to the Arctic during April 2008 with the global chemical transport model GEOS-Chem, and found that in the high Arctic (75–85 N), NH_4^+ and $SO_4^=$ were sensitive to European anthropogenic emissions at all altitudes, with a peak sensitivity between 2 and 5 km.

Pueschel and Kinne (1995) have shown that layers of aerosols containing black carbon, even with very high single scattering albedos (0.98), could warm the atmosphere over snow- or ice-covered surfaces. Because the transport of pollution from Europe to the Arctic is especially efficient in late winter and early spring when the Scandinavian snow cover is still extensive, aerosols transported to the Scandinavian Arctic may contribute to enhanced local atmospheric heating rates in this region (Flanner, 2013). We investigate this by calculating the DSRE (0.125 to 10 µm wavelengths) of aerosols at the top of atmosphere (TOA), in regions significantly influenced by in-domain anthropogenic and biomass burning emissions. The DSRE, shown in Fig. 4-13a, is estimated by taking the difference between the upward shortwave TOA flux calculated online by the Goddard shortwave module within WRF-Chem, in the CTL simulation minus the NODIRECT simulation. Because WRF-Chem upward radiative fluxes are by convention always negative, positive DSRE values at TOA indicate heating of the surface–atmosphere column. The DSRE is averaged over the period from 00:00 UTC 8 April to 00:00 UTC 12 April. In-domain anthropogenic and biomass burning emissions are considered significant if the $PM_{2.5}$ column sensitivity to anthropogenic and biomass burning emissions (shown in Fig. 4-13b) exceeds 50 % of the total column of CTL $PM_{2.5}$. We added this condition to exclude from our calculation of the DSRE the areas where the dominant contribution is due to aerosols originating from the boundary conditions (i.e., the Asian plume), from natural emissions (i.e., sea salt) or from background levels.

As expected, the DSRE is negative over land and ocean where snow and ice cover are low, but positive over regions with high snow and ice covers (see the snow and ice cover map on Fig. 4-13c). The 4-day average value of the DSRE at TOA north of 60 N in regions significantly influenced by European pollution is shown in Table 4.3. In addition to the total average effect north of 60 N, we compute values for the DSRE over surfaces with extensive snow and ice cover ($> 90\,\%$), and over the ocean surface. On average, the European aerosols have a cooling effect north of 60 N ($-0.98\ \mathrm{W\,m^{-2}}$). Over snow and ice, the average DSRE is $+0.58\ \mathrm{W\,m^{-2}}$, peaking near $+2\ \mathrm{W\,m^{-2}}$ over a large region in northern Scandinavia where AODs are the highest (0.5 at 400 nm). The DSRE is much lower over the Russian snowpack east of 42 E because the European mixed air mass in this region is either optically shallow (AOD from 0.05 to 0.2) or is located below clouds. Over the Arctic seas, the DSRE is negative due to the lower albedo of the ocean surface. The calculated DSRE in oceanic regions north of 60 N influenced by the European plumes is $-1.5\ \mathrm{W\,m^{-2}}$. Minimum values reach close to $-5\ \mathrm{W\,m^{-2}}$ over the Norwegian Sea close to the coast of Norway, where the cloud cover is the lowest, as shown in Fig. 4-13d.

In this study, we focus on the springtime Eu-

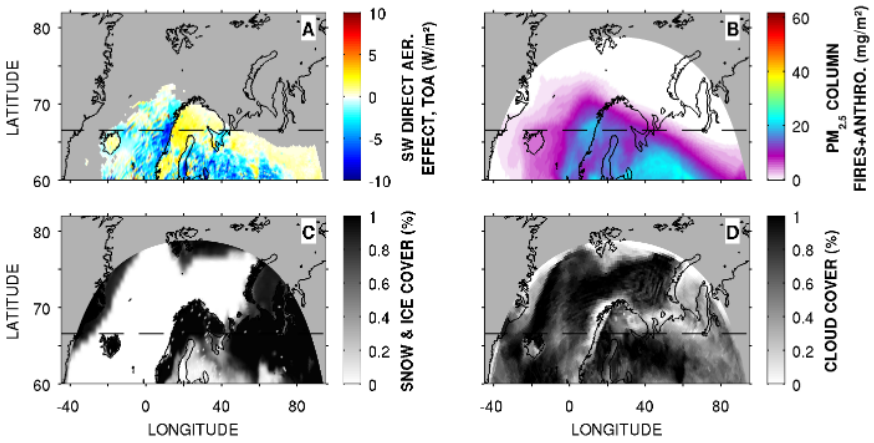

Figure 4-13 – Model averages over the period from 00:00 UTC 8 April 2008 to 00:00 UTC 12 April 2008 of the **(a)** aerosol DSRE, at the TOA, in regions significantly affected by in-domain anthropogenic and fire emissions, **(b)** $PM_{2.5}$ column sensitivity to anthropogenic and biomass burning emissions, and **(c)** fractional snow and sea ice cover, **(d)** fractional cloud cover. In panel **(a)**, regions not significantly affected by in-domain emissions are masked in gray. In panels **(b–d)**, regions outside of the WRF-Chem domain are masked in gray. The Arctic Circle is indicated by a dashed line.

Table 4.3 – Four-day average DSRE at the TOA north of 60 N, over regions significantly influenced by European pollution ($> 50\,\%$ of total $PM_{2.5}$ column due to in-domain anthropogenic and biomass burning emissions).

Type of land surface	DSRE at TOA ($\mathrm{W\,m^{-2}}$)
Snow and ice cover $> 90\,\%$	+0.58
Ocean	−1.52
All	−0.98

ropean Arctic and put our results into the context of other studies focusing on the same period in different locations within the Arctic. We summarize the other studies for comparison, but leave it to future studies to draw broader conclusions about whether these results are representative of wider spatial and temporal scales. Brock et al. (2011) calculated a direct radiative effect of +3.3 $\mathrm{W\,m^{-2}}$ over snow at TOA for the average of 10 typical polluted profiles measured during the ARCPAC campaign, not taking the semi-direct effect into account. Maximum modeled BC in WRF-Chem along the POLARCAT-France flight tracks is 150 $\mathrm{ng\,m^{-3}}$ (anthropogenic) and 260 $\mathrm{ng\,m^{-3}}$ (mixed fire/anthropogenic), which are comparable with the average BC values reported for anthropogenic (148 $\mathrm{ng\,m^{-3}}$) and fire plumes (312 $\mathrm{ng\,m^{-3}}$) in Brock et al. (2011). This means that, on average, the BC values for pollution-influenced plumes in our simulation are lower than values reported by Brock et al. (2011). Quinn et al. (2007) found a similar direct radiative effect value of +2.5 $\mathrm{W\,m^{-2}}$ over snow at TOA for the average polluted conditions encountered during the Arctic haze maximum at Barrow. Those results were obtained at solar noon, in clear sky conditions, over snow, and in polluted regions only, conditions that lead to a maximum

direct effect. Using a similar approach, we compute the DSRE in regions influenced by European pollution, close to noon (11:00 UTC), and above high snow covers (> 90 %). This results in an average DSRE of +1.9 W m^{-2} north of 60 N. If we exclude the snowpack in Russia, east of 42 E, the average DSRE in reaches +3.3 W m^{-2}. These values are in agreement with results from Brock et al. (2011) and Quinn et al. (2007). It should be noted that our retrievals are done in all-sky conditions and not exactly at local solar noon, introducing a slight low bias. Including the semi-direct effect in our calculations might have introduced a warming bias, which would be limited by the nudging of WRF-Chem temperature, relative humidity, and wind speed towards FNL reanalyses in the free troposphere. We verified that differences in cloud cover between the NODIRECT and CTL simulations were limited in magnitude and extent, with only a few local points over the sea affected (below 10 % cloud cover change for the 8 to 12 April average), that mostly cancel each other out when regionally averaged.

Lund Myhre et al. (2007) calculated the direct forcing of biomass burning aerosols transported from Europe to the Arctic in late April and early May 2006 from spaceborne AOD measurements. For those exceptionally intense plumes, they found that the cooling direct effect at TOA reached −35 W m^{-2} over the regions with the highest AOD in the Barents Sea, while the maximum warming direct effect over snow was limited to +5 W m^{-2} over Svalbard. Keeping in mind that our results are not directly comparable because of the different times of year and different averaging periods, we found a 4-day average direct and semi-direct effect reaching maximum values of +2 W m^{-2} over snow-covered Scandinavia, and maximum cooling values of −5 W m^{-2} over the Norwegian Sea. Several reasons could explain this different balance between warming and cooling effects. In our case, modeled European plumes contained higher levels of black carbon (2.5 to 3 % of submicron aerosol mass) than the measured value used in the study of (Lund Myhre et al., 2007) (1.98 %). The transport event studied here also featured a high-altitude anthropogenic plume that would have a local warming effect above the high-albedo low-level clouds. The inclusion of the semi-direct effect in our study might have also played a limited role.

At the surface, the direct aerosol effect causes local cooling for all types of land surfaces, including snow and ice (−1.1 W m^{-2} DSRE on average, −2.75 W m^{-2} at noon over Scandinavia and Finland). However, we also show in Fig. 4-12 that BC was enhanced at the surface in anthropogenic plumes, which could lead to surface warming through the effects of BC deposited on snow. Black carbon deposition is not coupled to snow albedo in WRF-Chem 3.5.1, however the global model study of Wang et al. (2011) showed that in spring 2008 (April–May), significant levels of anthropogenic BC (1 to 5 mgC m^{-2} month^{-1}) were deposited on snow in northern Europe, leading to 1 to 2 % change in the regional albedo of snow and ice. This change in snow albedo was estimated to cause a radiative effect of +1.7 W m^{-2} in April–May (average value for the Arctic north of 60 N). Wang et al. (2011) did not show the geographical distribution of this forcing, which should be higher in Scandinavia and Finland because the snow-albedo change from BC deposition is higher in their study in continental Eurasia than in the rest of the Arctic.

4.2.8 Summary and conclusions

In this study, we investigate an aerosol transport event from Europe to the European Arctic using measurements as well as regional chemical transport model simulations for the first time. Specifically, an event involving long-range transport of biomass burning and anthropogenic aerosols from Europe to the Arctic in April 2008 is studied using the regional model WRF-Chem (eight-bin

MOSAIC aerosol scheme), to quantify impacts on aerosol concentrations and resulting direct shortwave radiative effects in the Scandinavian Arctic. Modeled aerosols are evaluated against ground-based observations from the EMEP network in European source regions, and using POLARCAT-France aircraft measurements aloft in the European Arctic. The model reproduces background $PM_{2.5}$ levels at EMEP ground-based stations in Europe (NMB = −0.9 %) and in Arctic polluted air masses measured by the ATR42 aircraft (NMB = +8.8 %). Comparison with EMEP measurements shows that the model overestimates concentrations of particulate NO_3^- (NMB = +107 %) and NH_4^+ (NMB = +53 %) in source regions, probably because of overestimated NH_3 emissions and the lack of SOA formation, and may underestimate OC. Good agreement is found between simulated $SO_4^=$ and EMEP measurements (NMB = −0.6 %).

The model indicates that European biomass burning and anthropogenic emissions both had a significant influence on total aerosol mass concentrations (> 20 % of total $PM_{2.5}$) during portions of the POLARCAT-France spring campaign measurements analyzed in this study. Plumes influenced by biomass burning sources in the model are also found to be significantly influenced by anthropogenic emissions. These modeled mixed plumes contain elevated organic carbon and black carbon concentrations. They originated in eastern Europe and western Russia, and followed low-altitude (below 2 km) transport pathways into the Arctic. Significant wet scavenging is predicted in the model during transport over Finland, reducing PM_{10} levels by 55 %. Modeled high-altitude anthropogenic plumes, originating in central Europe, were rapidly uplifted (from 1 to 6 km in less than 24 h) by warm conveyor belt circulations over Poland and the North Sea. The model also predicts significant wet scavenging during transport of these anthropogenic plumes (PM_{10} reduced by 74 %). Evaluation of the model against in situ measurements and lidar profiles below the aircraft shows that the model correctly represents the average vertical distribution of aerosols during this European transport event, as well as the magnitude of the aerosol optical properties. However, this comparison suggests that the model underrepresents the rate of aerosol growth processes, especially condensation, which has the largest impact on the older mixed plumes (3 to 5 days old).

The model is used to investigate the average vertical structure of aerosol enhancements from European anthropogenic and biomass burning emissions in the Scandinavian Arctic. Anthropogenic emissions are shown to influence aerosols at both low (1.5 km) and higher altitudes (4.5 km), while biomass burning emissions influence aerosols between these altitudes (2.5 to 3 km). In anthropogenic plumes, BC and $SO_4^=$ aerosol concentrations are proportionally more enhanced at lower altitudes, including at the surface.

This transport event brought elevated aerosol concentrations north of the Arctic Circle for a rather short period of 4 days, from 8 to 12 April 2008. Due to the location of the polar front, these European aerosols did not mix significantly with local Arctic air further north. However, this event is particularly interesting because of the extensive seasonal snow cover present in northern Scandinavia during this period. We show that the event had a significant local atmospheric warming effect over snow and ice surfaces. The average 96 h TOA direct and semi-direct shortwave radiative effect from this event over snow and sea ice is found to be +0.58 $W\,m^{-2}$ north of 60 N. At solar noon, in regions significantly influenced by European aerosols, larger warming is predicted, +3.3 $W\,m^{-2}$ (TOA direct and semi-direct radiative effects) over the Scandinavian and Finnish snow cover north of 60 N. This result is of the same order of magnitude as values previously reported for aerosols in the

western Arctic (Brock et al., 2011; Quinn et al., 2007).

These radiative effect values do not include the impacts of cloud–aerosol interactions, which could be significant due to the extensive cloud cover in northern Scandinavia during this transport event. The indirect effect could offset the warming effect of European aerosols over snow and ice-covered surfaces we have shown here. Moreover, the indirect aerosol effect is still uncertain, especially in the Arctic, and further work is needed to estimate its magnitude. During POLARCAT-France, the ATR-42 aircraft also sampled an intense Asian plume that was not investigated in this study, which focuses on European aerosols. The contribution of Asian sources to Arctic pollution is an active area of research, and the POLARCAT-France data set, as well as the other POLARCAT data sets, could be the basis of a focused study on the transport of such plumes to the Arctic.

4.3 Main insights from the study

In this thesis, WRF-Chem simulations are used to investigate aerosol and ozone pollution in the Arctic. Previous work indicates that current Arctic pollution is mostly transported from the mid-latitudes, and often originates from Europe and Western Asia. For this reason, it is important to investigate if WRF-Chem is able to reproduce these transport events, and the associated Eurasian pollution in the Arctic. Previous studies also indicate that plume processing during transport (especially aerosol wet removal) is an important factor controlling Arctic pollution. In this Chapter, WRF-Chem simulations are combined with POLARCAT-France measurements to investigate pollution transport from Europe to the Arctic in spring 2008, and pollution processing during transport.

4.3.1 Aerosol transport to the Arctic

The case study presented in this Chapter shows that WRF-Chem is able to reproduce a long-range aerosol transport event from Europe to the Arctic. The model is evaluated over the European source region and in the Arctic in terms of aerosol concentrations, plume locations and optical properties, showing good agreement with two main exceptions. First, WRF-Chem seems to underestimate OA concentrations and overestimate NO_3^- concentrations in the mid-latitudes and in the Arctic. Second, comparison of model results with in-situ size distribution observations and airborne LIDAR measurements suggest that WRF-Chem underestimates aerosol growth in some older biomass burning plumes measured in altitude (4 km). These two exceptions can be explained by the lack of SOA formation in these simulations, since recent studies indicate that biomass burning emissions are an important global source of SOA (Shrivastava et al., 2015). SOA can be formed by the oxidation of VOCs by gaseous NO_3^- , which could also explain part of the NO_3^- overestimation. For this reason, SOA formation is later included in the Arctic wide simulations presented in Chapter 6.

This study also helps to identify that the transport event observed during POLARCAT-France involved a complex mix of sources (anthropogenic emissions, biomass burning), source regions (central Europe and West Asia), and transport pathways (fast high-altitude transport and slower low-level transport). These processes produced several aerosol pollution layers at different altitudes in the Arctic. Wet removal has a strong impact ($> 50\,\%$) on PM_{10} for both low-altitude transport and transport in frontal systems (in "warm conveyor belt" circulations), and is thus a critical process controlling aerosol amounts reaching the Arctic in spring. This study also illustrates that WRF-Chem can be used to estimate direct and semi-direct radiative effects of pollution aerosols. The estimate of the aerosol direct and semi-direct radiative effect at TOA associated with this event ($3.3\,W\,m^{-2}$ at solar noon and over snow- and ice-covered land) is comparable with previous estimates of the direct aerosol radiative effect in spring in the American Arctic ($3.3\,W\,m^{-2}$ and $2.5\,W\,m^{-2}$ respectively in

Brock et al., 2011 and Quinn et al., 2007). Since WRF-Chem temperature, wind speed and humidity are nudged to FNL, the semi-direct aerosol effect is probably damped in these runs, and values might be more representative of the direct effect alone.

4.3.2 Ozone transport to the Arctic in these simulations, and in the related work of Thomas et al. (2013)

Long-range ozone transport from the mid-latitudes was not investigated in the study presented in this Chapter, which is focused on aerosol pollution. Model representations of ozone were nonetheless evaluated by comparing simulation results to EMEP measurements of O_3. This comparison is shown in Figure 4-14, and indicates that these WRF-Chem simulations underestimate observed O_3 in spring 2008. Tuccella et al. (2012) also found a similar underestimation in spring in WRF-Chem simulations over Europe, using a different model setup. They attributed this underestimation to the lack of time-varying boundary conditions in their runs. However, our simulations include time-varying boundary conditions from the MOZART4 model but still show these discrepancies. Later analysis (Chapters 5 and 6) and results by Ahmadov et al. (2015) indicate that this bias is most likely due to incorrect values for UV-albedo over snow and ice in the photolysis scheme, and to overestimated gaseous dry deposition over snow- and ice-covered surfaces in WRF-Chem. These errors were corrected in the simulations presented in Chapters 5 and 6.

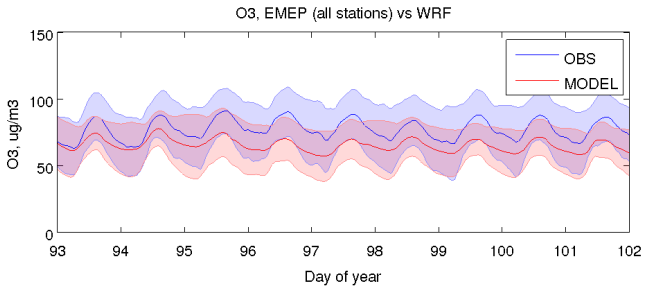

Figure 4-14 – Hourly mean O_3 measured at EMEP stations within the domain (in blue) and WRF-Chem O_3 extracted at the position of the stations (in red). The color shading indicates standard deviation between stations.

Thomas et al. (2013) also used WRF-Chem simulations to investigate long-range ozone transport from North America to Greenland in summer 2008. I contributed to this study by performing FLEXPART-WRF simulations similar to those described in Section 4.2.3.3.2, in order to estimate plume ages, plume origins and transport pathways for these transport events. Thomas et al. (2013) also showed that WRF-Chem was able to represent plume composition in the Arctic and in source regions, and that significant ozone production occurred during long-range transport of anthropogenic and biomass burning pollution plumes from the mid-latitudes during summer (6.5 ppbv and 3 ppbv respectively).

Chapter 5

Current impacts of Arctic shipping in Northern Norway

5.1 Motivation

Shipping is thought to be an important local source of Arctic pollution (AMAP, 2006; Arctic Council, 2009). Ships emit CO_2, and several air pollutants, notably BC, SO_2 and NO_x. Shipping emissions have a current net global cooling effect on climate (Eyring et al., 2010), due to the direct and indirect effects of sulfate aerosols formed from SO_2 emissions. However, since SO_2 has a much shorter lifetime than CO_2, the net long-term climate effect of shipping emissions is warming due to CO_2.

Arctic warming and the associated decline in sea ice are expected to unlock the Arctic Ocean to human activity, and trans-Arctic shipping routes could be widely used by mid-century (Smith and Stephenson, 2013). Currently, Arctic shipping is the highest along the Norwegian and Western Russian coasts, and previous studies investigating the impacts of Arctic shipping emissions in this region(Dalsøren et al., 2007; Ødemark et al., 2012) found that these emissions had some influence on ozone concentrations, sulfate and BC burdens, and radiative effects. However, these earlier studies were based on earlier emission inventories known to be incomplete (i.e. not representing fishing ships), to underestimate marine traffic, or to be biased towards specific ship types (i.e. large cargo ships). Recent shipping emission inventories based on AIS ship positioning developed by Winther et al. (2014) and Jalkanen et al. (2012) correspond to higher emissions in the Arctic ($\times 2$ for NO_x), which suggests that earlier studies could have been underestimating shipping impacts in this region. Furthermore, previous studies were mostly based on calculations by global models, which often struggle to reproduce O_3 (Dalsøren et al., 2007), and aerosols (Lee et al., 2013) at high latitudes.

In this Chapter, WRF-Chem simulations are combined with a new ship emission in-

ventory created by the STEAM2 model (Jalkanen et al., 2012), in order to evaluate the model representation of meteorological conditions and shipping pollution, to validate new shipping emission inventories and to quantify the current impacts of shipping emissions on atmospheric composition and radiative effects along the Norwegian coast. WRF-Chem simulation results and STEAM2 emissions are compared to new measurements from the ACCESS aircraft campaign (Roiger et al., 2015), using flights targeting shipping pollution in the Arctic region.

The WRF-Chem model setup used in this study (Table 5.2, described in Sect. 5.2.4.1) is similar to the base model setup described in Chapter 2, with two main exceptions. First, the boundary layer and surface schemes were changed from MYJ+Janji (Janji , 1994) to MYNN+MM5 (Mellor-Yamada-Nakanishi-Niino, Nakanishi and Niino, 2006, Fifth-Generation Penn State/NCAR Mesoscale Model, Zhang and Anthes, 1982). The reason for this change is that PBL heights from WRF-Chem are used in FLEXPART-WRF simulations, and the MYJ scheme often diagnoses very low PBL heights. Second, a different version of CBM-Z/MOSAIC including DMS and methane sulphonic acid (MSA) chemistry was used, since DMS is an important source of particles in the Arctic during summer (Ferek et al., 1995), and oceanic concentrations of DMS are particularly high in Northern Norway during summer (Lana et al., 2011). An online DMS emission scheme based on Nightingale et al. (2000) and Saltzman et al. (1993) was also implemented in WRF-Chem for these simulations.

This study was published in Atmospheric Chemistry and Physics as

Marelle, L., Thomas, J. L., Raut, J.-C., Law, K. S., Jalkanen, J.-P., Johansson, L., Roiger, A., Schlager, H., Kim, J., Reiter, A., and Weinzierl, B., Air quality and radiative impacts of Arctic shipping emissions in the summertime in northern Norway: from the local to the regional scale, *Atmospheric Chemistry and Physics*, 16(4), 2359–2379, doi: 10.5194/acp-16-2359-2016, URL `http://www.atmos-chem-phys.net/16/2359/2016/`, 2016.

The paper is reproduced in the following section.

5.2 Air quality and radiative impacts of Arctic shipping emissions in the summertime in northern Norway: from the local to the regional scale (Marelle et al., 2016).

5.2.1 Abstract

In this study, we quantify the impacts of shipping pollution on air quality and shortwave radiative effect in northern Norway, using WRF-Chem (Weather Research and Forecasting with chemistry) simulations combined with high-resolution, real-time STEAM2 (Ship Traffic Emissions Assessment Model version 2) shipping emissions. STEAM2 emissions are evaluated using airborne measurements from the ACCESS (Arctic Climate Change, Economy and Society) aircraft campaign, which was conducted in the summer 2012, in two ways. First, emissions of nitrogen oxides (NO_x) and sulfur dioxide (SO_2) are derived for specific ships by combining in situ measurements in ship plumes and FLEXPART-WRF plume dispersion modeling, and these values are compared to STEAM2 emissions for the same ships. Second, regional WRF-Chem runs with and without STEAM2 ship emissions are performed at two different resolutions, 3 km $\times$ 3 km and 15 km $\times$ 15 km, and evaluated against measurements along flight tracks and average campaign profiles in the marine boundary layer and lower troposphere. These comparisons show that differences between STEAM2 emissions and calculated emissions can be quite large (-57 to $+148$ %) for individual ships, but that WRF-Chem simulations using STEAM2 emissions reproduce well the average NO_x, SO_2 and O_3 measured during ACCESS flights. The same WRF-Chem simulations show that the magnitude of NO_x and ozone (O_3) production from ship emissions at the surface is not very sensitive (< 5 %) to the horizontal grid resolution (15 or 3 km), while surface PM_{10} particulate matter enhancements due to ships are moderately sensitive (15 %) to resolution. The 15 km resolution WRF-Chem simulations are used to estimate the regional impacts of shipping pollution in northern Norway. Our results indicate that ship emissions are an important source of pollution along the Norwegian coast, enhancing 15-day-averaged surface concentrations of NO_x (+80 %), SO_2 (+80 %), O_3 (+5 %), black carbon (+40 %), and $PM_{2.5}$ (+10 %). The residence time of black carbon originating from shipping emissions is 1.4 days. Over the same 15-day period, ship emissions in northern Norway have a global shortwave (direct + semi-direct + indirect) radiative effect of -9.3 mW m^{-2}.

5.2.2 Introduction

Shipping is an important source of air pollutants and their precursors, including carbon monoxide (CO), nitrogen oxides (NO_x), sulfur dioxide (SO_2), volatile organic compounds (VOCs) as well as organic carbon (OC) and black carbon (BC) aerosols (Corbett and Fischbeck, 1997; Corbett and Koehler, 2003). It is well known that shipping emissions have an important influence on air quality in coastal regions, often enhancing ozone (O_3) and increasing aerosol concentrations (e.g., Endresen et al., 2003). Corbett et al. (2007) and Winebrake et al. (2009) showed that aerosol pollution from ships might be linked to cardiopulmonary and lung diseases globally. Because of their negative impacts, shipping emissions are increasingly subjected to environmental regulations. The International Maritime Organization (IMO) has designated several regions as Sulfur Emission Control Areas (SECAs; including the North Sea and Baltic Sea in

Europe), where low sulfur fuels must be utilized to minimize the air quality impacts of shipping on particulate matter (PM) levels. The sulfur content in ship fuels in SECAs was limited to 1 % by mass in 2010, decreasing to 0.1 % in 2015, while the global average is 2.4 % (IMO, 2010). Less strict sulfur emission controls (0.5 %) will also be implemented worldwide, at the latest in 2025, depending on current negotiations. Ships produced or heavily modified recently must also comply to lower NO_x emissions factors limits, reducing emission factors (in $g\,kW^{-1}\,h$) by approximately -10 % (after 2000) and another -15 % (after 2011) compared to ships built before year 2000 (IMO, 2010). Jonson et al. (2015) showed that the creation of the North Sea and Baltic Sea SECAs was effective in reducing current pollution levels in Europe, and that further NO_x and sulfur emission controls in these regions could help to achieve strong health benefits by 2030 by reducing PM levels.

In addition to its impacts on air quality, maritime traffic already contributes to climate change, by increasing the concentrations of greenhouse gases (CO_2, O_3) and aerosols (SO_4, OC, BC) (Capaldo et al., 1999; Endresen et al., 2003). The current radiative forcing of shipping emissions is negative and is dominated by the cooling influence of sulfate aerosols formed from SO_2 emissions (Eyring et al., 2010). However, due to the long lifetime of CO_2 compared to sulfate, shipping emissions warm the climate in the long term (after 350 years; Fuglestvedt et al., 2009). In the future, global shipping emissions of SO_2 are expected to decrease due to IMO regulations, while global CO_2 emissions from shipping will continue to grow due to increased traffic. This combination is expected to cause warming relative to the present day (Fuglestvedt et al., 2009; Dalsøren et al., 2013).

In addition to their global impacts, shipping emissions are of particular concern in the Arctic, where they are projected to increase in the future as sea ice declines (for details of future sea ice, e.g., Stroeve et al., 2011. Decreased summer sea ice, associated with warmer temperatures, is progressively opening the Arctic region to transit shipping, and projections indicate that new trans-Arctic shipping routes should be available by mid-century (Smith and Stephenson, 2013). Other shipping activities are also predicted to increase, including shipping associated with oil and gas extraction (Peters et al., 2011). Sightseeing cruises have increased significantly during the last decades (Eckhardt et al., 2013), although it is uncertain whether or not this trend will continue. Future Arctic shipping is expected to have important impacts on air quality in a now relatively pristine region (e.g., Granier et al., 2006), and will influence both Arctic and global climate (Dalsøren et al., 2013; Lund et al., 2012). In addition, it has recently been shown that routing international maritime traffic through the Arctic, as opposed to traditional routes through the Suez and Panama canals, will result in warming in the coming century and cooling on the long term (150 years). This is due to the opposite sign of impacts due to reduced SO_2 linked to IMO regulations and reduced CO_2 and O_3 associated with fuel savings from using these shorter Arctic routes (Fuglestvedt et al., 2014). In addition, sulfate is predicted to cause a weaker cooling effect for the northern routes (Fuglestvedt et al., 2014).

Although maritime traffic is relatively minor at present in the Arctic compared to global shipping, even a small number of ships can significantly degrade air quality in regions where other anthropogenic emissions are low (Aliabadi et al., 2015; Eckhardt et al., 2013). Dalsøren et al. (2007) and Ødemark et al. (2012) have shown that shipping emissions also influence air quality and climate along the Norwegian and Russian coasts, where current Arctic ship traffic is the largest. Both studies (for years 2000 and 2004) were based on emission data sets

constructed using ship activity data from the AMVER (Automated Mutual-Assistance VEssel Rescue system) and COADS (Comprehensive Ocean–Atmosphere Data Set) data sets. However, the AMVER data set is biased towards larger vessels ($>20\,000$ t) and cargo ships (Endresen et al., 2003), and both data sets have limited coverage in Europe (Miola and Ciuffo, 2011). More recently, ship emissions using new approaches have been developed that use ship activity data more representative of European maritime traffic, based on the AIS (Automatic Identification System) ship positioning system. These include the STEAM2 (Ship Traffic Emissions Assessment Model version 2) shipping emissions, described in Jalkanen et al. (2012) and an Arctic-wide emission inventory described in Winther et al. (2014). To date, quantifying the impacts of Arctic shipping on air quality and climate has also been largely based on global model studies, which are limited in horizontal resolution. In addition, there have not been specific field measurements focused on Arctic shipping that could be used to study the local influence of shipping emissions in the European Arctic and to validate model predicted air quality impacts.

In this study, we aim to quantify the impacts of shipping along the Norwegian coast in July 2012, using airborne measurements from the ACCESS (Arctic Climate Change, Economy and Society) aircraft campaign (Roiger et al., 2015). This campaign (Sect. 5.2.3) took place in summer 2012 in northern Norway, and was primarily dedicated to the study of local pollution sources in the Arctic, including pollution originating from shipping. ACCESS measurements are combined with two modeling approaches, described in Sect. 5.2.4. First, we use the Weather Research and Forecasting (WRF) model to drive the Lagrangian particle dispersion model FLEXPART-WRF run in forward mode to predict the dispersion of ship emissions. FLEXPART-WRF results are used in combination with ACCESS aircraft measurements in Sect. 5.2.5 to derive emissions of NO_x and SO_2 for specific ships sampled during ACCESS. The derived emissions are compared to emissions from the STEAM2 model for the same ships. Then, we perform simulations with the WRF-Chem model, including STEAM2 ship emissions, in order to examine in Sect. 5.2.6 the local (i.e., at the plume scale) and regional impacts of shipping pollution on air quality and shortwave radiative effects along the coast of northern Norway.

5.2.3 The ACCESS aircraft campaign

The ACCESS aircraft campaign took place in July 2012 from Andenes, Norway (69.3 N, 16.1 W); it included characterization of pollution originating from shipping (four flights) as well as other local Arctic pollution sources (details are available in the ACCESS campaign overview paper; Roiger et al., 2015). The aircraft (DLR Falcon 20) payload included a wide range of instruments measuring meteorological variables and trace gases, described in detail by Roiger et al. (2015). Briefly, O_3 was measured by UV (ultraviolet) absorption (5 % precision, 0.2 Hz), nitrogen oxide (NO), and nitrogen dioxide (NO_2) by chemiluminescence and photolytic conversion (10 % precision for NO, 15 % for NO_2; 1 Hz), and SO_2 by chemical ionization ion trap mass spectrometry (20 % precision; 0.3 to 0.5 Hz). Aerosol size distributions between 60 nm and 1 µm were measured using a Ultra-High Sensitivity Aerosol Spectrometer Airborne.

The four flights focused on shipping pollution took place on 11, 12, 19, and 25 July 2012 and are shown in Fig. 5-1 a (details on the 11 and 12 July 2012 flights shown in Fig. 5-1b). The three flights on 11, 12, and 25 July 2012 sampled pollution from specific ships (referred to as single-plume flights). During these flights, the research aircraft repeatedly sampled relatively fresh emis-

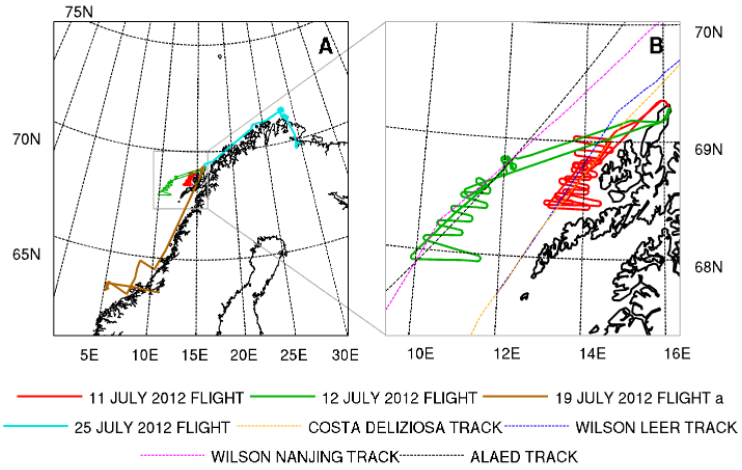

Figure 5-1 – WRF and WRF-Chem domain **(a)** outer domains used for the MET, CTRL, and NOSHIP runs. ACCESS flight tracks during 11, 12, 19a (a – denotes that this was the first flight that occurred on this day, flight 19b – the second flight was dedicated to hydrocarbon extraction facilities) and 25 July 2012 flights are shown in color. **(b)** Inner domain used for the CTRL3 and NOSHIPS3 simulations, with the tracks of the four ships sampled during the 11 and 12 July 2012 flights (routes extracted from the STEAM2 inventory).

sions from one or more ships during flight legs at constant altitudes, at several distances from the emission source, and in some cases at different altitudes. In this study, measurements from these single-plume flights are used in combination with ship plume dispersion simulations (described in Sects. 5.2.4.1 and 5.2.5.1) to estimate emissions from individual ships. This method relies on knowing the precise locations of the ships during sampling. Because those locations are not known for the ship emissions sampled on 25 July 2012 flight, emissions are only calculated for the three ships targeted during the 11 and 12 July flights (the *Costa Deliziosa*, *Wilson Leer*, and *Wilson Nanjing*), and for an additional ship (the *Alaed*) sampled during the 12 July flight, whose location could be retrieved from the STEAM2 shipping emission inventory (presented in Sect. 5.2.4.3). Table 5.1 gives more information about these four ships, one large cruise ship and three cargo ships. On 11 and 12 July 2012, the research aircraft sampled fresh ship emissions within the boundary layer, during flight legs at low altitudes (< 200 m). Fresh ship emissions were sampled less than 4 h after emission. In addition to the single-plume flights, the 19 July 2012 ACCESS flight targeted aged ship emissions in the marine boundary layer near Trondheim. Data collected during the 11 and 12 July 2012 flights are used to derive emissions from operating ships (Sect. 5.2.5), and data from the four flights (11, 12, 19, and 25 July 2012) are used to evaluate regional chemical transport simulations investigating the impacts of shipping in northern Norway (Sect. 5.2.6). Other flights from the ACCESS campaign were not used in this study because their flight objectives biased the measurements towards other emissions sources (e.g., oil platforms in the Norwegian Sea) or because they included limited sampling in the boundary layer (flights north to Svalbard and into the Arctic free troposphere; Roiger et al., 2015).

Table 5.1 – Description of the ships sampled during the ACCESS flights on 11 and 12 July 2012.

Ship name	Vessel type	Gross tonnage (tons)	Fuel type
Wilson Leer	Cargo ship	2446	Marine gas oil
Costa Deliziosa	Passenger ship	92 720	Heavy fuel oil
Wilson Nanjing	Cargo ship	6118	Heavy fuel oil
Alaed	Cargo ship	7579	Heavy fuel oil

* Ship present in STEAM2, not targeted during the campaign..

Table 5.2 – Parameterizations and options used for the WRF and WRF-Chem simulations.

Atmospheric process	WRF-Chem option
Planetary boundary layer	MYNN (Nakanishi and Niino, 2006)
Surface layer	MM5 Similarity scheme, Carlson–Boland viscous sublayer (Zhang and Anthes, 1982; Carlson and Boland, 1978)
Land surface	Unified Noah land-surface model (Chen and Dudhia, 2001)
Microphysics	Morrison (Morrison et al., 2009)
Shortwave radiation	Goddard (Chou and Suarez, 1999)
Longwave radiation	RRTM (Mlawer et al., 1997)
Cumulus parameterization	Grell-3D (Grell and Dévényi, 2002)
Photolysis	Fast-J (Wild et al., 2000)
Gas phase chemistry	CBM-Z (Zaveri and Peters, 1999)
Aerosol model	MOSAIC 8 bins (Zaveri et al., 2008)

5.2.4 Modeling tools

5.2.4.1 FLEXPART-WRF and WRF

Plume dispersion simulations are performed with FLEXPART-WRF for the four ships presented in Table 5.1, in order to estimate their emissions of NO_x and SO_2. FLEXPART-WRF (Brioude et al., 2013) is a version of the Lagrangian particle dispersion model FLEXPART (Stohl et al., 2005), driven by meteorological fields from the mesoscale weather forecasting model WRF (Skamarock et al., 2008). In order to drive FLEXPART-WRF, a meteorological simulation was performed with WRF version 3.5.1, from 4 to 25 July 2012, over the domain presented in Fig. 5-1a. The domain (15 km × 15 km horizontal resolution with 65 vertical eta levels between the surface and 50 hPa) covers most of northern Norway (62 to 75 N) and includes the region of all ACCESS flights focused on ship emissions. The first week of the simulation (4 to 10 July included) is used for model spin-up. WRF options and parameterizations used in these simulations are shown in Table 5.2. Meteorological initial and boundary conditions are obtained from the FNL (abbreviation for "final") analysis from NCEP (National Centers for Environmental Prediction). The simulation is also nudged to FNL winds, temperature, and humidity every 6 h. This WRF meteorological simulation is referred to as the MET simulation.

Ship emissions are represented in the FLEXPART-WRF plume dispersion simulations as moving 2 m × 2 m × 2 m box sources, whose locations are updated every 10 s along the ship trajectory (routes shown in Fig. 5-1b). In all,

1000 particles are released every 10 s into these volume sources, representing a constant emission flux with time of an inert tracer. During the ACCESS flights, targeted ships were moving at relatively constant speeds during the 3 h of the flight, meaning that fuel consumption and emission fluxes are likely to be constant during the flights if environmental conditions (wind speed, waves, and currents) were not varying strongly. FLEXPART-WRF takes into account a simple exponential decay using a prescribed lifetime. In our case, the lifetime of NO_x relative to reaction with OH was estimated using results from WRF-Chem simulations presented in Sect. 5.2.4.2. Specifically, we use OH concentrations, temperature, and air density from the CTRL3 simulation (Sects. 5.2.4.2 and 5.2.6.1). The NO_x lifetime was estimated to be 12 h on 11 July and 5 h on 12 July. The SO_2 lifetime was not taken into account, consistent with the findings of Lee et al. (2011), who reported a lifetime of 20 h over the mid-Atlantic during summer, which is significantly longer than the ages of plumes measured during ACCESS. The FLEXPART-WRF output consists of particle positions, each associated with a pollutant mass; these particles are mapped onto a 3-D output grid (600 m $\times$ 600 m, with 18 vertical levels between 0 and 1500 m a s l) to derive fields of volume mixing ratios every minute. Since emissions are assumed to be constant with time, and since our simulations only take into account transport processes depending linearly on concentrations, the intensity of these mixing ratio fields also depend linearly on the emission strength chosen for the simulation. Therefore, the model results can be scaled a posteriori to represent any constant emission flux value.

Ship emissions can continue to rise after leaving the exhaust, due to their vertical momentum and buoyancy. This was taken into account in the FLEXPART-WRF simulations by calculating effective injection heights for each targeted ship, using a simple plume rise model (Briggs, 1965). This model takes into account ambient temperature and wind speed, as well as the volume flow rate and temperature at the ship exhaust, to calculate a plume injection height above the ship stack. Ambient temperature and wind speed values at each ship's position are obtained from the WRF simulation. We use an average of measurements by Lyyränen et al. (1999) and Cooper (2001) for the exhaust temperature of the four targeted ships (350 C). The volume flows at the exhaust are derived for each ship using CO_2 emissions from the STEAM2 ship emission model (STEAM2 emissions described in Sect. 5.2.4.3). Specifically, CO_2 emissions from STEAM2 for the four targeted ships are converted to an exhaust gas flow based on the average composition of ship exhaust gases measured by Cooper (2001) and Petzold et al. (2008). Average injection heights, including stack heights and plume rise, are found to be approximately 230 m for the *Costa Deliziosa*, 50 m for the *Wilson Nanjing*, 30 m for the *Wilson Leer*, and 65 m for the *Alaed*. In order to estimate the sensitivity of plume dispersion to these calculated injection heights, two other simulations are performed for each ship, where injection heights are decreased and increased by 50 %. Details of the FLEXPART-WRF runs and how they are used to estimate emissions are presented in Sect. 5.2.5.

5.2.4.2 WRF-Chem

In order to estimate the impacts of shipping on air quality and radiative effects in northern Norway, simulations are performed using the 3-D chemical transport model WRF-Chem (Weather Research and Forecasting model, including chemistry, Grell et al., 2005; Fast et al., 2006). WRF-Chem has been used previously by Mölders et al. (2010) to quantify the influence of ship emissions on air quality in southern Alaska. Table 5.2 summarizes all the WRF-Chem options and parameterizations used in the present study, detailed

briefly below. The gas phase mechanism is the carbon bond mechanism, version Z (CBM-Z; Zaveri and Peters, 1999). The version of the mechanism used in this study includes dimethylsulfide (DMS) chemistry. Aerosols are represented by the 8 bin sectional MOSAIC (Model for Simulating Aerosol Interactions and Chemistry; Zaveri et al., 2008) mechanism. Aerosol optical properties are calculated by a Mie code within WRF-Chem, based on the simulated aerosol composition, concentrations, and size distributions. These optical properties are linked with the radiation modules (aerosol direct effect), and this interaction also modifies the modeled dynamics and can affect cloud formation (semi-direct effect). The simulations also include cloud–aerosol interactions, representing aerosol activation in clouds, aqueous chemistry for activated aerosols, and wet scavenging within and below clouds. Aerosol activation changes the cloud droplet number concentrations and cloud droplet radii in the Morrison microphysics scheme, thus influencing cloud optical properties (first indirect aerosol effect). Aerosol activation in MOSAIC also influences cloud lifetime by changing precipitation rates (second indirect aerosol effect).

Chemical initial and boundary conditions are taken from the global chemical-transport model MOZART-4 (model for ozone and related chemical tracers version 4; Emmons et al., 2010). In our simulations, the dry deposition routine for trace gases (Wesely, 1989) was modified to improve dry deposition on snow, following the recommendations of Ahmadov et al. (2015). The seasonal variation of dry deposition was also updated to include a more detailed dependence of dry deposition parameters on land use, latitude, and date, which was already in use in WRF-Chem for the MOZART-4 gas-phase mechanism. Anthropogenic emissions (except ships) are taken from the HTAPv2 (Hemispheric transport of air pollution version 2) inventory (0.1×0.1 resolution). Bulk VOCs are speciated for both shipping and anthropogenic emissions, based on Murrells et al. (2010). Ship VOC emissions are speciated using the "other transport" sector (transport emissions, excluding road transport) and anthropogenic VOC emissions are speciated using the average speciation for the remaining sectors. DMS emissions are calculated following the methodology of Nightingale et al. (2000) and Saltzman et al. (1993). The oceanic concentration of DMS in the Norwegian Sea in July, taken from Lana et al. (2011), is 5.8×10^{-6} mol m^{-3}. Other biogenic emissions are calculated online by the MEGAN (Model of Emissions of Gases and Aerosols from Nature; Guenther et al., 2006) model within WRF-Chem. Sea salt emissions are also calculated online within WRF-Chem.

The WRF-Chem simulations performed in this study are summarized in Table 5.3. The CTRL simulation uses the settings and emissions presented above, as well as ship emissions produced by the model STEAM2 (Sect. 5.2.4.3). The NOSHIPS simulation is similar to CTRL, but does not include ship emissions. The NOSHIPS and CTRL simulations are carried out from 4 to 25 July 2012, over the 15 km $\times$ 15 km simulation domain presented in Fig. 5-1a. The CTRL3 and NOSHIPS3 simulations are similar to CTRL and NOSHIPS, but are run on a smaller 3 km $\times$ 3 km resolution domain, shown in Fig. 5-1b, from 10 to 13 July 2012. The CTRL3 and NOSHIPS3 simulations are not nudged to FNL and do not include a subgrid parameterization for cumulus due to their high resolution. Boundary conditions for CTRL3 and NOSHIPS3 are taken from the CTRL and NOSHIPS simulations (using one-way nesting within WRF-Chem) and are updated every hour.

The CTRL and CTRL3 simulations are not nudged to the reanalysis fields in the boundary layer, in order to obtain a more realistic boundary layer structure. However, comparison with ACCESS meteorological measurements shows that on 11 July 2012 this leads to an over-

Table 5.3 – Description of WRF and WRF-Chem simulations.

Name	Description	Period	Remarks
MET	WRF meteorological simulation, 15 km × 15 km resolution (d01)	4–25 July 2012	Nudged to FNL
CTRL	WRF-Chem simulation, HTAPv2 anthropogenic emissions, STEAM2 ship emissions, online MEGAN biogenic emissions, online DMS and sea salt emissions, 15 km × 15 km horizontal resolution (d01)	4–25 July 2012	Nudged to FNL in the free troposphere only
NOSHIPS	CTRL without STEAM2 emissions, 15 km × 15 km horizontal resolution (d01)	4–25 July 2012	Nudged to FNL in the free troposphere only
CTRL3	CTRL setup and emissions, 3 km × 3 km horizontal resolution (d02)	10–12 July 2012	Boundary conditions from CTRL No nudging No cumulus parameterization
NOSHIPS3	NOSHIPS setup and emissions, 3 km × 3 km horizontal resolution (d02)	10–12 July 2012	Boundary conditions from NOSHIPS No nudging No cumulus parameterization

estimation of marine boundary layer wind speeds (normalized mean bias = +38 %). Since wind speed is one of the most critical parameters in the FLEXPART-WRF simulations, we decided to drive FLEXPART-WRF with the MET simulation instead of using CTRL or CTRL3. In the MET simulation, results are also nudged to FNL in the boundary layer in order to reproduce wind speeds (normalized mean bias of +14 % on 11 July 2012). All CTRL, NOSHIPS, CTRL3, NOSHIPS3 and MET simulations agree well with meteorological measurements during the other ACCESS ship flights.

5.2.4.3 High-resolution ship emissions from STEAM2

STEAM2 is a high-resolution, real-time bottom-up shipping emissions model based on AIS positioning data (Jalkanen et al., 2012). STEAM2 calculates fuel consumption for each ship based on its speed, engine type, fuel type, vessel length, and propeller type. The model can also take into account the effect of waves, and distinguishes ships at berth, maneuvering ships, and cruising ships. Contributions from weather effects were not included in this study, however. The presence of AIS transmitters is mandatory for large ships (gross tonnage > 300 ton) and voluntary for smaller ships.

Emissions from STEAM2 are compared with emissions derived from measurements for individual ships in Sect. 5.2.5. STEAM2 emissions of CO, NO_x, OC, BC (technically elemental carbon in STEAM2), sulfur oxides (SO_x), SO_4, and exhaust ashes are also used in the WRF-Chem CTRL and CTRL3 simulations. SO_x are emitted as SO_2 in WRF-Chem, and NO_x are emitted as 94 % NO, and 6 % NO_2 (EPA, 2000). VOC emissions are estimated from STEAM2 CO emissions using a bulk VOC / CO mass ratio of 53.15 %, the ratio used in the Arctic ship inventory from Corbett et al. (2010). STEAM2 emissions were generated on a 5 km × 5 km grid every 30 min for the CTRL simulation, and on a 1 km × 1 km grid every 15 min for the CTRL3 simulation, and were regridded on the WRF-Chem simulation grids. Shipping emissions of NO_x, SO_2, black carbon, and organic carbon are presented in Fig. 5-2 for the 15 km × 15 km simulation domain (emissions totals during the simulation period are indicated within the figure panels). For comparison, the

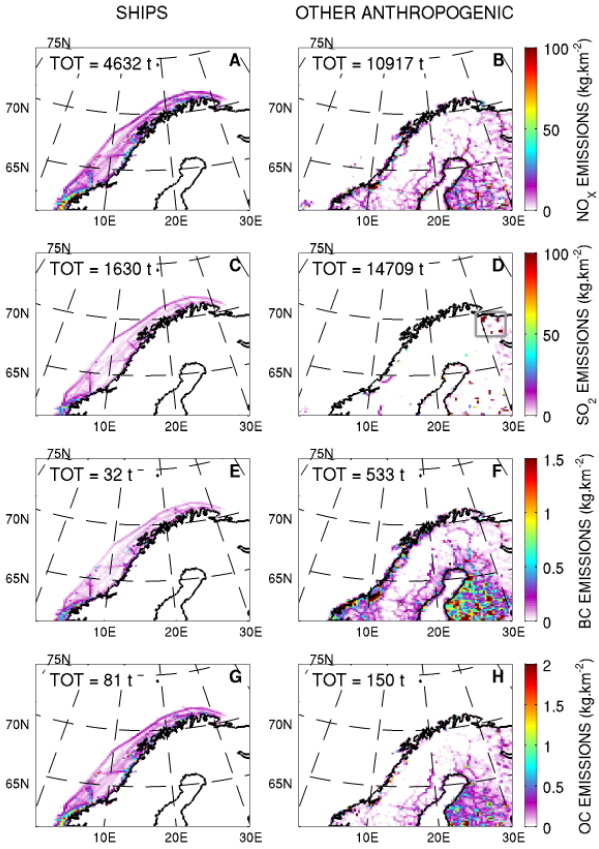

Figure 5-2 – **(a, c, e, g)** STEAM2 ship emissions and **(b, d, f, h)** HTAPv2 anthropogenic emissions (without ships) of **(a, b)** NO_x, **(c, d)** SO_2, **(e, f)** BC, and **(g, h)** OC in kg km^{-2} over the CTRL and NOSHIPS WRF-Chem domain, during the simulation period (00:00 UTC 4 July 2012 to 00:00 UTC 26 July 2012). On panel **(d)**, the location of the intense Kola Peninsula SO_2 emissions is highlighted by a gray box. The emissions totals for the simulation period are noted in each panel.

HTAPv2 emissions (without shipping emissions) are also shown. Ship emissions are, on average, located in main shipping lanes along the Norwegian coastline. However, they also include less traveled routes, which are apparent closer to shore. Other anthropogenic emissions are mainly located along the Norwegian coast (mostly in southern Norway) or farther inland and to the south in Sweden and Finland. Over the whole domain, NO_x and OC emissions from shipping are approximately one-third of total anthropogenic NO_x and OC emissions, but represent a lower proportion of anthropogenic SO_2 and BC emissions (5 and 10 %, respectively). However, other anthropogenic emissions are not co-located with shipping emissions, which represent an important source further north along the coast, as many ships are in transit between European ports and Murmansk in Russia. Very strong SO_2 emissions in Russia are included in the model domain (in the area highlighted in Fig. 5-2d), associated with smelting activities that occur on the Russian Kola Peninsula (Virkkula et al., 1997; Prank et al., 2010). The Kola Peninsula emissions represent 79 % of the total HTAPv2 SO_2 emissions in the domain.

STEAM2 emissions are based on AIS signals that are transmitted to base stations on shore

that have a limited range of 50–90 km, which explains why the emissions presented in Fig. 5-2 only represent near-shore traffic. In addition, our study is focused on shipping emissions in northern Norway, therefore STEAM2 emissions were only generated along the Norwegian coast. As a result, ship emissions in the northern Baltic and along the northwestern Russian coast are not included in this study. However, these missing shipping emissions are much lower than other anthropogenic sources inside the model domain. In the CTRL and CTRL3 simulations, ship emissions are injected in altitude using the plume rise model presented in Sect. 5.2.4.1. Stack height and exhaust fluxes are unknown for most of the ships present in the STEAM2 emissions, which were not specifically targeted during ACCESS. For these ships, exhaust parameters for the *Wilson Leer* (6000 gross tonnage) are used as a compromise between the smaller fishing ships (40 % of Arctic shipping emissions; Winther et al., 2014), and larger ships like the ones targeted during ACCESS. In the CTRL3 simulation, the four ships targeted during ACCESS are usually alone in a 3 km $\times$ 3 km grid cell, which enabled us to treat these ships separately and to inject their emissions in altitude using individual exhaust parameters (Sect. 5.2.4.1). In the CTRL simulation, there are usually several ships in the same 15 km $\times$ 15 km grid cell, and the four targeted ships were treated in the same way together with all unidentified ships, using the exhaust parameters of the *Wilson Leer* and local meteorological conditions to estimate injection heights. This means that, for the *Costa Deliziosa*, *Alaed* and *Wilson Nanjing*, the plume rise model is used in CTRL with exhaust parameters from a smaller ship (the *Wilson Leer*) than in CTRL3. Because of this, emission injection heights for these ships are lower in CTRL (0 to 30 m) than in CTRL3 (230 m for the *Costa Deliziosa*, 50 m for the *Wilson Nanjing*, 30 m for the *Wilson Leer*, and 65 m for the *Alaed*).

Primary aerosol emissions from STEAM2 (BC, OC, SO_4, and ash) are distributed into the eight MOSAIC aerosol bins in WRF-Chem, according to the mass size distribution measured in the exhaust of ships equipped with medium-speed diesel engines by Lyyränen et al. (1999). The submicron mode of this measured distribution is used to distribute primary BC, OC, and $SO_4^=$, while the coarse mode is used to distribute exhaust ash particles (represented as "other inorganics" in MOSAIC).

5.2.5 Ship emission evaluation

In this section, emissions of NO_x and SO_2 are determined for the four ships sampled during ACCESS flights (shown in Table 5.1). We compare airborne measurements in ship plumes and concentrations predicted by FLEXPART-WRF plume dispersion simulations. In order to derive emission fluxes, good agreement between measured and modeled plume locations is required (discussed in Sect. 5.2.5.1). The methods, derived emissions values for the four ships, and comparison with STEAM2 emissions are presented in Sect. 5.2.5.2.

5.2.5.1 Ship plume representation in FLEXPART-WRF and comparison with airborne measurements

FLEXPART-WRF plume dispersion simulations driven by the MET simulation are performed for the four ships sampled during ACCESS (Sect. 5.2.4.1). The MET simulation agrees well with airborne meteorological measurements on both days (shown in the Supplement, Fig. S1[1]) in terms of wind direction (mean bias of -16 on 11 July, $+6$ on 12 July) and wind speed (normalized mean bias of +14 % on 11 July,

[1] http://www.atmos-chem-phys.net/16/2359/2016/acp-16-2359-2016-supplement.pdf

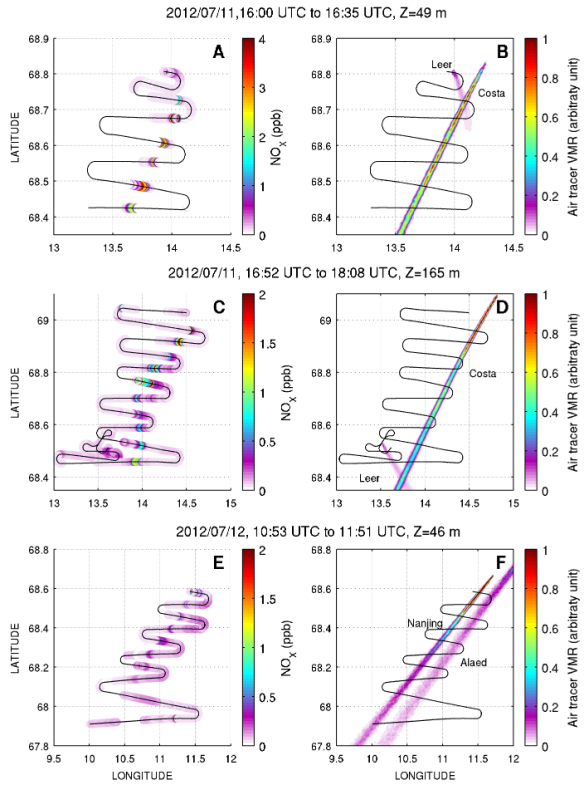

Figure 5-3 – Left panels: ACCESS airborne NO_x measurements between **(a)** 16:00 and 16:35 UTC, 11 July 2012 (flight leg at Z 49 m), **(c)** 16:52 and 18:08 UTC, 11 July 2012 (Z 165 m), and **(e)** 10:53 and 11:51 UTC, 12 July 2012 (Z 46 m). Right panels: corresponding FLEXPART-WRF plumes (relative air tracer mixing ratios): **(b, d)** *Wilson Leer* and *Costa Deliziosa* plumes and **(f)** *Wilson Nanjing* and *Alaed* plumes. FLEXPART-WRF plumes are shown for the closest model time step and vertical level.

−17 % on 12 July). Figure 5-3 shows the comparison between maps of the measured NO_x and plume locations predicted by FLEXPART-WRF. This figure also shows the typical meandering pattern of the plane during ACCESS, measuring the same ship plumes several times as they age, while moving further away from the ship (Roiger et al., 2015). *Wilson Leer* and *Costa Deliziosa* plumes were sampled during two different runs at two altitudes on 11 July 2012, and presented in Fig. 5-3a and b ($z = 49$ m) and Fig. 5-3c and d ($z = 165$ m). During the second altitude level on 11 July (Fig. 5-3c and d) the *Wilson Leer* was farther south and the *Costa Deliziosa* had moved further north. Therefore, the plumes are farther apart than during the first pass at 49 m. Modeled and measured plume locations agree well for the first run ($z = 49$ m). For the second run ($z = 165$ m), the modeled plume for the *Costa Deliziosa* is, on average, located 4.7 km to the west of the measured plume. This displacement is small considering that, at the end of this flight leg, the plume was being sampled 80 km away from its source. This displacement is caused by biases in the simulation (MET) used to drive the plume dispersion model (−16 for wind direction, +14 % for wind speed). On 12 July 2012, the aircraft targeted emissions from the *Wilson Nanjing* ship (Fig. 5-3e and f), but also sampled the plume of another ship, the *Alaed*. This

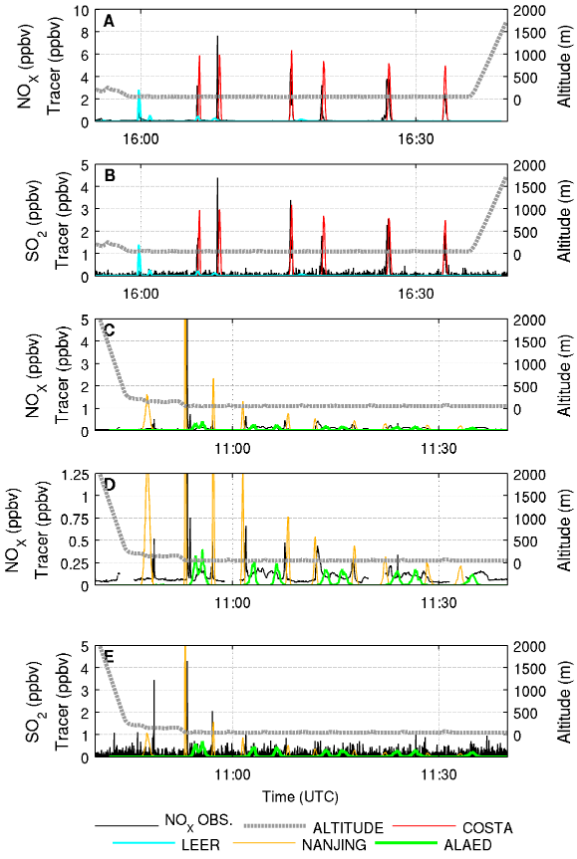

Figure 5-4 – **(a, c, d)** NO_x and **(b, e)** SO_2 aircraft measurements (black) compared to FLEXPART-WRF air tracer mixing ratios interpolated along flight tracks, for the plumes of the **(a, b)** *Costa Deliziosa* and *Wilson Leer* on 11 July 2012 (first constant altitude level (Z 49 m), also shown in Fig. 5-3a) and **(c, d, e)** *Wilson Nanjing* and *Alaed* on 12 July 2012. Panel **(d)** shows the same results as panel **(c)** in detail. Since model results depend linearly on the emission flux chosen a priori for each ship, model results have been scaled so that peak heights are comparable to the measurements.

last ship was identified during the post-campaign analysis, and we were able to extract its location and emissions from the STEAM2 inventory in order to perform the plume dispersion simulations shown here. The NO_x and FLEXPART-WRF predicted plume locations are in good agreement for both ships.

Modeled air tracer mixing ratios are interpolated in space and time to the aircraft location, and compared with airborne NO_x and SO_2 measurements (Fig. 5-4). Each peak in Fig. 5-4 corresponds to the aircraft crossing the ship plume once during the meandering pattern before turning around for an additional plume crossing. Figure 5-4a and b only show measurements for the first altitude level at $z = 49$ m on 11 July 2012 (results for the second altitude level are shown in the Supplement in Fig. S2[2]). As expected from the comparison shown in Fig. 5-3, modeled peaks are co-located with measured peaks in Fig. 5-4. The model is also able to reproduce the gradual decrease of concentrations measured in the

[2] `http://www.atmos-chem-phys.net/16/2359/2016/acp-16-2359-2016-supplement.pdf`

plume of the *Wilson Nanjing* on Fig. 5-4c–e, as the plane flies further away from the ship and the plume gets more dispersed. These peak concentrations vary less for the measured and modeled plume of the *Costa Deliziosa* (Fig. 5-4a and b). Measured plumes are less concentrated for the *Wilson Leer* since it is a smaller vessel, and for the *Alaed* because its emissions were sampled further away from their source.

5.2.5.2 Ship emission derivation and comparison with STEAM2

In this section, we describe the method for deriving ship emissions of NO_x and SO_2 using FLEXPART-WRF and measurements. This method relies on the fact that in the FLEXPART-WRF simulations presented in Sect. 5.2.4.1, there is a linear relationship between the constant emission flux of the tracer chosen for the simulation and the tracer concentrations in the modeled plume. The only source of non-linearity that cannot be taken into account is changes in the emission source strength, which is assumed to be constant in time for the plumes sampled. Given that the ship and meteorological conditions were consistent during sampling (shown in the Supplement, Fig. S1[3]), we expect that these effects would be very small. In our simulations, this constant emission flux is picked at $E = 0.1\ \mathrm{kg\,s^{-1}}$ and is identical for all ships. This initial value E is scaled for each ship by the ratio of the measured and modeled areas of the peaks in concentration corresponding to plume crossings, as shown in Fig. 5-4. Equation (1) shows how SO_2 emissions are derived by this method.

$$E_i = E \times \frac{\int_{t_i^{\mathrm{begin}}}^{t_i^{\mathrm{end}}} (\mathrm{SO_2}(t) - \mathrm{SO_2background})\mathrm{d}t}{\int_{t_i^{\mathrm{begin}}}^{t_i^{\mathrm{end}}} \mathrm{Tracer}(t)\mathrm{d}t} \times \frac{M_{\mathrm{SO_2}}}{M_{\mathrm{air}}} \tag{5.1}$$

In Eq. (1), $SO_2(t)$ is the measured SO_2 mixing ratio (pptv), SO_2background is the background SO_2 mixing ratio for each peak, Tracer(t) is the modeled tracer mixing ratio interpolated along the ACCESS flight track (pptv), t_i^{begin} and t_i^{end} are the beginning and end time of peak i (modeled or measured, in s) and $M_{\mathrm{SO_2}}$ and M_{air} are the molar masses of SO_2 and air ($\mathrm{g\,mol^{-1}}$). This method produces a different SO_2 emission flux value E_i ($\mathrm{kg\,s^{-1}}$) for each of the $i = 1$ to N peaks corresponding to all the crossings of a single ship plume by the aircraft. These N different estimates are averaged together to reduce the uncertainty in the estimated SO_2 emissions. A similar approach is used to estimate NO_x emissions. The background mixing ratios were determined by applying a 30 s running average to the SO_2 and NO_x measurements. Background values were then determined manually from the filtered time series. For each NO_x peak, an individual background value was identified and used to determine the NO_x enhancement for the same plume. For SO_2, a single background value was used for each flight leg (constant altitude).

In order to reduce sensitivity to the calculated emission injection heights, FLEXPART-WRF peaks that are sensitive to a ±50 % change in injection height are excluded from the analysis. Results are considered sensitive to injection heights if the peak area in tracer concentration changes by more than 50 % in the injection height sensitivity runs. Using a lower threshold of 25 % alters the final emission estimates by less than 6 %. Peaks sensitive to the calculated injection height typically correspond to samplings close to the ship, where the plumes are narrow. An intense SO_2 peak most likely associated with the *Costa Deliziosa* and sampled around 17:25 UTC on 11 July 2012 is also excluded from the calculations, because this large increase in SO_2 in an older, diluted part of the ship plume suggests contamination from another source. SO_2

[3] http://www.atmos-chem-phys.net/16/2359/2016/acp-16-2359-2016-supplement.pdf

emissions are not determined for the *Wilson Leer* and the *Alaed*, since SO_2 measurements in their plumes are too low to be distinguished from the background variability. For the same reason, only the higher SO_2 peaks (four peaks > 1ppbv) were used to derive emissions for the *Wilson Nanjing*. The number of peaks used to derive emissions for each ship is $N = 13$ for the *Costa Deliziosa*, $N = 4$ for the *Wilson Leer*, $N = 8$ for the *Wilson Nanjing* ($N = 4$ for SO_2) and $N = 5$ for the *Alaed*.

The derived emissions of NO_x (equivalent NO_2 mass flux in $kg\,day^{-1}$) and SO_2 are given in Table 5.4. The emissions extracted from the STEAM2 inventory for the same ships during the same time period are also shown. STEAM2 SO_2 emissions are higher than the value derived for the *Costa Deliziosa*, and lower than the value derived for the *Wilson Nanjing*. NO_x emissions from STEAM2 are higher than our calculations for all ships. In STEAM2, the NO_x emission factor is assigned according to IMO MARPOL (marine pollution) Annex VI requirements (IMO, 2008) and engine revolutions per minute (RPM), but all engines subject to these limits must emit less NO_x than this required value. For the *Wilson Leer*, two calculated values are reported: one calculated by averaging the estimates from the four measured peaks, and one value where an outlier value was removed before calculating the average. During the 11 July flight, the *Wilson Leer* was traveling south at an average speed of $4.5\,m\,s^{-1}$, with relatively slow tailwinds of $5.5\,m\,s^{-1}$. Because of this, the dispersion of this ship's plume on this day could be sensitive to small changes in modeled wind speeds, and calculated emissions are more uncertain.

The most important difference between the inventory NO_x and our estimates is 150 % for the *Costa Deliziosa*. Reasons for large discrepancy in predicted and measured NO_x emissions of *Costa Deliziosa* were investigated in more detail. A complete technical description of *Costa Deliziosa* was not available, but her sister vessel *Costa Luminosa* was described at length recently (RINA, 2010). The details of *Costa Luminosa* and *Costa Deliziosa* are practically identical and allow for in-depth analysis of emission modeling. With complete technical data, the STEAM2 SO_x and NO_x emissions of *Costa Deliziosa* were estimated to be 2684 and 5243 $kg\,d^{-1}$, respectively, whereas our derived estimates indicate 2399 and 2728 $kg\,d^{-1}$ (difference of +12 % for SO_x and +92 % for NO_x). The good agreement for SO_x indicates that the power prediction at vessel speed reported in AIS and associated fuel flow is well predicted by STEAM2, but emissions of NO_x are twice as high as the value derived from measurements. In case of *Costa Deliziosa*, the NO_x emission factor of $10.5\,g\,kW^{-1}\,h$ for a tier II compliant vessel with 500 RPM engine is assumed by STEAM2. Based on the measurement-derived value, a NO_x emission factor of $5.5\,g\,kW^{-1}\,h$ would be necessary, which is well below the tier II requirements. It was reported recently (IPCO, 2015) that NO_x emission reduction technology was installed on *Costa Deliziosa*, but it is unclear whether this technology was in place during the airborne measurement campaign in 2012.

The case of *Costa Deliziosa* underlines the need for accurate and up-to-date technical data for ships when bottom-up emission inventories are constructed. It also necessitates the inclusion of the effect of emission abatement technologies in ship emission inventories. Furthermore, model predictions for individual vessels are complicated by external contributions, like weather and sea currents, affecting vessel performance. However, the STEAM2 emission model is based on AIS real-time positioning data, which has a much better coverage than activity data sets used to generate older shipping emission inventories (e.g., COADS and AMVER). These earlier data sets also have known biases for ships of specific sizes or types. In addition, components of the

Table 5.4 – NO_x and SO_2 emissions estimated from FLEXPART-WRF and ACCESS measurements, compared with STEAM2 emissions. Values in parentheses indicate the relative difference between STEAM2 and calculated values. SO_2 emissions were not calculated for the *Wilson Leer* and *Alaed* since the measured SO_2 concentrations in the plumes were too low above background.

Ship name	NO_x calculated from measurements ($kg\,day^{-1}$)	NO_x from STEAM2 ($kg\,day^{-1}$)	SO_2 calculated from measurements ($kg\,day^{-1}$)	SO_x from STEAM2 ($kg\,day^{-1}$)
Costa Deliziosa	2728	6767/5243[a] (+148/+92 %[a])	2399	3285/2684[a] (+37/+12 %[a])
Wilson Leer	167/82[b]	287 (+72/+250 %[b])	NA	88 (NA)
Wilson Nanjing	561	602 (+7 %)	504	219 (−57 %)
Alaed	1362	1809 (+33 %)	NA	1130 (NA)

[a] The second value corresponds to STEAM2 calculations using complete technical data from the *Costa Deliziosa* sister ship *Costa Luminosa*.
[b] Value with outliers removed.

Table 5.5 – July emission totals in northern Norway (60.6–73 N, 0 to 31 W) of NO_x, SO_2, BC, OC, and $SO_4^=$ in different ship emission inventories.

Inventory	Year	NO_x (kt)	SO_2 (kt)	BC (t)	OC (t)	$SO_4^=$ (t)
STEAM2	2012	7.1	2.4	48.1	123.4	197.3
Winther et al. (2014)	2012	9.3	3.4	47.7	82.9	–
Dalsøren et al. (2009)	2004	3.1	1.9	7.3	24.5	–
Corbett et al. (2010)	2004	2.4	1.6	10.6	32.5	–
Dalsøren et al. (2007)	2000	5.5	1.1	24.	479.3	–

STEAM2 inventory, such as fuel consumption, engine loads, and emission factors have already been studied in detail in the Baltic Sea by Jalkanen et al. (2009, 2012) and Beecken et al. (2015). Beecken et al. (2015) compared STEAM2 emission factors to measurements for 300 ships in the Baltic Sea. Their results showed that, while important biases were possible for individual ships, STEAM2 performed much better on average for a large fleet. In the Baltic Sea, STEAM2 NO_x emission factors were found to be biased by +4 % for passenger ships, based on 29 ships, and −11 % for cargo ships, based on 118 ships. For SO_x, the biases were respectively +1 and +14 % for the same ships. Therefore, we expect that the large discrepancy in NO_x for one individual ship (the *Costa Deliziosa*) has only a small impact on the total regional emissions generated by STEAM2. The results presented later in Sect. 5.2.6.1 also indicate that STEAM2 likely performs better on average in the Norwegian Sea during ACCESS than for individual ships.

5.2.5.3 Comparison of STEAM2 to other shipping emission inventories for northern Norway

We compare in Table 5.5 the July emission totals for NO_x, SO_2, BC, OC and $SO_4^=$ in northern Norway (latitudes 60.6 to 73 N, longitudes 0 to 31 W) for STEAM2 and four other shipping emission inventories used in previous studies investigating shipping impacts in the Arctic. We include emissions from the Winther et al. (2014), Dalsøren et al. (2009, 2007), and Corbett et al. (2010) inventories. The highest shipping emissions in the region of northern Norway are found in the STEAM2 and Winther et al. (2014) inventories, which are both based on 2012 AIS ship activity data (Sect. 5.2.4.3 for a description of

the methodology used for STEAM2). We note that, except for OC, the emissions are higher in the Winther et al. (2014) inventory because of the larger geographical coverage: Winther et al. (2014) used both ground-based and satellite retrieved AIS signals, whereas the current study is restricted to data received by ground based AIS stations (capturing ships within 50 to 90 km of the Norwegian coastline). Despite lower coverage, the horizontal and temporal resolutions are better described in land-based AIS networks than satellite AIS data. The terrestrial AIS data used in this study is thus more comparable to the spatial extent and temporal resolution of the measurements collected close to the Norwegian coast. STEAM2 is the only inventory including sulfate emissions, which account for SO_2 to $SO_4^=$ conversion in the ship exhaust. Ship emissions from Dalsøren et al. (2009) and Corbett et al. (2010) are based on ship activity data from 2004, when marine traffic was lower than in 2012. Furthermore, the gridded inventory from Corbett et al. (2010) does not include emissions from fishing ships, which represent close to 40 % of Arctic shipping emissions (Winther et al., 2014). These emissions could not be precisely distributed geospatially using earlier methodologies, since fishing ships do not typically follow a simple course (Corbett et al., 2010). Dalsøren et al. (2007) emissions for coastal shipping in Norwegian waters are estimated based on Norwegian shipping statistics for the year 2000, and contain higher NO_x, BC, and OC emissions, but less SO_2, than the 2004 inventories. This comparison indicates that earlier ship emission inventories usually contain lower emissions in this region, which can be explained by the current growth in shipping traffic in northern Norway. This means that up-to-date emissions are required in order to assess the current impacts of shipping in this region.

5.2.6 Modeling the impacts of ship emissions along the Norwegian coast

In this section, WRF-Chem, using STEAM2 ship emissions, is employed to study the influence of ship pollution on atmospheric composition along the Norwegian coast, at both the local (i.e., at the plume scale) and regional scale. As shown in Fig. 5-4, shipping pollution measured during ACCESS is inhomogeneous, with sharp NO_x and SO_2 peaks in thin ship plumes, emitted into relatively clean background concentrations. The measured concentrations are on spatial scales that can only be reproduced using very high-resolution WRF-Chem simulations (a few kilometers of horizontal resolution), but such simulations can only be performed for short periods and over small domains. Therefore, high-resolution simulations cannot be used to estimate the regional impacts of shipping emissions. In order to bridge the scale between measurements and model runs that can be used to make conclusions about the regional impacts of shipping pollution, we compare in Sect. 5.2.6.1 WRF-Chem simulations using STEAM2 ship emissions, at 3 km $\times$ 3 km resolution (CTRL3) and at 15 km $\times$ 15 km resolution (CTRL). Specifically, we show in Sect. 5.2.6.1 that both the CTRL3 and CTRL simulations reproduce the average regional influence of ships on NO_x, O_3, and SO_2, compared to ACCESS measurements. In Sect. 5.2.6.2 we use the CTRL simulation to quantify the regional contribution of ships to surface pollution and shortwave radiative fluxes in northern Norway.

5.2.6.1 Model evaluation from the plume scale to the regional scale

It is well known that ship plumes contain fine-scale features that cannot be captured by most

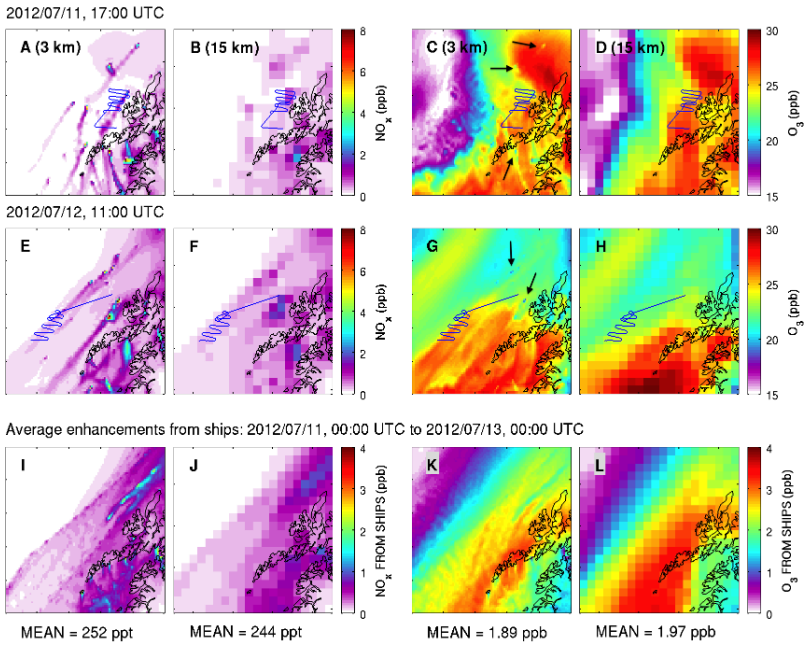

Figure 5-5 – Snapshots of model predicted surface NO_x and O_3 from the CTRL3 (3 km) simulation **(a, c, e, g)** and the CTRL (15 km) simulation **(b, d, f, h)** during the flights on 11 and 12 July 2012. Model results for the CTRL3 simulation are shown over the full model domain. CTRL run results are shown over the same region for comparison. The aircraft flight tracks are indicated in blue. On panels **(c)** and **(g)**, black arrows indicate several areas of O_3 titration due to high NO_x from ships. **(i, j)** NO_x and **(k, l)** O_3 2-day average surface enhancements (00:00 UTC 11 July 2012 to 00:00 UTC 13 July 2012) due to shipping emissions, **(i, k)** CTRL3 simulation, **(j, l)** CTRL simulation. The 2-day average enhancements of NO_x and O_3 over the whole area are given below each respective panel.

regional or global chemical transport models. This fine plume structure influences the processing of ship emissions, including O_3 and aerosol formation, which are non-linear processes that largely depend on the concentration of species inside the plume. Some models take into account the influence of the instantaneous mixing of ship emissions in the model grid box by including corrections to the O_3 production and destruction rates (Huszar et al., 2010) or take into account plume ageing before dilution by using corrections based on plume chemistry models (Vinken et al., 2011). Here, we take an alternative approach by running the model at a sufficient resolution to distinguish individual ships in the Norwegian Sea (CTRL3 run at 3 km × 3 km resolution), and at a lower resolution (CTRL run at 15 km × 15 km resolution). It is clear that a 3 km × 3 km horizontal resolution is not sufficiently small to capture all small-scale plume processes. However, by comparing the CTRL3 simulation to ACCESS measurements, we show in this section that this resolution is sufficient to resolve individual ship plumes and to reproduce some of the plume macroscopic properties. The CTRL and CTRL3 simulations (presented in Table 5.3) are then compared to evaluate if non-linear effects are important for this study period and region.

WRF-Chem results from CTRL and CTRL3 for surface (0 to 30 m) NO_x and O_3 are shown in Fig. 5-5. On 11 and 12 July, the aircraft specif-

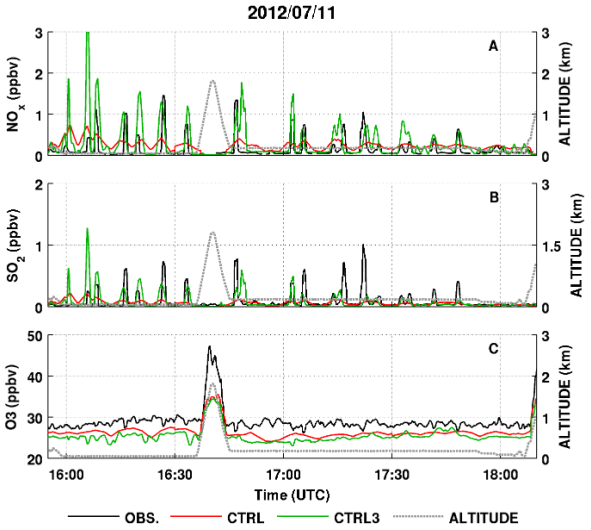

Figure 5-6 – Time series of measured O_3 and NO_x on 11 July 2012 compared to model results extracted along the flight track for the CTRL and CTRL3 runs. Observations are in black, the CTRL run is in red, and the CTRL3 run is in green. A 56 s averaging window is applied to the measured data for model comparison (approximately the time for the aircraft to travel 2×3 km). Flight altitude is given as a dashed gray line. After the first run at 49 m, a vertical profile was performed (16:35 to 16:45 UTC) providing information about the vertical structure of the boundary layer.

ically targeted plumes from the *Wilson Leer*, *Costa Deliziosa*, *Wilson Nanjing* and, in addition, sampled emissions from the *Alaed*, identified later during the post-campaign analysis (Fig. 5-3). All these ships are individually present in the STEAM2 emissions inventory (Sect. 5.2.5 and Table 5.4). Emissions from these ships, as well as from other vessels traveling in that area, are clearly resolved in the CTRL3 model results for NO_x (Fig. 5-5a and e). Ship NO_x emissions are smoothed out in the CTRL run, seen in Fig. 5-5b and f, and the individual ship plumes cannot be clearly distinguished in the NO_x surface concentrations. The predicted surface O_3 concentrations are shown in Fig. 5-5c, d, g, and h. On the 11 and 12 July 2012, titration of O_3 by NO_x from fresh ship emissions can be identified in Fig. 5-5c and g for the 3 km run (areas indicated by black arrows on Fig. 5-5c and g). However, evidence for O_3 titration quickly disappears away from the fresh emissions sources. In contrast, O_3 titration is not apparent in the CTRL run. However, NO_x and O_3 patterns and average surface concentrations are very similar. This is illustrated in the lower panels, showing 2-day-averaged NO_x and O_3 enhancements due to ships in the CTRL3 (CTRL3 – NOSHIPS3) and CTRL (CTRL – NOSHIPS) simulations. The results show that changing the horizontal resolution from 3 km $\times$ 3 km (1 km $\times$ 1 km emissions, 15 min emissions injection) to 15 km $\times$ 15 km (5 km $\times$ 5 km emissions, 1 h emissions injection) does not have a large influence on the domain-wide average NO_x (-3.2 %) or O_3 ($+0.08$ppbv, $+4.2$ %) enhancements due to ships. This is in agreement with earlier results by Cohan et al. (2006), who showed that regional model simulations at similar resolutions (12 km) were sufficient to reproduce the average O_3 response. Results by Vinken et al. (2011) suggest that simulations at

a lower resolution more typical of global models (2 × 2.5) would lead to an overestimation of O_3 production from ships in this region by 1 to 2ppbv. The influence of model resolution on surface aerosol concentrations is also moderate, and PM_{10} due to ships are 15 % lower on average in CTRL than in CTRL3 (not shown here).

To further investigate the ability of these different model runs to represent single ship plumes, we compare measured NO_x, SO_2, and O_3 along the flight track on 11 July 2012 with WRF-Chem predictions (Fig. 5-6). Corresponding results for 12 July 2012 are shown in the Supplement (Fig. S3[4]). Large enhancements of NO_x and SO_2 are seen during plume crossings in measurements, as already noted in Sect. 5.2.5. For comparison with WRF-Chem, we have averaged the measured data using a 56 s running average, equivalent to the aircraft crossing 6 km (two model grid cells) at its average speed during this flight (107 $m\,s^{-1}$). Using a running average takes into account plume dilution in grid cells, as well as additional smoothing introduced when modeled results are spatially interpolated onto the flight track. The CTRL3 simulation captures both the width and magnitude of NO_x and SO_2 peaks, suggesting that the individual plumes are correctly represented in space and time. During the second part of the flight (17:20 UTC), the model does not reproduce two intense measured SO_2 peaks. We already noted in Sect. 5.2.5.2 that measurements in this part of the flight might be contaminated by another source. In contrast, the CTRL run has wider NO_x and SO_2 peaks and lower peak concentrations, because of dilution in larger grids. Another difference between the simulations is the treatment of plume rise (Sect. 5.2.4.3), such that the *Costa Deliziosa* plume is located at lower altitudes in CTRL than in CTRL3. The CTRL3 simulation tends to overestimate NO_x in ship plumes, which is in agreement with the results shown in Table 5.4, indicating that STEAM2 NO_x emissions are overestimated for the ships targeted during ACCESS. This overestimation is unlikely to be caused by chemistry issues, since an overestimated NO_x lifetime would lead to comparatively larger biases at the end of the constant altitude runs, when older parts of the plume were sampled. Figure 5-6b shows O_3 during the same flight. The CTRL3 simulation reproduces the ozone variability better than the CTRL run, but both runs perform relatively well on average (mean bias $= -3$ppbv during the constant altitude legs). This negative bias is due to a small underestimation in the background ozone, which could be caused by a number of reasons, including the boundary chemical conditions from the MOZART4 model, photolysis rates, cloud properties and locations, ozone deposition, and/or emissions. Both measurements and CTRL3 results show evidence of O_3 titration in the most concentrated NO_x plumes, where ozone is 1.5 to 3ppbv lower than out of the plumes. However, precise quantification of this titration is difficult because these values are the same order of magnitude as the spatial variability of O_3 outside of the plumes. O_3 titration is not apparent in the CTRL run. Results are similar for the 12 July 2012 flight (shown in the Supplement, Fig. S3[5]), with lower model biases for O_3 but a stronger overestimation of NO_x.

In order to evaluate modeled aerosols in ship plumes, modeled aerosols are evaluated using size distributions measured during the 11 July 2012 flight. Size distributions are integrated to estimate submicron aerosol mass (PM_1), assuming a density of 1700 $kg\,m^{-3}$ and spherical particles. This indicates that observed PM_1 enhancements in plumes (0.1 to 0.5 $\mu g\,m^{-3}$) are relatively low compared to background PM_1 (0.7 to 1.1 $\mu g\,m^{-3}$), because of the presence of high sea salt concentrations in the marine boundary layer

[4] http://www.atmos-chem-phys.net/16/2359/2016/acp-16-2359-2016-supplement.pdf
[5] http://www.atmos-chem-phys.net/16/2359/2016/acp-16-2359-2016-supplement.pdf

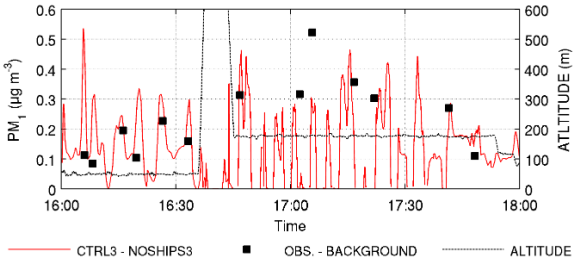

Figure 5-7 – Observed background-corrected PM_1 enhancements in the plume of the *Costa Deliziosa* on 11 July 2012 (black squares), compared to modeled PM_1 enhancements in ship plumes (in red), extracted along the flight track (CTRL3 – NOSHIPS3 PM_1). A 56 s averaging window is applied to the measured data to simulate dilution in the model grid. Flight altitude is given as dashed black line.

(54 % of the modeled background PM_1 during ship plume sampling is sea salt in NOSHIPS3). Because of this, comparing modeled and observed in-plume PM_1 directly would be mostly representative of background aerosols, especially sea salt, which is not the focus of this paper. Figure 5-7 shows the comparison between modeled and measured enhancements in PM_1 in the plume of the *Costa Deliziosa* (11 July 2012), removing from the model and measurements the contribution from sea salt and other aerosols not associated with shipping. Similarly to Fig. 5-6, a 56 s moving average was applied to the measurement (representing plume dilution in the model grid). This comparison indicates a generally good agreement between modeled and measured PM_1 enhancements in ship plumes. There is a discrepancy between the model and the measurements for the first two PM_1 plumes measured close to the ships (around 16:05 UTC), which could be an artifact of the limited resolution of this simulation (3 km). If these peaks are excluded, the model slightly overestimates peak PM_1 enhancements in ship plumes (+26 %). Since this enhancement is modeled as 80 % $SO_4^=$, this overestimation can be linked to the +37 % overestimation of SO_2 emissions for the *Costa Deliziosa* in STEAM2 (Table 5.4).

Analysis of O_3 maps, average surface enhancements due to ships (Fig. 5-5) and analysis of model results along flight tracks (Fig. 5-6) show that both runs capture the NO_x and O_3 concentrations in this region reasonably well. Furthermore, Fig. 5-7 shows that PM_1 enhancements in ship plumes are well reproduced in the CTRL3 simulation, and we found that PM_{10} production from ships over the simulation domain was not very sensitive to resolution. This suggests that the CTRL simulation is sufficient to assess the impacts of ship emissions at a larger scale during July 2012. This is investigated further by comparing modeled NO_x, SO_2, and O_3 in the CTRL and NOSHIPS simulations with the average vertical profiles (200–1500 m) measured during four ACCESS flights from 11 to 25 July 2012 (flights shown in Fig. 5-1a); this comparison is shown in Fig. 5-8. Modeled vertical profiles of $PM_{2.5}$ are also shown in Fig. 5-8. This comparison allows us to estimate how well CTRL represents the average impact of shipping over a larger area and a longer period.

Figure 5-8 shows that the NOSHIPS simulation significantly underestimates NO_x and SO_2, and moderately underestimates O_3 along the ACCESS flights, indicating that ship emissions are needed to improve the agreement between the model and observations. In the CTRL simulation, NO_x, SO_2, and O_3 vertical structure and concentrations are generally well reproduced, with normalized mean biases of +14.2, −6.8, and

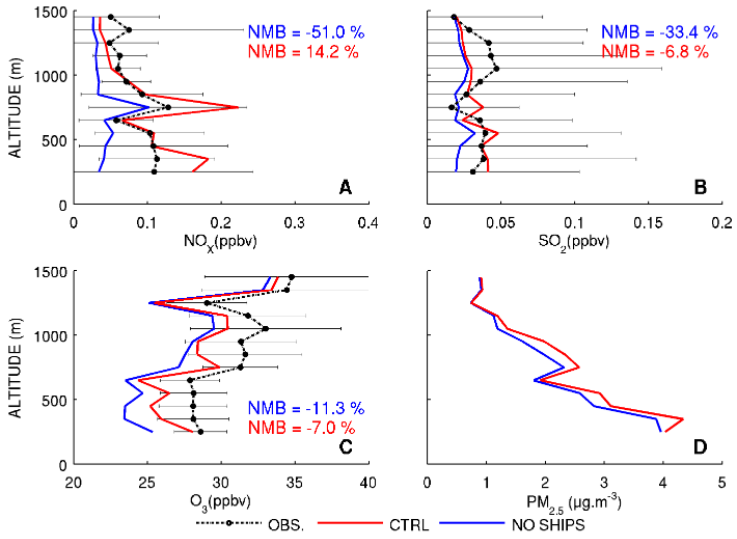

Figure 5-8 – Average vertical profiles of **(a)** NO_x, **(b)** SO_2, **(c)** O_3 and **(d)** $PM_{2.5}$ observed during the four ACCESS ship flights (in black, with error bars showing standard deviations), and interpolated along the ACCESS flight tracks in the CTRL simulation (red line) and in the NOSHIPS simulation (blue line). For $PM_{2.5}$ only simulation results are shown.

−7.0 %, respectively. Correlations between modeled (CTRL) and measured profiles are significant for NO_x and O_3 ($r^2 = 0.82$ and 0.90). However, the correlation is very low between measured and modeled SO_2 ($r^2 = 0.02$), and it is not improved compared to the NOSHIPS simulation. Ships have the largest influence on NO_x and SO_2 profiles, a moderate influence on O_3 and do not strongly influence $PM_{2.5}$ profiles along the ACCESS flights. However, this small increase in $PM_{2.5}$ corresponds to a larger relative increase in sulfate concentrations and in particle numbers in the size ranges typically activated as cloud condensation nuclei (shown in Fig. S4 in the Supplement[6]).

NO_x concentrations are overestimated in the parts of the profile strongly influenced by shipping emissions. This is in agreement with the findings of Sect. 5.2.5.2, showing that STEAM2 NO_x emissions were overestimated for the ships sampled during ACCESS. However, the CTRL simulation performs well on average, suggesting that the STEAM2 inventory is able to represent the average NO_x emissions from ships along the northern Norwegian coast during the study period. The bias for SO_2 is very low compared to results from Eyring et al. (2007), which showed that global models significantly underestimated SO_2 in the polluted marine boundary layer in July. Since aerosols from ships contain mostly secondary sulfate formed from SO_2 oxidation, the validation of modeled SO_2 presented in Fig. 5-8 also gives some confidence in our aerosol results compared to earlier studies investigating the air quality and radiative impacts of shipping aerosols. We therefore use the 15 km × 15 km CTRL run for further analysis of the regional influence of ships on pollution and the shortwave radiative effect in this region in Sect. 5.2.6.2.

[6] http://www.atmos-chem-phys.net/16/2359/2016/acp-16-2359-2016-supplement.pdf

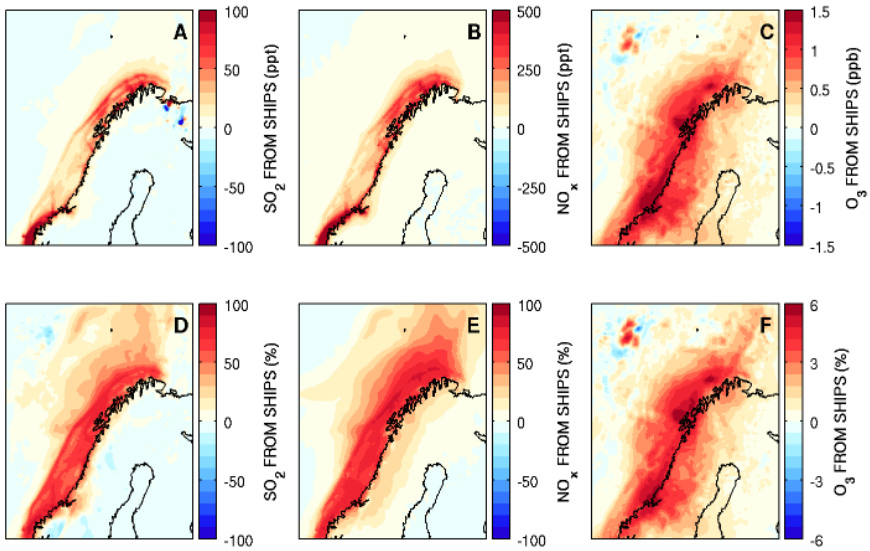

Figure 5-9 – 15-day average (00:00 UTC 11 July 2012 to 00:00 UTC 26 July 2012) of (top) absolute and (bottom) relative surface enhancements (CTRL – NOSHIPS) in **(a, d)** SO_2, **(b, e)** NO_x, and **(c, e)** O_3 due to ship emissions in northern Norway from STEAM2.

5.2.6.2 Regional influence of ship emissions in July 2012

5.2.6.2.1 Surface air pollution from ship emissions in northern Norway

The regional-scale impacts of ships on surface atmospheric composition in northern Norway are estimated by calculating the 15-day (00:00 UTC, 11 July 2012 to 00:00 UTC, 26 July 2012) average difference between the CTRL and NOSHIPS simulations. Figure 5-9 shows maps of these anomalies at the surface, for SO_2, NO_x, and O_3. Ship emissions have the largest influence on surface NO_x and SO_2 concentrations, with 75 to 100 % increases along the coast. Average O_3 increases from shipping are 6 % (1.5ppbv) in the coastal regions, with slightly lower enhancements (1ppbv, 4 %,) further inland over Sweden.

Dalsøren et al. (2007) studied the impact of maritime traffic in northern Norway in the summer using ship emission estimates for the year 2000. They found, for July 2000, a 1 to 1.5 % increase in surface O_3 from coastal shipping in Norwegian waters. However, unlike the present study, the estimate of Dalsøren et al. (2007) did not include the impact of international transit shipping along the Norwegian coast. Our estimated impact on O_3 in this region (6 % and 1.5ppbv increase) is about half of the one determined by Ødemark et al. (2012) (12 % and 3ppbv), for the total Arctic fleet in the summer (June–Aug–Sept) 2004, using ship emissions for the year 2004 from Dalsøren et al. (2009). It is important to note that we expect lower impacts of shipping in studies based on earlier years, because of the continued growth of shipping emissions along the Norwegian coast (as discussed in Sect. 5.2.5.3 and illustrated in Table 5.5). However, stronger or lower emissions do not seem to completely explain the different modeled impacts. Ødemark et al. (2012) found that Arctic ships had a strong influence on surface O_3 in northern Norway for relatively low 2004 shipping emissions. This could be explained by the different processes included in both models, or by dif-

ferent meteorological situations in the two studies based on two different meteorological years (2004 and 2012). However, it is also likely that the higher O_3 in the Ødemark et al. (2012) study could be caused, in part, by nonlinear effects associated with global models run at low resolutions. For example Vinken et al. (2011) estimated that instant dilution of shipping NO_x emissions in 2 $\times$ 2.5 model grids leads to a 1 to 2ppbv overestimation in ozone in the Norwegian and Barents seas during July 2005. This effect could explain a large part of the difference in O_3 enhancements from shipping between the simulations of Ødemark et al. (2012) (2.8 $\times$ 2.8 resolution) and the simulations presented in this paper (15 km $\times$ 15 km resolution).

The impact of ships in northern Norway on surface $PM_{2.5}$, BC, and $SO_4^=$ during the same period is shown in Fig. 5-10. The impact on $PM_{2.5}$ is relatively modest, less than 0.5 µg m^{-3}. However, these values correspond to an important relative increase of 10 % over inland Norway and Sweden because of the low background $PM_{2.5}$ in this region. Over the sea surface, the relative effect of ship emissions is quite low because of higher sea salt aerosol background. Aliabadi et al. (2015) have observed similar increases in $PM_{2.5}$ (0.5 to 1.9 µg m^{-3}) in air masses influenced by shipping pollution in the remote Canadian Arctic. In spite of the higher traffic in northern Norway, we find lower values than Aliabadi et al. (2015) because results in Fig. 5-10 are smoothed by the 15-day average. Impacts on surface sulfate and BC concentrations are quite large, reaching up to 20 and 50 %, respectively. We note that Eckhardt et al. (2013) found enhancements in summertime equivalent BC of 11 % in Svalbard from cruise ships alone. As expected, absolute $SO_4^=$ and BC enhancements in our simulations are higher in the southern part of the domain, where ship emissions are the strongest. We estimated the lifetime (residence time) of BC originating from ship emissions using the method presented in Samset et al. (2014). This residence time is defined as the ratio of the average BC burden from ships divided by the average BC emissions in STEAM2 during the simulation. Using this method, we find a BC lifetime of 1.4 days. This short lifetime can be explained by the negative sea level pressure anomalies over northern Norway during the ACCESS campaign (Roiger et al., 2015), which indicates more rain and clouds than normal during summer. Given this short lifetime, BC is not efficiently transported away from the source region.

5.2.6.2.2 Shortwave radiative effect of ship emissions in northern Norway

The present-day climate effect of ship emissions is mostly due to aerosols, especially sulfate, which cool the climate through their direct and indirect effects (Capaldo et al., 1999). However, large uncertainties still exist concerning the magnitude of the aerosol indirect effects (Boucher et al., 2013). In this section, we determine the total shortwave radiative effect of ships by calculating the difference between the top-of-atmosphere (TOA) upwards shortwave (0.125 to 10 µm wavelengths) radiative flux in the CTRL and the NOSHIPS simulations. Since the CTRL and NOSHIPS simulations take into account aerosol–radiation interactions and their feedbacks (the so-called direct and semi-direct effects) as well as cloud–aerosol interactions (indirect effects), this quantity represents the sum of modeled direct, semi-direct and indirect effects from aerosols associated with ship emissions. Yang et al. (2011) and Saide et al. (2012) showed that including cloud aerosol couplings in WRF-Chem improved significantly the representation of simulated clouds, indicating that the indirect effect was relatively well simulated using CBM-Z/MOSAIC chemistry within WRF-Chem. Our calculations do not include the effect of BC on snow, since this effect

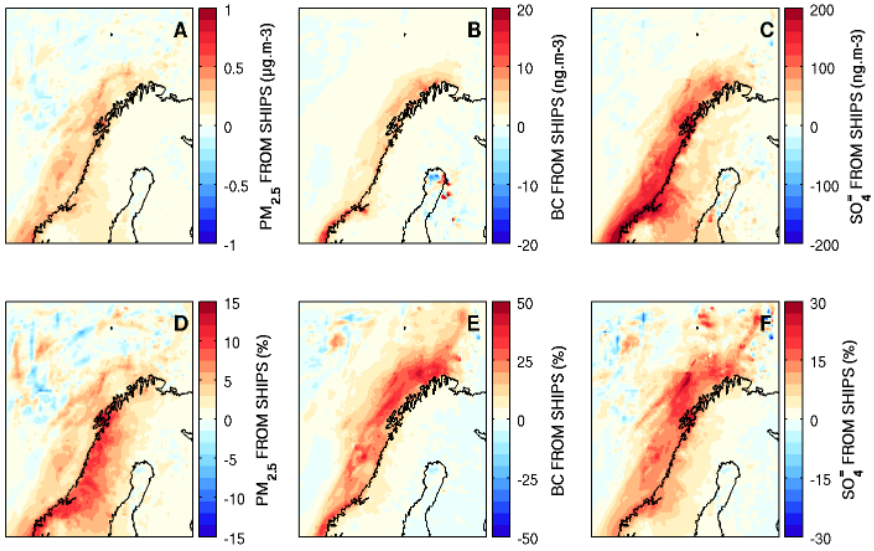

Figure 5-10 – 15-day average (00:00 UTC 11 July 2012 to 00:00 UTC 26 July 2012) of (top) absolute and (bottom) relative surface enhancements (CTRL – NOSHIPS) in **(a, d)** $PM_{2.5}$, **(b, e)** BC and **(c, f)** $SO_4^=$ due to ship emissions in northern Norway from STEAM2.

is not currently included in WRF-Chem.

The shortwave radiative effect at TOA of in-domain ship emissions is -1.77 W m^{-2} (15-day average). We multiply this value by the area of our simulation domain to obtain a forcing value in watts (W), and divide it by the surface area of the Earth in order to obtain an equivalent global radiative effect in mW m^{-2} that can be compared to results from global studies. This equivalent global radiative effect at TOA is -9.3 mW m^{-2}. This value is strongly negative, indicating that ship emissions cause a net cooling effect in this region (likely due to sulfate) despite the strong relative increase in BC concentrations from shipping emissions (up to +50 %, Fig. 5-10). This can be explained by the fact that these strong relative enhancements in BC correspond to low absolute values (at most 20 ng m^{-3}) above very low background concentrations.

The radiative effect calculated in this study, -9.3 mW m^{-2}, is similar to the estimate by Ødemark et al. (2012), who found a direct and indirect shortwave effect of aerosols from Arctic-wide shipping in July 2004 of -10.4 mW m^{-2}. However, since the present study only represents the effect of shipping along the Norwegian coast, this implies that current ship emissions in northern Norway have a stronger effect in this study than in Ødemark et al. (2012), which was based on ship emissions from Dalsøren et al. (2009) corresponding to 24 % less SO_2 emissions than STEAM2. Higher emissions in our simulations could explain the stronger local shortwave effect of Arctic ships, since this effect is mostly associated with the direct and indirect effect of sulfate aerosols. However, the total sulfate column due to ship emissions in our study is 100 to 200 µg m^{-2} along the Norwegian coast, about half of the value (250 to 300 µg m^{-2}) found by Ødemark et al. (2012). This means that the stronger effect found here is not due to increased sulfate concentrations from larger emissions, but is likely due to the way aerosol–cloud interactions are treated in both models: the indirect aerosol effect was calculated by Ødemark et al. (2012) based on parameteriza-

tions of the relationship between clouds droplet numbers and aerosol mass, whereas the MOSAIC aerosol module used in this study explicitly treats aerosol activation within clouds and their impacts on cloud properties (Yang et al., 2011). It is also important to note here that the indirect radiative effect of shipping emissions is uncertain and that the difference between the estimate of Ødemark et al. (2012) and the one in this work can also be explained by these uncertainties. Based on the work of Eyring et al. (2007), Lauer et al. (2007), and Fuglestvedt et al. (2008), Eyring et al. (2010) estimated that the radiative forcing of global shipping emissions was -0.408 W m^{-2}, but found an uncertainty range of ± 0.425 W m^{-2}. Ødemark et al. (2012) considered that the uncertainty in the indirect effect in their simulations was the same as the uncertainty in the global indirect forcing of aerosols as estimated by the IPCC (Forster et al., 2007, Table 2.12). Using this method, Ødemark et al. (2012) estimated a range of $[-3.9$ mW m^{-2}, -1.3 mW m$^{-2}]$ for the global and annual indirect effect of Arctic shipping emissions. It is important to better understand and constrain this effect, which would require more aerosol measurements in shipping lanes (including number concentrations and aerosol compositions in ship plumes) and more model case studies.

5.2.7 Conclusions

The focus of this work, linking modeling and measurements, is to better quantify regional atmospheric impacts of ships in northern Norway in July 2012. The study relies on measurements from the ACCESS aircraft campaign, emissions evaluation, and regional modeling in order to evaluate both individual ship plumes and their regional-scale effects. STEAM2 emissions, which represent individual ships based on high-resolution AIS ship positioning data, are compared with emissions for specific ships derived from measurements and plume dispersion modeling using FLEXPART-WRF. Regional WRF-Chem simulations run with and without ship emissions are performed at two different resolutions to quantify the surface air quality changes and radiative effects from ship emissions in northern Norway in July 2012. The most important conclusions from our study are

1. *Validation of the STEAM2 emissions* – emissions of NO_x and SO_2 are determined for individual ships, by comparing airborne measurements with plume dispersion modeling results. These calculated emissions are compared with bottom-up emissions determined for the same ships by the STEAM2 emission model. Results show that STEAM2 overestimates NO_x emissions for the four ships sampled during ACCESS. SO_2 emissions are also determined for two ships. Large biases are possible for individual ships in STEAM2, especially for ships for which there is incomplete technical data or where emission reduction techniques have been employed. Nevertheless, combining WRF-Chem simulations and STEAM2 emissions leads to reasonable predictions of NO_x, SO_2, and O_3 compared to ACCESS profiles in the lower troposphere (normalized mean biases of $+14.2$, -6.8, and -7.0 %, respectively). These results also indicate that shipping emissions comprise a significant source of NO_x and SO_2 at low altitudes during the ACCESS flights, even though specific ship plume sampling near the surface was excluded from these profiles. Pollution sampled during these flights thus represents shipping pollution that had time to mix vertically in the marine boundary layer and is more representative of the regional pollution from shipping in northern Norway. These results are in agreement with the recent evaluation of STEAM2 in the Baltic Sea by Beecken et al. (2015), which

showed that STEAM2 performed well for an average fleet (200 ships), despite biases for individual ships.

2. *Regional model representation of ship plumes and their local-scale influence* – WRF-Chem runs including shipping emissions from STEAM2 are performed at 15 km × 15 km and 3 km × 3 km horizontal resolutions, and compared with airborne measurements of NO_x and ozone. The high-resolution simulation is better at reproducing measured NO_x peaks and suggests some ozone titration in ship plumes, but the NO_x and ozone enhancements due to ships in both simulations are within less than 5 % of each other when averaged over the whole domain and simulation period. The 3 km × 3 km simulation also reproduces observed PM_1 enhancements in ship plumes. Surface PM_{10} enhancements due to ships are 15 % higher in the 3 km × 3 km resolution simulation.

3. *Average influence of ship pollution in July 2012* – the difference between runs with and without ship emissions are compared with campaign average profiles (excluding flights focused on oil platforms, smelters, and biomass burning emissions from outside the simulation domain). Including STEAM2 emissions reduces the mean bias between measured and modeled trace gases NO_x, SO_2, and O_3. At the surface, ship emissions enhance 15-day-averaged concentrations along the Norwegian coast by approximately 80 % for NO_x, 80 % for SO_2, 5 % for O_3, 40 % for BC, and 10 % for $PM_{2.5}$, suggesting that these emissions are already having an impact on atmospheric composition in this region. Regional model results presented in this study predict lower ozone production from ships compared to certain earlier studies using global models. However, it is known that global models run at low resolution tend to overestimate ozone production (underestimate ozone titration) from fresh ship emissions because of nonlinearities introduced when diluting concentrated emissions from ships into coarse model grid cells.

4. *Influence on the radiative budget* – northern Norwegian ship emissions contribute $-9.3\ \mathrm{mW\,m^{-2}}$ to the global shortwave radiative budget of ship emissions, including semi-direct and indirect effects. These results are more significant than found previously in a study using a global model that did not explicitly resolve aerosol activation in clouds. This suggests that global models may be underestimating the radiative impacts of shipping in this region.

Our study shows that local shipping emissions along the northern Norwegian coast already have a significant influence on regional air quality and aerosol shortwave radiative effects. As Arctic shipping continues to grow and new regulations are implemented, the magnitude of these impacts is expected to change. Due to the limited region (northern Norway) and the short timescale (15 days) considered here, it is not possible to assess the radiative effect of other climate forcers associated with shipping in northern Norway, including O_3 which global model studies have suggested are also significant (Dalsøren et al., 2013; Ødemark et al., 2012). However, since shipping emissions are highly variable and localized, quantifying impacts using global models can be challenging. Our approach used a regional chemical-transport model at different scales, with high-resolution ship emissions, to evaluate model results against observations and estimate the regional impact of shipping emissions. In the future, additional work is needed in other regions and at different spatial scales (measurements and modeling) in order to investigate the impacts of shipping over the wider Arctic area.

5.3 Main insights from the study

Local sources of aerosol and ozone pollution in the Arctic are thought to be rather small, but are expected to grow along with future Arctic warming and sea-ice loss. In particular, the decline in sea-ice should unlock the Arctic Ocean to human activity, and Arctic shipping emissions are expected to increase. Trans-Arctic shipping (Northern Sea Route information office, 2013) and Arctic cruise tourism (Stewart et al., 2009) are already thought to be on the rise . Currently, Arctic shipping emissions are estimated to be highest along the Norwegian and Western Russian coasts. However, there was, until the recent ACCESS aircraft campaign in summer 2012, no dedicated measurement dataset to study the impacts of these emissions. In this Chapter, WRF-Chem simulations at 15 km $\times$ 15 km and 3 km $\times$ 3 km horizontal resolutions are combined with a new shipping emission inventory created for this study (by researchers at the Finnish Meteorological Institute) using the emission model STEAM2 . These simulations are used to analyze measurements from the ACCESS aircraft campaign, in order to evaluate the current effect of shipping emissions in this region on aerosol and ozone concentrations and aerosol radiative effects.

This study shows that WRF-Chem simulations at a 15 km $\times$ 15 km horizontal resolution are able to reproduce meteorological conditions observed during the ACCESS campaign, as well as the average observed profiles of SO_2, O_3 and NO_x in the polluted marine boundary layer. SO_2 comparisons are improved compared to earlier model intercomparisons in similar conditions (Eyring et al., 2007). This improvement might be due, in part, to the detailed shipping emission inventory used and, in part, to the representation of the SO_2 source from DMS, which appears to constitute most of the background concentrations.

Model results also indicate that WRF-Chem simulations compare relatively well with measurements, at both plume-resolving (3 km $\times$ 3 km) and non-plume-resolving (15 km $\times$ 15 km) scales. Modeled enhancements of PM_{10} and O_3 from ships do not appear to be significantly affected by this change in resolution, but it is not certain from this study how well shipping impacts would be represented by simulations at even lower resolutions (100 km $\times$ 100 km in Chapter 6). For example, Cohan et al. (2006) found little sensitivity of O_3 production in an urban area to horizontal resolution when comparing runs at 4 km and 12 km resolutions, but showed that simulations at a 36 km resolution did not perform as well.

This study also aimed to validate the new STEAM2 AIS shipping emission inventory of Jalkanen et al. (2012), by comparing it to emissions of NO_x and SO_2 derived for individual ships measured during ACCESS. This comparison shows that, for individual ships, very large differences are possible between STEAM2 emissions and emissions calculated from measurements, although previous evaluations of STEAM2 for a larger number of ships (Beecken et al., 2015) indicate that these differences are reduced when integrated over a large

fleet. This indicates that the ACCESS dataset (4 ships) is too small to draw conclusions for the whole STEAM2 inventory used in this Chapter (1366 individual ships). However, WRF-Chem simulations using STEAM2 agree relatively well with ACCESS average profiles in the polluted marine boundary layer, indicating that STEAM2 emissions in this region are qualitatively correct. STEAM2 July emission totals in this region are similar to emission totals from the Winther et al. (2014) inventory (also based on AIS) used in Chapter 6.

The results from this study also indicate that shipping in Northern Norway already has significant regional impacts on SO_2, NO_x, BC and SO_4^{2-} concentrations, as well as strong radiative impacts due to cloud/aerosol interactions. The complex treatment of aerosol/cloud interactions included in WRF-Chem does not lead to a very different estimate of indirect aerosol radiative effect than the one made by Ødemark et al. (2012) using a simpler approach. BC concentrations at the surface increase by up to 40 % due to shipping emissions, but this does not appear to be associated with a strong positive radiative effect, probably because these increases in BC occur over the low-albedo open ocean, and often below clouds. BC from ships could have a higher direct radiative effect if emissions are located close to or within sea-ice.

Shipping impacts on O_3 are relatively modest (approximately 6 %) and lower than previous estimates. This could be due, in part, to lower non-linear effects due to lower dilution of shipping NO_x emissions in relatively fine (15 km $\times$ 15 km) model grids. However, this lower impact on O_3 could also be an artifact of the limited domain size, as our simulations only represent the effect of local emissions and do not include transport of ozone produced from shipping emissions in other parts of the Arctic. These results are put into a larger Arctic-wide context in Chapter 6.

Chapter 6

Current and future impacts of local Arctic sources of aerosols and ozone

6.1 Introduction and motivation

The Arctic is increasingly open to human activity, due to rapid Arctic warming associated with decreased sea ice extent and snow cover. Pollution from in-Arctic sources was previously thought to be low, but oil and gas extraction and marine traffic could already be important sources of short-lived pollutants (aerosols, ozone) in the Arctic. Arctic shipping has been shown to increase O_3 concentrations along the Northern Norwegian Coast during summer by 1.5 ppbv–3 ppbv (Dalsøren et al., 2007; Ødemark et al., 2012; Marelle et al., 2016), and could also significantly enhance summertime surface black carbon and sulfate (up to + 50 and +30 % respectively, Marelle et al., 2016) and black carbon and sulfate burdens in this region (Ødemark et al., 2012). The resulting radiative impact of Arctic shipping emissions is thought to be negative (Ødemark et al., 2012; Dalsøren et al., 2013; Marelle et al., 2016), due to the direct and indirect effect of sulfate aerosols.

Oil and gas activity was shown by Ødemark et al. (2012) to increase the black carbon burden in Northern Russia, causing significant warming due to the effect of BC in air and BC deposited on snow and ice. Recent emission estimates for the Arctic oil and gas sector by Klimont et al. (2015) and Huang et al. (2015) indicate that BC emissions from gas flaring in the Arctic could be much higher than previously thought, and that their impacts might have been underestimated in past studies (Stohl et al., 2013).

In the future, global and Arctic shipping emissions are expected to increase due to enhanced traffic, except sulfur emissions which will decrease (by mass of fuel burned) due to new regulations (IMO, 2010; Corbett et al., 2010). As a result, Dalsøren et al. (2013) found that BC and O_3 burdens due to Arctic shipping could increase between 2004 and 2030, but that sulfate burdens could decrease. Because of this, shipping in 2030 is expected

to cause warming in the Arctic relative to the present day, due to the reduced cooling effect from reduced sulfate, and the increased warming effect of rising BC and O_3. Fuglestvedt et al. (2014) investigated the impacts of shifting a fraction of global shipping through the Arctic Ocean (NSR and NWP), and showed that this would result in warming in the coming century and cooling on the long term (150 years). This response is due to the opposite sign of impacts due to reduced SO_2 (stricter regulations) and reduced CO_2 and O_3 (fuel savings from using shorter Arctic routes). In addition, sulfate is predicted to cause a weaker cooling effect in the Arctic. Fuglestvedt et al. (2014) also showed that the response to increased Arctic shipping can be complex, since increased oxidant levels from Arctic shipping emissions could decrease the lifetime of Arctic CH_4 and SO_2, and cause changes in concentrations and radiative effects further away from the Arctic.

There is, to our knowledge, no study investigating the future impacts of oil and gas activity in the Arctic. It is also currently still unclear if these local sources can become significant in the future compared to other sources of Arctic Pollution, such as long-range transport of anthropogenic pollution from the mid-latitudes, and emissions from biomass burning. In this Chapter, quasi-hemispheric WRF-Chem simulations are performed in order to quantify the impact of remote and local Arctic emission sources on aerosol and ozone concentrations, aerosol and ozone radiative effects, and aerosol deposition.

6.2 Methods

In this study, the WRF-Chem model is run with new inventories for local Arctic shipping (Winther et al., 2014) and gas flaring associated with oil and gas extraction (Klimont et al., 2015). The objecive of these simulations is to study the effect of these local emission sources on aerosols and ozone concentrations, on black carbon deposition and on the radiative impacts of aerosols and ozone in the Arctic. This study also aims to determine if these impacts could be significant relative to the impacts of remote emissions transported to the Arctic. These impacts are determined by performing 6-month long (March-August), quasi-hemispheric WRF-Chem simulations over the Arctic region.

In order to represent both local Actic emissions and emissions transported from the mid-latitudes, the simulation domain needs to include all sources of emissions potentially transported from the mid-latitudes to the Arctic. Based on the previous work of Stohl (2006), the model domain was selected to include sources of pollution potentially transported in the Arctic in less than 30 days (Figures 8, 9 and 10 in Stohl, 2006), a transport time larger than the mean ozone and aerosol lifetimes in the troposphere. This domain is shown in Figure 6-1. It covers most of the Northern Hemisphere, and in order to be computationally feasible, simulations are run at a relatively low resolution (similar to the ones used in global models) of 100 km $\times$ 100 km.

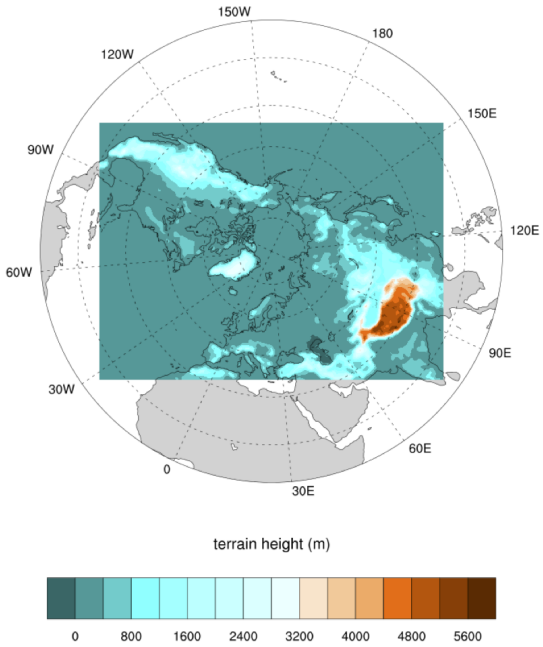

Figure 6-1 – Map of the Northern Hemisphere, showing the quasi-hemispheric simulation domain.

The model setup is presented in Table 6.1. There are 4 major changes compared to earlier model setups presented in Table 4.1 and Table 5.2. First, simulations presented in this chapter use a version of MOSAIC coupled with a SOA formation mechanism, VBS-2 (Volatility Basis Set with 2 volatility species, Shrivastava et al., 2011). The VBS-2 mechanism treats the partitioning of OA between the volatile and the condensed phase using the "volatility basis set" approach (Robinson et al., 2007), and includes SOA formation from the oxidation of anthropogenic VOCs, biogenic VOCs and Semi-volatile and Intermediate-Volatility Organic Compounds (S/IVOCs, Robinson et al., 2007). For reasons explained in Section 6.3, SOA formation from S/IVOCs was not included in these simulations. Second, the gas-phase chemistry mechanism was changed from CBM-Z to SAPRC-99, since SAPRC-99/MOSAIC is the only chemistry and aerosol mechanism in WRF-Chem 3.5.1 including both VBS-2 SOA and aerosol/cloud interactions. Third, LW and SW radiative calculations are now performed by the RRTMG scheme, which is coupled with WRF-Chem aerosol optical properties, and can be easily coupled with WRF-Chem predicted ozone (Sect. 6.3 and 6.8). Fourth, sub-grid (cumulus) clouds are represented here by the KF-CuP (Kain-Fritsch + cumulus potential scheme) parameterization (Berg et al., 2015). The KF-CuP scheme was developped to include aerosol/cloud and chemistry/cloud interactions in sub-grid clouds in MOSAIC, including tracer convection, wet removal, and aqueous chemistry. Taking into account these processes is especially critical in these low-resolution simulations, since sub-grid

clouds are expected to be make up a larger proportion of total clouds as resolution decreases. In the context of this thesis, the model was also updated and several bugs were corrected for these simulations (Sect. 6.3).

Table 6.1 – WRF-Chem setup for the quasi-hemispheric, 6-months long simulations.

Option name	Selected option
Chemistry & aerosol options	
Gas-phase chemistry	SAPRC-99 (Carter, 2000)
Aerosols	MOSAIC 8-bins (Zaveri et al., 2008), including VBS-2 (SOA formation, Shrivastava et al., 2011) and aqueous chemistry
Photolysis	Fast-J (Wild et al., 2000)
Metrorological options	
Planetary boundary layer	MYJ (Janji , 1994)
Surface layer	Monin-Obukhov Janjic Eta scheme (Janji , 1994)
Land surface	Unified Noah land-surface model (Chen and Dudhia, 2001)
Microphysics	Morrison (Morrison et al., 2009)
SW radiation	RRTMG (Iacono et al., 2008)
LW radiation	RRTMG (Iacono et al., 2008)
Cumulus parameterization	KF-CuP (Berg et al., 2015)

The model is run for 6-months, from March 1 to September 1, with an additional 15 days for model spin-up (February 15 to February 29, discarded for analysis). This period includes spring, when long-range pollution transport to the Arctic is relatively efficient, and summer, when local Arctic emissions from shipping are highest. The different simulations are presented in Table 6.2. All simulations use the setup presented above, and are forced by 2012 sea ice, SST and vegetation, as well as 2012 meteorological, chemical and stratospheric boundary conditions. The 2050 simulations also use 2012 biomass burning emissions from FINNv1.5. As a result, "2050" simulations only consider the impact of changing anthropogenic emissions in 2050, and do not estimate the effect of climate change and its consequences on e.g. sea ice, natural emissions, transport pathways, clouds and precipitation. In this chapter, "impacts in 2050" and similar expressions are used as a shorthand for "impacts of 2050 anthropogenic emissions".

The emission inventories used in these simulations are presented in Chapter 3, Section 3.2. Local emissions from Arctic flares and Arctic ships are from the ECLIPSEv5 and Winther et al. (2014) inventories, respectively. In 2050, additional Arctic "diversion shipping" emissions from Corbett et al. (2010) are used. These simulations assume that diversion shipping occurs in July–November (July–August in these simulations ending on September

Table 6.2 – List of simulations

Simulation name	Description
2012 emissions	
2012_BASE	All 2012 emissions (ECLIPSEv5; Winther et al. (2014) Arctic shipping; RCP8.5 subarctic shipping; FINNv1.5 2012 biomass burning emissions) + natural (biogenic, sea salt, soil, lightning, dust, DMS) emissions.
2012_NOSHIPS	2012_BASE, without shipping emissions north of 60°N
2012_NOFLR	2012_BASE, without gas flaring emissions north of 60°N
2012_NOANTHRO	2012_BASE, without anthropogenic emissions south of 60°N
2012_NOFIRES	2012_BASE, without biomass burning emissions
2050 emissions	
2050_BASE	All 2050 emissions (ECLIPSEv5 CLE; Winther et al. (2014) High-growth Arctic shipping; Corbett et al. (2010) High-growth diversion Arctic shipping; RCP8.5 subarctic shipping) + FINNv1.5 2012 biomass burning emissions + natural 2012 emissions
2050_NOSHIPS	2050_BASE, without shipping emissions north of 60°N
2050_NOFLR	2050_BASE, without gas flaring emissions north of 60°N
2050_NOANTHRO	2050_BASE, without anthropogenic emissions south of 60°N
2050_NOFIRES	2050_BASE, without FINNv1.5 2012 biomass burning emissions

1), in agreement with Corbett et al. (2010), and that diversion shipping emissions are equally divided between the NSR and the NWP routes. All future shipping emissions are based on worst-case "High-growth" projections (Corbett et al., 2010; Winther et al., 2014). Emission totals of NO_x, SO_2 and BC in Arctic shipping and Arctic flaring inventories in 2012 and 2050 are given in Table 6.3. Arctic shipping mostly emits NO_x and SO_2, and flaring is an important source of BC. This Table shows that flaring emissions are relatively stable between 2012 and 2050 (in agreement with earlier findings by Peters et al., 2011), but that diversion shipping in summer 2050 causes a very strong increase in local emissions of BC, NO_x and SO_2. In summer 2050, SO_2 emissions from Arctic shipping are higher than in 2012 because of this large increase in summertime marine traffic, although SO_2 emissions by ship are lower due to expected reductions in emission factors (IMO and EU regulations). This increase in Arctic shipping emissions is associated with a decrease in international shipping emissions elsewhere (partly diverted to the Arctic), whose benefits on air quality and climate are not presented here but are investigated in Fuglestvedt et al. (2014).

6.3 Model updates for quasi-hemispheric Arctic simulations

Results from the case studies presented in Chapters 4 and 5 show that WRF-Chem is able to reproduce aerosol transport events from Europe to the Arctic, aerosol and ozone pollution in

Table 6.3 – Emission totals for Arctic local sources in spring (MAM) and summer (JJA) 2012 and 2050. Relative emission increases from 2012 to 2050 are also given.

Emission source	BC emissions (kton)	NO_x emissions (kton)	SO_2 emissions (kton)
2012 emissions, spring			
Arctic ships	0.210	28.4	10.5
Arctic flares	12.7	8.75	6.49
2012 emissions, summer			
Arctic ships	0.297	39.0	16.9
Arctic flares	9.58	6.58	4.87
2050 emissions, spring			
Arctic ships	0.325 (+55 %)	31.1 (+9.5 %)	7.22 (−31 %)
Arctic flares	13.4 (+5.5 %)	9.20 (+5.1 %)	6.55 (+0.92 %)
2050 emissions, summer			
Arctic ships	4.35 (+1400 %)	445 (+1500 %)	135 (+1200 %)
Arctic flares	10.1 (+5.4 %)	6.91 (+5.0 %)	4.92 (+1.0 %)

the Arctic, and pollution from local sources. However, when quasi-hemispheric WRF-Chem simulations (without sub-grid cloud-aerosol interactions or SOA formation) were compared by Eckhardt et al. (2015) to results from several global models and to aerosol observations in the Arctic, this intercomparison revealed that WRF-Chem struggled to reproduce BC and SO_4^{2-} concentrations at Arctic surface sites, as well as aerosol concentrations aloft during summer. The source of these discrepancies has been investigated here and three main sources of error have been identified and corrected in this Chapter:

- The computation of skin temperatures over the prescribed sea ice in the Noah Land Surface Module were found to produce unrealistically high temperatures (5 to 10 K) during the ice-melt season. These biases reduced atmospheric stability in the Arctic, and increased vertical mixing, bringing high altitude pollution to the surface. These calculations were corrected to take into account the fact that, during ice melt, the skin temperature of sea ice cannot rise above the freezing temperature (Deluc, 1772).
- WRF-Chem simulations presented in Eckhardt et al. (2015) did not take into account wet removal of aerosols from sub-grid clouds, which make up a large part of the total simulated cloud cover and total simulated precipitation amounts in low resolution simulations. Simulations presented in this chapter include these processes as represented by the KF-CuP cumulus scheme, recently developed by Berg et al. (2015).
- In earlier simulations, aerosol sedimentation was only performed in the first model level and only took into account the contribution of sedimentation to dry deposition, but not its role in bringing large particles from higher altitudes to the surface. An explicit size-resolved sedimentation scheme was developed for MOSAIC, using the same

algorithm for calculating settling velocities than the one already included in MOSAIC for sedimentation at the surface.

Further analysis of the WRF-Chem simulations presented in Chapter 4 (discussed in Sect. 4.3) also revealed that the model tends to underestimate ozone concentrations over snow and ice and in the Arctic troposphere. In order to perform the new simulations presented in this Chapter, two main reasons for this underestimation were found and corrected:

- Dry deposition (Wesely, 1989 in WRF-Chem) is known to be lower in winter and over snow- and ice-covered ground, due to reduced stomatal uptake of gases by plants, and enhanced atmospheric stability. In previous versions of the model, the predicted snow cover and the prescribed ice cover were not coupled to the dry deposition scheme for the CBM-Z and SAPRC-99 mechanisms. For this reason, the model only took into account reduced deposition over snow and ice over "permanently" snow- and ice covered surfaces, e.g. mountain tops, the Greenland ice sheet... Here, WRF-Chem sea-ice and snow-cover were coupled to the dry deposition scheme, to force "wintertime" conditions ("Winter, snow on ground and near freezing" category in Wesely, 1989) when snow height and ice cover are above 10 cm and 15 % respectively.
- The Fast-J photolysis scheme implemented in WRF-Chem uses one single value for the broadband UV albedo at the surface (0.055). While UV-albedo does not vary much over most land types, this value should be much higher over bare snow or ice (approximately 0.85). The UV-albedo in Fast-J was corrected according to the satellite measurements from Tanskanen and Manninen (2007). UV-albedo values derived from satellite measurements for different land-cover types by Tanskanen and Manninen (2007) were mapped to WRF-Chem land use categories, and a weighted average of snow- or ice-covered albedos and snow- and ice-free albedos was calculated based on snow and ice covers in the model.

Other important model improvements developed for these runs include the coupling of model predicted O_3 with RRTMG SW and LW radiation, as well as the coupling of KF-CuP cloud properties to RRTMG (following the approach of Alapaty et al., 2012). KF-CuP was also coupled with "online" lightning NO_x emissions developed by Barth et al. (2014). A simplified treatment of DMS chemistry from MOZART4 (Emmons et al., 2010; Chin et al., 1996) was implemented in SAPRC-99, as well as an "online" DMS emission scheme based on Nightingale et al. (2000), Saltzman et al. (1993) and Lana et al. (2011).

SOA formation from S/IVOC (Semi-volatile and Intermediate-Volatility Organic Compounds) was removed from our version of the MOSAIC/VBS-2 mechanism for two reasons. First, there is no inventory of S/IVOC emissions yet, and emissions have been previously estimated in WRF-Chem by multiplying POA or VOC emissions by a factor of 6.5 (Shrivastava et al., 2011), based on case studies for Mexico City (Hodzic et al., 2010). This factor

is extremely uncertain, and recent studies (Shrivastava et al., 2015) indicate that it cannot be used to estimate global S/IVOC emissions. Second, the treatment of S/IVOC formation as currently implemented in WRF-Chem was found to be prohibitively computationally expensive for quasi-hemispheric simulations. The VBS-2 mechanism used in this Chapter still includes formation of SOA from the oxidation of biogenic and anthropogenic VOC.

6.4 Model validation

Simulations presented in Table 6.2 are performed using the setup, emissions and model updates presented above. The resulting modeled BC and O_3 concentrations from the 2012_BASE simulation are compared in Figures 6-2 and 6-3 to measurements at Arctic ground stations (Alert, Canada; Barrow, Alaska; Tiski, Russia; Nord, Greenland; Pallas, Finland; Summit, Greenland and Zeppelin, Svalbard, Norway). The BC comparison shown in Figure 6-2 is significantly improved compared to WRF-Chem results presented in Eckhardt et al. (2015), which strongly overestimated BC during summer. Note that, due to the high uncertainty of EBC measurements in the Arctic (approximately a factor of 2), a close agreement is not expected. The model fails to reproduce strong BC peaks at Tiksi, Russia during spring, which are probably due to the influence of a local pollution source (possibly the town or port of Tiksi), which cannot be reproduced in a 100 km×100 km-resolution simulation. The high "Arctic Haze" BC concentrations in spring and lower pollution in summer are reproduced where observed, at Alert (Canada), Barrow (Alaska) and Zeppelin (Svalbard), and the model also reproduces biomass burning pollution at Barrow and Tiksi during summer. In terms of O_3, the base simulation compares well to measurements during summer, although it seems to strongly overestimate biomass burning influence at Tiksi and to slightly underestimate measurements at Nord and Summit. During spring, the model does not reproduce O_3 depletion events at Barrow, Tiksi, Nord and Zeppelin. These events are due to catalytic halogen reactions happening at the Arctic surface over snow and ice (Bottenheim et al., 1990), and these chemical reactions are not currently included in WRF-Chem. Furthermore, simulated surface O_3 is used in Section 6.6 to assess the impact of local emissions on photochemical O_3 production, which is larger during summer because of higher solar radiation and higher emissions from Arctic shipping (Section 6.6).

The base simulation is compared in Figure 6-4 to average vertical profiles from the ACCESS campaign, for refractive black carbon (rBC, measured by a single-particle soot photometer, SP2) and O_3 (measured by UV-absorption). The model agrees very well with O_3 measurements up to 4 km, but overestimates O_3 above. This is likely due to uncertainties in the stratospheric upper boundary condition in WRF-Chem, or to overestimated stratosphere-troposphere exchange. Similar issues were found by Emmons et al. (2015) when comparing global models and WRF-Chem simulations to aircraft and radiosonde observa-

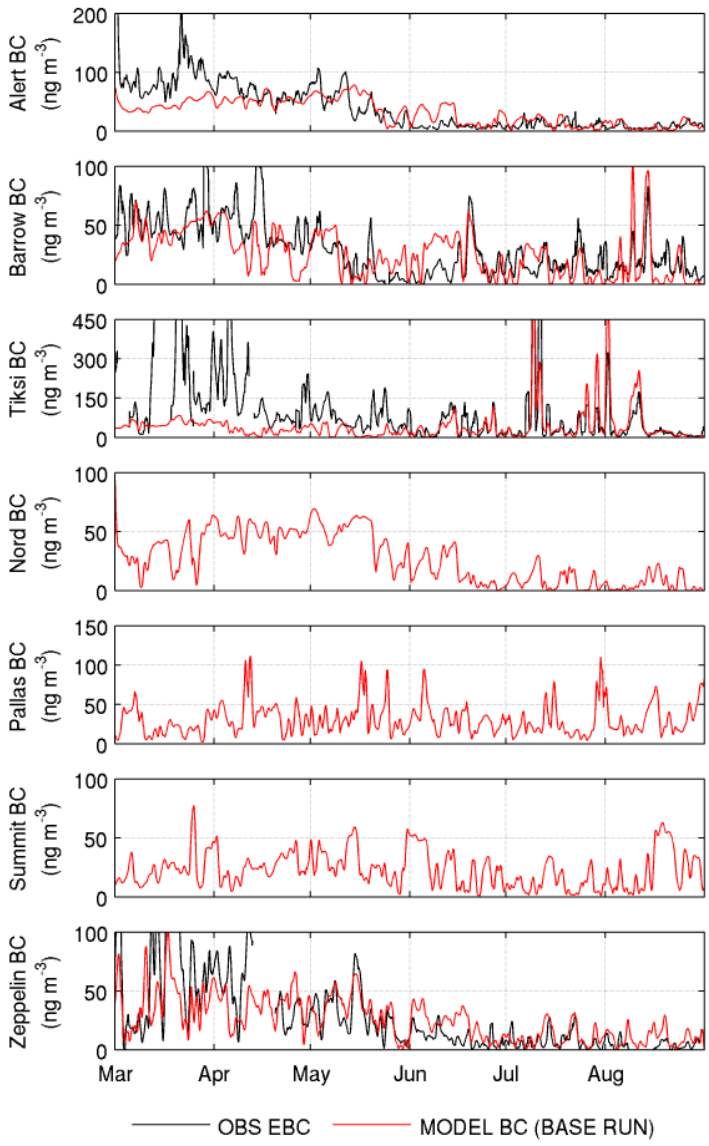

Figure 6-2 – Comparison between WRF-Chem BC in the base simulation and surface EBC measurements in the Arctic (a 24 h running average is applied to both datasets).

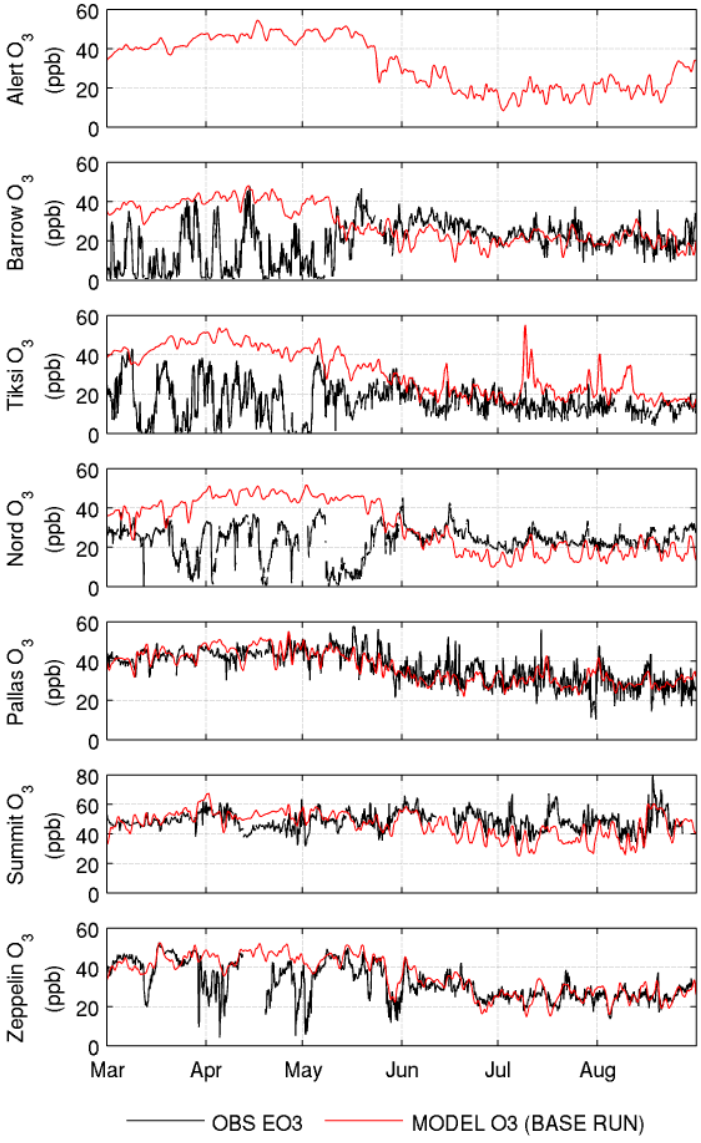

oversize

Figure 6-3 – Comparison between WRF-Chem O_3 in the base simulation (3 h resolution) and measurements at Arctic ground stations (1 h resolution). Note that a different scale is used to present results at Summit.

tions in the Arctic .

WRF-Chem BC is overestimated compared to ACCESS rBC profiles, although this bias is greatly reduced compared to previous results in summer 2008 (Figure 9 in Eckhardt et al., 2015, shows WRF-Chem concentrations of 50 to 70 ng m^{-3} in the summertime Arctic upper troposphere). This improved agreement can be attributed to model updates discussed in 6.3, especially to the new cumulus parameterization by Berg et al. (2015) which increases wet removal of BC during vertical transport in sub-grid clouds.

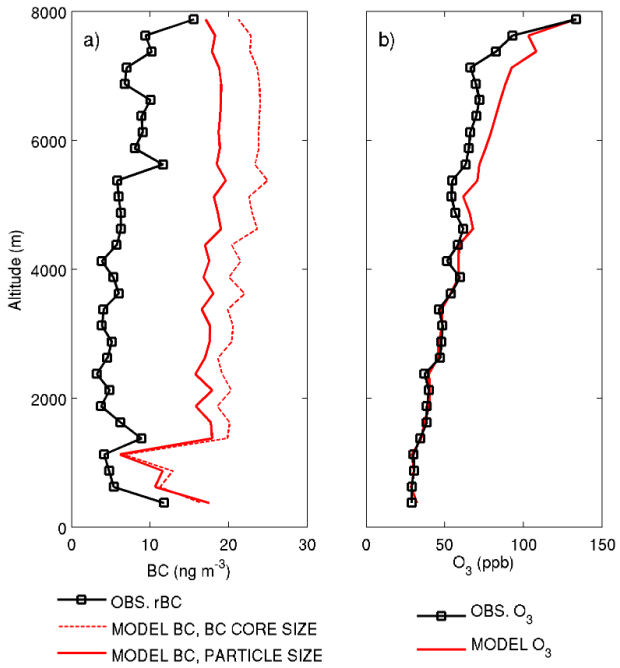

Figure 6-4 – Mean (a) SP2 rBC and (b) O_3 profiles from the ACCESS aircraft campaign (black, July 2012, Northern Norway) compared to WRF-Chem BC and O_3 interpolated along ACCESS flights (base simulation). SP2 rBC measurements cover the size range 80 to 470 nm, and WRF-Chem 80 to 470 nm BC was calculated in two ways 1) from the size distribution of the internally mixed particles in MOSAIC (thick continuous red line) and 2) by estimating the size of BC "cores" within each MOSAIC size bin (thin dotted red line)

The model overestimates rBC at all altitudes, including at the surface, despite good agreement with surface EBC measurements at Zeppelin (Figure 6-2) in July 2012, in the region and at the time of the ACCESS flights. However, this overestimation appears to be larger in the free troposphere. This discrepancy could be caused by underestimated black carbon removal, because the model does not include BC removal due to ice nucleation, and only includes a simplified treatment of secondary activation during deep convection in sub-grid-scale clouds. Since SP2 measurements do not span the full possible size distribution of

BC, WRF-Chem BC contained in the SP2 size range (80 to 470 nm) had to be estimated from the modeled size distributions, introducing additional uncertainties. It is also possible that WRF-Chem BC (technically EC) and SP2 rBC do not exactly correspond, depending on how well emission inventories distinguish EC emissions from other light-absorbing compounds (Petzold et al., 2013). Overestimated convective uplift is another possible source of this high-altitude BC bias (Allen and Landuyt, 2014). This bias could also be due, in part, to errors in mid-latitude emissions.

6.5 Model internal variability and noise: issues when quantifying sensitivities to small emission perturbations with WRF-Chem

In this Chapter, the effect on Arctic aerosols and ozone of local and remote sources of pollutant emissions are calculated by performing sensitivity WRF-Chem simulations, with and without each source of emissions. In order to compute the model response to a perturbation in emissions, e.g. the atmospheric impacts of 2012 Arctic shipping emissions, results from the 2012_NOSHIPS simulations (without Arctic shipping emissions) are substracted from the 2012_BASE simulation (including all 2012 emissions). This assumes that differences between both simulations are only driven by the addition of Arctic shipping emissions. For example, the absolute and relative changes in surface BC concentrations due to Arctic shipping emissions ($2012\_BASE - 2012\_NOSHIPS$ and $[2012\_BASE - 2012\_NOSHIPS]/2012\_BASE$) are shown in Figure 6-5.

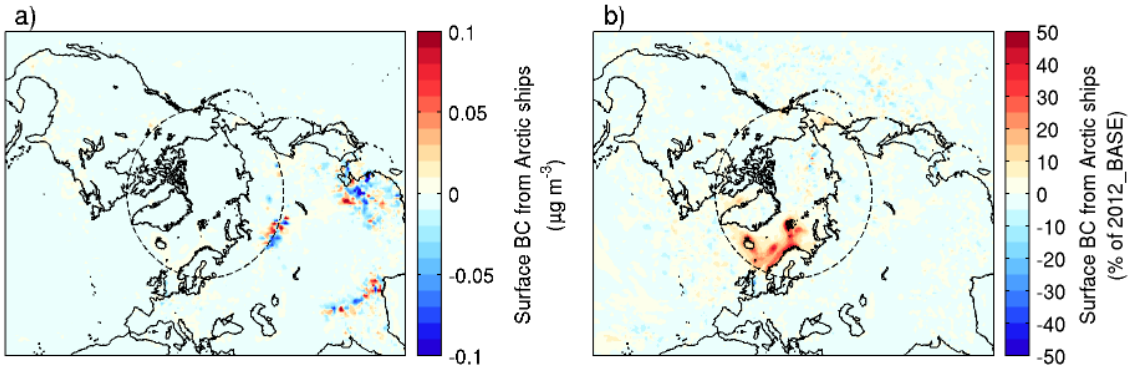

Figure 6-5 – (a) Absolute and (b) relative differences in surface ($0 - -50$ m) BC concentrations between BASE and NOSHIPS simulations in 2012, July average.

Figure 6-5a shows that the largest changes in surface BC due to Arctic shipping emissions are located in very polluted regions such as Siberia where boreal fires occur, India, and Eastern Asia. Some of these regions are located far away from the Arctic, where little

influence of Arctic shipping emissions is expected. However, Figure 6-5b indicates that the relative change in BC in these regions is low ($< 5\,\%$), while the strongest relative changes in surface BC (up to $30\,\%$) occur as expected in the European Arctic, where emissions are high. These relative values are lso similar to results from the high-resolution simulations presented in Chapter 5.

The 2012_BASE and 2012_NOSHIPS simulations use the same boundary conditions, the same model setup, the same emissions other than from Arctic shipping, and are nudged (wind, temperature, humidity) to the same meteorological analysis (FNL) in the free troposphere. This indicates that the unexpected results over China and India showed in Figure 6-5a are due to internal variability in modeled meteorology, chemistry or transport. The most likely cause is variability in clouds and precipitation, since these quantities are not directly nudged to FNL in our simulations. This is also shown in Figure 6-6. Specifically, there are significant local differences in modeled rainfall ($\pm 20\,\mathrm{mm\,month^{-1}}$) between both simulations, even though domain-wide total monthly precipitation varies very little between runs ($0.02\,\%$). Since aerosol wet removal is approximately proportional to precipitation amounts and aerosol concentrations, these large local changes in rainfall can lead to spurious absolute variations in BC concentrations over polluted regions (e.g. Eastern Asia, India, Siberia). Similar issues related to modeled cloud variability in coupled runs were reported by AMAP (2015).

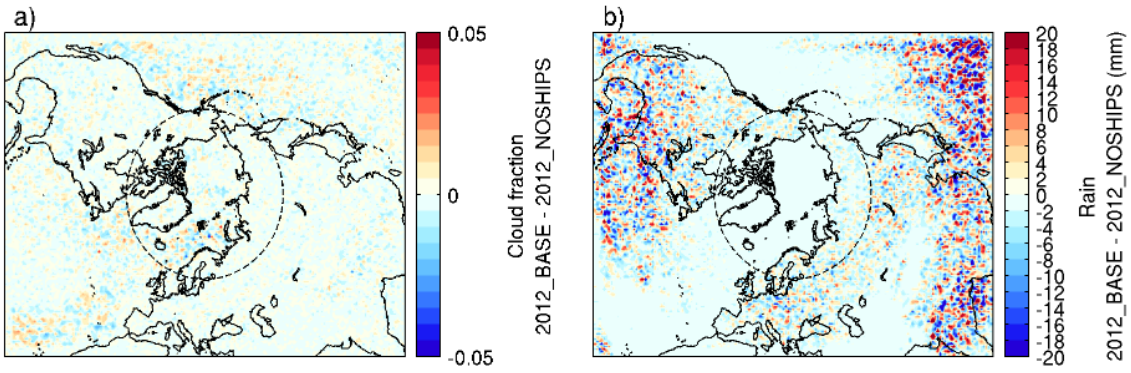

Figure 6-6 – Differences in (a) total cloud fraction, July 2012 average (b) July 2012 monthly rainfall between BASE and NOSHIPS simulations.

These variations can be averaged out when integrating model results over long periods (i.e. several years), or when averaging together a large number of different model realizations (ensemble modeling). These two approaches were not possible in this study due to the high computational costs of running these long or ensemble WRF-Chem simulations at this scale with detailed treatments of chemistry, aerosols and indirect effects. In order to limit the magnitude of this noise, the following Figures show, when possible, relative impacts instead

of absolute impacts (e.g. $[2012\_BASE - 2012\_NOSHIPS]/2012\_BASE$), and seasonally averaged results instead of shorter (e.g. monthly) averages.

6.6 Local and distant contributions to surface concentrations and BC deposition in the Arctic

In this Chapter, WRF-Chem simulations are used to investigate the impacts of emissions from anthropogenic activity in the mid-latitudes, from domain-wide biomass burning, from Arctic shipping, and from Arctic oil and gas flaring, on Arctic aerosols and ozone pollution. This Section shows the impacts of these different sources on surface aerosol and ozone pollution (0 to 50 m altitudes), and BC deposition at the surface in the Arctic. The vertical distribution of this pollution, and the associated radiative effects are discussed in the next Section 6.7.

6.6.1 Surface concentrations and BC deposition in spring and summer 2012

Simulated ozone and aerosol surface concentrations in spring (MAM) 2012 and summer (JJA) 2012 as estimated by WRF-Chem are presented in Figures 6-7 and 6-8. Panels on the left column show the seasonally averaged surface concentrations of ozone and aerosols in the BASE simulation, and other columns show the relative surface contributions from each source: mid-latitude anthropogenic emissions, biomass burning emissions, Arctic flares and Arctic shipping. Figures 6-7 and 6-8 show that mid-latitude anthropogenic emissions are the dominant source of Arctic surface O_3 and aerosols in both seasons, and that biomass burning emissions are an equally important source during summer, when boreal fires occur. Biomass burning appears to be the main source of Arctic organic aerosols.

Arctic flaring emissions appear to be a major source of surface BC in 2012, and an important local source of OA. However, these emissions do not contribute much to surface concentrations of ozone or other aerosol types. Arctic flaring emissions contribute 10 to 20 % of total BC concentrations over the central Arctic in spring, and 50 to 100 % over snow- and ice-covered regions in Northern Russia and in the Kara Sea. In these regions, flaring emissions are also responsible from 50 to 100 % of the total BC deposition (Figure 6-9). Flares have a more local influence on Arctic BC concentrations and deposition during summer 2012, which could be due to a lower lifetime or to a change in transport patterns.

Shipping emission have larger impacts at the surfaceduring summer, when emissions and photochemistry are stronger. Shipping appears to be a major current source of Arctic O_3 (15 to 35 %, 3 to 8 ppbv) and NO_3^-, and also slightly increases BC, SO_4^{2-} and NH_4^+. This increase in NH_4^+ could be due to increased NH_4NO_3 and $(NH_4)_2SO_4$ aerosol formation driven by increased NO_3^- and SO_4^{2-}.

Adding Arctic shipping emissions in simulations seems to reduce concentrations of several compounds at lower latitudes over North America and Russia: NO_x (−20 to 0 %), SO_2 (−20 to 0 %), SO_4^{2-} (−10 to 0 %), NH_4^+ (−10 to 0 %), and O_3 (−10 to 0 %). These effects are however much smaller than the direct increase in surface pollution due to Arctic shipping, and these small localized concentration reductions away from emission regions could correspond to unphysical effects due to the internal variability in our model (see Sect. 6.5 for a discussion about model noise). However, Fuglestvedt et al. (2014) also found that increased oxidants (OH,O_3, H_2O_2) due to Arctic shipping could cause a reduction in SO_4^{2-} aerosols at lower latitudes, and identified the following mechanism: 1) Increased Arctic oxidants due to shipping emission increases SO_2 to SO_4^{2-} conversion in the Arctic boundary layer. 2) Since the lifetime of SO_4^{2-} is low over the open Arctic Ocean, this additional SO_4^{2-} is efficiently removed, effectively reducing the lifetime of sulfur-containing compounds. 3) As a result, transport of SO_2 out of the Arctic is reduced, as well as SO_4^{2-} formation downwind.

Simulation results for Arctic shipping in summer 2012 (Figure 6-8) can be compared to the high-resolution simulation results in Northern Norway in July 2012 presented in Chapter 5 (Marelle et al., 2016). The contributions of Arctic shipping emissions to surface BC and SO_4^{2-} are comparable between both simulations (here, 10–40 % for BC, 10–20 % for SO_4^{2-}; in Chapter 5, 10–30 % for BC, 10–25 % for SO_4^{2-}). However, the O_3 enhancement over the Norwegian and Barents Seas is much stronger here (4 to 5 ppbv than in previous simulations (1 to 1.5 ppbv in Marelle et al., 2015). In Figure 6-8, shipping O_3 enhancements are also located quite far from the stronger shipping emissions regions. This suggests that simulation results presented in Chapter 5 could have been underestimating O_3 production from Arctic shipping emissions, since the limited simulation domain did not allow O_3 production further downwind from Northern Norway, or transport of Arctic shipping O_3 to Northern Norway from afar. This discrepancy could also be due, in part, to higher NO_x emissions, here (Winther et al., 2014) than in Chapter 5 (STEAM2). Overestimated O_3 production is also a known artifact of chemical-transport simulations run at low resolutions (Huszar et al., 2010; Vinken et al., 2011), due to the instant dilution of localized NO_x emissions in large model grids. However, previous studies indicate that this dilution effect causes at most 1 to 2 ppbv overestimations in total Arctic O_3 (Vinken et al., 2011), which are significantly lower than the 3 to 8 ppbv enhancements in O_3 found here. There is also a good agreement between modeled and observed summer O_3 at Zeppelin (Svalbard, Norway), where shipping influence is high (Figure 6-3), which gives some confidence in these results.

Arctic shipping emissions have little influence on O_3 concentrations over land (< 10 %), and flaring NO_x emissions have very little influence on O_3 concentrations despite being approximately a third of the Arctic shipping NO_x emissions. This might be due to different sensitivities of O_3 to NO_x emissions between these different regions, since the simulated O_3 and NO_x backgrounds are much higher over land than over the Arctic Ocean.

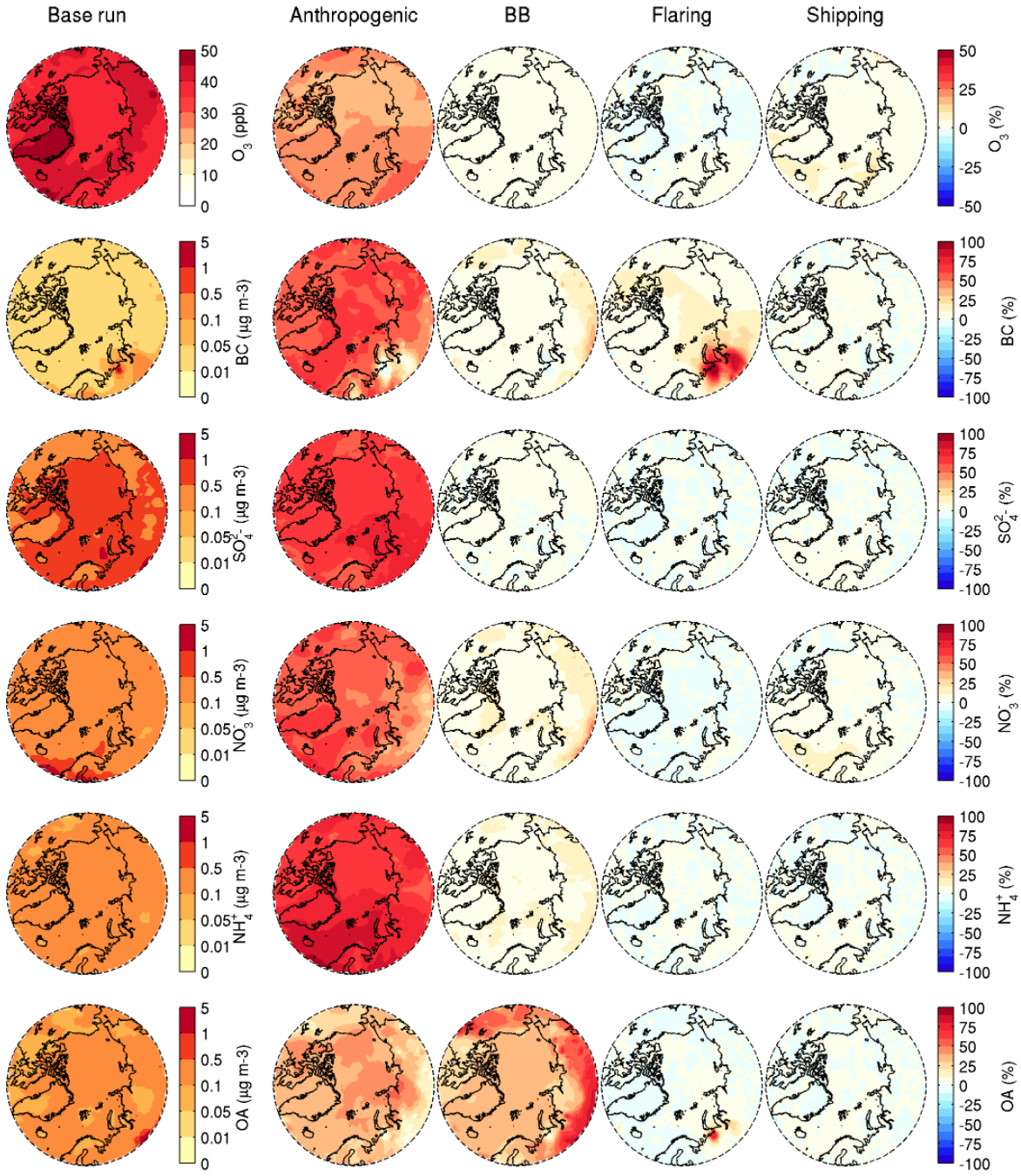

Figure 6-7 – Seasonally averaged spring (MAM) 2012 surface concentrations of O_3 (row 1), BC (row 2), SO_4^{2-} (row 3), NO_3^- (row 4), NH_4^+ (row 5), OA (row 7). (column 1) Total concentration in the 2012_BASE simulation, (columns 2–5) relative contributions from individual emission sources: (column 2) anthropogenic emissions in the mid-latitudes, (column 3) biomass burning, (column 4) Arctic gas flaring, (column 5) Arctic shippping.

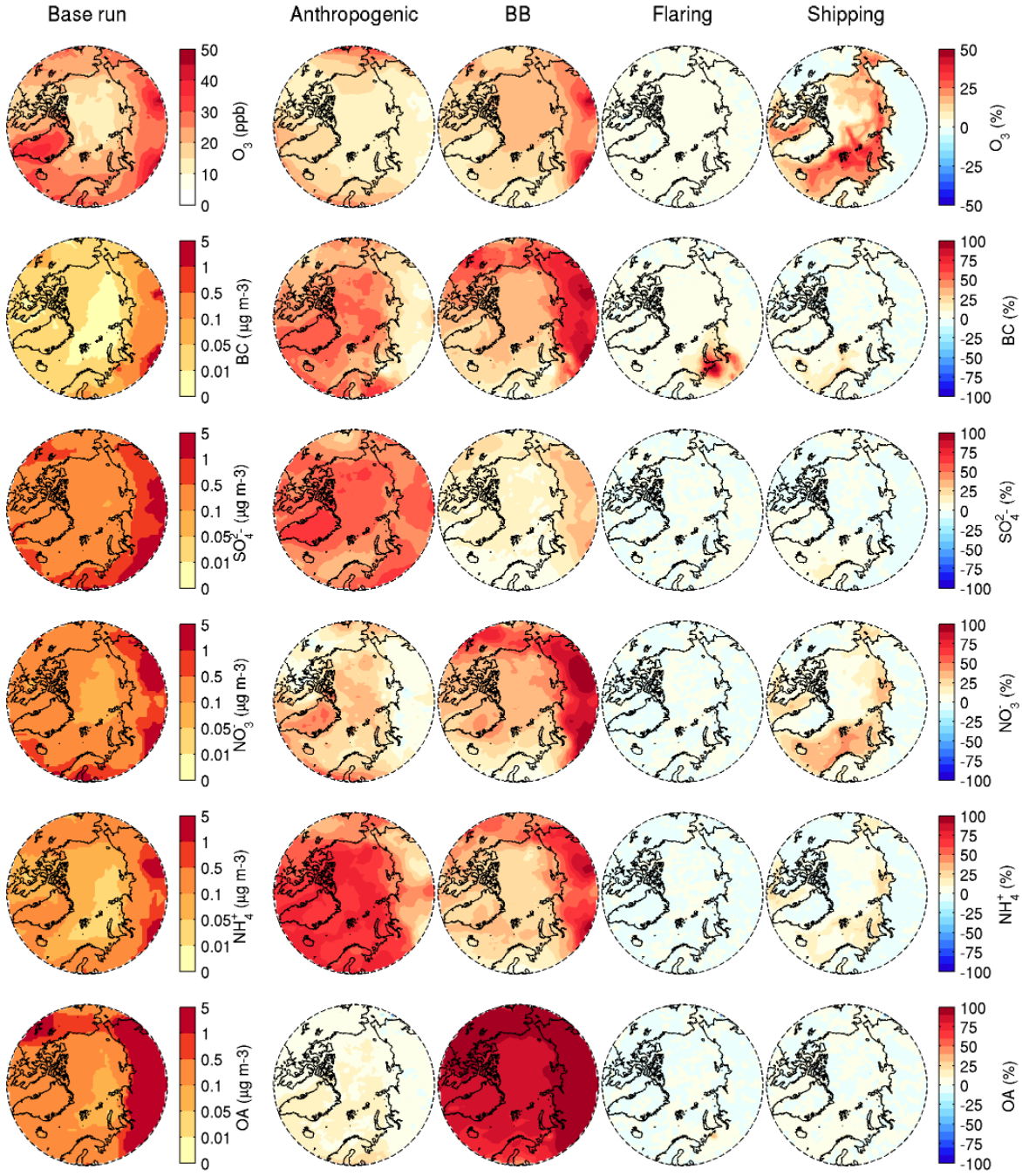

Figure 6-8 – Same as Figure 6-7, for summer (JJA) 2012.

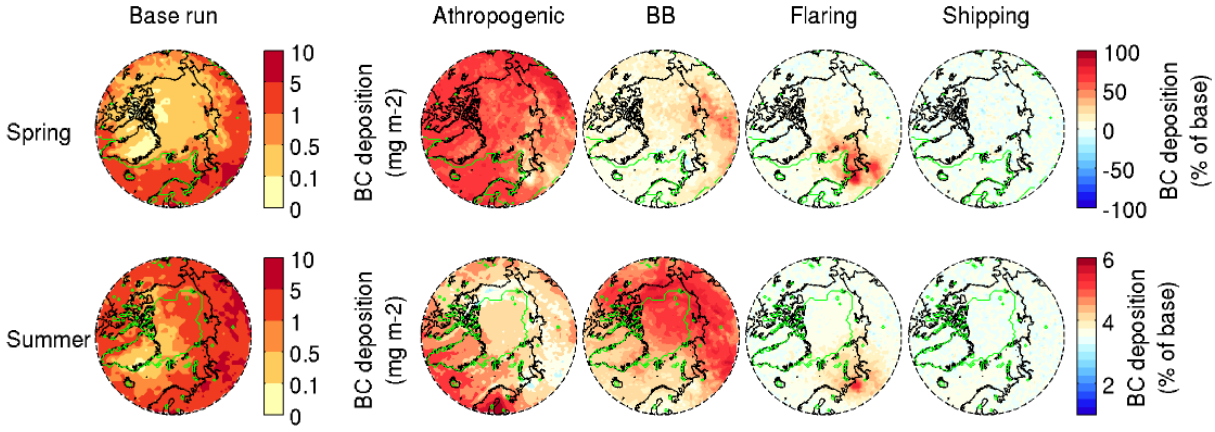

Figure 6-9 – Left column: Seasonally integrated BC deposition in (top) spring (MAM) and (bottom) summer (JJA) 2012 in the base simulation. The 4 columns on the right show the relative contributions from each source to total BC deposition: mid-latitude anthropogenic emissions, biomass burning, Arctic flares and Arctic shipping. The 50 % snow and ice limit in 2012 is also shown as a green line on each panel.

6.6.2 Surface concentrations and BC deposition in spring and summer 2050 (2050 emissions)

The main difference between simulations in 2012 and 2050 is the occurrence of diversion shipping in July and August 2050. As a result, Arctic shipping emissions become the main source of summertime surface O_3, BC and NO_3^- pollution along diversion shipping lanes in the future. Shipping emission also becomes an important source of other aerosol components (SO_4^{2-}, NH_4^+, NO_3^- and OA), this is likely due to a combination of increased emissions (NO_x, SO_2, POA), increased secondary aerosol formation from higher OH, and changes to aerosol chemistry. Over the open Arctic Ocean, 50 % of the total modeled OH is due to shipping emissions. At lower latitudes (over Northern America and Russia), shipping emissions appear once again to cause small reductions in SO_4^{2-}, NH_4^+ and OA over land at lower latitudes , and stronger reductions in SO_2 over the same region (0 to −20 %, lower negative values of 0 to −50 % over Greenland and over the ice pack). However, the robustness of this result is still not certain.

Diversion shipping emissions are responsible for most of the total surface BC along diversion shipping lanes during summer 2050, but do not appear to cause a strong increase in BC deposition at the surface. In our simulations, BC deposition is mainly due to wet removal, which also depends on BC concentrations aloft that are not very sensitive to shipping emissions in these simulations. The contribution of diversion shipping emissions to total BC deposition is high along the Northwest Passage, because of the lower background deposition in this region. However, in agreement with Browse et al. (2013) and Ménégoz et al. (2013), these results also show that diversion shipping does not significantly increase

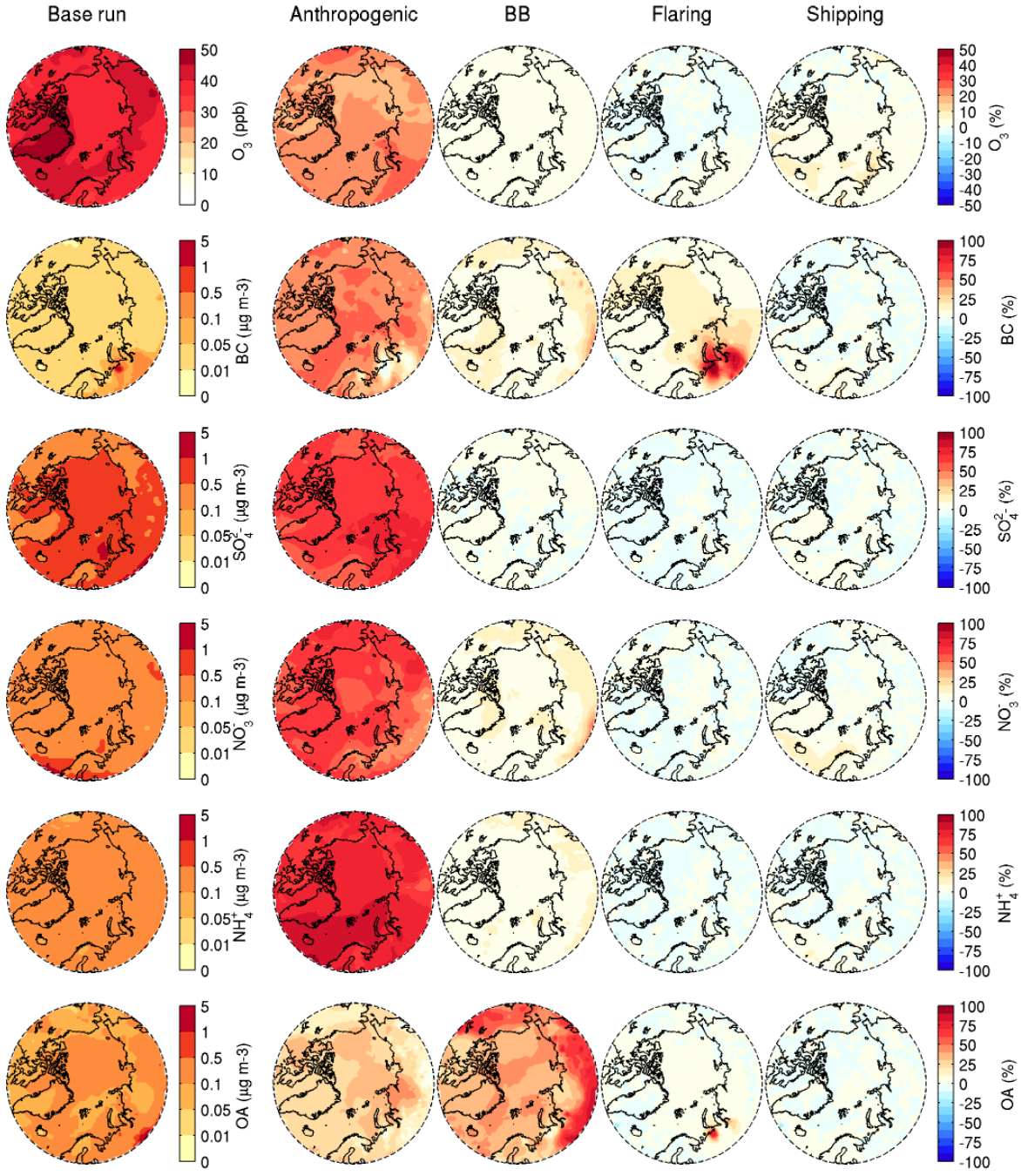

Figure 6-10 – Same as Figure 6-7, for spring (MAM) 2050.

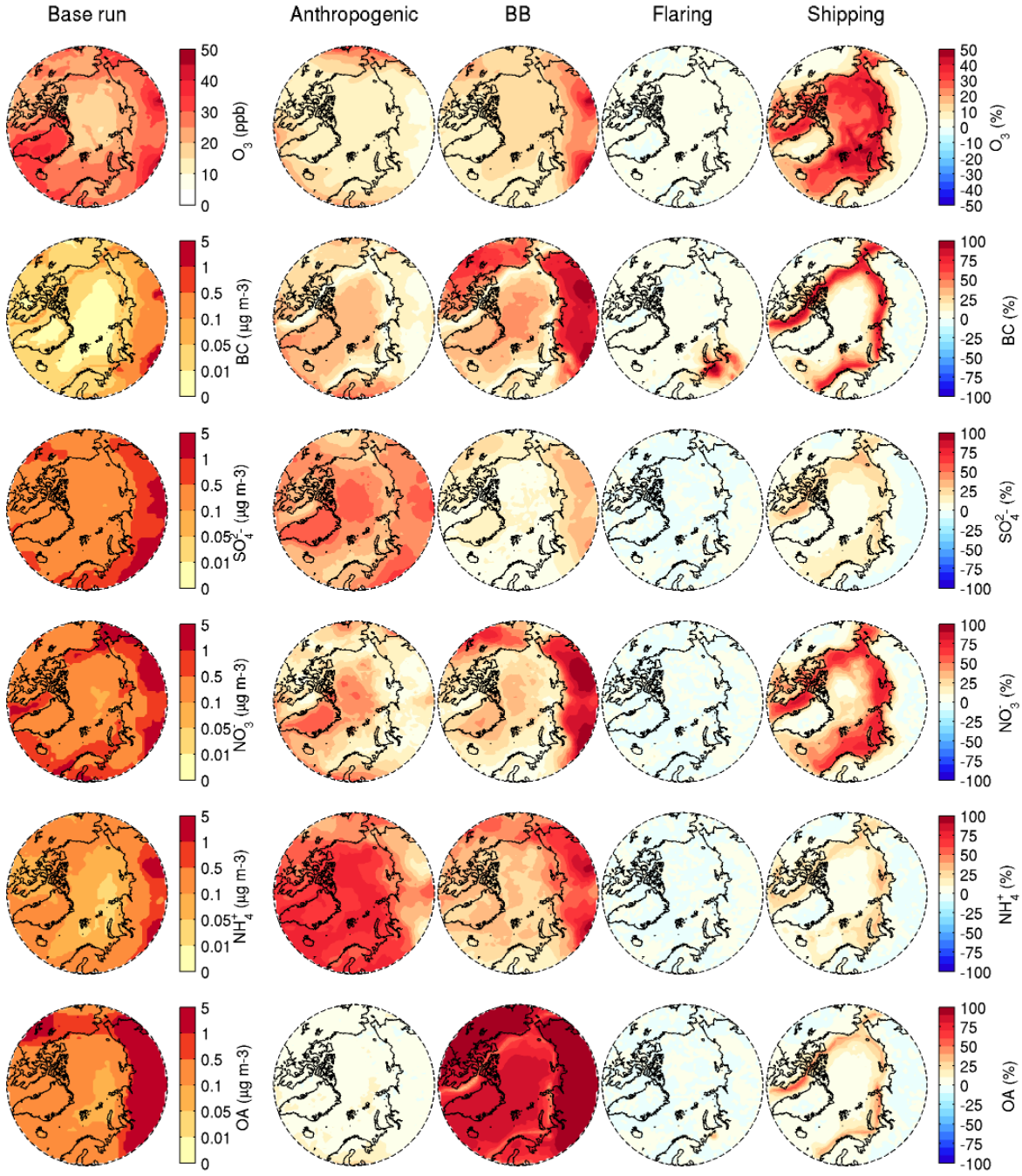

Figure 6-11 – Same as Figure 6-7, for summer (JJA) 2050.

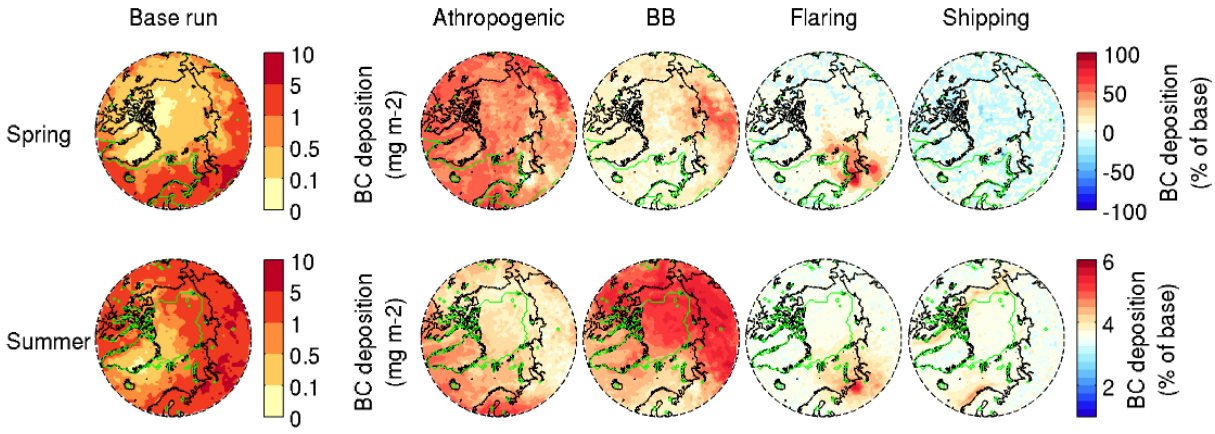

Figure 6-12 – Left column: Seasonally integrated BC deposition in spring (MAM, top) and summer (JJA, bottom) 2050 in the base simulation. The 4 columns on the right show the relative contributions from each source to total BC deposition: mid-latitude anthropogenic emissions, biomass burning, Arctic flares and Arctic shipping. The 50 % snow and ice limit in 2012 is also shown as a green line on each panel.

BC deposition over snow and ice, even in this extreme "High-growth" future scenario. This is due to the short residence time of Arctic shipping BC (1.4 days during summer 2050), limiting transport away from the shipping lanes.

The impacts of Arctic flaring and Arctic shipping emissions on surface concentrations are very similar in spring 2050 (Figure 6-10) and spring 2012. However, since mid-latitude anthropogenic emissions of BC are lower in 2050 than in 2012 (due to global emission controls), the relative influence of Arctic flaring BC increases slightly in spring 2050. The contibution of local emissions to concentrations of other compounds is still relatively low. Arctic flaring remains a major source of BC deposition over snow and ice in Northern Russia and in the Kara Sea, and shipping emission impacts on springtime BC deposition remain indistinguishable from model noise.

6.7 Vertical distribution of Arctic aerosol and ozone pollution from remote and local sources

Results presented in the previous section indicate that local Arctic emissions already contribute to aerosol and ozone pollution at the surface, and that this contribution should grow in the future. Since local Arctic emissions are directly emitted at the Arctic surface, their impacts are expected to be the highest at low altitudes. However, the direct and indirect radiative effects of aerosols and ozone do not scale with surface concentrations, and are usually related to the total column burden. In addition, the radiative effect of BC and of O_3 in the Arctic is known to be very sensitive to vertical distributions (Lacis et al., 1990;

Rap et al., 2015; Flanner, 2013, Sections 2.1.7, 2.2.5.1 and 2.2.5.2.2.

Figures 6-13 and 6-14 present the 6-month-averaged vertical distributions of BC and O_3 enhancements due to remote and local sources in 2050. These figures also show the average cloud cover during the simulation, indicating strong surface cloudiness (30 to 40 %) in the Arctic. Results for 2050 are shown because of the stronger enhancements from shipping give a clearer picture, but results in 2012 are qualitatively similar.

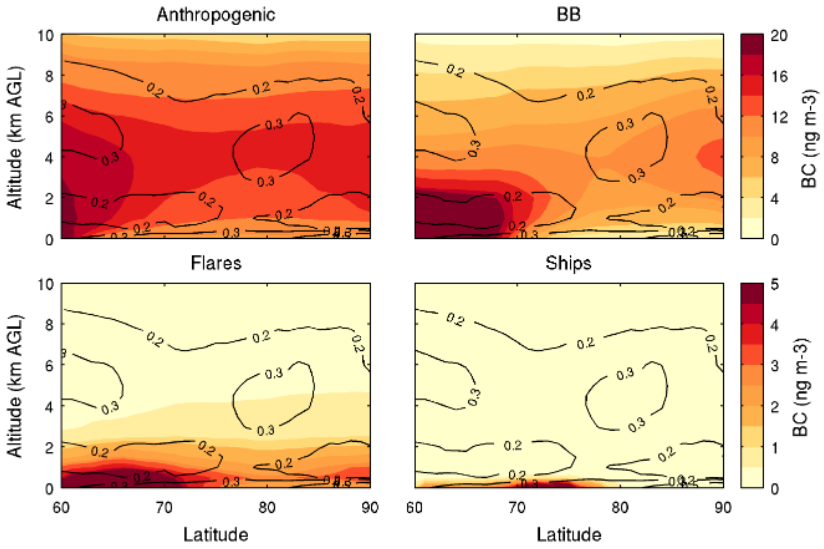

Figure 6-13 – 6-month averaged zonal mean BC enhancements in 2050 associated with each source, black contour lines indicate the 6-month averaged modeled cloud fraction.

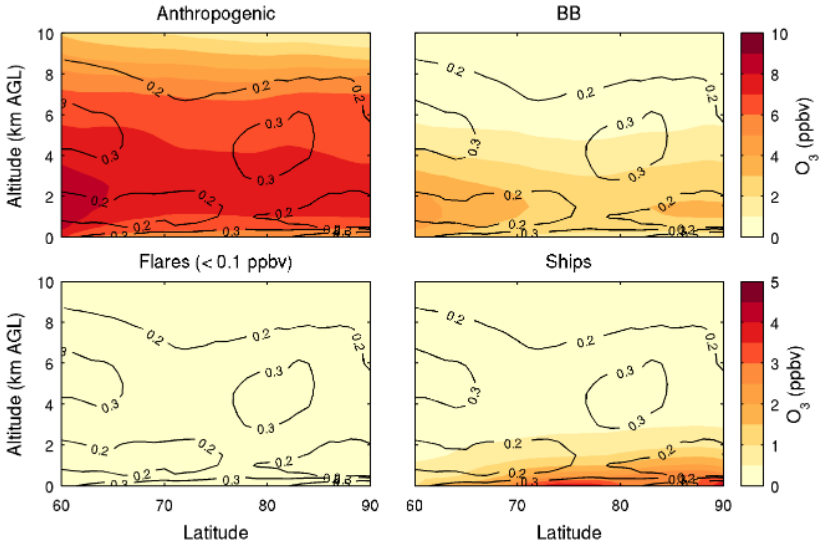

Figure 6-14 – 6 month averaged zonal mean O_3 enhancements in 2050 associated with each source, black contour lines indicate the 6-month averaged modeled cloud fraction.

These figures indicate that pollution from mid-latitude anthropogenic emissions and biomass burning dominates at higher altitudes, and that these remote sources are responsible for the marjority of the Arctic-wide burden of aerosol and ozone pollution. Shipping pollution is confined at very low altitudes, which is probably due to atmospheric stability and to the short residence time of Arctic shipping BC (1.4 days during summer). BC enhancements from Arctic shipping and Arctic flaring are often located below and within clouds, which should reduce aerosol direct effects from these sources (reduced SW radiation below clouds), but which could also lead to more efficient cloud-aerosol interactions (cloud albedo, cloud lifetime, cloud burn-off effects).

6.8 Radiative effects of aerosols and ozone in the Arctic.

The direct and indirect radiative effects of aerosols and ozone are calculated offline using the RRTMG radiative transfer model. RRTMG, as implemented in WRF-Chem, takes as input predicted meteorological, cloud and surface properties, as well as predicted aerosol optical properties. Ozone and other absorbing gases are usually taken into account as climatological profiles or monthly resolved zonal means; in this work, RRTMG was modified to use model-predicted ozone instead.

6.8.1 Direct radiative effects of pollution aerosols and ozone in the Arctic.

RRTMG is used to calculate top-of-atmosphere (TOA) direct radiative effects (DRE, instantaneous radiative effect before adjustments) from aerosols (shortwave) and ozone (shortwave+longwave), averaged over the Arctic region (north of 60°N). First, monthly-averaged 3D meteorological properties, cloud properties, size-resolved aerosol number and speciated, size-resolved aerosol mass were calculated for each simulation. Second, the total DRE of a compound e.g. BC was calculated by performing 24-hour RRTMG simulations (using solar zenith angles for the 15^{th} of each month) with and without the monthly-averaged 3D field for this compound. Aerosol optical properties were calculated with and without e.g. BC, and passed to RRTMG to compute the resulting change in TOA flux.

$$DRE_{BC\_base} = F_{withBC\_base} - F_{noBC\_base} \tag{6.1}$$

$$= (F_{withBC\_base} - F_{withBC\_base}) - (F_{noBC\_base} - F_{noBC\_base}) \tag{6.2}$$

Where all fluxes are upwelling TOA fluxes. Since $F_{withBC\_base} = F_{noBC\_base}$

$$DRE_{BC\_base} = F_{noBC\_base} - F_{withBC\_base} \tag{6.3}$$

Third, the BC DRE from a specific source, e.g. 2012 Arctic shipping, was then determined by substracting the total BC DRE in the 2012_BASE simulation and the total BC DRE in

the sensitivity run, e.g. 2012_NOSHIPS, simulation.

$$DRE_{BC\_ships} = DRE_{BC\_base} - DRE_{BC\_noships} \tag{6.4}$$

In order to separate the DRE from cross-effects on DRE of changed cloud and meteorological properties between base and sensitivity simulations (due to indirect/semi-direct effects), all aerosol DRE calculations were performed using ozone, meteorological and cloud properties from the base simulations. Similarly, ozone DRE calculations (SW and LW) were performed using aerosol, meteorological and cloud properties from the base simulations.

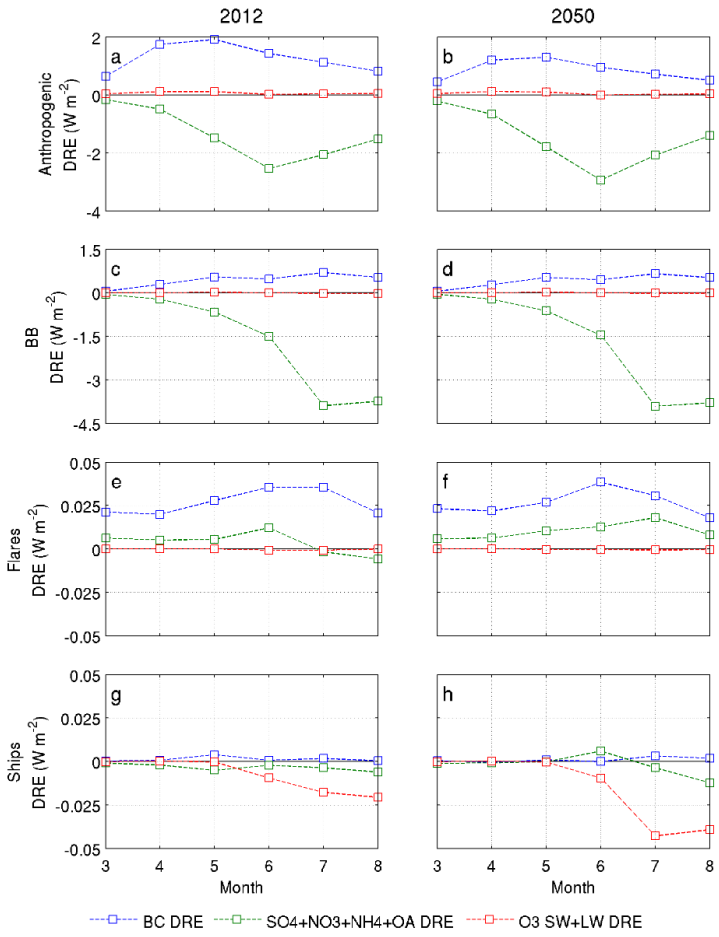

Figure 6-15 – Average Arctic (latitude > 60°N) all-sky direct radiative effects (DRE) of scattering aerosols ($SO_4^{2-} + NO_3^- + NH_4^+ + OA$), absorbing aerosols (BC) and ozone, from each source, at top-of-atmosphere. Note differences in scales for DRE.

The resulting March-August DRE from BC, scattering aerosols ($SO_4^{2-} + NO_3^- + NH_4^+ +$ OA) and (shortwave + longwave) ozone are presented in Figure 6-15 (DRE values are averaged over the Arctic region, north of 60°N). Figure 6-15 indicates that, even in 2050, the effect of biomass burning and mid-latitude anthropogenic emissions is approximately two

orders of magnitude larger than the effect of local Arctic shipping and flaring emissions. This is mainly a consequence of the larger emission amounts from these sources, leading to higher pollution burdens in the Arctic. Pollution from biomass burning and midlatitude anthropogenic emissions is also located at higher altitudes, where O_3 and aerosols have a proportionally higher direct radiative effect. The cooling effect of $SO_4^{2-} + NO_3^- + NH_4^+ + OA$ is mostly due to sulfate for anthropogenic emissions, and due to OA for biomass burning emissions. The most significant radiative impacts of local Arctic emissions are BC warming from flaring emissions ($25\,mW\,m^{-2}$ in 2012 and 2050), and O_3 cooling from shipping emissions ($-20\,mW\,m^{-2}$ in summer 2012, $-30\,mW\,m^{-2}$ in summer 2050).

This cooling O_3 effect is surprising, since O_3 usually causes warming at TOA. This cooling is due to the LW (greenhouse) effect of O_3, and appears to be caused by the surface temperature inversion in the Arctic. Figure 6-14 shows that O_3 pollution from Arctic shipping is confined in the lower atmosphere. In the model, temperatures in the lower Arctic troposphere are often warmer than ground skin temperatures, a situation known as a temperature inversion, which is commonly observed in the Arctic. As a result, enhanced ozone in these comparatively hot atmospheric layers increases LW emission and heat loss into space. In the 2012_BASE simulation, inversions occur over 70 % of the Arctic area (north of 66.6°N) during spring, 58 % during summer. Using clear-sky satellite measurements, Devasthale et al. (2010) estimated similarly high inversion frequencies, 88 to 92 % during winter, 69 to 86 % during summer. Rap et al. (2015) also showed that increasing O_3 at the surface in the Arctic and Antarctic was causing a negative LW effect (Figure 1b in Rap et al., 2015), although they estimated that this effect would be compensated by an associated positive SW effect. This compensation does not occur in the runs presented here, where the positive SW effect is weaker than the negative LW effect. The SW effect might be lower here because O_3 enhancements are often located below clouds, or the LW effect might be larger due to stronger temperature inversions. All in all, this net O_3 cooling effect can be expected to depend strongly on the strength and occurrence of the surface inversion in the Arctic, and whether or not it is accurately represented in models.

In summer 2050, diversion shipping emissions cause a strong increase in surface aerosol concentrations, but a relatively low aerosol DRE (Figure 6-15). Figure 6-13 shows that shipping BC in 2050 is confined in the lowest levels of the troposphere. In addition, the residence time of BC originating from Arctic shipping emissions is very low during summer, 1.4 days. Figure 6-13 also shows that BC from shipping is mostly located below and within clouds, further reducing their SW direct effect.

The direct radiative effects of O_3 and scattering aerosols are low year-roung for Arctic flaring emission, and are also low during spring for Arctic shipping emissions (Figure 6-15). These effects also exhibit unexpected abrupt variations between months, wich indicates that they are too small to be separated from model noise. For this reason, these values, shown in

Figure 6-15 are not discussed in detail here. The only exception is the combined radiative effect of $SO_4^{2-}+NO_3^-+NH_4^++OA$ from Arctic flares, which appears to be positive and rather large. This warming effect appears to be due to a large reduction in Arctic OA burdens when introducing Arctic Flaring emissions, causing a reduction in direct OA cooling. This effect seems to be due to interactions between Arctic flaring emissions and nearby intense biomass burning emissions, but the exact mechanism for this interaction is unclear.

6.8.2 Semi-direct and indirect radiative effects.

WRF-Chem calculates aerosol activation in clouds and the resulting effects on cloud properties, including cloud albedo and cloud lifetime. This effect is taken into account in both grid-scale clouds (Morrison microphysics scheme) and sub-grid clouds (KFCuP). As a result, changes in aerosol concentrations, composition and size between 2 simulations, e.g. 2012_BASE and 2012_NOANTHRO also cause changes in cloud properties (aerosol indirect effects). In addition, since predicted aerosol optical properties and ozone concentrations are coupled to radiation calculations in WRF-Chem, changes in emissions also have an influence on heating rates, temperature profiles and relative humidity profiles, causing additional changes in cloud formation, cloud properties and cloud lifetime (semi-direct effects).

Here, RRTMG is used to calculate SW and LW indirect and semi-direct radiative effects (ISRE) at TOA, averaged over the Arctic region (north of 60°N). Calculations are similar to the ones presented in the previous Section 6.8.1, but here RRTMG simulations are performed by changing only cloud and meteorological properties between runs, while keeping aerosol and ozone concentrations set to the values from the 2012 or 2050 BASE simulations. Since model-predicted ozone is also coupled to radiations in the WRF-Chem simulations, this value also includes the "semi-direct" (cloud adjustment) effect of ozone, but this effect is expected to be low. The corresponding seasonally-averaged results for 2012 and 2050 are presented in Figure 6-16. As discussed in Section 6.5, cloud properties and precipitation appear to be chaotic in WRF-Chem; as a result the confidence in ISRE values is low, and is very low for the small emission perturbations due to Arctic shipping and Arctic flaring. Another weakness of this approach is that the simulations presented in this Chapter do not include the winter and fall seasons, when indirect effects are qualitatively different and when LW effects (due to changes in cloud LW emissivity, see Zhao and Garrett, 2015) tend to dominate.

The sums of the ISRE due to Anthropogenic and Biomass burning in spring 2012 ($-2.0\,\mathrm{W\,m^{-2}}$) and summer 2012 ($-4.0\,\mathrm{W\,m^{-2}}$) are comparable to previous results for the indirect effect by, e.g. Shindell (2007) (-0.25 to $-1\,\mathrm{W\,m^{-2}}$ in spring; -1 to $-2\,\mathrm{W\,m^{-2}}$, during summer). However, results for Arctic shipping and flaring appear to be very different than previous estimates, with stronger month-to-month variations. For example, calculations in Chapter 5 (Marelle et al., 2016) indicate that Arctic shipping emissions in Northern Norway

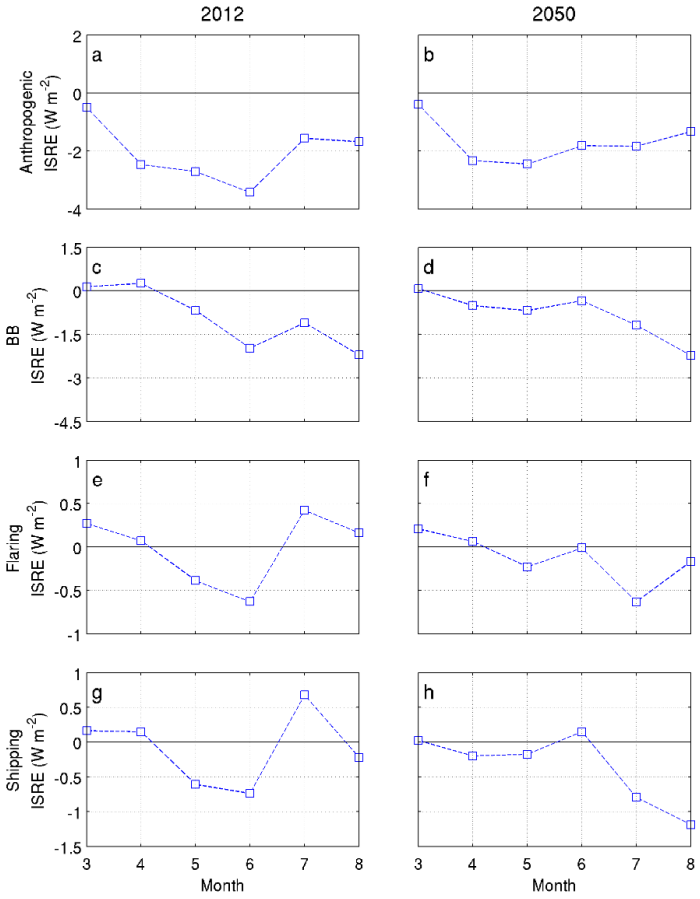

Figure 6-16 – Average Arctic (latitude > 60°N) indirect and semi-direct radiative effects (ISRE) from each source in spring and summer 2012, at top-of-atmosphere. Note differences in scales. The values for Arctic shipping and Arctic flaring are likely to be spurious results due to cloud variability within the model.

have an Arctic wide total (indirect + direct) radiative effect of $-140\,\mathrm{mW\,m^{-2}}$ in July 2012, and Ødemark et al. (2012), estimate an indirect effect of $-105\,\mathrm{mW\,m^{-2}}$ in summer 2012, varying relatively smoothly between months. AMAP (2015) found that the yearly averaged indirect effect of flaring BC in the Arctic was +5 to $+30\,\mathrm{mW\,m^{-2}}$. The results presented here for Arctic shipping and flaring emissions appear to be spurious effects of the chaotic cloud variability within the model. In order to estimate the radiative effect due to the cloud response to small emission perturbations from local Arctic emissions, it is thus necessary to either perform longer simulations (several years at least) or to average ensemble model results to lower this noise. These points can be addressed as part of future work on assessing the climate impacts of Arctic pollution.

6.9 Conclusions and perspectives

This study investigates the impacts of local Arctic pollutant emissions on aerosols and ozone, in terms of surface concentrations, direct radiative impacts, and BC deposition in the Arctic. Recent work (Ødemark et al., 2012; Winther et al., 2014; Larsen et al., 2014) indicates that local Arctic emissions from shipping and resource extraction are currently growing and could become an important source of pollution in the Arctic, relative to other, better-known sources (i.e. long-range transport). However, few previous studies investigated this question, and to our knowledge no previous study investigated simultaneously the current and future impacts of these sources in terms of air quality, radiative effects and BC deposition using a single methodology.

In this study, 6-months long quasi hemispheric simulations are performed using the regional WRF-Chem model, combined with new emission inventories for Arctic shipping Winther et al. (2014), and Arctic gas flaring from petroleum activities (ECLIPSEv5, Klimont et al., 2015. This work is also, to our knowledge, the first successful attempt at using a regional model to investigate Arctic-wide aerosol and ozone pollution and their radiative impacts. In order to perform these regional simulations, several components of the model were improved, including surface temperatures over sea-ice, cloud-aerosol interactions in sub-grid clouds, aerosol sedimentation, DMS chemistry, trace gas deposition over snow and ice, and photolysis (UV-albedo) over snow and ice. Updated simulations compare well to surface O_3 and BC measurements in the Arctic, and to airborne O_3 measurements, but indicate that our simulations might overestimate BC concentrations aloft and O_3 near the tropopause. Improving the representation of aerosol removal in ice clouds and of stratosphere-troposphere exchange could help to further improve model performance.

The main findings from this study are the following:

- *Current Arctic shipping:* Arctic shipping emissions already have a significant influence on surface O_3 and surface aerosol concentrations (BC, NO_3^-, NH_4^+, SO_4^{2-}) in Northern

Europe during summer 2012. This confirms earlier results from the WRF-Chem case study in July 2012 presented in Chapter 4. Impacts on surface O_3 (15 to 35 % of total, 3 to 8 ppbv) are higher than previous estimates, and are also associated with a strong increase in surface OH concentrations (a factor of 2 in the Norwegian Sea). Surprisingly, our results indicate that the main direct radiative effect of Arctic shipping emissions is LW O_3 cooling. This appears to be due to strong surface temperature inversions in the Arctic, and to the vertical distribution of Arctic shipping O_3, which is in our simulations confined in atmospheric layers warmer than the ground surface. In order to confirm this finding, further work is needed to validate the model representation of surface and boundary layer temperatures in the Arctic. Direct radiative effects from Arctic shipping aerosols appear to be very limited, which can be due, in part, to the limited residence time of aerosols emitted in the Arctic marine boundary layer 1.4 days and to the location of Arctic aerosols within clouds, decreasing the available SW radiation.

- *Current gas flaring from petroleum activities in the Arctic:* Arctic gas flaring appears to be a major source of current surface BC year-round, and of BC deposition over snow and ice in spring. Flaring BC is also associated with a significant positive direct radiative effect of 25 mW m^{-2} (60°N–90°N average). However, this warming effect is still approximately two orders of magnitude lower than BC warming from anthropogenic emissions transported from the mid-latitudes to the Arctic, and than BC warming from biomass burning emissions. The radiative impact of increased BC deposition could not be investigated here due to the lack of a detailed snow-albedo model within WRF-Chem. However, the simulation dataset presented here could be used in future work to assess the radiative effects of local sources due to these processes.

- *Future (2050) Arctic gas flaring:* Simulations were performed using future anthropogenic emissions for 2050, and show that Arctic flaring should remain an important source of surface BC, BC deposition and BC direct radiative effects in the Arctic. Furthermore, the relative influence from Arctic flaring BC is expected to increase due to anthropogenic BC emission reductions in the mid-latitudes (here, in the ECLIPSEv5 future CLE scenarios).

- *Future (2050) Arctic shipping:* Future Arctic shipping emissions in 2050 increase significantly during summer, due to the occurrence of diversion shipping in July–November (i.e. July–August here, since simulations were only performed for 6-months, March–August). In this "high-growth" diversion scenario, Arctic shipping become a major source of surface ozone and aerosols (locally, the main source of BC and NO_3^-) during the Arctic summer. This strong increase in O_3 (8 to 15 ppbv) is also associated with a strong increase in surface OH concentrations (a factor of 2) over the Arctic Ocean.

However, diversion shipping does not enhance significantly BC deposition over snow and ice, likely because of limited atmospheric transport to the ice pack, due to efficient wet removal over the open Arctic Ocean (the residence time of BC is 1.4 days during summer). The simulations presented here do not estimate the effects of the reduced (diverted) international shipping emissions at lower latitudes in 2050, which has been shown by Fuglestvedt et al. (2014) to have some air quality and (short-term) climate benefits.

The results presented in this Chapter also put the findings of previous case studies (Chapters 4 and 5) in the broader context of Arctic-wide aerosol and ozone pollution. These results indicate that, even though emissions from local sources are relatively low compared to global totals, they already have significant local relative impacts in the Arctic in terms of surface aerosol and ozone concentrations, chemistry (though the effect of increasing OH), and direct aerosol and ozone radiative effects. This relative influence can also be expected to increase in the future. However, even for worst-case future local emission scenarios, mid-latitude anthropogenic emissions and biomass burning emissions can be expected to remain the main source of Arctic ozone and aerosol burdens in the troposphere, as well as the main source contributing to direct aerosol and ozone radiative effects in the Arctic.

Future projections performed in this study only consider the consequences of changing anthropogenic emissions in 2050. In order to obtain a complete picture of the future influence of local emission sources, it is also necessary to consider the impacts of the changing climate, causing decreased sea ice and snow covers, changing long-range pollution transport from the mid-latitudes, and increasing dry deposition (due to vegetation) and wet removal (due to stronger precipitation and precipitation phase change from solid to liquid). Jiao and Flanner (2016) indicate that, by the end of the 21st century, the change in transport patterns and deposition processes could decrease the mean BC burden in the Arctic by 13.6 %. It is also necessary to quantify the future impacts on Arctic aerosols and ozone of changing natural or semi-natural emission sources such as biomass burning, biogenic activity, and the increasingly open Arctic Ocean.

General Conclusions

Summary

This thesis aims to improve our understanding of Arctic aerosol and ozone pollution from local and remote sources. In this work, regional meteorology-chemistry-aerosol simulations are performed with the WRF-Chem model, using new emission inventories for local Arctic sources. These results indicate that regional modeling using WRF-Chem is an effective tool for investigating aerosol and ozone pollution in the Arctic. Throughout this thesis, comparisons with airborne, ground-based, and satellite measurements in the Arctic show that the model is able to reproduce ozone and aerosol plumes from long-range pollution transport, local shipping pollution in the marine boundary layer, and seasonal (6-months simulations) aerosol and ozone pollution at the surface in the Arctic.

First of all, WRF-Chem is used to investigate pollution transport from Europe to the Arctic, which is currently thought to be one of the main sources of Arctic aerosol and ozone pollution. Simulations are used to analyze airborne aerosol measurements from the POLARCAT-France spring campaign, which took place in Northern Europe in Spring 2008. The model reproduces the complex vertical distribution of European pollution aerosols observed in the Arctic during the campaign, and show that these observed aerosol layers were due to different emission types (industrial and urban emissions; agricultural fires), different geographical origins (central Europe; Western Russia and Ukraine) and different transport pathways (fast transport in altitude in frontal systems; slower stransport at low altitudes). These findings also show that aerosol amounts reaching the European Arctic in spring are strongly influenced by wet removal ($> 50\,\%$ of aerosol mass), for both low-level and frontal transport. In terms of direct radiative effects, this event causes top-of-atmosphere (TOA) cooling due to the scattering effect of aerosols, but causes TOA warming over snow and ice due to the high surface albedo, and causes surface cooling over all surface types.

Second, local Arctic emissions associated with shipping and resource extraction are expected to grow in the future. Several studies suggested that these sources could already be significant. In this thesis, WRF-Chem is used to investigate the impacts of the emerging source of Arctic pollution from shipping, by performing plume-scale and regional-scale simulations in Northern Norway in July 2012, where current Arctic shipping emissions are thought

to be the highest. The model is combined with shipping emissions from a new bottom-up inventory, STEAM2, and simulations are used to analyze measurements of Arctic shipping pollution from the ACCESS aircraft campaign. These simulations show that current Arctic shipping has significant local impacts on NO_x, SO_2, SO_4^{2-}, BC and O_3 concentrations at the surface during summer. WRF-Chem includes a relatively complex treatment of cloud/aerosol interactions, which is used to estimate the total (direct+semi-direct+indirect) radiative effect of aerosols from shipping emissions in this region in July 2012. These emissions cause a strong local TOA cooling due to the effect of cloud/aerosol interactions. On average, new inventories such as STEAM2 appear to represent reasonably well Arctic shipping pollution, but considerable uncertainty remains on emissions from individual ships. Additional measurements focused on Arctic shipping pollution are necessary in order to fully validate these new emission inventories.

The WRF-Chem model can be run at fine, plume-resolving scales to analyze high-resolution measurements, or at large, quasi-hemispheric scales to investigate Arctic-wide aerosol and ozone pollution. In order to perform Arctic-wide simulations, a new model setup is defined for Arctic studies and the model is improved when key Arctic processes are missing. This new setup includes recent model developments (SOA formation, aerosol/cloud interactions in sub-grid scale clouds, lightning NO_x emissions) as well as additional modules developed specifically for this thesis. I find that some of these additional processes appear to be critical in order to model Arctic ozone and aerosol pollution. For ozone, it is important to model the increase in UV-albedo over snow and ice and its impacts on photolysis rates. Simulations also need to take into account the reduced dry deposition velocity of ozone over snow- and ice-covered surfaces. In terms of Arctic aerosols, the representations of Arctic boundary layer structure and of the wet removal of aerosols by sub-grid scale clouds appear to be critical. Comparisons to groundbased and airborne measurements of aerosols and ozone in the Arctic are greatly improved in the updated simulations.

Finally, this updated version of WRF-Chem is used to investigate the current (2012) and future (2050) impacts of Arctic shipping and Arctic gas flaring emissions, in terms of air quality and radiative effects. Results show that Arctic flaring emissions are and should remain a major source of local black carbon aerosols, causing warming, and that Arctic shipping is already a significant source of aerosols and ozone during summer. In 2050, diversion shipping through the Arctic Ocean could become the main source of local NO_3^-, BC, and ozone pollution. I also find that the main direct radiative effect of Arctic ships appears to be longwave TOA ozone cooling. This cooling effect is due to the temperature inversion in the Arctic boundary layer. Direct shortwave radiative effects from ships are small, due to the short lifetime of shipping aerosols (1.4 days) and because short-lived pollution from Arctic ships is often located below clouds. As a result, it also appears that an accurate representation of surface temperatures, boundary layer structure and clouds is critical to

correctly compute the direct radiative effect of aerosols and ozone from local Arctic emissions.

Perspectives

The work presented in this thesis improves our understanding of aerosol and ozone pollution in the Arctic. However, it is important to keep in mind that results presented in this thesis are based on relatively short simulations (at most 6 months), and do not consider the effect of year-to-year variability in, e.g., boreal fire activity, weather, or snow and sea ice cover, which can influence Arctic aerosols and ozone.

In addition, the results presented in Chapter 6 indicate that modeled changes in aerosols due to small emission perturbations (e.g. adding Arctic shipping or Arctic flaring emissions) are relatively uncertain, due to the chaotic nature of modeled clouds and precipitation. In order to improve the robustness of these calculations, it is important to investigate these chaotic effects in order to properly separate signal from noise in modeled results. This could be carried out in the future, based on these simulations, by performing ensemble sensitivity simulations to e.g. Arctic shipping and Arctic flaring, on a smaller Arctic simulation domain embedded (nested) in the domain presented in Chapter 6. Because of this variability, the radiative effect of cloud-aerosol interactions (indirect effects) due to local Arctic emissions are even less certain than their direct effects.

Additionally, results presented in this thesis show that the direct aerosol and ozone radiative effects in the Arctic appear to depend strongly on modeled Arctic meteorology (vertical temperature profiles for LW radiative effects, cloud cover for SW effects). In order to better constrain these radiative effects, it is important to better validate model representations of Arctic meteorology, especially surface temperature inversions and Arctic clouds.

Simulations presented in this thesis also indicate that improving the representation of the following processes in WRF-Chem could be important for Arctic studies:

- *Organic aerosols:* Simulations presented in Chapters 4 and 5 do not include any mechanism for secondary organic aerosol (SOA) formation. The study presented in Chapter 6 includes a mechanism for "traditional" SOA formation from the oxidation of biogenic and anthropogenic VOC, but recent work (Shrivastava et al., 2015; Hodzic et al., 2015) indicates that non-traditional SOA formed from semivolatile organic compounds and intermediate volatility organic compounds (S/IVOC) constitutes another major source of OA. Results from Chapter 4 also show that not including SOA formation leads to underestimated aerosol concentrations in some biomass burning plumes in the Arctic, and, in general, to underestimated OA and overestimated NO_3^- in all plumes. SOA formation from S/IVOC formation was removed from the simulations presented in Chapter 6 because of the lack of a reliable global S/IVOC emission inventory. However, several recent approaches can be used to estimate these emissions (e.g., Hodzic

et al., 2015, suggest to use 60 % of POA emissions for SVOC, and 20 % of NMVOC emissions for IVOC). Simulation results presented in Chapter 6 indicate that biomass burning emissions are a strong source of OA in the Arctic, and that these OA enhancements cause a significant cooling (negative) direct radiative effect at TOA. The effect of non-traditional SOA formation on Arctic pollution, especially from biomass burning, could be investigated using WRF-Chem in the future. "Brown Carbon" aerosols (absorbing organic aerosols), whichare not included in these runs, could also play an important role.

- *BC wet removal:* In the Arctic-wide WRF-Chem simulations performed in this thesis, BC concentrations at the surface are well represented, but BC appears to be overestimated in the Arctic mid- and upper troposphere during summer. This overestimation could be caused, in part, by the absence of a scheme for ice nucleation in mixed-phase clouds in these simulations, since BC aerosols are efficient ice nuclei. Secondary aerosol activation in liquid clouds could also be an important sink for high-altitude aerosols. This last process is included in our simulations, but it is based in the KFCuP sub-grid cloud scheme on a simplifying assumption for the critical supersaturation. The effect of this assumption could be studied in the future.

- *Snow and ice modeling:* Simulations presented in this thesis do not include snow-NO_x emissions, or halogen chemistry over snow and ice. Comparison with surface measurements show that the lack of halogen chemistry is a source of strong discrepancies in O_3 during winter and spring at Arctic surface stations, as the model is unable to reproduce ozone depletion events. The effect of the lack of snow-NO_x emissions is not clear from these simulations; however, including these processes could change the modeled response of Arctic surface O_3 to local and remote sources near the ice edge and over snow. The released version of WRF-Chem does not include a snow-albedo model, which could also be used to estimate the radiative impacts of BC deposition on snow, which could be significant for Arctic flares (Flanner et al., 2007; AMAP, 2015).

- *Stratospheric upper boundary condition:* Simulation results indicate that the stratospheric O_3 source might to be too high in our simulations. This upper boundary condition is based on a climatology for years 1996-2005. It is not clear if using an updated climatology could improve these results, or if this overestimation is caused by other (e.g. transport) processes.

Last but not least is necessary to calculate the climate impacts of longer-lived greenhouse gases (CO_2 and CH_4) in order to obtain a complete picture of the climate effects of local Arctic emissions. For example, the warming effect of CO_2 from ships is known to outweigh the cooling effect of shipping aerosols in the long-term (Eyring et al., 2010). The

ECLIPSEv5 emission inventory used here also estimates that Arctic flares emit significant amounts of CH_4, with strong potential warming effects (AMAP, 2015). In the simulations presented in Chapter 6, future (2050) projections only consider the effect of changing anthropogenic emissions in 2050. In order to improve these projections, it is also necessary to consider the effect of changing natural and biomass burning emissions, as well as the effect of future climate change on e.g. removal processes and long-range transport. Other long term radiative impacts, such as the effects increased Arctic O_3 due to ships on CH_4 lifetime and on the carbon sink (damaged vegetation due to O_3) also need to be estimated. These effects, and other long-term or large-scale effects relevant for the study of Arctic climate change (e.g. climate feedbacks) cannot be easily studied using WRF-Chem. As a result, it appears that regional models such as WRF-Chem should be used in combination with global climate models in order to study Arctic climate change. On the one hand, global climate models have the capability to study these long-term effects, and to estimate the Arctic surface temperature response in these different scenarios. On the other hand, results from this thesis indicate that regional models are very useful tools in order to bridge the gap between measurements and regional air quality and climate (concentrations, radiative effects), and can also be used in detailed case studies to identify important processes and improve global models.

Conclusion

Le but de cette thèse est d'améliorer les connaissances sur la pollution à l'ozone et aux aérosols en Arctique. Dans cette thèse, des simulations de météorologie-chimie-aérosols sont effectuées à l'aide du modèle WRF-Chem, combiné à de nouveaux inventaires des émissions locales en Arctique. Ces simulations sont utilisées pour analyser les mesures issues de campagnes aéroportées récentes consacrées au transport de pollution depuis les moyennes latitudes jusqu'en Arctique, et à la pollution liée aux bateaux et à l'extraction de pétrole et de gaz en Arctique. Les résultats indiquent que la modélisation régionale avec WRF-Chem est un outil adapté pour étudier la pollution à l'ozone et aux aérosols dans cette région.

Les résultats de simulations WRF-Chem sont en bon accord avec les mesures par avion de la campagne POLARCAT-France au printemps 2008, en termes de quantité d'aérosols et de propriétés optique des aérosols. Les simulations parviennent à reproduire la distribution verticale complexe des aérosols de pollution européens observés en Arctique. Ces simulations montrent que les différentes couches d'aérosols observés pendant POLARCAT-France sont dues à différents types d'émission (émissions industrielles et urbaines ; feux agricoles), différentes régions géographiques (Europe centrale, ouest de la Russie et Ukraine) et différents mécanismes de transport (transport rapide en altitude dans des systèmes frontaux ; transport lent à basse altitude). Ces résultats confirment l'importance du dépôt humide, qui contrôle les quantités d'aérosols transportées jusqu'en Arctique ($> 50\,\%$ de la masse totale déposée), tant pour le transport dans les systèmes frontaux que pour le transport à basse altitude. Les résultats indiquent aussi que la prise en compte des aérosols organiques secondaires (SOA, non pris en compte dans ces simulation initiales) semble être importante pour reproduire les quantités d'aérosols dans les panaches de feux, et la composition des panaches pour tous types de sources. En termes d'effets directs des aérosols, cet évènement cause un refroidissement au sommet de l'atmosphère (TOA), dû à la diffusion du rayonnement solaire par les aérosols, mais cause un réchauffement au TOA au dessus des surfaces couvertes de neige ou de glace, et un refroidissement de surface pour tous les types de surface.

Le modèle est aussi combiné avec un nouvel inventaire d'émission des bateaux pour effectuer des simulations au nord de la Norvège en été 2012, pendant les dates de la campagne aéroportée ACCESS, dédiée aux émissions locales de pollution en Arctique. Ces simulations montrent que l'impact actuel des émissions de la navigation dans cette région est significatif

sur les concentrations de surface en NO_x, SO_2, SO_4^{2-}, BC et O_3. WRF-Chem comprend un schéma relativement complexe d'intéractions aérosols/nuages, qui est utilisé pour estimer l'effet radiatif total (direct + semi-direct + indirect) des émissions des bateaux dans cette région en juillet 2012. L'effet principal de ces émissions est un fort refroidissement au TOA, dû aux interactions aérosols/nuages. Les nouveaux inventaires d'émission semblent bien représenter la pollution en Arctique, mais de nouvelles campagnes de mesures consacrées à la pollution des bateaux en Arctique sont nécessaires afin de valider précisément ces nouveaux inventaires.

Cette thèse montre que le modèle WRF-Chem peut être utilisé à des échelles fines résolvant les panaches individuels pour analyser des mesures à hautes résolutions, ou à de grandes échelles quasi-hémisphériques pour étudier la pollution à l'échelle de l'Arctique. Afin d'effectuer ces simulations à grande échelle, j'ai défini une configuration du modèle pour les études arctiques, et amélioré le modèle quand certains processus clés n'étaient pas pris en compte. Cette configuration comprend des développements récents du modèle (formation de SOA, interactions aérosols/nuages dans les nuages sous-maille, émission de NO_x par la foudre), ainsi que de nouveaux modules développés spécialement pour cette thèse. J'ai trouvé que certains de ces nouveaux processus étaient critiques en région arctique. Pour l'ozone, il semble important de prendre correctement en compte l'albedo UV au-dessus de la neige et de la glace et son influence sur les taux de photolyse, ainsi que le dépôt sec réduit au dessus de la neige et de la glace. Pour les aérosols en Arctique, la représentation de la couche limite arctique et le dépôt humide dans les nuages sous-maille semblent primordiaux. Ces améliorations du modèle entraînent de meilleurs résultats pour les aérosols et l'ozone, comparés à des mesures effectuées par avion et au sol en Arctique.

La version améliorée du modèle est utilisée pour quantifier les impacts actuels (2012) et futurs (2050) de la navigation et des émissions liées au torchage de gaz en Arctique, en termes de qualité de l'air et d'effets radiatifs. Les résultats de simulation indiquent que les torches pétrolières sont et devraient rester une source majeure de carbone suie en Arctique, entraînant un effet réchauffant, et que la navigation en Arctique est déjà une source importante de carbone suie et d'ozone en été. En 2050, la navigation de diversion à travers l'Océan Arctique pourrait devenir la source principale de pollution locale. J'ai aussi déterminé que l'effet radiatif principal des bateaux en Arctique semblait être un refroidissement infra-rouge au TOA dû à l'ozone. Cet effet refroidissant est dû à l'inversion de température dans la couche limite arctique. Les effets radatifs directs dans l'UV et le visible sont faibles pour les bateaux, en raison du faible temps de vie des aérosols dans cette région (1.4 jours pour le carbone suie) et parce que la pollution liée aux bateaux est souvent située sous les nuages. En conséquence, il semble primordial de bien représenter les températures de peau, la structure de la couche limite et les nuages en Arctique pour prendre en compte correctement les effets radiatifs liés à ces sources locales de pollution.

References

Abdul-Razzak, H. and Ghan, S. J., A parameterization of aerosol activation: 2. Multiple aerosol types, *Journal of Geophysical Research: Atmospheres*, 105(D5), 6837–6844, doi: 10.1029/1999JD901161, URL http://dx.doi.org/10.1029/1999JD901161, 2000.

Abdul-Razzak, H. and Ghan, S. J., A parameterization of aerosol activation 3. Sectional representation, *Journal of Geophysical Research: Atmospheres*, 107(D3), AAC 1–1–AAC 1–6, doi: 10.1029/2001JD000483, URL http://dx.doi.org/10.1029/2001JD000483, 2002.

Ackerman, A. S., Toon, O. B., Stevens, D. E., Heymsfield, A. J., Ramanathan, V., and Welton, E. J., Reduction of Tropical Cloudiness by Soot, *Science*, 288(5468), 1042–1047, doi: 10.1126/science.288.5468.1042, URL http://science.sciencemag.org/content/288/5468/1042, 2000.

Adam de Villiers, R., Ancellet, G., Pelon, J., Quennehen, B., Schwarzenboeck, A., Gayet, J. F., and Law, K. S., Airborne measurements of aerosol optical properties related to early spring transport of mid-latitude sources into the Arctic, *Atmospheric Chemistry and Physics*, 10(11), 5011–5030, doi: 10.5194/acp-10-5011-2010, URL http://www.atmos-chem-phys.net/10/5011/2010/, 2010.

Adams, P. J., Seinfeld, J. H., and Koch, D. M., Global concentrations of tropospheric sulfate, nitrate, and ammonium aerosol simulated in a general circulation model, *Journal of Geophysical Research: Atmospheres*, 104(D11), 13791–13823, doi: 10.1029/1999JD900083, URL http://dx.doi.org/10.1029/1999JD900083, 1999.

Ahmadov, R., McKeen, S., Trainer, M., Banta, R., Brewer, A., Brown, S., Edwards, P. M., de Gouw, J. A., Frost, G. J., Gilman, J., Helmig, D., Johnson, B., Karion, A., Koss, A., Langford, A., Lerner, B., Olson, J., Oltmans, S., Peischl, J., Pétron, G., Pichugina, Y., Roberts, J. M., Ryerson, T., Schnell, R., Senff, C., Sweeney, C., Thompson, C., Veres, P. R., Warneke, C., Wild, R., Williams, E. J., Yuan, B., and Zamora, R., Understanding high wintertime ozone pollution events in an oil- and natural gas-producing region of the western US, *Atmospheric Chemistry and Physics*, 15(1), 411–429, doi: 10.5194/acp-15-411-2015, URL http://www.atmos-chem-phys.net/15/411/2015/, 2015.

Alapaty, K., Herwehe, J. A., Otte, T. L., Nolte, C. G., Bullock, O. R., Mallard, M. S., Kain, J. S., and Dudhia, J., Introducing subgrid-scale cloud feedbacks to radiation for regional meteorological and climate modeling, *Geophysical Research Letters*, 39(24), doi: 10.1029/2012GL054031, URL http://dx.doi.org/10.1029/2012GL054031, l24809, 2012.

Albrecht, A., Bruce, Aerosols, Cloud Microphysics, and Fractional Cloudiness, *Science*, 245(4923), 1227–1230, doi: 10.1126/science.245.4923.1227, URL http://science.sciencemag.org/content/245/4923/1227, 1989.

Aliabadi, A. A., Staebler, R. M., and Sharma, S., Air quality monitoring in communities of the Canadian Arctic during the high shipping season with a focus on local and marine pollution, *Atmospheric Chemistry and Physics*, 15(5), 2651–2673, doi: 10.5194/acp-15-2651-2015, URL http://www.atmos-chem-phys.net/15/2651/2015/, 2015.

Allen, R. J. and Landuyt, W., The vertical distribution of black carbon in CMIP5 models: Comparison to observations and the importance of convective transport, *Journal of Geophysical Research: Atmospheres*, 119(8), 4808–4835, doi: 10.1002/2014JD021595, URL http://dx.doi.org/10.1002/2014JD021595, 2014.

Amann, M., Bertok, I., Borken-Kleefeld, J., Cofala, J., Heyes, C., Höglund-Isaksson, L., Klimont, Z., Nguyen, B., Posch, M., Rafaj, P., Sandler, R., Schöpp, W., Wagner, F., and Winiwarte, W., Cost-effective control of air quality and greenhouse gases in Europe: Modeling and policy applications, *Environmental Modelling & Software*, 26(12), 1489 – 1501, doi: http://dx.doi.org/10.1016/j.envsoft.2011.07.012, URL http://www.sciencedirect.com/science/article/pii/S1364815211001733, 2011.

AMAP, AMAP Assessment 2006: Acidifying Pollutants, Arctic Haze, and Acidification in the Arctic, Technical report, Arctic Monitoring and Assessment Programme (AMAP), Oslo, Norway, 2006.

AMAP, AMAP Assessment 2015: Black carbon and ozone as Arctic climate forcers, Technical report, Arctic Monitoring and Assessment Programme (AMAP), Oslo, Norway, 2015.

Ancellet, G., Pelon, J., Blanchard, Y., Quennehen, B., Bazureau, A., Law, K. S., and Schwarzenboeck, A., Transport of aerosol to the Arctic: analysis of CALIOP and French aircraft data during the spring 2008 POLARCAT campaign, *Atmospheric Chemistry and Physics*, 14(16), 8235–8254, doi: 10.5194/acp-14-8235-2014, URL http://www.atmos-chem-phys.net/14/8235/2014/, 2014.

Andreae, M. and Rosenfeld, D., Aerosol-cloud-precipitation interactions. Part 1. The nature and sources of cloud-active aerosols, *Earth-Science Reviews*, 89(1â 2), 13–41, doi: http://dx.doi.org/10.1016/j.earscirev.2008.03.001, URL http://www.sciencedirect.com/science/article/pii/S0012825208000317, 2008.

Ångström, A. K., On the atmospheric transmission of sun radiation and on dust in the air, *Geogr. Ann.*, 11, 156–Ð166, doi: 10.2307/519399, 1929.

Arctic Council, Arctic Marine Shipping Assessment 2009 Report, Technical report, Arctic Council, Tromsø, Norway,, 2009.

Asman, W. A. H., Sutton, M. A., R., and Schjørring, J. K., Ammonia: emission, atmospheric transport and deposition, *New Phytologist*, 139(1), 27–48, doi: 10.1046/j.1469-8137.1998.00180.x, URL http://dx.doi.org/10.1046/j.1469-8137.1998.00180.x, 1998.

Barnard, J. C., Fast, J. D., Paredes-Miranda, G., Arnott, W. P., and Laskin, A., Technical Note: Evaluation of the WRF-Chem "Aerosol Chemical to Aerosol Optical Properties" Module using data from the MILAGRO campaign, *Atmospheric Chemistry and Physics*, 10(15), 7325–7340, doi: 10.5194/acp-10-7325-2010, URL http://www.atmos-chem-phys.net/10/7325/2010/, 2010.

Barrie, L. A., Arctic air pollution: An overview of current knowledge, *Atmospheric Environment (1967)*, 20(4), 643 – 663, doi: http://dx.doi.org/10.1016/0004-6981(86)90180-0, URL http://www.sciencedirect.com/science/article/pii/0004698186901800, 1986.

Barth, M. C., Wong, J., Bela, M. M., Pickering, K. E., Li, Y., and Cummings, K., Simulations of Lightning-Generated NOx for Parameterized Convection in the WRF-Chem model, in *XV International Conference on Atmospheric Electricity, 15-20 June 2014, Norman, Oklahoma, U.S.A.*, 2014.

Beecken, J., Mellqvist, J., Salo, K., Ekholm, J., Jalkanen, J.-P., Johansson, L., Litvinenko, V., Volodin, K., and Frank-Kamenetsky, D. A., Emission factors of SO_2, NO_x and particles from ships in Neva Bay from ground-based and helicopter-borne measurements and AIS-based modeling, *Atmospheric Chemistry and Physics*, 15(9), 5229–5241, doi: 10.5194/acp-15-5229-2015, URL http://www.atmos-chem-phys.net/15/5229/2015/, 2015.

Berg, L. K., Shrivastava, M., Easter, R. C., Fast, J. D., Chapman, E. G., Liu, Y., and Ferrare, R. A., A new WRF-Chem treatment for studying regional-scale impacts of cloud processes on aerosol and trace gases in parameterized cumuli, *Geoscientific Model Development*, 8(2), 409–429, doi: 10.5194/gmd-8-409-2015, URL http://www.geosci-model-dev.net/8/409/2015/, 2015.

Berntsen, T. K., Isaksen, I. S. A., Myhre, G., Fuglestvedt, J. S., Stordal, F., Larsen, T. A., Freckleton, R. S., and Shine, K. P., Effects of anthropogenic emissions on tropospheric ozone and its radiative forcing, *Journal of Geophysical Research: Atmospheres*, 102(D23), 28101–28126, doi: 10.1029/97JD02226, URL http://dx.doi.org/10.1029/97JD02226, 1997.

Bessagnet, B., Menut, L., Curci, G., Hodzic, A., Guillaume, B., Liousse, C., Moukhtar, S., Pun, B., Seigneur, C., and Schulz, M., Regional modeling of carbonaceous aerosols over Europe—focus on secondary organic aerosols, *Journal of Atmospheric Chemistry*, 61(3), 175–202, doi: 10.1007/s10874-009-9129-2, URL http://dx.doi.org/10.1007/s10874-009-9129-2, 2009.

Bindoff, N., Stott, P., Achuta Rao, K., Allen, M., Gillett, N., Gutzler, D., Hansingo, K., Hegerl, G., Hu, Y., Jain, S., Mokhov, I., Overland, J., Perlwitz, J., Sebbari, R., and Zhang, X., *Detection and Attribution of Climate Change: from Global to Regional*, book section 10, pp. 867–952, Cambridge University Press, Cambridge, United Kingdom and New York, NY, USA, ISBN ISBN 978-1-107-66182-0, doi: 10.1017/CBO9781107415324.022, URL www.climatechange2013.org, 2013.

Blasing, T., Recent greenhouse gas concentrations, doi: 10.3334/CDIAC/atg.032, URL http://cdiac.ornl.gov/pns/current_ghg.html, 2014.

Bodeker, G. E., Hassler, B., Young, P. J., and Portmann, R. W., A vertically resolved, global, gap-free ozone database for assessing or constraining global climate model simulations, *Earth System Science Data*, 5(1), 31–43, doi: 10.5194/essd-5-31-2013, URL http://www.earth-syst-sci-data.net/5/31/2013/, 2013.

Bohren, C. F. and Huffman, D. R., *Absorption and Scattering of Light by Small Particles.*, Wiley, New York, 1983.

Bond, T. C., Habib, G., and Bergstrom, R. W., Limitations in the enhancement of visible light absorption due to mixing state, *Journal of Geophysical Research: Atmospheres*, 111(D20), doi: 10.1029/2006JD007315, URL http://dx.doi.org/10.1029/2006JD007315, d20211, 2006.

Bottenheim, J. W., Barrie, L. A., Atlas, E., Heidt, L. E., Niki, H., Rasmussen, R. A., and Shepson, P. B., Depletion of lower tropospheric ozone during Arctic spring: The Polar Sunrise Experiment 1988, *Journal of Geophysical Research: Atmospheres*, 95(D11), 18555–18568, doi: 10.1029/JD095iD11p18555, URL http://dx.doi.org/10.1029/JD095iD11p18555, 1990.

Boucher, O., On Aerosol Direct Shortwave Forcing and the Henyey-Greenstein Phase Function, *Journal of the Atmospheric Sciences*, 55(1), 128–134, doi: 10.1175/1520-0469(1998)055<0128:OADSFA>2.0.CO;2, URL http://dx.doi.org/10.1175/1520-0469(1998)055<0128:OADSFA>2.0.CO;2, 1998.

Boucher, O., Randall, D., Artaxo, P., Bretherton, C., Feingold, G., Forster, P., Kerminen, V.-M., Kondo, Y., Liao, H., Lohmann, U., Rasch, P., Satheesh, S., Sherwood, S., Stevens, B., and Zhang, X., *Clouds and Aerosols*, book section 7, pp. 571–658, Cambridge University Press, Cambridge, United Kingdom and New York, NY, USA, ISBN ISBN 978-1-107-66182-0, doi: 10.1017/CBO9781107415324.016, URL www.climatechange2013.org, 2013.

Briggs, G. A., A Plume Rise Model Compared with Observations, *Journal of the Air Pollution Control Association*, 15(9), 433–438, doi: 10.1080/00022470.1965.10468404, URL http://dx.doi.org/10.1080/00022470.1965.10468404, 1965.

Brioude, J., Arnold, D., Stohl, A., Cassiani, M., Morton, D., Seibert, P., Angevine, W., Evan, S., Dingwell, A., Fast, J. D., Easter, R. C., Pisso, I., Burkhart, J., and Wotawa, G., The Lagrangian particle dispersion model FLEXPART-WRF version 3.1, *Geoscientific Model Development*, 6(6), 1889–1904, doi: 10.5194/gmd-6-1889-2013, URL http://www.geosci-model-dev.net/6/1889/2013/, 2013.

Brock, C. A., Cozic, J., Bahreini, R., Froyd, K. D., Middlebrook, A. M., McComiskey, A., Brioude, J., Cooper, O. R., Stohl, A., Aikin, K. C., de Gouw, J. A., Fahey, D. W., Ferrare, R. A., Gao, R.-S., Gore, W., Holloway, J. S., Hübler, G., Jefferson, A., Lack, D. A., Lance, S., Moore, R. H., Murphy, D. M., Nenes, A., Novelli, P. C., Nowak, J. B., Ogren, J. A., Peischl, J., Pierce, R. B., Pilewskie, P., Quinn, P. K., Ryerson, T. B., Schmidt, K. S., Schwarz, J. P., Sodemann, H., Spackman, J. R., Stark, H., Thomson, D. S., Thornberry, T., Veres, P., Watts, L. A., Warneke, C., and Wollny, A. G., Characteristics, sources, and transport of aerosols measured in spring 2008 during the aerosol, radiation, and cloud processes affecting Arctic Climate (ARCPAC) Project, *Atmospheric Chemistry and Physics*, 11(6), 2423–2453, doi: 10.5194/acp-11-2423-2011, URL http://www.atmos-chem-phys.net/11/2423/2011/, 2011.

Browse, J., Carslaw, K. S., Arnold, S. R., Pringle, K., and Boucher, O., The scavenging processes controlling the seasonal cycle in Arctic sulphate and black carbon aerosol, *Atmospheric Chemistry and Physics*, 12(15), 6775–6798, doi: 10.5194/acp-12-6775-2012, URL http://www.atmos-chem-phys.net/12/6775/2012/, 2012.

Browse, J., Carslaw, K. S., Schmidt, A., and Corbett, J. J., Impact of future Arctic shipping on high-latitude black carbon deposition, *Geophysical Research Letters*, 40(16), 4459–4463, doi: 10.1002/grl.50876, URL http://dx.doi.org/10.1002/grl.50876, 2013.

Buhaug, ., Corbett, J. J., Endresen, Ø., Eyring, V., Faber, J., Hanayama, S., Lee, D. S., Lee, D., Lindstad, H., Markowska, A. Z., Mjelde, A., Nelissen, D., Nilsen, J., Palsson, C., Winebrake, J. J., Wu, W.-Q., and Yoshida, K., Second IMO GHG study, Technical report, International Maritime Organization (IMO), London, UK, 2009.

Capaldo, K., Corbett, J. J., Kasibhatla, P., Fischbeck, P., and Pandis, S. N., Effects of ship emissions on sulphur cycling and radiative climate forcing over the ocean, *Nature*, 400(6746), 743–746, URL http://dx.doi.org/10.1038/23438, 1999.

Carlson, T. N. and Boland, F. E., Analysis of Urban-Rural Canopy Using a Surface Heat Flux/Temperature Model, *Journal of Applied Meteorology*, 17(7), 998–1013, doi: 10.1175/1520-0450(1978)017<0998:AOURCU>2.0.CO;2, URL http://dx.doi.org/10.1175/1520-0450(1978)017<0998:AOURCU>2.0.CO;2, 1978.

Carter, W. P. L., Documentation of the SAPRC-99 chemical mechanism for VOC reactivity assessment. Final Report to California Air Resources Board Contract 92-329 and Contract 95-308,, Technical report, Air Pollution Research Center and College of Engineering Center for Environmental Research and Technology, University of California Riverside, California, 2000.

Carter, W. P. L., Development of an Improved Chemical Speciation Database for Processing Emissions of Volatile Organic Compounds for Air Quality Models, URL http://www.engr.ucr.edu/~carter/emitdb/, (last access: 29 February 2016), 2014.

Cecil, D. J., Buechler, D. E., and Blakeslee, R. J., Gridded lightning climatology from TRMM-LIS and OTD: Dataset description, *Atmospheric Research*, 135â 136, 404–414, doi: http://dx.doi.org/10.1016/j.atmosres.2012.06.028, URL http://www.sciencedirect.com/science/article/pii/S0169809512002323, 2014.

Cesana, G., Kay, J. E., Chepfer, H., English, J. M., and de Boer, G., Ubiquitous low-level liquid-containing Arctic clouds: New observations and climate model constraints from CALIPSO-GOCCP, *Geophysical Research Letters*, 39(20), doi: 10.1029/2012GL053385, URL http://dx.doi.org/10.1029/2012GL053385, l20804, 2012.

Chameides, W. and Walker, J. C. G., A photochemical theory of tropospheric ozone, *Journal of Geophysical Research*, 78(36), 8751–8760, doi: 10.1029/JC078i036p08751, URL http://dx.doi.org/10.1029/JC078i036p08751, 1973.

Chapman, S., A theory of upper stratospheric ozone, *Mem. R. Meteorol. Soc.*, 3, 103Ð125, 1930.

Charlson, R. J., Schwartz, S. E., Hales, J. M., Cess, R. D., Coakley, J. A., Hansen, J. E., and Hofmann, D. J., Climate Forcing by Anthropogenic Aerosols, *Science*, 255(5043), 423–430, doi: 10.1126/science.255.5043.423, URL http://science.sciencemag.org/content/255/5043/423, 1992.

Chen, F. and Dudhia, J., Coupling an Advanced Land Surface-Hydrology Model with the Penn State-NCAR MM5 Modeling System. Part I: Model Implementation and Sensitivity, *Mon. Wea. Rev.*, 129(4), 569–585, doi: 10.1175/1520-0493(2001)129<0569:CAALSH>2.0.CO;2, URL http://dx.doi.org/10.1175/1520-0493(2001)129<0569:CAALSH>2.0.CO;2, 2001.

Chin, M., Ginoux, P., Kinne, S., Torres, O., Holben, B. N., Duncan, B. N., Martin, R. V., Logan, J. A., Higurashi, A., and Nakajima, T., Tropospheric Aerosol Optical Thickness from the GOCART Model and Comparisons with Satellite and Sun Photometer Measurements, *J. Atmos. Sci.*, 59(3), 461–483, doi: 10.1175/1520-0469(2002)059<0461:TAOTFT>2.0.CO;2, URL http://dx.doi.org/10.1175/1520-0469(2002)059<0461:TAOTFT>2.0.CO;2, 2002.

Chin, M., Jacob, D. J., Gardner, G. M., Foreman-Fowler, M. S., Spiro, P. A., and Savoie, D. L., A global three-dimensional model of tropospheric sulfate, *Journal of Geophysical Research: Atmospheres*, 101(D13), 18667–18690, doi: 10.1029/96JD01221, URL http://dx.doi.org/10.1029/96JD01221, 1996.

Chou, M.-D. and Suarez, M. J., A Solar Radiation Parameterization (CLIRAD-SW) for Atmospheric Studies, nASA/TM-1999-104606, 15, 48 pp., 1999.

Chýlek, P., Srivastava, V., Pinnick, R. G., and Wang, R. T., Scattering of electromagnetic waves by composite spherical particles: experiment and effective medium approximations, *Appl. Opt.*, 27(12), 2396–2404, doi: 10.1364/AO.27.002396, URL http://ao.osa.org/abstract.cfm?URI=ao-27-12-2396, 1988.

Ciais, P., Sabine, C., Bala, G., Bopp, L., Brovkin, V., Canadell, J., Chhabra, A., DeFries, R., Galloway, J., Heimann, M., Jones, C., Le Quéré, C., Myneni, R., Piao, S., and Thornton, P., *Carbon and Other Biogeochemical Cycles*, book section 6, pp. 465–570, Cambridge University Press, Cambridge, United Kingdom and New York, NY, USA, ISBN ISBN 978-1-107-66182-0, doi: 10.1017/CBO9781107415324.015, URL www.climatechange2013.org, 2013.

Cohan, D. S., Hu, Y., and Russell, A. G., Dependence of ozone sensitivity analysis on grid resolution, *Atmospheric Environment*, 40(1), 126–135, doi: http://dx.doi.org/10.1016/j.atmosenv.2005.09.031, URL http://www.sciencedirect.com/science/article/pii/S1352231005008666, 2006.

Collins, M., Knutti, R., Arblaster, J., Dufresne, J.-L., Fichefet, T., Friedlingstein, P., Gao, X., Gutowski, W., Johns, T., Krinner, G., Shongwe, M., Tebaldi, C., Weaver, A., and Wehner, M., *Long-term Climate Change: Projections, Commitments and Irreversibility*, book section 12, pp. 1029–1136, Cambridge University Press, Cambridge, United Kingdom and New York, NY, USA, ISBN ISBN 978-1-107-66182-0, doi: 10.1017/CBO9781107415324.024, URL www.climatechange2013.org, 2013.

Cooper, D., Exhaust emissions from high speed passenger ferries, *Atmospheric Environment*, 35(24), 4189–4200, doi: http://dx.doi.org/10.1016/S1352-2310(01)00192-3, URL http://www.sciencedirect.com/science/article/pii/S1352231001001923, 2001.

Corbett, J. J. and Fischbeck, P., Emissions from Ships, *Science*, 278(5339), 823–824, doi: 10.1126/science.278.5339.823, URL http://science.sciencemag.org/content/278/5339/823, 1997.

Corbett, J. J. and Koehler, H. W., Updated emissions from ocean shipping, *Journal of Geophysical Research: Atmospheres*, 108(D20), doi: 10.1029/2003JD003751, URL http://dx.doi.org/10.1029/2003JD003751, 4650, 2003.

Corbett, J. J., Lack, D. A., Winebrake, J. J., Harder, S., Silberman, J. A., and Gold, M., Arctic shipping emissions inventories and future scenarios, *Atmospheric Chemistry and Physics*, 10(19), 9689–9704, doi: 10.5194/acp-10-9689-2010, URL http://www.atmos-chem-phys.net/10/9689/2010/, 2010.

Corbett, J. J., Winebrake, J. J., Green, E. H., Kasibhatla, P., Eyring, V., and Lauer, A., Mortality from Ship Emissions: A Global Assessment, *Environmental Science & Technology*, 41(24), 8512–8518, doi: 10.1021/es071686z, URL http://dx.doi.org/10.1021/es071686z, pMID: 18200887, 2007.

Cowling, E. B., Acid precipitation in historical perspective, *Environmental Science & Technology*, 16(2), 110A–123A, doi: 10.1021/es00096a725, URL http://dx.doi.org/10.1021/es00096a725, pMID: 22656201, 1982.

Crutzen, P., Photochemical reactions initiated by and influencing ozone in unpolluted tropospheric air, *Tellus A*, 26(1-2), 47–57, URL http://www.tellusa.net/index.php/tellusa/article/view/9736, 1974.

Crutzen, P. J. and Zimmerman, P. H., The changing photochemistry of the troposphere, *Tellus A*, 43(4), 136–151, doi: 10.1034/j.1600-0870.1991.00012.x, URL http://dx.doi.org/10.1034/j.1600-0870.1991.00012.x, 1991.

Dalsøren, S. B., Eide, M. S., Endresen, Ø., Mjelde, A., Gravir, G., and Isaksen, I. S. A., Update on emissions and environmental impacts from the international fleet of ships: the contribution from major ship types and ports, *Atmospheric Chemistry and Physics*, 9(6), 2171–2194, doi: 10.5194/acp-9-2171-2009, URL http://www.atmos-chem-phys.net/9/2171/2009/, 2009.

Dalsøren, S. B., Endresen, Ø., Isaksen, I. S. A., Gravir, G., and Sørgård, E., Environmental impacts of the expected increase in sea transportation, with a particular focus on oil and gas scenarios for Norway and northwest Russia, *Journal of Geophysical Research: Atmospheres*, 112(D2), doi: 10.1029/2005JD006927, URL http://dx.doi.org/10.1029/2005JD006927, d02310, 2007.

Dalsøren, S. B., Samset, B. H., Myhre, G., Corbett, J. J., Minjares, R., Lack, D., and Fuglestvedt, J. S., Environmental impacts of shipping in 2030 with a particular focus on the Arctic region, *Atmospheric Chemistry and Physics*, 13(4), 1941–1955, doi: 10.5194/acp-13-1941-2013, URL http://www.atmos-chem-phys.net/13/1941/2013/, 2013.

Delmas, R., Mégie, G., and Peuch, V.-H., *Physique et chimie de l'atmosphère*, 2005.

Deluc, J. A., *Recherches sur les modifications de l'atmosphère*, 2 Vol., Geneva, 1772.

Denier van der Gon, H., Hendriks, C., Kuenen, J., Segers, A. A., and Visschedijk, A., Description of current temporal emission patterns and sensitivity of predicted AQ for temporal emission patterns, TNO Report, EU FP7 MACC deliverable report D_DEMIS_1.3, Technical report, TNO, Princetonlaan 6, 3584 CB Utrecht, The Netherlands, 2011.

Devasthale, A., Willén, U., Karlsson, K.-G., and Jones, C. G., Quantifying the clear-sky temperature inversion frequency and strength over the Arctic Ocean during summer and winter seasons from AIRS profiles, *Atmospheric Chemistry and Physics*, 10(12), 5565–5572, doi: 10.5194/acp-10-5565-2010, URL http://www.atmos-chem-phys.net/10/5565/2010/, 2010.

Dingenen, R. V., Dentener, F. J., Raes, F., Krol, M. C., Emberson, L., and Cofala, J., The global impact of ozone on agricultural crop yields under current and future air quality legislation, *Atmospheric Environment*, 43(3), 604–618, doi: http://dx.doi.org/10.1016/j.atmosenv.2008.10.033, URL http://www.sciencedirect.com/science/article/pii/S1352231008009424, 2009.

Dusek, U., Frank, G. P., Hildebrandt, L., Curtius, J., Schneider, J., Walter, S., Chand, D., Drewnick, F., Hings, S., Jung, D., Borrmann, S., and Andreae, M. O., Size Matters More Than Chemistry for Cloud-Nucleating Ability of Aerosol Particles, *Science*, 312(5778), 1375–1378, doi: 10.1126/science.1125261, URL http://science.sciencemag.org/content/312/5778/1375, 2006.

Eckhardt, S., Hermansen, O., Grythe, H., Fiebig, M., Stebel, K., Cassiani, M., Baecklund, A., and Stohl, A., The influence of cruise ship emissions on air pollution in Svalbard – a harbinger of a more polluted Arctic?, *Atmospheric Chemistry and Physics*, 13(16), 8401–8409, doi: 10.5194/acp-13-8401-2013, URL http://www.atmos-chem-phys.net/13/8401/2013/, 2013.

Eckhardt, S., Quennehen, B., Olivié, D. J. L., Berntsen, T. K., Cherian, R., Christensen, J. H., Collins, W., Crepinsek, S., Daskalakis, N., Flanner, M., Herber, A., Heyes, C., Hodnebrog, Ø., Huang, L., Kanakidou, M., Klimont, Z., Langner, J., Law, K. S., Lund, M. T., Mahmood, R., Massling, A., Myriokefalitakis, S., Nielsen, I. E., Nøjgaard, J. K., Quaas, J., Quinn, P. K., Raut, J.-C., Rumbold, S. T., Schulz, M., Sharma, S., Skeie, R. B., Skov, H., Uttal, T., von Salzen, K., and Stohl, A., Current model capabilities for simulating black carbon and sulfate concentrations in the Arctic atmosphere: a multi-model evaluation using a comprehensive measurement data set, *Atmospheric Chemistry and Physics*, 15(16), 9413–9433, doi: 10.5194/acp-15-9413-2015, URL http://www.atmos-chem-phys.net/15/9413/2015/, 2015.

Elvidge, C. D., Baugh, K. E., Tuttle, B. T., Howard, D. W., A. T. abd Pack, Milesi, C., and Erwin, E. H., A twelve year record of national and global gas flaring volumes estimated using satellite data: final report to the World Bank, URL http://www.ngdc.noaa.gov/dmsp/interest/gas_flares.html, nOAA National Geophysical Data Center, Boulder, US, 2007.

Elvidge, C. D., Ziskin, D., Baugh, K. E., Tuttle, B. T., Ghosh, T., Pack, D. W., Erwin, E. H., and Zhizhin, M., A Fifteen Year Record of Global Natural Gas Flaring Derived from Satellite Data, *Energies*, 2(3), 595, doi: 10.3390/en20300595, URL http://www.mdpi.com/1996-1073/2/3/595, 2009.

Emmons, L. K., Arnold, S. R., Monks, S. A., Huijnen, V., Tilmes, S., Law, K. S., Thomas, J. L., Raut, J.-C., Bouarar, I., Turquety, S., Long, Y., Duncan, B., Steenrod, S., Strode, S., Flemming, J., Mao, J., Langner, J., Thompson, A. M., Tarasick, D., Apel, E. C., Blake, D. R., Cohen, R. C., Dibb, J., Diskin, G. S., Fried, A., Hall, S. R., Huey, L. G., Weinheimer, A. J., Wisthaler, A., Mikoviny, T., Nowak, J., Peischl, J., Roberts, J. M., Ryerson, T., Warneke, C., and Helmig, D., The POLARCAT Model Intercomparison Project (POLMIP): overview and evaluation with observations, *Atmospheric Chemistry and Physics*, 15(12), 6721–6744, doi: 10.5194/acp-15-6721-2015, URL http://www.atmos-chem-phys.net/15/6721/2015/, 2015.

Emmons, L. K., Walters, S., Hess, P. G., Lamarque, J.-F., Pfister, G. G., Fillmore, D., Granier, C., Guenther, A., Kinnison, D., Laepple, T., Orlando, J., Tie, X., Tyndall, G., Wiedinmyer, C., Baughcum, S. L., and Kloster, S., Description and evaluation of the Model for Ozone and Related chemical Tracers, version 4 (MOZART-4), *Geoscientific Model Development*, 3(1), 43–67, doi: 10.5194/gmd-3-43-2010, URL http://www.geosci-model-dev.net/3/43/2010/, 2010.

Endresen, Ø., Sørgård, E., Sundet, J. K., Dalsøren, S. B., Isaksen, I. S. A., Berglen, T. F., and Gravir, G., Emission from international sea transportation and environmental impact, *Journal of Geophysical Research: Atmospheres*, 108(D17), doi: 10.1029/2002JD002898, URL http://dx.doi.org/10.1029/2002JD002898, 4560, 2003.

EPA, Analysis of commercial marine vessels emissions and fuel consumption data,, Technical report, Tech. Rep. EPA420-R-00-002, United States Environmental Protection Agency, 2000.

Erisman, J. W., Pul, A. V., and Wyers, P., Parametrization of surface resistance for the quantification of atmospheric deposition of acidifying pollutants and ozone, *Atmospheric Environment*, 28(16), 2595–2607, doi: http://dx.doi.org/10.1016/1352-2310(94)90433-2, URL http://www.sciencedirect.com/science/article/pii/1352231094904332, 1994.

Eyring, V., Isaksen, I. S., Berntsen, T., Collins, W. J., Corbett, J. J., Endresen, O., Grainger, R. G., Moldanova, J., Schlager, H., and Stevenson, D. S., Transport impacts on atmosphere and climate: Shipping, *Atmospheric Environment*, 44(37), 4735–4771, doi: http://dx.doi.org/10.1016/j.atmosenv.2009.04.059, URL http://www.sciencedirect.com/science/article/pii/S1352231009003379, transport Impacts on Atmosphere and Climate: The {ATTICA} Assessment Report, 2010.

Eyring, V., Stevenson, D. S., Lauer, A., Dentener, F. J., Butler, T., Collins, W. J., Ellingsen, K., Gauss, M., Hauglustaine, D. A., Isaksen, I. S. A., Lawrence, M. G., Richter, A., Rodriguez, J. M., Sanderson, M., Strahan, S. E., Sudo, K., Szopa, S., van Noije, T. P. C., and Wild, O., Multi-model simulations of the impact of international shipping on Atmospheric Chemistry and Climate in 2000 and 2030, *Atmospheric Chemistry and Physics*, 7(3), 757–780, doi: 10.5194/acp-7-757-2007, URL http://www.atmos-chem-phys.net/7/757/2007/, 2007.

Fahey, K. M. and Pandis, S. N., Optimizing model performance: variable size resolution in cloud chemistry modeling, *Atmospheric Environment*, 35(26), 4471–4478, doi: http://dx.doi.org/10.1016/S1352-2310(01)00224-2, URL http://www.sciencedirect.com/science/article/pii/S1352231001002242, 2001.

Fast, J. D. and Easter, R. C., A Lagrangian particle dispersion model compatible with WRF, 7th WRF Users Workshop, NCAR, 19Ð 22 June 2006, Boulder, CO, 2006.

Fast, J. D., Gustafson, W. I., Easter, R. C., Zaveri, R. A., Barnard, J. C., Chapman, E. G., Grell, G. A., and Peckham, S. E., Evolution of ozone, particulates, and aerosol direct radiative forcing in the vicinity of Houston using a fully coupled meteorology-chemistry-aerosol model, *Journal of Geophysical Research: Atmospheres*, 111(D21), doi: 10.1029/2005JD006721, URL http://dx.doi.org/10.1029/2005JD006721, d21305, 2006.

Fast, J. D., Gustafson Jr., W. I., Berg, L. K., Shaw, W. J., Pekour, M., Shrivastava, M., Barnard, J. C., Ferrare, R. A., Hostetler, C. A., Hair, J. A., Erickson, M., Jobson, B. T., Flowers, B., Dubey, M. K., Springston, S., Pierce, R. B., Dolislager, L., Pederson, J., and Zaveri, R. A., Transport and mixing patterns over Central California during the carbonaceous aerosol and radiative effects study (CARES), *Atmospheric Chemistry and Physics*, 12(4), 1759–1783, doi: 10.5194/acp-12-1759-2012, URL http://www.atmos-chem-phys.net/12/1759/2012/, 2012.

Ferek, R. J., Hobbs, P. V., Radke, L. F., Herring, J. A., Sturges, W. T., and Cota, G. F., Dimethyl sulfide in the Arctic atmosphere, *Journal of Geophysical Research: Atmospheres*, 100(D12), 26093–26104, doi: 10.1029/95JD02374, URL http://dx.doi.org/10.1029/95JD02374, 1995.

Finlayson-Pitts, B. and Pitts, J., *Chemistry of the Upper and Lower Atmosphere: Theory, Experiments, and Applica- tions*, Academic Press, New York, 1999.

Fisher, J. A., Jacob, D. J., Wang, Q., Bahreini, R., Carouge, C. C., Cubison, M. J., Dibb, J. E., Diehl, T., Jimenez, J. L., Leibensperger, E. M., Lu, Z., Meinders, M. B., Pye, H. O., Quinn, P. K., Sharma, S., Streets, D. G., van Donkelaar, A., and Yantosca, R. M., Sources, distribution, and acidity of sulfate-ammonium aerosol in the Arctic in winter-spring, *Atmospheric Environment*, 45(39), 7301–7318, doi: http://dx.doi.org/10.1016/j.atmosenv.2011.08.030, URL http://www.sciencedirect.com/science/article/pii/S1352231011008545, 2011.

Fishman, J., Wozniak, A. E., and Creilson, J. K., Global distribution of tropospheric ozone from satellite measurements using the empirically corrected tropospheric ozone residual technique: Identification of the regional aspects of air pollution, *Atmospheric Chemistry and Physics*, 3(4), 893–907, doi: 10.5194/acp-3-893-2003, URL http://www.atmos-chem-phys.net/3/893/2003/, 2003.

Flamant, C. and Pelon, J., Atmospheric boundary-layer structure over the Mediterranean during a Tramontane event, *Quarterly Journal of the Royal Meteorological Society*, 122(536), 1741–1778, doi: 10.1002/qj.49712253602, URL http://dx.doi.org/10.1002/qj.49712253602, 1996.

Flanner, M. G., Arctic climate sensitivity to local black carbon, *Journal of Geophysical Research: Atmospheres*, 118(4), 1840–1851, doi: 10.1002/jgrd.50176, URL http://dx.doi.org/10.1002/jgrd.50176, 2013.

Flanner, M. G., Zender, C. S., Randerson, J. T., and Rasch, P. J., Present-day climate forcing and response from black carbon in snow, *Journal of Geophysical Research: Atmospheres*, 112(D11), doi: 10.1029/2006JD008003, URL http://dx.doi.org/10.1029/2006JD008003, d11202, 2007.

Flato, G., Marotzke, J., Abiodun, B., Braconnot, P., Chou, S., Collins, W., Cox, P., Driouech, F., Emori, S., Eyring, V., Forest, C., Gleckler, P., Guilyardi, E., Jakob, C., Kattsov, V., Reason, C., and Rummukainen, M., *Evaluation of Climate Models*, book section 9, pp. 741–866, Cambridge University Press, Cambridge, United Kingdom and New York, NY, USA, ISBN ISBN 978-1-107-66182-0, doi: 10.1017/CBO9781107415324.020, URL www.climatechange2013.org, 2013.

Forster, F. P. M., Freckleton, S. R., and Shine, P. K., On aspects of the concept of radiative forcing, *Climate Dynamics*, 13(7), 547–560, doi: 10.1007/s003820050182, URL http://dx.doi.org/10.1007/s003820050182, 1997.

Forster, P., Ramaswamy, V., Artaxo, P., Berntsen, T., Betts, R., Fahey, D., Haywood, J., Lean, J., Lowe, D., Myhre, G., Nganga, J., Prinn, R., Raga, M., G. Schulz, and Van Dorland, R., *Climate Change 2007: The Physical Science Basis. Contribution of Working Group I to the Fourth Assessment Report of the Intergovernmental Panel on Climate Change*, chapter Changes in Atmospheric Constituents and in Radiative Forcing, Cambridge University Press, Cambridge, United Kingdom and New York, NY, USA, 2007.

Freitas, S. R., Longo, K. M., Chatfield, R., Latham, D., Silva Dias, M. A. F., Andreae, M. O., Prins, E., Santos, J. C., Gielow, R., and Carvalho Jr., J. A., Including the sub-grid scale plume rise of vegetation fires in low resolution atmospheric transport models, *Atmospheric Chemistry and Physics*, 7(13), 3385–3398, doi: 10.5194/acp-7-3385-2007, URL http://www.atmos-chem-phys.net/7/3385/2007/, 2007.

Frossard, A. A., Shaw, P. M., Russell, L. M., Kroll, J. H., Canagaratna, M. R., Worsnop, D. R., Quinn, P. K., and Bates, T. S., Springtime Arctic haze contributions of submicron organic particles from European and Asian combustion sources, *Journal of Geophysical Research: Atmospheres*, 116(D5), doi: 10.1029/2010JD015178, URL http://dx.doi.org/10.1029/2010JD015178, d05205, 2011.

Fuchs, N. A., *The mechanics of aerosols. Translated by R. E. Daisley and Marina Fuchs*, volume 91, John Wiley & Sons, Ltd, doi: 10.1002/qj.49709138822, URL http://dx.doi.org/10.1002/qj.49709138822, 1964.

Fuglestvedt, J., Berntsen, T., Eyring, V., Isaksen, I., Lee, D. S., and Sausen, R., Shipping Emissions: From Cooling to Warming of Climate-and Reducing Impacts on Health, *Environmental Science & Technology*, 43(24), 9057–9062, doi: 10.1021/es901944r, URL http://dx.doi.org/10.1021/es901944r, pMID: 19924852, 2009.

Fuglestvedt, J., Berntsen, T., Myhre, G., Rypdal, K., and Skeie, R. B., Climate forcing from the transport sectors, *Proceedings of the National Academy of Sciences*, 105(2), 454–458, doi: 10.1073/pnas.0702958104, URL http://www.pnas.org/content/105/2/454.abstract, 2008.

Fuglestvedt, J. S., Daløren, S. B., Samset, B. H., Berntsen, T., Myhre, G., Hodnebrog, Ø., Eide, M. S., and Bergh, T. F., Climate Penalty for Shifting Shipping to the Arctic, *Environmental Science & Technology*, 48(22), 13273–13279, doi: 10.1021/es502379d, URL http://dx.doi.org/10.1021/es502379d, pMID: 25347302, 2014.

Garrett, T. J., Brattström, S., Sharma, S., Worthy, D. E. J., and Novelli, P., The role of scavenging in the seasonal transport of black carbon and sulfate to the Arctic, *Geophysical Research Letters*,

38(16), doi: 10.1029/2011GL048221, URL http://dx.doi.org/10.1029/2011GL048221, l16805, 2011.

Garrett, T. J. and Zhao, C., Increased Arctic cloud longwave emissivity associated with pollution from mid-latitudes, *Nature*, 440(7085), 787–789, URL http://dx.doi.org/10.1038/nature04636, 2006.

Gautier, D. L., Bird, K. J., Charpentier, R. R., Grantz, A., Houseknecht, D. W., Klett, T. R., Moore, T. E., Pitman, J. K., Schenk, C. J., Schuenemeyer, J. H., Sørensen, K., Tennyson, M. E., Valin, Z. C., and Wandrey, C. J., Assessment of Undiscovered Oil and Gas in the Arctic, *Science*, 324(5931), 1175–1179, doi: 10.1126/science.1169467, URL http://science.sciencemag.org/content/324/5931/1175, 2009.

Gong, S. L., Barrie, L. A., and Blanchet, J.-P., Modeling sea-salt aerosols in the atmosphere: 1. Model development, *Journal of Geophysical Research: Atmospheres*, 102(D3), 3805–3818, doi: 10.1029/96JD02953, URL http://dx.doi.org/10.1029/96JD02953, 1997.

Granier, C., Niemeier, U., Jungclaus, J. H., Emmons, L., Hess, P., Lamarque, J.-F., Walters, S., and Brasseur, G. P., Ozone pollution from future ship traffic in the Arctic northern passages, *Geophysical Research Letters*, 33(13), n/a–n/a, doi: 10.1029/2006GL026180, URL http://dx.doi.org/10.1029/2006GL026180, l13807, 2006.

Grannas, A. M., Jones, A. E., Dibb, J., Ammann, M., Anastasio, C., Beine, H. J., Bergin, M., Bottenheim, J., Boxe, C. S., Carver, G., Chen, G., Crawford, J. H., Dominé, F., Frey, M. M., Guzmán, M. I., Heard, D. E., Helmig, D., Hoffmann, M. R., Honrath, R. E., Huey, L. G., Hutterli, M., Jacobi, H. W., Klán, P., Lefer, B., McConnell, J., Plane, J., Sander, R., Savarino, J., Shepson, P. B., Simpson, W. R., Sodeau, J. R., von Glasow, R., Weller, R., Wolff, E. W., and Zhu, T., An overview of snow photochemistry: evidence, mechanisms and impacts, *Atmospheric Chemistry and Physics*, 7(16), 4329–4373, doi: 10.5194/acp-7-4329-2007, URL http://www.atmos-chem-phys.net/7/4329/2007/, 2007.

Greenaway, K., Experiences with Arctic flying weather, in *Royal Meteorological Society Canadian Branch (Nov. 30, 1950), Toronto, Ontario.*, 1950.

Grell, G. A. and Dévényi, D., A generalized approach to parameterizing convection combining ensemble and data assimilation techniques, *Geophysical Research Letters*, 29(14), 38–1–38–4, doi: 10.1029/2002GL015311, URL http://dx.doi.org/10.1029/2002GL015311, 2002.

Grell, G. A., Peckham, S. E., Schmitz, R., McKeen, S. A., Frost, G., Skamarock, W. C., and Eder, B., Fully coupled "online" chemistry within the WRF model, *Atmospheric Environment*, 39(37), 6957–6975, doi: http://dx.doi.org/10.1016/j.atmosenv.2005.04.027, URL http://www.sciencedirect.com/science/article/pii/S1352231005003560, 2005.

Grenfell, T. C., Warren, S. G., and Mullen, P. C., Reflection of solar radiation by the Antarctic snow surface at ultraviolet, visible, and near-infrared wavelengths, *Journal of Geophysical Research: Atmospheres*, 99(D9), 18669–18684, doi: 10.1029/94JD01484, URL http://dx.doi.org/10.1029/94JD01484, 1994.

Guenther, A., Karl, T., Harley, P., Wiedinmyer, C., Palmer, P. I., and Geron, C., Estimates of global terrestrial isoprene emissions using MEGAN (Model of Emissions of Gases and Aerosols from Nature), *Atmospheric Chemistry and Physics*, 6(11), 3181–3210, doi: 10.5194/acp-6-3181-2006, URL http://www.atmos-chem-phys.net/6/3181/2006/, 2006.

Gustafson, W. I., Qian, Y., and Fast, J. D., Downscaling aerosols and the impact of neglected subgrid processes on direct aerosol radiative forcing for a representative global climate model grid spacing, *Journal of Geophysical Research: Atmospheres*, 116(D13), doi: 10.1029/2010JD015480, URL http://dx.doi.org/10.1029/2010JD015480, d13303, 2011.

Hansen, J., Sato, M., and Ruedy, R., Radiative forcing and climate response, *Journal of Geophysical Research: Atmospheres*, 102(D6), 6831–6864, doi: 10.1029/96JD03436, URL http://dx.doi.org/10.1029/96JD03436, 1997.

Hartmann, D., Klein Tank, A., Rusticucci, M., Alexander, L., Brönnimann, S., Charabi, Y., Dentener, F., Dlugokencky, E., Easterling, D., Kaplan, A., Soden, B., Thorne, P., Wild, M., and Zhai, P., *Observations: Atmosphere and Surface*, book section 2, pp. 159–254, Cambridge University Press, Cambridge, United Kingdom and New York, NY, USA, ISBN ISBN 978-1-107-66182-0, doi: 10.1017/CBO9781107415324.008, URL www.climatechange2013.org, 2013.

Haylock, M. R., Hofstra, N., Klein Tank, A. M. G., Klok, E. J., Jones, P. D., and New, M., A European daily high-resolution gridded data set of surface temperature and precipitation for 1950–2006, *Journal of Geophysical Research: Atmospheres*, 113(D20), doi: 10.1029/2008JD010201, URL http://dx.doi.org/10.1029/2008JD010201, d20119, 2008.

Haywood, J. and Boucher, O., Estimates of the direct and indirect radiative forcing due to tropospheric aerosols: A review, *Reviews of Geophysics*, 38(4), 513–543, doi: 10.1029/1999RG000078, URL http://dx.doi.org/10.1029/1999RG000078, 2000.

Haywood, J. M. and Shine, K. P., The effect of anthropogenic sulfate and soot aerosol on the clear sky planetary radiation budget, *Geophysical Research Letters*, 22(5), 603–606, doi: 10.1029/95GL00075, URL http://dx.doi.org/10.1029/95GL00075, 1995.

Haywood, J. M. and Shine, K. P., Multi-spectral calculations of the direct radiative forcing of tropospheric sulphate and soot aerosols using a column model, *Quarterly Journal of the Royal Meteorological Society*, 123(543), 1907–1930, doi: 10.1002/qj.49712354307, URL http://dx.doi.org/10.1002/qj.49712354307, 1997.

Heller, W., Remarks on Refractive Index Mixture Rules, *The Journal of Physical Chemistry*, 69(4), 1123–1129, doi: 10.1021/j100888a006, URL http://dx.doi.org/10.1021/j100888a006, 1965.

Hodzic, A., Jimenez, J. L., Madronich, S., Canagaratna, M. R., DeCarlo, P. F., Kleinman, L., and Fast, J., Modeling organic aerosols in a megacity: potential contribution of semi-volatile and intermediate volatility primary organic compounds to secondary organic aerosol formation, *Atmospheric Chemistry and Physics*, 10(12), 5491–5514, doi: 10.5194/acp-10-5491-2010, URL http://www.atmos-chem-phys.net/10/5491/2010/, 2010.

Hodzic, A., Kasibhatla, P. S., Jo, D. S., Cappa, C., Jimenez, J. L., Madronich, S., and Park, R. J., Rethinking the global secondary organic aerosol (SOA) budget: stronger production, faster removal, shorter lifetime, *Atmospheric Chemistry and Physics Discussions*, 15, 32413–32468, doi: 10.5194/acpd-15-32413-2015, URL http://www.atmos-chem-phys-discuss.net/15/32413/2015/, 2015.

Huang, K., Fu, J. S., Prikhodko, V. Y., Storey, J. M., Romanov, A., Hodson, E. L., Cresko, J., Morozova, I., Ignatieva, Y., and Cabaniss, J., Russian anthropogenic black carbon: Emission reconstruction and Arctic black carbon simulation, *Journal of Geophysical Research: Atmospheres*, 120(21), 11,306–11,333, doi: 10.1002/2015JD023358, URL http://dx.doi.org/10.1002/2015JD023358, 2015JD023358, 2015.

Huang, L., Gong, S. L., Jia, C. Q., and Lavoué, D., Importance of deposition processes in simulating the seasonality of the Arctic black carbon aerosol, *Journal of Geophysical Research: Atmospheres*, 115(D17), doi: 10.1029/2009JD013478, URL http://dx.doi.org/10.1029/2009JD013478, d17207, 2010.

Huszar, P., Cariolle, D., Paoli, R., Halenka, T., Belda, M., Schlager, H., Miksovsky, J., and Pisoft, P., Modeling the regional impact of ship emissions on NO_x and ozone levels over the Eastern Atlantic and Western Europe using ship plume parameterization, *Atmospheric Chemistry and Physics*,

10(14), 6645–6660, doi: 10.5194/acp-10-6645-2010, URL http://www.atmos-chem-phys.net/10/6645/2010/, 2010.

Iacono, M. and Nehrkorn, T., Assessment of Radiation Options in the Advanced Research WRF weather forecast model. In Proceedings, in *1st Atmospheric System Research Science Team Meeting*, OfÞce of Science, U.S. Department of Energy, Bethesda, MD, URL http://www.arm.gov/publications/db, 2010.

Iacono, M. J., Delamere, J. S., Mlawer, E. J., Shephard, M. W., Clough, S. A., and Collins, W. D., Radiative forcing by long-lived greenhouse gases: Calculations with the AER radiative transfer models, *Journal of Geophysical Research: Atmospheres*, 113(D13), doi: 10.1029/2008JD009944, URL http://dx.doi.org/10.1029/2008JD009944, d13103, 2008.

IMO, Revised MARPOL Annex VI, Resolution MEP C. 176, Technical report, International Maritime Organization, URL http://www.imo.org/blast/blastDataHelper.asp?data_id=23760, 2008.

IMO, Report of the Marine Environment Protection Committee on the Sixty-First Session, Technical Report MEPC 61/24, International Maritime Organization, URL http://docs.imo.org, 2010.

IPCC, *Annex II: Climate System Scenario Tables*, book section AII, pp. 1395–1446, Cambridge University Press, Cambridge, United Kingdom and New York, NY, USA, ISBN ISBN 978-1-107-66182-0, doi: 10.1017/CBO9781107415324.030, URL www.climatechange2013.org, 2013a.

IPCC, *Climate Change 2013: The Physical Science Basis. Contribution of Working Group I to the Fifth Assessment Report of the Intergovernmental Panel on Climate Change*, Cambridge University Press, Cambridge, United Kingdom and New York, NY, USA, ISBN ISBN 978-1-107-66182-0, doi: 10.1017/CBO9781107415324, URL www.climatechange2013.org, 2013b.

IPCC, *Climate Change 2014: Impacts, Adaptation, and Vulnerability. Part B: Regional Aspects. Contribution of Working Group II to the Fifth Assessment Report of the Intergovernmental Panel on Climate Change*, Cambridge University Press, Cambridge, United Kingdom and New York, NY, USA, 2014.

IPCO, Costa Deliziosa and Favolosa equipped with WFE systems from IPCO Power, URL http://www.ipcopower.com/blog/costa-deliziosa-and-favolosa-equipped-with-wfe-systems-from-ipco-power, iPCO Power, 2015.

Iversen, T. and Joranger, E., Arctic air pollution and large scale atmospheric flows, *Atmospheric Environment (1967)*, 19(12), 2099–2108, doi: http://dx.doi.org/10.1016/0004-6981(85)90117-9, URL http://www.sciencedirect.com/science/article/pii/0004698185901179, 1985.

Jacob, D. J., *Introduction to Atmospheric Chemistry*, Princeton University Press, 1999.

Jacob, D. J., Heterogeneous chemistry and tropospheric ozone, *Atmospheric Environment*, 34(12–14), 2131–2159, doi: http://dx.doi.org/10.1016/S1352-2310(99)00462-8, URL http://www.sciencedirect.com/science/article/pii/S1352231099004628, 2000.

Jacob, D. J., Wofsy, S. C., Bakwin, P. S., Fan, S.-M., Harriss, R. C., Talbot, R. W., Bradshaw, J. D., Sandholm, S. T., Singh, H. B., Browell, E. V., Gregory, G. L., Sachse, G. W., Shipham, M. C., Blake, D. R., and Fitzjarrald, D. R., Summertime photochemistry of the troposphere at high northern latitudes, *Journal of Geophysical Research: Atmospheres*, 97(D15), 16421–16431, doi: 10.1029/91JD01968, URL http://dx.doi.org/10.1029/91JD01968, 1992.

Jacobson, M. Z., Short-term effects of controlling fossil-fuel soot, biofuel soot and gases, and methane on climate, Arctic ice, and air pollution health, *Journal of Geophysical Research: Atmospheres*, 115(D14), doi: 10.1029/2009JD013795, URL http://dx.doi.org/10.1029/2009JD013795, d14209, 2010.

Jacobson, M. Z., Turco, R. P., Jensen, E. J., and Toon, O. B., Modeling coagulation among particles of different composition and size, *Atmospheric Environment*, 28(7), 1327–1338, doi: http://dx.doi.org/10.1016/1352-2310(94)90280-1, URL http://www.sciencedirect.com/science/article/pii/1352231094902801, 1994.

Jalkanen, J.-P., Brink, A., Kalli, J., Pettersson, H., Kukkonen, J., and Stipa, T., A modelling system for the exhaust emissions of marine traffic and its application in the Baltic Sea area, *Atmospheric Chemistry and Physics*, 9(23), 9209–9223, doi: 10.5194/acp-9-9209-2009, URL http://www.atmos-chem-phys.net/9/9209/2009/, 2009.

Jalkanen, J.-P., Johansson, L., Kukkonen, J., Brink, A., Kalli, J., and Stipa, T., Extension of an assessment model of ship traffic exhaust emissions for particulate matter and carbon monoxide, *Atmospheric Chemistry and Physics*, 12(5), 2641–2659, doi: 10.5194/acp-12-2641-2012, URL http://www.atmos-chem-phys.net/12/2641/2012/, 2012.

Janji , Z. I., The Step-Mountain Eta Coordinate Model: Further Developments of the Convection, Viscous Sublayer, and Turbulence Closure Schemes, *Mon. Wea. Rev.*, 122(5), 927–945, doi: 10.1175/1520-0493(1994)122<0927:TSMECM>2.0.CO;2, URL http://dx.doi.org/10.1175/1520-0493(1994)122<0927:TSMECM>2.0.CO;2, 1994.

Janssens-Maenhout, G., Crippa, M., Guizzardi, D., Dentener, F., Muntean, M., Pouliot, G., Keating, T., Zhang, Q., Kurokawa, J., Wankmüller, R., Denier van der Gon, H., Kuenen, J. J. P., Klimont, Z., Frost, G., Darras, S., Koffi, B., and Li, M., HTAP_v2.2: a mosaic of regional and global emission grid maps for 2008 and 2010 to study hemispheric transport of air pollution, *Atmospheric Chemistry and Physics*, 15(19), 11411–11432, doi: 10.5194/acp-15-11411-2015, URL http://www.atmos-chem-phys.net/15/11411/2015/, 2015.

Jiao, C. and Flanner, M., Changing black carbon transport to the Arctic from present day to the end of 21st century, *Journal of Geophysical Research: Atmospheres*, doi: 10.1002/2015JD023964, URL http://dx.doi.org/10.1002/2015JD023964, 2015JD023964, 2016.

Johnson, D. W., Cresser, M. S., Nilsson, S. I., Turner, J., Ulrich, B., Binkley, D., and Cole, D. W., Soil changes in forest ecosystems: evidence for and probable causes, *Proceedings of the Royal Society of Edinburgh Section B: Biological Sciences*, 97, 81–116, doi: 10.1017/S0269727000005303, URL http://journals.cambridge.org/article_S0269727000005303, 1990.

Jonson, J. E., Jalkanen, J. P., Johansson, L., Gauss, M., and Denier van der Gon, H. A. C., Model calculations of the effects of present and future emissions of air pollutants from shipping in the Baltic Sea and the North Sea, *Atmospheric Chemistry and Physics*, 15(2), 783–798, doi: 10.5194/acp-15-783-2015, URL http://www.atmos-chem-phys.net/15/783/2015/, 2015.

Kanakidou, M., Seinfeld, J. H., Pandis, S. N., Barnes, I., Dentener, F. J., Facchini, M. C., Van Dingenen, R., Ervens, B., Nenes, A., Nielsen, C. J., Swietlicki, E., Putaud, J. P., Balkanski, Y., Fuzzi, S., Horth, J., Moortgat, G. K., Winterhalter, R., Myhre, C. E. L., Tsigaridis, K., Vignati, E., Stephanou, E. G., and Wilson, J., Organic aerosol and global climate modelling: a review, *Atmospheric Chemistry and Physics*, 5(4), 1053–1123, doi: 10.5194/acp-5-1053-2005, URL http://www.atmos-chem-phys.net/5/1053/2005/, 2005.

Karl, M., Guenther, A., Köble, R., Leip, A., and Seufert, G., A new European plant-specific emission inventory of biogenic volatile organic compounds for use in atmospheric transport models, *Biogeosciences*, 6(6), 1059–1087, doi: 10.5194/bg-6-1059-2009, URL http://www.biogeosciences.net/6/1059/2009/, 2009.

Kellogg, W. W., Climatic feedback mechanisms involving the polar regions, *Climate of the Arctic*, pp. 111–116, 1975.

Khon, V. C., Mokhov, I. I., Latif, M., Semenov, V. A., and Park, W., Perspectives of Northern Sea Route and Northwest Passage in the twenty-first century, *Climatic Change*, 100(3), 757–768, doi: 10.1007/s10584-009-9683-2, URL http://dx.doi.org/10.1007/s10584-009-9683-2, 2009.

Kirtman, B., Power, S., Adedoyin, J., Boer, G., Bojariu, R., Camilloni, I., Doblas-Reyes, F., Fiore, A., Kimoto, M., Meehl, G., Prather, M., Sarr, A., Schär, C., Sutton, R., van Oldenborgh, G., Vecchi, G., and Wang, H., *Near-term Climate Change: Projections and Predictability*, book section 11, pp. 953–1028, Cambridge University Press, Cambridge, United Kingdom and New York, NY, USA, ISBN ISBN 978-1-107-66182-0, doi: 10.1017/CBO9781107415324.023, URL www.climatechange2013.org, 2013.

Klimont, Z., Hoglund, L., Heyes, C., Rafaj, P., Schoepp, W., Cofala, J., Borken-Kleefeld, J., Purohit, P., Kupiainen, K., Winiwarter, W., Amann, M., Zhao, B., Wang, S. X., Bertok, I., and Sander, R., Global scenarios of air pollutants and methane: 1990–2050, in preparation, 2015.

Klonecki, A., Hess, P., Emmons, L., Smith, L., Orlando, J., and Blake, D., Seasonal changes in the transport of pollutants into the Arctic troposphere-model study, *Journal of Geophysical Research: Atmospheres*, 108(D4), doi: 10.1029/2002JD002199, URL http://dx.doi.org/10.1029/2002JD002199, 8367, 2003.

Koch, D. and Del Genio, A. D., Black carbon semi-direct effects on cloud cover: review and synthesis, *Atmospheric Chemistry and Physics*, 10(16), 7685–7696, doi: 10.5194/acp-10-7685-2010, URL http://www.atmos-chem-phys.net/10/7685/2010/, 2010.

Koch, D., Schulz, M., Kinne, S., McNaughton, C., Spackman, J. R., Balkanski, Y., Bauer, S., Berntsen, T., Bond, T. C., Boucher, O., Chin, M., Clarke, A., De Luca, N., Dentener, F., Diehl, T., Dubovik, O., Easter, R., Fahey, D. W., Feichter, J., Fillmore, D., Freitag, S., Ghan, S., Ginoux, P., Gong, S., Horowitz, L., Iversen, T., Kirkevåg, A., Klimont, Z., Kondo, Y., Krol, M., Liu, X., Miller, R., Montanaro, V., Moteki, N., Myhre, G., Penner, J. E., Perlwitz, J., Pitari, G., Reddy, S., Sahu, L., Sakamoto, H., Schuster, G., Schwarz, J. P., Seland, Ø., Stier, P., Takegawa, N., Takemura, T., Textor, C., van Aardenne, J. A., and Zhao, Y., Evaluation of black carbon estimations in global aerosol models, *Atmospheric Chemistry and Physics*, 9(22), 9001–9026, doi: 10.5194/acp-9-9001-2009, URL http://www.atmos-chem-phys.net/9/9001/2009/, 2009.

Kumar, R., Naja, M., Pfister, G. G., Barth, M. C., Wiedinmyer, C., and Brasseur, G. P., Simulations over South Asia using the Weather Research and Forecasting model with Chemistry (WRF-Chem): chemistry evaluation and initial results, *Geoscientific Model Development*, 5(3), 619–648, doi: 10.5194/gmd-5-619-2012, URL http://www.geosci-model-dev.net/5/619/2012/, 2012.

Lacis, A. A., Wuebbles, D. J., and Logan, J. A., Radiative forcing of climate by changes in the vertical distribution of ozone, *Journal of Geophysical Research: Atmospheres*, 95(D7), 9971–9981, doi: 10.1029/JD095iD07p09971, URL http://dx.doi.org/10.1029/JD095iD07p09971, 1990.

Lamarque, J.-F., Bond, T. C., Eyring, V., Granier, C., Heil, A., Klimont, Z., Lee, D., Liousse, C., Mieville, A., Owen, B., Schultz, M. G., Shindell, D., Smith, S. J., Stehfest, E., Van Aardenne, J., Cooper, O. R., Kainuma, M., Mahowald, N., McConnell, J. R., Naik, V., Riahi, K., and van Vuuren, D. P., Historical (1850–2000) gridded anthropogenic and biomass burning emissions of reactive gases and aerosols: methodology and application, *Atmospheric Chemistry and Physics*, 10(15), 7017–7039, doi: 10.5194/acp-10-7017-2010, URL http://www.atmos-chem-phys.net/10/7017/2010/, 2010.

Lana, A., Bell, T. G., Simó, R., Vallina, S. M., Ballabrera-Poy, J., Kettle, A. J., Dachs, J., Bopp, L., Saltzman, E. S., Stefels, J., Johnson, J. E., and Liss, P. S., An updated climatology of surface dimethlysulfide concentrations and emission fluxes in the global ocean, *Global Biogeochemical Cycles*, 25(1), doi: 10.1029/2010GB003850, URL http://dx.doi.org/10.1029/2010GB003850, gB1004, 2011.

Laprise, R., The Euler Equations of Motion with Hydrostatic Pressure as an Independent Variable, *Monthly Weather Review*, 120(1), 197–207, doi: 10.1175/1520-0493(1992)120<0197:TEEOMW>2.0.CO;2, URL http://dx.doi.org/10.1175/1520-0493(1992)120<0197:TEEOMW>2.0.CO;2, 1992.

Larsen, J. N., Anisimov, O. A., Constable, A., Hollowed, A. B., Maynard, N., Prestrud, P., Prowse, T. D., and Stone, J. M. R., Polar regions, in V. R. Barros, C. B. Field, D. J. Dokken, M. D. Mastrandrea, K. J. Mach, T. E. Bilir, M. Chatterjee, K. L. Ebi, Y. O. Estrada, R. C. Genova, B. Girma, E. S. Kissel, A. N. Levy, S. MacCracken, P. R. Mastrandrea, and L. L. White (editors), *Climate Change 2014: Impacts, Adaptation, and Vulnerability. Part B: Regional Aspects. Contribution of Working Group II to the Fifth Assessment Report of the Intergovernmental Panel of Climate Change*, pp. 1567–1612–, Cambridge University Press, Cambridge, United Kingdom and New York, NY, USA, 2014.

Lauer, A., Eyring, V., Hendricks, J., Jöckel, P., and Lohmann, U., Global model simulations of the impact of ocean-going ships on aerosols, clouds, and the radiation budget, *Atmospheric Chemistry and Physics*, 7(19), 5061–5079, doi: 10.5194/acp-7-5061-2007, URL http://www.atmos-chem-phys.net/7/5061/2007/, 2007.

Law, K. S., Stohl, A., Quinn, P. K., Brock, C. A., Burkhart, J. F., Paris, J.-D., Ancellet, G., Singh, H. B., Roiger, A., Schlager, H., Dibb, J., Jacob, D. J., Arnold, S. R., Pelon, J., and Thomas, J. L., Arctic Air Pollution: New Insights from POLARCAT-IPY, *Bull. Amer. Meteor. Soc.*, 95(12), 1873–1895, doi: 10.1175/BAMS-D-13-00017.1, URL http://dx.doi.org/10.1175/BAMS-D-13-00017.1, 2014.

Lee, C., Martin, R. V., van Donkelaar, A., Lee, H., Dickerson, R. R., Hains, J. C., Krotkov, N., Richter, A., Vinnikov, K., and Schwab, J. J., SO2 emissions and lifetimes: Estimates from inverse modeling using in situ and global, space-based (SCIAMACHY and OMI) observations, *Journal of Geophysical Research: Atmospheres*, 116(D6), n/a–n/a, doi: 10.1029/2010JD014758, URL http://dx.doi.org/10.1029/2010JD014758, d06304, 2011.

Lee, Y. H., Lamarque, J.-F., Flanner, M. G., Jiao, C., Shindell, D. T., Berntsen, T., Bisiaux, M. M., Cao, J., Collins, W. J., Curran, M., Edwards, R., Faluvegi, G., Ghan, S., Horowitz, L. W., McConnell, J. R., Ming, J., Myhre, G., Nagashima, T., Naik, V., Rumbold, S. T., Skeie, R. B., Sudo, K., Takemura, T., Thevenon, F., Xu, B., and Yoon, J.-H., Evaluation of preindustrial to present-day black carbon and its albedo forcing from Atmospheric Chemistry and Climate Model Intercomparison Project (ACCMIP), *Atmospheric Chemistry and Physics*, 13(5), 2607–2634, doi: 10.5194/acp-13-2607-2013, URL http://www.atmos-chem-phys.net/13/2607/2013/, 2013.

Lelieveld, J., Evans, J. S., Fnais, M., Giannadaki, D., and Pozzer, A., The contribution of outdoor air pollution sources to premature mortality on a global scale, *Nature*, 525(7569), 367–371, URL http://dx.doi.org/10.1038/nature15371, 2015.

Levy, H., Photochemistry of the lower troposphere, *Planetary and Space Science*, 20(6), 919–935, doi: http://dx.doi.org/10.1016/0032-0633(72)90177-8, URL http://www.sciencedirect.com/science/article/pii/0032063372901778, 1972.

Likens, G. E., Bormann, F. H., and Johnson, N. M., Acid Rain, *Environment: Science and Policy for Sustainable Development*, 14(2), 33–40, doi: 10.1080/00139157.1972.9933001, URL http://dx.doi.org/10.1080/00139157.1972.9933001, 1972.

Lindholt, L., *The Economy of the North*, chapter Arctic natural resources in a global perspective, pp. 27–39, Statistics Norway, Oslo, Norway, 2006.

Lindholt, L. and Glomsrød, S., The Arctic: No big bonanza for the global petroleum industry, *Energy Economics*, 34(5), 1465 – 1474, doi: http://dx.doi.org/10.1016/j.eneco.2012.06.020, URL http://www.sciencedirect.com/science/article/pii/S0140988312001296, 2012.

Liu, M. and Kronbak, J., The potential economic viability of using the Northern Sea Route (NSR) as an alternative route between Asia and Europe, *Journal of Transport Geography*, 18(3), 434–444, doi: http://dx.doi.org/10.1016/j.jtrangeo.2009.08.004, URL http://www.sciencedirect.com/science/article/pii/S0966692309001252, tourism and climate change, 2010.

Liu, X., Easter, R. C., Ghan, S. J., Zaveri, R., Rasch, P., Shi, X., Lamarque, J.-F., Gettelman, A., Morrison, H., Vitt, F., Conley, A., Park, S., Neale, R., Hannay, C., Ekman, A. M. L., Hess, P., Mahowald, N., Collins, W., Iacono, M. J., Bretherton, C. S., Flanner, M. G., and Mitchell, D., Toward a minimal representation of aerosols in climate models: description and evaluation in the Community Atmosphere Model CAM5, *Geoscientific Model Development*, 5(3), 709–739, doi: 10.5194/gmd-5-709-2012, URL http://www.geosci-model-dev.net/5/709/2012/, 2012.

Lund, M. T., Eyring, V., Fuglestvedt, J., Hendricks, J., Lauer, A., Lee, D., and Righi, M., Global-Mean Temperature Change from Shipping toward 2050: Improved Representation of the Indirect Aerosol Effect in Simple Climate Models, *Environmental Science & Technology*, 46(16), 8868–8877, doi: 10.1021/es301166e, URL http://dx.doi.org/10.1021/es301166e, pMID: 22830995, 2012.

Lund Myhre, C., Toledano, C., Myhre, G., Stebel, K., Yttri, K. E., Aaltonen, V., Johnsrud, M., Frioud, M., Cachorro, V., de Frutos, A., Lihavainen, H., Campbell, J. R., Chaikovsky, A. P., Shiobara, M., Welton, E. J., and Tørseth, K., Regional aerosol optical properties and radiative impact of the extreme smoke event in the European Arctic in spring 2006, *Atmospheric Chemistry and Physics*, 7(22), 5899–5915, doi: 10.5194/acp-7-5899-2007, URL http://www.atmos-chem-phys.net/7/5899/2007/, 2007.

Lyyränen, J., Jokiniemi, J., Kauppinen, E. I., and Joutsensaari, J., Aerosol characterisation in medium-speed diesel engines operating with heavy fuel oils, *Journal of Aerosol Science*, 30(6), 771–784, doi: http://dx.doi.org/10.1016/S0021-8502(98)00763-0, URL http://www.sciencedirect.com/science/article/pii/S0021850298007630, 1999.

Manabe, S., Bryan, K., and Spelman, M. J., Transient Response of a Global Ocean-Atmosphere Model to a Doubling of Atmospheric Carbon Dioxide, *J. Phys. Oceanogr.*, 20(5), 722–749, doi: 10.1175/1520-0485(1990)020<0722:TROAGO>2.0.CO;2, URL http://dx.doi.org/10.1175/1520-0485(1990)020<0722:TROAGO>2.0.CO;2, 1990.

Marelle, L., Raut, J.-C., Thomas, J. L., Law, K. S., Quennehen, B., Ancellet, G., Pelon, J., Schwarzenboeck, A., and Fast, J. D., Transport of anthropogenic and biomass burning aerosols from Europe to the Arctic during spring 2008, *Atmospheric Chemistry and Physics*, 15(7), 3831–3850, doi: 10.5194/acp-15-3831-2015, URL http://www.atmos-chem-phys.net/15/3831/2015/, 2015.

Marelle, L., Thomas, J. L., Raut, J.-C., Law, K. S., Jalkanen, J.-P., Johansson, L., Roiger, A., Schlager, H., Kim, J., Reiter, A., and Weinzierl, B., Air quality and radiative impacts of Arctic shipping emissions in the summertime in northern Norway: from the local to the regional scale, *Atmospheric Chemistry and Physics*, 16(4), 2359–2379, doi: 10.5194/acp-16-2359-2016, URL http://www.atmos-chem-phys.net/16/2359/2016/, 2016.

Mauritsen, T., Sedlar, J., Tjernström, M., Leck, C., Martin, M., Shupe, M., Sjogren, S., Sierau, B., Persson, P. O. G., Brooks, I. M., and Swietlicki, E., An Arctic CCN-limited cloud-aerosol regime, *Atmospheric Chemistry and Physics*, 11(1), 165–173, doi: 10.5194/acp-11-165-2011, URL http://www.atmos-chem-phys.net/11/165/2011/, 2011.

Mauzerall, D. L., Jacob, D. J., Fan, S.-M., Bradshaw, J. D., Gregory, G. L., Sachse, G. W., and Blake, D. R., Origin of tropospheric ozone at remote high northern latitudes in summer, *Journal of Geophysical Research: Atmospheres*, 101(D2), 4175–4188, doi: 10.1029/95JD03224, URL http://dx.doi.org/10.1029/95JD03224, 1996.

McEwen, J. D. and Johnson, M. R., Black carbon particulate matter emission factors for buoyancy-driven associated gas flares, *Journal of the Air & Waste Management Association*, 62(3), 307–321, doi: 10.1080/10473289.2011.650040, URL http://dx.doi.org/10.1080/10473289.2011.650040, 2012.

McKuin, B. and Campbell, J. E., Emissions and climate forcing from global and Arctic fishing vessels, *Journal of Geophysical Research: Atmospheres*, 121(4), 1844–1858, doi: 10.1002/2015JD023747, URL http://dx.doi.org/10.1002/2015JD023747, 2015JD023747, 2016.

Meloni, D., di Sarra, A., Iorio, T. D., and Fiocco, G., Influence of the vertical profile of Saharan dust on the visible direct radiative forcing, *Journal of Quantitative Spectroscopy and Radiative Transfer*, 93(4), 397 – 413, doi: http://dx.doi.org/10.1016/j.jqsrt.2004.08.035, URL http://www.sciencedirect.com/science/article/pii/S0022407304003486, 2005.

Ménégoz, M., Krinner, G., Balkanski, Y., Cozic, A., Boucher, O., and Ciais, P., Boreal and temperate snow cover variations induced by black carbon emissions in the middle of the 21st century, *The Cryosphere*, 7(2), 537–554, doi: 10.5194/tc-7-537-2013, URL http://www.the-cryosphere.net/7/537/2013/, 2013.

Meng, Z., Dabdub, D., and Seinfeld, J. H., Chemical Coupling Between Atmospheric Ozone and Particulate Matter, *Science*, 277(5322), 116–119, doi: 10.1126/science.277.5322.116, URL http://science.sciencemag.org/content/277/5322/116, 1997.

Mie, G., Beiträge zur Optik trüber Medien, speziell kolloidaler Metallösungen, *Annalen der Physik*, 330(3), 377–445, doi: 10.1002/andp.19083300302, URL http://dx.doi.org/10.1002/andp.19083300302, 1908.

Miola, A. and Ciuffo, B., Estimating air emissions from ships: Meta-analysis of modelling approaches and available data sources, *Atmospheric Environment*, 45(13), 2242–2251, doi: http://dx.doi.org/10.1016/j.atmosenv.2011.01.046, URL http://www.sciencedirect.com/science/article/pii/S1352231011000872, 2011.

Mitchell, M., Visual range in the polar regions with particular reference to the Alaskan Arctic, *Journal of Atmospheric and Terrestrial Physics*, Special Supplement, 195–211, 1956.

Mlawer, E. J., Taubman, S. J., Brown, P. D., Iacono, M. J., and Clough, S. A., Radiative transfer for inhomogeneous atmospheres: RRTM, a validated correlated-k model for the longwave, *Journal of Geophysical Research: Atmospheres*, 102(D14), 16663–16682, doi: 10.1029/97JD00237, URL http://dx.doi.org/10.1029/97JD00237, 1997.

Mokhov, I. and Khon, V., *Natural Processes in Polar Regions, Part 2*, chapter Assessment of the Northern Sea Route perspectives under climate changes on the basis of simulations with the climate models ensemble, pp. 20–27, The Institute of Geography (IG), Russian Academy of Sciences (RAS), IG RAS, Moscow, Russia, 2008.

Mölders, N., Porter, S. E., Cahill, C. F., and Grell, G. A., Influence of ship emissions on air quality and input of contaminants in southern Alaska National Parks and Wilderness Areas during the 2006 tourist season, *Atmospheric Environment*, 44(11), 1400–1413, doi: http://dx.doi.org/10.1016/j.atmosenv.2010.02.003, URL http://www.sciencedirect.com/science/article/pii/S1352231010001044, 2010.

Morrison, H., Thompson, G., and Tatarskii, V., Impact of Cloud Microphysics on the Development of Trailing Stratiform Precipitation in a Simulated Squall Line: Comparison of One- and Two-Moment Schemes, *Mon. Wea. Rev.*, 137(3), 991–1007, doi: 10.1175/2008MWR2556.1, URL http://dx.doi.org/10.1175/2008MWR2556.1, 2009.

Muniz, I. P., Freshwater acidification: its effects on species and communities of freshwater microbes, plants and animals, *Proceedings of the Royal Society of Edinburgh Section B: Biological Sciences*, 97, 227–254, doi: 10.1017/S0269727000005364, URL http://journals.cambridge.org/article_S0269727000005364, 1990.

Murrells, T. P., Passant, N. R., Thistlethwaite, G., Wagner, A., Li, Y., Bush, T., Norris, J., Coleman, P. J., Walker, C., Stewart, R. A., Tsagatakis, I., Conolly, C., Brophy, N. C. J., , and Okamura, S., UK Emissions of Air Pollutants 1970 to 2007, Technical report, AEA, URL http://naei.defra.gov.uk/reports/reports?report_id=630), (last access: 29 June 2015), 2010.

Myhre, G., Shindell, D., Bréon, F.-M., Collins, W., Fuglestvedt, J., Huang, J., Koch, D., Lamarque, J.-F., Lee, D., Mendoza, B., Nakajima, T., Robock, A., Stephens, G., Takemura, T., and Zhang, H., *Anthropogenic and Natural Radiative Forcing*, book section 8, pp. 659–740, Cambridge University Press, Cambridge, United Kingdom and New York, NY, USA, ISBN ISBN 978-1-107-66182-0, doi: 10.1017/CBO9781107415324.018, URL www.climatechange2013.org, 2013.

Nakanishi, M. and Niino, H., An Improved Mellor–Yamada Level-3 Model: Its Numerical Stability and Application to a Regional Prediction of Advection Fog, *Boundary-Layer Meteorology*, 119(2), 397–407, doi: 10.1007/s10546-005-9030-8, URL http://dx.doi.org/10.1007/s10546-005-9030-8, 2006.

Nick, F. M., Vieli, A., Andersen, M. L., Joughin, I., Payne, A., Edwards, T. L., Pattyn, F., and van de Wal, R. S. W., Future sea-level rise from Greenland main outlet glaciers in a warming climate, *Nature*, 497(7448), 235–238, URL http://dx.doi.org/10.1038/nature12068, 2013.

Nicolet, M., On the molecular scattering in the terrestrial atmosphere : An empirical formula for its calculation in the homosphere, *Planetary and Space Science*, 32(11), 1467–1468, doi: http://dx.doi.org/10.1016/0032-0633(84)90089-8, URL http://www.sciencedirect.com/science/article/pii/0032063384900898, 1984.

Nightingale, P. D., Malin, G., Law, C. S., Watson, A. J., Liss, P. S., Liddicoat, M. I., Boutin, J., and Upstill-Goddard, R. C., In situ evaluation of air-sea gas exchange parameterizations using novel conservative and volatile tracers, *Global Biogeochemical Cycles*, 14(1), 373–387, doi: 10.1029/1999GB900091, URL http://dx.doi.org/10.1029/1999GB900091, 2000.

Northern Sea Route information office, Transit statistics, URL http://www.arctic-lio.com/nsr_transits, 2013.

Ødemark, K., Dalsøren, S. B., Samset, B. H., Berntsen, T. K., Fuglestvedt, J. S., and Myhre, G., Short-lived climate forcers from current shipping and petroleum activities in the Arctic, *Atmospheric Chemistry and Physics*, 12(4), 1979–1993, doi: 10.5194/acp-12-1979-2012, URL http://www.atmos-chem-phys.net/12/1979/2012/, 2012.

Ooyama, K. V., A Thermodynamic Foundation for Modeling the Moist Atmosphere, *Journal of the Atmospheric Sciences*, 47(21), 2580–2593, doi: 10.1175/1520-0469(1990)047<2580:ATFFMT>2.0.CO;2, URL http://dx.doi.org/10.1175/1520-0469(1990)047<2580:ATFFMT>2.0.CO;2, 1990.

Peckham, S., Grell, G., Pagowski, M., McKeen, S., Ahmadov, R., , Barth, M., Wiedinmyer, C., Pfister, G., Kumar, R., Knote, C., Hodzic, A., Guenther, A., Fast, J., Gustafson, W., Easter, R., Shrivastava, M., Zaveri, R., Barnard, J., Lowe, D., McFiggans, G., and Archer-Nicholls, S., Best Practices for Applying WRF-Chem, URL http://ruc.noaa.gov/wrf/WG11/wrf_tutorial_2015/WRF_CHEM_bestpractices.pdf, last accessed: 2016/02/29, 2015.

Penner, J. E., Prather, M. J., Isaksen, I. S., Fuglestvedt, J. S., Klimont, Z., and Stevenson, D. S., Short-lived uncertainty?, *Nature Geoscience*, 3(9), 587–588, 2010.

Peters, G. P., Nilssen, T. B., Lindholt, L., Eide, M. S., Glomsrød, S., Eide, L. I., and Fuglestvedt, J. S., Future emissions from shipping and petroleum activities in the Arctic, *Atmospheric Chemistry and Physics*, 11(11), 5305–5320, doi: 10.5194/acp-11-5305-2011, URL http://www.atmos-chem-phys.net/11/5305/2011/, 2011.

Petty, G. W., *A first course in atmospheric radiation*, Sundog Publishing, 2006.

Petzold, A., Hasselbach, J., Lauer, P., Baumann, R., Franke, K., Gurk, C., Schlager, H., and Weingartner, E., Experimental studies on particle emissions from cruising ship, their characteristic properties, transformation and atmospheric lifetime in the marine boundary layer, *Atmospheric Chemistry and Physics*, 8(9), 2387–2403, doi: 10.5194/acp-8-2387-2008, URL http://www.atmos-chem-phys.net/8/2387/2008/, 2008.

Petzold, A., Ogren, J. A., Fiebig, M., Laj, P., Li, S.-M., Baltensperger, U., Holzer-Popp, T., Kinne, S., Pappalardo, G., Sugimoto, N., Wehrli, C., Wiedensohler, A., and Zhang, X.-Y., Recommendations for reporting "black carbon" measurements, *Atmospheric Chemistry and Physics*, 13(16), 8365–8379, doi: 10.5194/acp-13-8365-2013, URL http://www.atmos-chem-phys.net/13/8365/2013/, 2013.

Pilinis, C., Pandis, S. N., and Seinfeld, J. H., Sensitivity of direct climate forcing by atmospheric aerosols to aerosol size and composition, *Journal of Geophysical Research: Atmospheres*, 100(D9), 18739–18754, doi: 10.1029/95JD02119, URL http://dx.doi.org/10.1029/95JD02119, 1995.

Pommier, M., Law, K. S., Clerbaux, C., Turquety, S., Hurtmans, D., Hadji-Lazaro, J., Coheur, P.-F., Schlager, H., Ancellet, G., Paris, J.-D., Nédélec, P., Diskin, G. S., Podolske, J. R., Holloway, J. S., and Bernath, P., IASI carbon monoxide validation over the Arctic during POLARCAT spring and summer campaigns, *Atmospheric Chemistry and Physics*, 10(21), 10655–10678, doi: 10.5194/acp-10-10655-2010, URL http://www.atmos-chem-phys.net/10/10655/2010/, 2010.

Prank, M., Sofiev, M., Denier van der Gon, H. A. C., Kaasik, M., Ruuskanen, T. M., and Kukkonen, J., A refinement of the emission data for Kola Peninsula based on inverse dispersion modelling, *Atmospheric Chemistry and Physics*, 10(22), 10849–10865, doi: 10.5194/acp-10-10849-2010, URL http://www.atmos-chem-phys.net/10/10849/2010/, 2010.

Prowse, T. D., Furgal, C., Chouinard, R., Melling, H., Milburn, D., and Smith, S. L., Implications of Climate Change for Economic Development in Northern Canada: Energy, Resource, and Transportation Sectors, *AMBIO: A Journal of the Human Environment*, 38(5), 272–281, doi: 10.1579/0044-7447-38.5.272, URL http://dx.doi.org/10.1579/0044-7447-38.5.272, 2009.

Pueschel, R. and Kinne, S., Physical and radiative properties of Arctic atmospheric aerosols, *Science of The Total Environment*, 160–161, 811–824, doi: http://dx.doi.org/10.1016/0048-9697(95)04414-V, URL http://www.sciencedirect.com/science/article/pii/004896979504414V, ecological Effects of Arctic Airborne Contaminants, 1995.

Quennehen, B., *Etude des aérosols transportés en Arctique à partir des mesures aéroportées (ATR-42) du LaMP durant le projet POLARCART*, Ph.D. thesis, Université Blaise Pascal - Clermont-Ferrand II, 2011.

Quennehen, B., Raut, J.-C., Law, K. S., Ancellet, G., Clerbaux, C., Kim, S.-W., Lund, M. T., Myhre, G., Olivié, D. J. L., Safieddine, S., Skeie, R. B., Thomas, J. L., Tsyro, S., Bazureau, A., Bellouin, N., Daskalakis, N., Hu, M., Kanakidou, M., Klimont, Z., Kupiainen, K., Myriokefalitakis, S., Quaas, J., Rumbold, S. T., Schulz, M., Cherian, R., Shimizu, A., Wang, J., Yoon, S.-C., and Zhu, T., Multi-model evaluation of short-lived pollutant distributions over East Asia during summer 2008, *Atmospheric Chemistry and Physics Discussions*, 15, 11049–11109, doi: 10.5194/acpd-15-11049-2015, URL http://www.atmos-chem-phys-discuss.net/15/11049/2015/, 2015.

Quennehen, B., Schwarzenboeck, A., Matsuki, A., Burkhart, J. F., Stohl, A., Ancellet, G., and Law, K. S., Anthropogenic and forest fire pollution aerosol transported to the Arctic: observations from the POLARCAT-France spring campaign, *Atmospheric Chemistry and Physics*, 12(14), 6437–6454, doi: 10.5194/acp-12-6437-2012, URL http://www.atmos-chem-phys.net/12/6437/2012/, 2012.

Quennehen, B., Schwarzenboeck, A., Schmale, J., Schneider, J., Sodemann, H., Stohl, A., Ancellet, G., Crumeyrolle, S., and Law, K. S., Physical and chemical properties of pollution aerosol particles transported from North America to Greenland as measured during the POLARCAT summer campaign, *Atmospheric Chemistry and Physics*, 11(21), 10947–10963, doi: 10.5194/acp-11-10947-2011, URL http://www.atmos-chem-phys.net/11/10947/2011/, 2011.

Quinn, P. K., Bates, T. S., Baum, E., Doubleday, N., Fiore, A. M., Flanner, M., Fridlind, A., Garrett, T. J., Koch, D., Menon, S., Shindell, D., Stohl, A., and Warren, S. G., Short-lived pollutants in the Arctic: their climate impact and possible mitigation strategies, *Atmospheric Chemistry and Physics*, 8(6), 1723–1735, doi: 10.5194/acp-8-1723-2008, URL http://www.atmos-chem-phys.net/8/1723/2008/, 2008.

Quinn, P. K., Miller, T. L., Bates, T. S., Ogren, J. A., Andrews, E., and Shaw, G. E., A 3-year record of simultaneously measured aerosol chemical and optical properties at Barrow, Alaska, *Journal of Geophysical Research: Atmospheres*, 107(D11), AAC 8–1–AAC 8–15, doi: 10.1029/2001JD001248, URL http://dx.doi.org/10.1029/2001JD001248, 2002.

Quinn, P. K., Shaw, G., Andrews, E., Dutton, E. G., T., R.-A., and Gong, S. L., Arctic haze: current trends and knowledge gaps, *Tellus B*, 59(1), 99–114, doi: 10.1111/j.1600-0889.2006.00238.x, URL http://dx.doi.org/10.1111/j.1600-0889.2006.00238.x, 2007.

Rahn, K. A., Arctic Air Chemistry Proceedings of the Second Symposium Relative importances of North America and Eurasia as sources of arctic aerosol, *Atmospheric Environment (1967)*, 15(8), 1447–1455, doi: http://dx.doi.org/10.1016/0004-6981(81)90351-6, URL http://www.sciencedirect.com/science/article/pii/0004698181903516, 1981.

Rahn, K. A., Borys, R. D., and Shaw, G. E., The Asian source of Arctic haze bands, *Nature*, 268(5622), 713–715, URL http://dx.doi.org/10.1038/268713a0, 1977.

Rap, A., Richards, N. A. D., Forster, P. M., Monks, S. A., Arnold, S. R., and Chipperfield, M. P., Satellite constraint on the tropospheric ozone radiative effect, *Geophysical Research Letters*, 42(12), 5074–5081, doi: 10.1002/2015GL064037, URL http://dx.doi.org/10.1002/2015GL064037, 2015GL064037, 2015.

Raut, J.-C. and Chazette, P., Radiative budget in the presence of multi-layered aerosol structures in the framework of AMMA SOP-0, *Atmospheric Chemistry and Physics*, 8(22), 6839–6864, doi: 10.5194/acp-8-6839-2008, URL http://www.atmos-chem-phys.net/8/6839/2008/, 2008.

Reich, P. B., Effects of Low Concentrations of O3 on Net Photosynthesis, Dark Respiration, and Chlorophyll Contents in Aging Hybrid Poplar Leaves, *Plant Physiology*, 73(2), 291–296, doi: 10.1104/pp.73.2.291, URL http://www.plantphysiol.org/content/73/2/291.abstract, 1983.

Riahi, K., Rao, S., Krey, V., Cho, C., Chirkov, V., Fischer, G., Kindermann, G., Nakicenovic, N., and Rafaj, P., RCP 8.5—A scenario of comparatively high greenhouse gas emissions, *Climatic Change*, 109(1), 33–57, doi: 10.1007/s10584-011-0149-y, URL http://dx.doi.org/10.1007/s10584-011-0149-y, 2011.

RINA, *Significant Ships of 2009*, Pensord Press, Blackwood, UK, 2010.

Ripperton, L. A., Jeffries, H., and Worth, J. J. B., Natural synthesis of ozone in the troposphere, *Environmental Science & Technology*, 5(3), 246–248, doi: 10.1021/es60050a001, URL http://dx.doi.org/10.1021/es60050a001, 1971.

Robinson, A. L., Donahue, N. M., Shrivastava, M. K., Weitkamp, E. A., Sage, A. M., Grieshop, A. P., Lane, T. E., Pierce, J. R., and Pandis, S. N., Rethinking Organic Aerosols: Semivolatile Emissions and Photochemical Aging, *Science*, 315(5816), 1259–1262, doi: 10.1126/science.1133061, URL http://science.sciencemag.org/content/315/5816/1259, 2007.

Roiger, A., Thomas, J.-L., Schlager, H., Law, K. S., Kim, J., Schäfler, A., Weinzierl, B., Dahlkötter, F., Krisch, I., Marelle, L., Minikin, A., Raut, J.-C., Reiter, A., Rose, M., Scheibe, M., Stock, P., Baumann, R., Bouarar, I., Clerbaux, C., George, M., Onishi, T., and Flemming, J., Quantifying Emerging Local Anthropogenic Emissions in the Arctic Region: The ACCESS Aircraft Campaign Experiment, *Bull. Amer. Meteor. Soc.*, 96(3), 441–460, doi: 10.1175/BAMS-D-13-00169.1, URL http://dx.doi.org/10.1175/BAMS-D-13-00169.1, 2015.

Saide, P. E., Spak, S. N., Carmichael, G. R., Mena-Carrasco, M. A., Yang, Q., Howell, S., Leon, D. C., Snider, J. R., Bandy, A. R., Collett, J. L., Benedict, K. B., de Szoeke, S. P., Hawkins, L. N., Allen, G., Crawford, I., Crosier, J., and Springston, S. R., Evaluating WRF-Chem aerosol indirect effects in Southeast Pacific marine stratocumulus during VOCALS-REx, *Atmospheric Chemistry and Physics*, 12(6), 3045–3064, doi: 10.5194/acp-12-3045-2012, URL http://www.atmos-chem-phys.net/12/3045/2012/, 2012.

Saltzman, E. S., King, D. B., Holmen, K., and Leck, C., Experimental determination of the diffusion coefficient of dimethylsulfide in water, *Journal of Geophysical Research: Oceans*, 98(C9), 16481–16486, doi: 10.1029/93JC01858, URL http://dx.doi.org/10.1029/93JC01858, 1993.

Samset, B. H., Myhre, G., Herber, A., Kondo, Y., Li, S.-M., Moteki, N., Koike, M., Oshima, N., Schwarz, J. P., Balkanski, Y., Bauer, S. E., Bellouin, N., Berntsen, T. K., Bian, H., Chin, M., Diehl, T., Easter, R. C., Ghan, S. J., Iversen, T., Kirkevåg, A., Lamarque, J.-F., Lin, G., Liu, X., Penner, J. E., Schulz, M., Seland, Ø., Skeie, R. B., Stier, P., Takemura, T., Tsigaridis, K., and Zhang, K., Modelled black carbon radiative forcing and atmospheric lifetime in AeroCom Phase II constrained by aircraft observations, *Atmospheric Chemistry and Physics*, 14(22), 12465–12477, doi: 10.5194/acp-14-12465-2014, URL http://www.atmos-chem-phys.net/14/12465/2014/, 2014.

Sand, M., Berntsen, T. K., Seland, Ø., and Kristjánsson, J. E., Arctic surface temperature change to emissions of black carbon within Arctic or midlatitudes, *Journal of Geophysical Research: Atmospheres*, 118(14), 7788–7798, doi: 10.1002/jgrd.50613, URL http://dx.doi.org/10.1002/jgrd.50613, 2013.

Sandu, A., Verwer, J., Blom, J., Spee, E., Carmichael, G., and Potra, F., Benchmarking stiff ode solvers for atmospheric chemistry problems II: Rosenbrock solvers, *Atmospheric Environment*, 31(20), 3459–3472, doi: http://dx.doi.org/10.1016/S1352-2310(97)83212-8, URL http://www.sciencedirect.com/science/article/pii/S1352231097832128, 1997.

Schmale, J., Schneider, J., Ancellet, G., Quennehen, B., Stohl, A., Sodemann, H., Burkhart, J. F., Hamburger, T., Arnold, S. R., Schwarzenboeck, A., Borrmann, S., and Law, K. S., Source identification and airborne chemical characterisation of aerosol pollution from long-range transport over Greenland during POLARCAT summer campaign 2008, *Atmospheric Chemistry and Physics*, 11(19), 10097–10123, doi: 10.5194/acp-11-10097-2011, URL http://www.atmos-chem-phys.net/11/10097/2011/, 2011.

Schuster, G. L., Dubovik, O., Holben, B. N., and Clothiaux, E. E., Inferring black carbon content and specific absorption from Aerosol Robotic Network (AERONET) aerosol retrievals, *Journal of Geophysical Research: Atmospheres*, 110(D10), doi: 10.1029/2004JD004548, URL http://dx.doi.org/10.1029/2004JD004548, d10S17, 2005.

Schwarz, J. P., Spackman, J. R., Gao, R. S., Watts, L. A., Stier, P., Schulz, M., Davis, S. M., Wofsy, S. C., and Fahey, D. W., Global-scale black carbon profiles observed in the remote atmosphere

and compared to models, *Geophysical Research Letters*, 37(18), doi: 10.1029/2010GL044372, URL http://dx.doi.org/10.1029/2010GL044372, l18812, 2010.

Schwarzenboeck, A., Heintzenberg, J., and Mertes, S., Incorporation of aerosol particles between 25 and 850 nm into cloud elements: measurements with a new complementary sampling system, *Atmospheric Research*, 52(4), 241–260, doi: http://dx.doi.org/10.1016/S0169-8095(99)00034-4, URL http://www.sciencedirect.com/science/article/pii/S0169809599000344, 2000.

Seinfeld, J. H. and Pandis, S. N., *Atmospheric Chemistry and Physics Ð from Air Pollution to Climate Change*, Wiley-Interscience, New York, NY, 2006.

Serreze, M. C. and Barry, R. G., Processes and impacts of Arctic amplification: A research synthesis, *Global and Planetary Change*, 77(1–2), 85–96, doi: http://dx.doi.org/10.1016/j.gloplacha.2011.03.004, URL http://www.sciencedirect.com/science/article/pii/S0921818111000397, 2011.

Sessions, W. R., Fuelberg, H. E., Kahn, R. A., and Winker, D. M., An investigation of methods for injecting emissions from boreal wildfires using WRF-Chem during ARCTAS, *Atmospheric Chemistry and Physics*, 11(12), 5719–5744, doi: 10.5194/acp-11-5719-2011, URL http://www.atmos-chem-phys.net/11/5719/2011/, 2011.

Shaw, G. E., The Arctic Haze Phenomenon, *Bull. Amer. Meteor. Soc.*, 76(12), 2403–2413, doi: 10.1175/1520-0477(1995)076<2403:TAHP>2.0.CO;2, URL http://dx.doi.org/10.1175/1520-0477(1995)076<2403:TAHP>2.0.CO;2, 1995.

Shindell, D., Local and remote contributions to Arctic warming, *Geophysical Research Letters*, 34(14), doi: 10.1029/2007GL030221, URL http://dx.doi.org/10.1029/2007GL030221, l14704, 2007.

Shindell, D. and Faluvegi, G., Climate response to regional radiative forcing during the twentieth century, *Nature Geosci*, 2(4), 294–300, URL http://dx.doi.org/10.1038/ngeo473, 2009.

Shindell, D., Faluvegi, G., Lacis, A., Hansen, J., Ruedy, R., and Aguilar, E., Role of tropospheric ozone increases in 20th-century climate change, *Journal of Geophysical Research: Atmospheres*, 111(D8), doi: 10.1029/2005JD006348, URL http://dx.doi.org/10.1029/2005JD006348, d08302, 2006.

Shindell, D. T., Chin, M., Dentener, F., Doherty, R. M., Faluvegi, G., Fiore, A. M., Hess, P., Koch, D. M., MacKenzie, I. A., Sanderson, M. G., Schultz, M. G., Schulz, M., Stevenson, D. S., Teich, H., Textor, C., Wild, O., Bergmann, D. J., Bey, I., Bian, H., Cuvelier, C., Duncan, B. N., Folberth, G., Horowitz, L. W., Jonson, J., Kaminski, J. W., Marmer, E., Park, R., Pringle, K. J., Schroeder, S., Szopa, S., Takemura, T., Zeng, G., Keating, T. J., and Zuber, A., A multi-model assessment of pollution transport to the Arctic, *Atmospheric Chemistry and Physics*, 8(17), 5353–5372, doi: 10.5194/acp-8-5353-2008, URL http://www.atmos-chem-phys.net/8/5353/2008/, 2008.

Shrivastava, M., Easter, R. C., Liu, X., Zelenyuk, A., Singh, B., Zhang, K., Ma, P.-L., Chand, D., Ghan, S., Jimenez, J. L., Zhang, Q., Fast, J., Rasch, P. J., and Tiitta, P., Global transformation and fate of SOA: Implications of low-volatility SOA and gas-phase fragmentation reactions, *Journal of Geophysical Research: Atmospheres*, 120(9), 4169–4195, doi: 10.1002/2014JD022563, URL http://dx.doi.org/10.1002/2014JD022563, 2014JD022563, 2015.

Shrivastava, M., Fast, J., Easter, R., Gustafson Jr., W. I., Zaveri, R. A., Jimenez, J. L., Saide, P., and Hodzic, A., Modeling organic aerosols in a megacity: comparison of simple and complex representations of the volatility basis set approach, *Atmospheric Chemistry and Physics*, 11(13), 6639–6662, doi: 10.5194/acp-11-6639-2011, URL http://www.atmos-chem-phys.net/11/6639/2011/, 2011.

Shupe, M. D. and Intrieri, J. M., Cloud Radiative Forcing of the Arctic Surface: The Influence of Cloud Properties, Surface Albedo, and Solar Zenith Angle, *J. Climate*, 17(3), 616–628, doi: 10.1175/1520-0442(2004)017<0616:CRFOTA>2.0.CO;2, URL http://dx.doi.org/10.1175/1520-0442(2004)017<0616:CRFOTA>2.0.CO;2, 2004.

Sillman, S., The relation between ozone, NO_x and hydrocarbons in urban and polluted rural environments, *Atmospheric Environment*, 33(12), 1821 – 1845, doi: http://dx.doi.org/10.1016/S1352-2310(98)00345-8, URL http://www.sciencedirect.com/science/article/pii/S1352231098003458, 1999.

Sindelarova, K., Granier, C., Bouarar, I., Guenther, A., Tilmes, S., Stavrakou, T., Müller, J.-F., Kuhn, U., Stefani, P., and Knorr, W., Global data set of biogenic VOC emissions calculated by the MEGAN model over the last 30 years, *Atmospheric Chemistry and Physics*, 14(17), 9317–9341, doi: 10.5194/acp-14-9317-2014, URL http://www.atmos-chem-phys.net/14/9317/2014/, 2014.

Singh, H. B., Salas, L. J., and Viezee, W., Global distribution of peroxyacetyl nitrate, *Nature*, 321(6070), 588–591, URL http://dx.doi.org/10.1038/321588a0, 1986.

Sitch, S., Cox, P. M., Collins, W. J., and Huntingford, C., Indirect radiative forcing of climate change through ozone effects on the land-carbon sink, *Nature*, 448(7155), 791–794, URL http://dx.doi.org/10.1038/nature06059, 2007.

Skamarock, W. C., Klemp, J., Dudhia, J., Gill, D., Barker, D., Duda, M., Huang, X., Wang, W., and Powers., J., A description of the Advanced Research WRF Version 3, Technical report, NCAR, 2008.

Skamarock, W. C. and Klemp, J. B., The Stability of Time-Split Numerical Methods for the Hydrostatic and the Nonhydrostatic Elastic Equations, *Monthly Weather Review*, 120(9), 2109–2127, doi: 10.1175/1520-0493(1992)120<2109:TSOTSN>2.0.CO;2, URL http://dx.doi.org/10.1175/1520-0493(1992)120<2109:TSOTSN>2.0.CO;2, 1992.

Skamarock, W. C., Klemp, J. B., Duda, M. G., Fowler, L. D., Park, S.-H., and Ringler, T. D., A Multiscale Nonhydrostatic Atmospheric Model Using Centroidal Voronoi Tesselations and C-Grid Staggering, *Monthly Weather Review*, 140(9), 3090–3105, doi: 10.1175/MWR-D-11-00215.1, URL http://dx.doi.org/10.1175/MWR-D-11-00215.1, 2012.

Smith, L. C. and Stephenson, S. R., New Trans-Arctic shipping routes navigable by midcentury, *Proceedings of the National Academy of Sciences*, 110(13), 1191–1195, doi: 10.1073/pnas.1214212110, URL http://www.pnas.org/content/110/13/E1191.abstract, 2013.

Solberg, S., Dye, C., Schmidbauer, N., Herzog, A., and Gehrig, R., Carbonyls and nonmethane hydrocarbons at rural European sites from the mediterranean to the arctic, *Journal of Atmospheric Chemistry*, 25(1), 33–66, doi: 10.1007/BF00053285, URL http://dx.doi.org/10.1007/BF00053285, 1996.

Somanathan, S., Flynn, P., and Szymanski, J., The Northwest Passage: A simulation, *Transportation Research Part A: Policy and Practice*, 43(2), 127–135, doi: http://dx.doi.org/10.1016/j.tra.2008.08.001, URL http://www.sciencedirect.com/science/article/pii/S0965856408001444, 2009.

Spracklen, D. V., Jimenez, J. L., Carslaw, K. S., Worsnop, D. R., Evans, M. J., Mann, G. W., Zhang, Q., Canagaratna, M. R., Allan, J., Coe, H., McFiggans, G., Rap, A., and Forster, P., Aerosol mass spectrometer constraint on the global secondary organic aerosol budget, *Atmospheric Chemistry and Physics*, 11(23), 12109–12136, doi: 10.5194/acp-11-12109-2011, URL http://www.atmos-chem-phys.net/11/12109/2011/, 2011.

Stevenson, D. S., Dentener, F. J., Schultz, M. G., Ellingsen, K., van Noije, T. P. C., Wild, O., Zeng, G., Amann, M., Atherton, C. S., Bell, N., Bergmann, D. J., Bey, I., Butler, T., Cofala, J., Collins, W. J., Derwent, R. G., Doherty, R. M., Drevet, J., Eskes, H. J., Fiore, A. M., Gauss, M., Hauglustaine, D. A., Horowitz, L. W., Isaksen, I. S. A., Krol, M. C., Lamarque, J.-F., Lawrence, M. G., Montanaro, V., Müller, J.-F., Pitari, G., Prather, M. J., Pyle, J. A., Rast, S., Rodriguez, J. M., Sanderson, M. G., Savage, N. H., Shindell, D. T., Strahan, S. E., Sudo, K., and Szopa, S., Multimodel ensemble simulations of present-day and near-future tropospheric ozone, *Journal of Geophysical Research: Atmospheres*, 111(D8), doi: 10.1029/2005JD006338, URL http://dx.doi.org/10.1029/2005JD006338, d08301, 2006.

Stevenson, D. S., Young, P. J., Naik, V., Lamarque, J.-F., Shindell, D. T., Voulgarakis, A., Skeie, R. B., Dalsoren, S. B., Myhre, G., Berntsen, T. K., Folberth, G. A., Rumbold, S. T., Collins, W. J., MacKenzie, I. A., Doherty, R. M., Zeng, G., van Noije, T. P. C., Strunk, A., Bergmann, D., Cameron-Smith, P., Plummer, D. A., Strode, S. A., Horowitz, L., Lee, Y. H., Szopa, S., Sudo, K., Nagashima, T., Josse, B., Cionni, I., Righi, M., Eyring, V., Conley, A., Bowman, K. W., Wild, O., and Archibald, A., Tropospheric ozone changes, radiative forcing and attribution to emissions in the Atmospheric Chemistry and Climate Model Intercomparison Project (ACCMIP), *Atmospheric Chemistry and Physics*, 13(6), 3063–3085, doi: 10.5194/acp-13-3063-2013, URL http://www.atmos-chem-phys.net/13/3063/2013/, 2013.

Stewart, E., Howell, S., Draper, D., Yackel, J., and Tivy, A., Sea Ice in Canada's Arctic: Implications for Cruise Tourism, *ARCTIC*, 60(4), 370–380, doi: 10.14430/arctic194, URL http://arctic.journalhosting.ucalgary.ca/arctic/index.php/arctic/article/view/194, 2009.

Stohl, A., Characteristics of atmospheric transport into the Arctic troposphere, *Journal of Geophysical Research: Atmospheres*, 111(D11), doi: 10.1029/2005JD006888, URL http://dx.doi.org/10.1029/2005JD006888, d11306, 2006.

Stohl, A., Aamaas, B., Amann, M., Baker, L. H., Bellouin, N., Berntsen, T. K., Boucher, O., Cherian, R., Collins, W., Daskalakis, N., Dusinska, M., Eckhardt, S., Fuglestvedt, J. S., Harju, M., Heyes, C., Hodnebrog, Ø., Hao, J., Im, U., Kanakidou, M., Klimont, Z., Kupiainen, K., Law, K. S., Lund, M. T., Maas, R., MacIntosh, C. R., Myhre, G., Myriokefalitakis, S., Olivié, D., Quaas, J., Quennehen, B., Raut, J.-C., Rumbold, S. T., Samset, B. H., Schulz, M., Seland, Ø., Shine, K. P., Skeie, R. B., Wang, S., Yttri, K. E., and Zhu, T., Evaluating the climate and air quality impacts of short-lived pollutants, *Atmospheric Chemistry and Physics*, 15(18), 10529–10566, doi: 10.5194/acp-15-10529-2015, URL http://www.atmos-chem-phys.net/15/10529/2015/, 2015.

Stohl, A., Berg, T., Burkhart, J. F., Fjæraa, A. M., Forster, C., Herber, A., Hov, Ø., Lunder, C., McMillan, W. W., Oltmans, S., Shiobara, M., Simpson, D., Solberg, S., Stebel, K., Ström, J., Tørseth, K., Treffeisen, R., Virkkunen, K., and Yttri, K. E., Arctic smoke – record high air pollution levels in the European Arctic due to agricultural fires in Eastern Europe in spring 2006, *Atmospheric Chemistry and Physics*, 7(2), 511–534, doi: 10.5194/acp-7-511-2007, URL http://www.atmos-chem-phys.net/7/511/2007/, 2007.

Stohl, A., Forster, C., Frank, A., Seibert, P., and Wotawa, G., Technical note: The Lagrangian particle dispersion model FLEXPART version 6.2, *Atmospheric Chemistry and Physics*, 5(9), 2461–2474, doi: 10.5194/acp-5-2461-2005, URL http://www.atmos-chem-phys.net/5/2461/2005/, 2005.

Stohl, A., Klimont, Z., Eckhardt, S., Kupiainen, K., Shevchenko, V. P., Kopeikin, V. M., and Novigatsky, A. N., Black carbon in the Arctic: the underestimated role of gas flaring and residential combustion emissions, *Atmospheric Chemistry and Physics*, 13(17), 8833–8855, doi: 10.5194/acp-13-8833-2013, URL http://www.atmos-chem-phys.net/13/8833/2013/, 2013.

Stroeve, J., Holland, M. M., Meier, W., Scambos, T., and Serreze, M., Arctic sea ice decline: Faster than forecast, *Geophysical Research Letters*, 34(9), doi: 10.1029/2007GL029703, URL http://dx.doi.org/10.1029/2007GL029703, l09501, 2007.

Stroeve, J. C., Serreze, M. C., Holland, M. M., Kay, J. E., Malanik, J., and Barrett, A. P., The Arctic's rapidly shrinking sea ice cover: a research synthesis, *Climatic Change*, 110(3), 1005–1027, doi: 10.1007/s10584-011-0101-1, URL http://dx.doi.org/10.1007/s10584-011-0101-1, 2011.

Takacs, L. L., Sawyer, W., Suarez, M. J., and Fox-Rabinowitz, M. S., Technical Report Series on Global Modeling and Data Assimilation. Volume 16; Filtering Techniques on a Stretched Grid General Circulation Model, Technical Report NASA/TM-1999-104606/VOL16, NAS 1.15:104606/VOL16, Rept-2000-00443-0, NASA Goddard Space Flight Center, Greenbelt, MD United States, 1999.

Tanskanen, A. and Manninen, T., Effective UV surface albedo of seasonally snow-covered lands, *Atmospheric Chemistry and Physics*, 7(10), 2759–2764, doi: 10.5194/acp-7-2759-2007, URL http://www.atmos-chem-phys.net/7/2759/2007/, 2007.

Tessum, C. W., Hill, J. D., and Marshall, J. D., Twelve-month, 12 km resolution North American WRF-Chem v3.4 air quality simulation: performance evaluation, *Geoscientific Model Development*, 8(4), 957–973, doi: 10.5194/gmd-8-957-2015, URL http://www.geosci-model-dev.net/8/957/2015/, 2015.

Textor, C., Schulz, M., Guibert, S., Kinne, S., Balkanski, Y., Bauer, S., Berntsen, T., Berglen, T., Boucher, O., Chin, M., Dentener, F., Diehl, T., Easter, R., Feichter, H., Fillmore, D., Ghan, S., Ginoux, P., Gong, S., Grini, A., Hendricks, J., Horowitz, L., Huang, P., Isaksen, I., Iversen, I., Kloster, S., Koch, D., Kirkevåg, A., Kristjansson, J. E., Krol, M., Lauer, A., Lamarque, J. F., Liu, X., Montanaro, V., Myhre, G., Penner, J., Pitari, G., Reddy, S., Seland, Ø., Stier, P., Takemura, T., and Tie, X., Analysis and quantification of the diversities of aerosol life cycles within AeroCom, *Atmospheric Chemistry and Physics*, 6(7), 1777–1813, doi: 10.5194/acp-6-1777-2006, URL http://www.atmos-chem-phys.net/6/1777/2006/, 2006.

Thomas, J. L., Raut, J.-C., Law, K. S., Marelle, L., Ancellet, G., Ravetta, F., Fast, J. D., Pfister, G., Emmons, L. K., Diskin, G. S., Weinheimer, A., Roiger, A., and Schlager, H., Pollution transport from North America to Greenland during summer 2008, *Atmospheric Chemistry and Physics*, 13(7), 3825–3848, doi: 10.5194/acp-13-3825-2013, URL http://www.atmos-chem-phys.net/13/3825/2013/, 2013.

Toon, O. B. and Ackerman, T. P., Algorithms for the calculation of scattering by stratified spheres, *Appl. Opt.*, 20(20), 3657–3660, doi: 10.1364/AO.20.003657, URL http://ao.osa.org/abstract.cfm?URI=ao-20-20-3657, 1981.

Trenberth, K. E., Fasullo, J. T., and Kiehl, J., Earth's Global Energy Budget, *Bull. Amer. Meteor. Soc.*, 90(3), 311–323, doi: 10.1175/2008BAMS2634.1, URL http://dx.doi.org/10.1175/2008BAMS2634.1, 2009.

Tuccella, P., Curci, G., Visconti, G., Bessagnet, B., Menut, L., and Park, R. J., Modeling of gas and aerosol with WRF/Chem over Europe: Evaluation and sensitivity study, *Journal of Geophysical Research: Atmospheres*, 117(D3), doi: 10.1029/2011JD016302, URL http://dx.doi.org/10.1029/2011JD016302, d03303, 2012.

Turpin, B. J., Saxena, P., and Andrews, E., Measuring and simulating particulate organics in the atmosphere: problems and prospects, *Atmospheric Environment*, 34(18), 2983–3013, doi: http://dx.doi.org/10.1016/S1352-2310(99)00501-4, URL http://www.sciencedirect.com/science/article/pii/S1352231099005014, 2000.

Twomey, S., The Influence of Pollution on the Shortwave Albedo of Clouds, *J. Atmos. Sci.*, 34(7), 1149–1152, doi: 10.1175/1520-0469(1977)034<1149:TIOPOT>2.0.CO;2, URL http://dx.doi.org/10.1175/1520-0469(1977)034<1149:TIOPOT>2.0.CO;2, 1977.

Vaughan, D., Comiso, J., Allison, I., Carrasco, J., Kaser, G., Kwok, R., Mote, P., Murray, T., Paul, F., Ren, J., Rignot, E., Solomina, O., Steffen, K., and Zhang, T., *Observations: Cryosphere*, book section 4, pp. 317–382, Cambridge University Press, Cambridge, United Kingdom and New York, NY, USA, ISBN ISBN 978-1-107-66182-0, doi: 10.1017/CBO9781107415324.012, URL www.climatechange2013.org, 2013.

Vinken, G. C. M., Boersma, K. F., Jacob, D. J., and Meijer, E. W., Accounting for non-linear chemistry of ship plumes in the GEOS-Chem global chemistry transport model, *Atmospheric Chemistry and Physics*, 11(22), 11707–11722, doi: 10.5194/acp-11-11707-2011, URL http://www.atmos-chem-phys.net/11/11707/2011/, 2011.

Virkkula, A., Hillamo, R. E., Kerminen, V. M., and Stohl, A., The influence of Kola Peninsula, continental European and marine sources on the number concentrations and scattering coefficients of the atmospheric aerosol in Finnish Lapland, *Boreal Environ. Res.*, 2, 317–336, 1997.

Wang, H., Easter, R. C., Rasch, P. J., Wang, M., Liu, X., Ghan, S. J., Qian, Y., Yoon, J.-H., Ma, P.-L., and Vinoj, V., Sensitivity of remote aerosol distributions to representation of cloud-aerosol interactions in a global climate model, *Geoscientific Model Development*, 6(3), 765–782, doi: 10.5194/gmd-6-765-2013, URL http://www.geosci-model-dev.net/6/765/2013/, 2013.

Wang, H., Rasch, P. J., Easter, R. C., Singh, B., Zhang, R., Ma, P.-L., Qian, Y., Ghan, S. J., and Beagley, N., Using an explicit emission tagging method in global modeling of source-receptor relationships for black carbon in the Arctic: Variations, sources, and transport pathways, *Journal of Geophysical Research: Atmospheres*, 119(22), 12,888–12,909, doi: 10.1002/2014JD022297, URL http://dx.doi.org/10.1002/2014JD022297, 2014JD022297, 2014a.

Wang, H., Skamarock, W. C., and Feingold, G., Evaluation of Scalar Advection Schemes in the Advanced Research WRF Model Using Large-Eddy Simulations of Aerosol-Cloud Interactions, *Monthly Weather Review*, 137(8), 2547–2558, doi: 10.1175/2009MWR2820.1, URL http://dx.doi.org/10.1175/2009MWR2820.1, 2009.

Wang, J., Cubison, M. J., Aiken, A. C., Jimenez, J. L., and Collins, D. R., The importance of aerosol mixing state and size-resolved composition on CCN concentration and the variation of the importance with atmospheric aging of aerosols, *Atmospheric Chemistry and Physics*, 10(15), 7267–7283, doi: 10.5194/acp-10-7267-2010, URL http://www.atmos-chem-phys.net/10/7267/2010/, 2010.

Wang, M. and Overland, J. E., A sea ice free summer Arctic within 30 years: An update from CMIP5 models, *Geophysical Research Letters*, 39(18), doi: 10.1029/2012GL052868, URL http://dx.doi.org/10.1029/2012GL052868, l18501, 2012.

Wang, Q., Jacob, D. J., Fisher, J. A., Mao, J., Leibensperger, E. M., Carouge, C. C., Le Sager, P., Kondo, Y., Jimenez, J. L., Cubison, M. J., and Doherty, S. J., Sources of carbonaceous aerosols and deposited black carbon in the Arctic in winter-spring: implications for radiative forcing, *Atmospheric Chemistry and Physics*, 11(23), 12453–12473, doi: 10.5194/acp-11-12453-2011, URL http://www.atmos-chem-phys.net/11/12453/2011/, 2011.

Wang, Q., Jacob, D. J., Spackman, J. R., Perring, A. E., Schwarz, J. P., Moteki, N., Marais, E. A., Ge, C., Wang, J., and Barrett, S. R. H., Global budget and radiative forcing of black carbon aerosol: Constraints from pole-to-pole (HIPPO) observations across the Pacific, *Journal of Geophysical Research: Atmospheres*, 119(1), 195–206, doi: 10.1002/2013JD020824, URL http://dx.doi.org/10.1002/2013JD020824, 2013JD020824, 2014b.

Warneke, C., Bahreini, R., Brioude, J., Brock, C. A., de Gouw, J. A., Fahey, D. W., Froyd, K. D., Holloway, J. S., Middlebrook, A., Miller, L., Montzka, S., Murphy, D. M., Peischl, J., Ryerson, T. B., Schwarz, J. P., Spackman, J. R., and Veres, P., Biomass burning in Siberia and Kazakhstan as an important source for haze over the Alaskan Arctic in April 2008, *Geophysical Research*

Letters, 36(2), doi: 10.1029/2008GL036194, URL http://dx.doi.org/10.1029/2008GL036194, l02813, 2009.

Warneke, C., Froyd, K. D., Brioude, J., Bahreini, R., Brock, C. A., Cozic, J., de Gouw, J. A., Fahey, D. W., Ferrare, R., Holloway, J. S., Middlebrook, A. M., Miller, L., Montzka, S., Schwarz, J. P., Sodemann, H., Spackman, J. R., and Stohl, A., An important contribution to springtime Arctic aerosol from biomass burning in Russia, *Geophysical Research Letters*, 37(1), doi: 10.1029/2009GL041816, URL http://dx.doi.org/10.1029/2009GL041816, l01801, 2010.

Warren, S. G. and Wiscombe, W. J., A Model for the Spectral Albedo of Snow. II: Snow Containing Atmospheric Aerosols, *J. Atmos. Sci.*, 37(12), 2734–2745, doi: 10.1175/1520-0469(1980)037<2734:AMFTSA>2.0.CO;2, URL http://dx.doi.org/10.1175/1520-0469(1980)037<2734:AMFTSA>2.0.CO;2, 1980.

Wesely, M., Parameterization of surface resistances to gaseous dry deposition in regional-scale numerical models, *Atmospheric Environment (1967)*, 23(6), 1293–1304, doi: http://dx.doi.org/10.1016/0004-6981(89)90153-4, URL http://www.sciencedirect.com/science/article/pii/0004698189901534, 1989.

Wespes, C., Emmons, L., Edwards, D. P., Hannigan, J., Hurtmans, D., Saunois, M., Coheur, P.-F., Clerbaux, C., Coffey, M. T., Batchelor, R. L., Lindenmaier, R., Strong, K., Weinheimer, A. J., Nowak, J. B., Ryerson, T. B., Crounse, J. D., and Wennberg, P. O., Analysis of ozone and nitric acid in spring and summer Arctic pollution using aircraft, ground-based, satellite observations and MOZART-4 model: source attribution and partitioning, *Atmospheric Chemistry and Physics*, 12(1), 237–259, doi: 10.5194/acp-12-237-2012, URL http://www.atmos-chem-phys.net/12/237/2012/, 2012.

Wexler, A. S., Lurmann, F. W., and Seinfeld, J. H., Modelling urban and regional aerosolsâ Part I - Model development, *Atmospheric Environment*, 28(3), 531–546, doi: http://dx.doi.org/10.1016/1352-2310(94)90129-5, URL http://www.sciencedirect.com/science/article/pii/1352231094901295, 1994.

WHO, Burden of disease from Ambient Air Pollution for 2012, URL http://www.who.int/phe/health_topics/outdoorair/databases/FINAL_HAP_AAP_BoD_24March2014.pdf, (last accessed: 2016/01/17), 2014.

Wiedinmyer, C., Akagi, S. K., Yokelson, R. J., Emmons, L. K., Al-Saadi, J. A., Orlando, J. J., and Soja, A. J., The Fire INventory from NCAR (FINN): a high resolution global model to estimate the emissions from open burning, *Geoscientific Model Development*, 4(3), 625–641, doi: 10.5194/gmd-4-625-2011, URL http://www.geosci-model-dev.net/4/625/2011/, 2011.

Wiedinmyer, C., Quayle, B., Geron, C., Belote, A., McKenzie, D., Zhang, X., Oâ Neill, S., and Wynne, K. K., Estimating emissions from fires in North America for air quality modeling, *Atmospheric Environment*, 40(19), 3419–3432, doi: http://dx.doi.org/10.1016/j.atmosenv.2006.02.010, URL http://www.sciencedirect.com/science/article/pii/S1352231006002032, 2006.

Wiedinmyer, C., Yokelson, R. J., and Gullett, B. K., Global Emissions of Trace Gases, Particulate Matter, and Hazardous Air Pollutants from Open Burning of Domestic Waste, *Environmental Science & Technology*, 48(16), 9523–9530, doi: 10.1021/es502250z, URL http://dx.doi.org/10.1021/es502250z, pMID: 25019173, 2014.

Wild, O., Modelling the global tropospheric ozone budget: exploring the variability in current models, *Atmospheric Chemistry and Physics*, 7(10), 2643–2660, doi: 10.5194/acp-7-2643-2007, URL http://www.atmos-chem-phys.net/7/2643/2007/, 2007.

Wild, O. and Akimoto, H., Intercontinental transport of ozone and its precursors in a three-dimensional global CTM, *Journal of Geophysical Research: Atmospheres*, 106(D21), 27729–27744, doi: 10.1029/2000JD000123, URL http://dx.doi.org/10.1029/2000JD000123, 2001.

Wild, O., Zhu, X., and Prather, M. J., Fast-J: Accurate Simulation of In- and Below-Cloud Photolysis in Tropospheric Chemical Models, *Journal of Atmospheric Chemistry*, 37(3), 245–282, doi: 10.1023/A:1006415919030, URL http://dx.doi.org/10.1023/A:1006415919030, 2000.

Winebrake, J. J., Corbett, J. J., Green, E. H., Lauer, A., and Eyring, V., Mitigating the Health Impacts of Pollution from Oceangoing Shipping: An Assessment of Low-Sulfur Fuel Mandates, *Environmental Science & Technology*, 43(13), 4776–4782, doi: 10.1021/es803224q, URL http://dx.doi.org/10.1021/es803224q, pMID: 19673264, 2009.

Winther, M., Christensen, J. H., Plejdrup, M. S., Ravn, E. S., Eriksson, Ó. F., and Kristensen, H. O., Emission inventories for ships in the arctic based on satellite sampled AIS data, *Atmospheric Environment*, 91, 1–14, doi: http://dx.doi.org/10.1016/j.atmosenv.2014.03.006, URL http://www.sciencedirect.com/science/article/pii/S1352231014001678, 2014.

Yang, Q., Jr., W. I. G., Fast, J. D., Wang, H., Easter, R. C., Morrison, H., Lee, Y.-N., Chapman, E. G., Spak, S. N., and Mena-Carrasco, M. A., Assessing regional scale predictions of aerosols, marine stratocumulus, and their interactions during VOCALS-REx using WRF-Chem, *Atmospheric Chemistry and Physics*, 11(23), 11951–11975, doi: 10.5194/acp-11-11951-2011, URL http://www.atmos-chem-phys.net/11/11951/2011/, 2011.

Zaveri, R. A., Easter, R. C., Fast, J. D., and Peters, L. K., Model for Simulating Aerosol Interactions and Chemistry (MOSAIC), *Journal of Geophysical Research: Atmospheres*, 113(D13), doi: 10.1029/2007JD008782, URL http://dx.doi.org/10.1029/2007JD008782, d13204, 2008.

Zaveri, R. A. and Peters, L. K., A new lumped structure photochemical mechanism for large-scale applications, *Journal of Geophysical Research: Atmospheres*, 104(D23), 30387–30415, doi: 10.1029/1999JD900876, URL http://dx.doi.org/10.1029/1999JD900876, 1999.

Zhang, D. and Anthes, R. A., A High-Resolution Model of the Planetary Boundary Layer – Sensitivity Tests and Comparisons with SESAME-79 Data, *Journal of Applied Meteorology*, 21(11), 1594–1609, doi: 10.1175/1520-0450(1982)021<1594:AHRMOT>2.0.CO;2, URL http://dx.doi.org/10.1175/1520-0450(1982)021<1594:AHRMOT>2.0.CO;2, 1982.

Zhang, Y., Sartelet, K., Wu, S.-Y., and Seigneur, C., Application of WRF/Chem-MADRID and WRF/Polyphemus in Europe - Part 1: Model description, evaluation of meteorological predictions, and aerosol-meteorology interactions, *Atmospheric Chemistry and Physics*, 13(14), 6807–6843, doi: 10.5194/acp-13-6807-2013, URL http://www.atmos-chem-phys.net/13/6807/2013/, 2013a.

Zhang, Y., Sartelet, K., Zhu, S., Wang, W., Wu, S.-Y., Zhang, X., Wang, K., Tran, P., Seigneur, C., and Wang, Z.-F., Application of WRF/Chem-MADRID and WRF/Polyphemus in Europe - Part 2: Evaluation of chemical concentrations and sensitivity simulations, *Atmospheric Chemistry and Physics*, 13(14), 6845–6875, doi: 10.5194/acp-13-6845-2013, URL http://www.atmos-chem-phys.net/13/6845/2013/, 2013b.

Zhao, C. and Garrett, T. J., Effects of Arctic haze on surface cloud radiative forcing, *Geophysical Research Letters*, 42(2), 557–564, doi: 10.1002/2014GL062015, URL http://dx.doi.org/10.1002/2014GL062015, 2014GL062015, 2015.